Alma Mater Studiorum – Università di Bologna

DOTTORATO DI RICERCA IN

FISICA

Ciclo 35

Settore Concorsuale: 02/B1 – FISICA SPERIMENTALE DELLA MATERIA

Settore Scientifico Disciplinare: FIS/03 – FISICA DELLA MATERIA

HYBRID LEAD-HALIDE PEROVSKITES AS NOVEL MATERIALS FOR THIN FILM DIRECT AND FLEXIBLE IONIZING RADIATION DETECTORS

Presentata da: Matteo Verdi

Coordinatore Dottorato

Prof. Michele Cicoli

Supervisore

Prof. Beatrice Fraboni

Co-Supervisore

Dr. Andrea Ciavatti

Esame finale anno 2023

Abstract

Ionizing radiation fields are important tools employed every day in the modern society. In medicine they are routinely used for diagnostic and therapy, to treat cancer in addition to other diseases. In civil security for controls in airports and other sensitive targets. In scientific research, ionizing radiation is used and studied to see the invisible, design new materials and explore the universe. The large variety of applications leads to the need of novel, more efficient, low-cost ionizing radiation detectors with new functionalities. Personal dosimetry and dose monitoring would benefit from wearable detectors able to conform to the body surfaces. Traditional semiconductors used for ionizing radiation direct detectors, like Si, CZT and α-Se, offer high level performance but they are intrinsically stiff, brittle and require high voltages to operate. Moreover, their fabrication requires high energy budget process involving high temperatures and vacuum deposition techniques hard to scale up. Hybrid lead-halide perovskites emerged recently as a novel class of materials for ionizing radiation detection. They combine high absorption coefficient of radiation, solution processability through printing techniques and high charge transport capability, enabling efficient and low-cost detection. The deposition from solution allows the fabrication of thin-film flexible devices that can be developed for the creation of wearable detectors. In this thesis, I

designed, realized and studied the detection properties of different types of hybrid perovskites, deposited from solution in thin film form, and tested under X-rays, gamma-rays and protons beams. I developed the first ultraflexible X-ray detector with exceptional conformability by studying the perovskite/interlayers interfaces and identifying the best conditions. The effect of coupling organic layers with perovskites was studied at the nanoscale giving a direct demonstration of trap passivation effect at the grain boundaries. Different perovskite formulations and the effect of additives in the starting solution were deposited and tested to improve the film stability. I report about the longest aging studies on perovskite X-ray detectors showing that the addition of starch in the precursors' solution can improve the stability in time with only a 7% decrease in sensitivity after 630 days of storage in ambient conditions. 2D perovskites were also explored as direct detector for X-rays and gamma-rays. Detection of 511 keV photons by a thin-film device is here demonstrated and was validated for monitoring a radiotracer injection. At last, a new approach has been used that combines the low dark current of 2D perovskite and the high charge transport of the 3D one: a 2D/3Dmixed perovskite thin film demonstrated to reliably detect 5 MeV protons, envisioning wearable dose monitoring during proton/hadron therapy treatments.

Contents

Introduction

The detection of ionizing radiation is vital for the development of several fields of extreme importance for humankind. Ionizing radiation is continuously used and has a huge impact on people's daily lives. In the medical field, they are used to diagnose and treat tumours, the second cause of death in the developed countries. X-rays are used for public security controls in airports and other sensitive targets. In scientific research, ionizing radiations are employed from astrophysics to nanoscience to explore the biggest and the tiniest objects in the universe. Despite the potential risk of ionizing radiation for the human body, several professionals deal with them every day. Therefore, monitoring workers and environments with intense radiation field risk is of extreme importance. Ionizing radiation detectors are used by astronauts to understand the effects on the human body of prolonged period in space creating the basis for future long space travels. In many of these application, new requirements for radiation detectors recently emerged: mechanical flexibility and conformability, portability, low-power operation and low-cost fabrication processes. If these requirements were properly addressed, they could lead to the realization of innovative and extremely needed wearable ionizing radiation sensors, appealing devices for improved dose monitoring, patient's and worker's comfort and safety. Hence, in the last decades a huge effort has been done by the scientific community to find new materials, processes and technologies able to achieve the novel emerging requirements since traditional semiconductors cannot. The recent development of organic and hybrid semiconductor materials as well

as flexible electronics offers new opportunities for the progress of innovative radiation sensors.

The most used traditional semiconductor for large area radiation detection is amorphous silicon (α-Si), used coupled with a scintillating material. Instead, amorphous selenium (α-Se) is used in flat-panels for the direct detection of ionizing radiation. Direct α-Se detectors offer a high spatial resolution compared to α-Si but they require high voltage to operate effectively, making the technology impossible to be portable. Polycrystalline cadmium zinc telluride (poly-CZT) is an interesting alternative thanks to its high effective atomic number and good transport properties. However, these inorganic semiconductors are fabricated with high energy budget processes involving high temperatures and high vacuum facilities, difficult to scale up. Moreover, they are intrinsically stiff and the fabrication techniques make them incompatible with flexible plastic substrates. As an alternative, organic semiconductors have been recently used for realizing solution-grown direct ionizing radiation sensors, deposited over large areas at low temperatures and thus onto plastic flexible substrates. Organic semiconductors operate at extremely low-voltage and with huge signal gain, however, the low absorption coefficient to X-rays and the slow time response limit their applications.

In this thesis, I explored hybrid lead-halide perovskites as novel materials for thin-film based flexible direct ionizing radiation detectors. Since 2015 hybrid lead-halide perovskites have attracted increasing attention because of their exceptional optoelectronic properties: high absorption coefficient and great charge transport even in polycrystalline films. Moreover, perovskite can be deposited over large flexible plastic substrates with low-cost scalable printing techniques at low temperature, reducing the production cost.

The first chapter discusses the main figures of merit of ionizing radiations and focuses on their operating principles. The different types of ionizing radiation and their applications in modern society are reviewed. For the most important medical applications, a description of the more relevant techniques and relative ionizing radiation used is given. The last part of the chapter describes the interaction of different types of radiations with matter, and explains the direct and indirect detection mode for solid-state detectors. Example of traditional semiconductor-based detectors are discussed.

The second chapter is focused on hybrid lead-halide perovskite as novel material for direct ionizing radiation detection. The perovskite structure is described differentiating between 3D and 2D lead-halide perovskites. One of the advantage of perovskites is the large variety of fabrication techniques available; the fabrication processes, for both single crystals and films, used in literature to fabricate perovskite ionizing radiation detectors are reported. The properties that make them interesting candidates for future applications in radiation detectors are reviewed together with the main degradation mechanisms. The most important results recently reported in the literature are summarized and discussed, providing an update on the state-of-the-art of the technology.

In the third chapter the experimental methods are described, starting from the fabrication techniques used for the fabrication of the detectors here employed. Two structures were analysed: photoconductor and photodiode architectures. In all the devices tested, the perovskites as well as most of the material used are solution deposited, to demonstrate the possible scalability. The experimental techniques employed to study the materials properties and the ionizing radiation sources utilized are explained. The final part of the chapter illustrates the apparatus used at synchrotron facilities to study perovskite materials.

The experimental results on 3D perovskite thin-films for direct X-ray detection are presented in chapter 4. In thin-film devices, understanding the role of interfaces is fundamental. Perovskite photodiodes with different interfaces and materials were fabricated in collaboration with the Johannes Kepler University in Linz, Austria. This study elucidates the effect of different perovskite/interface materials have on the X-ray detection performances by characterizing, for different structures, sensitivity, Limit of Detection and dark current. In this framework the first ultraflexible X-ray detector was fabricated by employing ultra-thin plastic foil substrates. Moreover, I studied the role of phenyl-C61-butyric acid methyl ester (PCBM), a widely used perovskite interfacing material, on the detection performance and degradation of X-ray photoconductors. The experiments were conducted at the European Synchrotron Radiation Facility (ESRF) in collaboration with the Istituto Italiano di Tecnologia (IIT) of Milan.

The following chapter 5 reports about strategies to improve the detector stability. Despite the high performances of 3D hybrid perovskites, their use in real-lfe applications is limited by their poor environmental stability. Here different perovskite formulations have been explored to achieve stable devices operating in air, in collaboration with the Istituto per lo Studio di Materiali Nanostrutturati (CNR-ISMN). Further, in collaboration with the CNR-NANOTECH I studied a new perovskite formulation with starch as an additive with exceptional air stability. The detector response was monitored for 1.7 years finding only a 7% degradation, and thus providing the current record performance for unencapsulated thin-film perovskite X-ray detectors.

In chapter 6 the results about 2D and mixed 3D/2D perovskite are shown. 2D perovskites offers some advantages like the high environmental stability and the extremely low dark current when compared to 3D perovskites. Here the results on the 2D perovskite PEA_2PbBr_4 used as absorbing layer in a photoconductor geometry are reported and discussed. Thin-films obtained by spin-coating were characterized under

high energy X-rays (150 kVp) shoving high stability under operation. The developed detectors were used in the framework of the FORTRESS (POR-FESR 2014-2020) project for the detection of gamma-rays emitted by radiotracer used in medical diagnostics and therapy. A mixture- combining 2D and 3D perovskite was developed for the first perovskite-based proton detector characterized at the LABEC laboratory of the Istituto Nazionale di Fisica Nucleare (INFN).

List of Acronyms

AVC – Anti-solvent Vapour-assisted Crystallization

BA – Butylammonium

BCP – Bathocuproine

CNAO – Centro Nazionale di Adroterapia Oncologica

CT – Computed Tomography

CVD – Chemical Vapour Deposition

CZT – Cadmium Zinc Telluride

DLCP – Drive Level Capacitance Profiling

DMSO – Dimethyl sulfoxide

DMF – N,N-dimethylformamide

DSSC – Dye Sensitized Solar Cell

EDX – Energy-Dispersion X-rays

ESRF – European Synchrotron Radiation Facility

ETL – Electron Transport Layer

FA – Formamidinium

FWHM – Full Width Half Maximum

GIXRD – Grazing Incidence X-ray Difraction

INFN – Istituto Nazionale di Fisica Nucleare

IPA – Isopropyl Alcohol

ITO – Indium Tin Oxide

HOMO – Highest Occupied Molecular Orbital

HTL – Hole Transport Layer

ITC – Inverse Temperature Crystallization

LABEC – Laboratorio di Tecniche Nucleari Applicate ai Beni Culturali

LoD – Limit of Detection

LUMO – Lowest Unoccupied Molecular Orbitals

MA – Methylammonium

NTCP – Normal Tissue Complication Probability

PCBM – Phenyl-C_{61}-butyric acid methyl ester

PEA – Phenethylammonium

PEDOT:PSS – Poly(3,4-ethylenedioxythiophene) polystyrene sulfonate

PEN – Polyethylene Naphthalate

PET – Positron Emission Tomography

PET – Polyethylene Terephthalate

PDMS – Poly(dimethylsiloxane)

PL – Photoluminescence

Poly-TPD – Poly(N,N'-bis-4-butylphenyl-N,N'-bisphenyl)benzidine

PP – Polypropylene

PSC – Perovskite Solar Cell

PTCDI – N,N′-dimethyl-3,4,9,10-perylentetracarboxylic diimide

PU – Polyurethane

QTH – Quartz Tungsten Halogen

SEM – Scanning Electron Microscope

SMU – Source Meter Unit

SPECT – Single Photon Emission Computed Tomography.

TCP- Tumour Control Probability

TEM – Transmission Electron Microscope

TFT – Thin Film Transistor

TIFPA – Trento Institute for Fundamental Physics and Applications

XBIC – X-ray Beam Induced Current

XRF – X-ray Fluorescence

1. Ionizing Radiations

The first chapter of this work is the introductory part on perovskite as a novel class of semiconductor materials for ionizing radiation detectors. The chapter is divided into two parts: the first part explains the concept of ionizing radiations and their application in modern society; the second part is focused on the methods for detecting high energy radiation.

1.1 Definition, classification and sources

Ionizing radiation is a generic term used to identify a large number of different radiations. In the following are reported the definition and classification of ionizing radiations. In the end, different applications in which ionizing radiations are used on daily basis in society are also reported.

Ionizing radiations can be defined as radiations that transport sufficient energy to ionize atoms and molecules. This definition is quite vague because it does not exist an energy value constituting a threshold for the ionization of matter. In fact, the ionization energy of an element or a molecule depends on the element or molecule itself. Visible photons, with energy between 1.7 eV (red) and 3.1 eV (violet), are not ionizing radiations because the energy is not sufficient for ionizing matter. Therefore, also the part of the electromagnetic spectrum with energy below the visible photons cannot be

considered ionizing radiation. In the UV range, photons with energy higher than 10 eV have sufficient energy to ionize most of the elements of the periodic table. At higher energy, soft (1 keV – 10 keV) and hard (>10 keV) X-rays are for sure ionizing radiations. They have sufficient energy to eject core electrons from the inner shell of atoms. But not only photons are ionizing radiation. In fact, according to quantum mechanics every particle can be considered like a wave and can transport energy through space, thus also accelerated particles like electrons, protons and neutrons with sufficient energy can be considered ionizing radiation. In biology and in medicine the concept of ionizing radiation is strictly correlated to DNA and cell damage. Ionizing radiation can interact with biological molecules inside the cells, if the interaction ionizes the DNA or other functional organic molecule it can produce irreversible damage to the cell. The possible damage that ionizing radiation can cause to the human body makes them dangerous and it is very important to properly monitor them. That is one of the reasons why ionizing radiation detectors are so important for modern society.

In the following the most important ionizing radiation will be discussed, they can be divided into charged and neutral particles. They can be also classified by their mass in heavy and light particles.

X-rays and gamma-rays

X-ray and Gamma-rays are both composed of high energy photons. X-rays were discovered by Wilhelm Conrad Röntgen in late 1895.[1] He discovered immediately the ability of X-rays to penetrate matter and show what is inside. The first X-ray picture of his wife's hand became very famous. For the discovery of X-rays Röntgen was awarded the first Nobel prize in history in 1905. Since then the use of X-rays in medicine became more and more important and now is the most used medical imaging technique. The difference between X-ray and gamma-ray relies on the sources. Like

visible photons, there are different sources of ionizing radiation. For X-rays the most common is the X-ray tube which was developed from the Crooks tube. An X-ray tube is composed of a glass tube under vacuum with a tungsten filament in which an electric current flows. The heat generated by the current creates the thermionic effect and electrons are ejected from the filament. A strong electric field (kV) is present between the filament and a metal target. The electrons are accelerated at high energy and impact the target. The energy released in the target by the electron is transformed into high energy photons through bremsstrahlung and atomic characteristic emission of target: X-rays. The apparatus is explained in detail in section 3.2.3. On the other and, gamma-rays are produced by a nuclear de-excitement. For example, when an instable element decade often decades in an excited and unstable state. When it decays to the ground state it releases energy in form of high energy photons. Those photons are called gamma-ray. The energy of the gamma photons emitted depends on the energy difference between the two nuclear levels involved in the transition. Usually, they have higher energies than the X-rays produced with an X-ray tube but this is not always the case.

Neutrons

Neutrons are neutral particles with a mass equal to 1.675×10^{-27} kg that together with protons constitute the atomic nucleus. If a nucleus is in an excited state, it can decay by releasing neutrons if the energy difference between the two nuclear levels is higher than the neutron binding energy, i.e. the energy necessary to remove a neutron from an atom. The high energy states necessary for the production of neutrons are not common. Few nuclei decay in excited states that are able to emit neutrons, the ones which do have a life-time of a few seconds. The only practical ways to produce neutrons are spontaneous fission, nuclear reaction or particle accelerators. The most common

fission source is ^{252}Cf with 2.65 years of half-life sufficiently long to make it convenient.[2] The energy spectrum of the neutrons is peaked between 0.5 and 1MeV but the tail can extend up to 8MeV with small intensity. In addition, several materials can be used as targets for (α, n) reaction, i.e. a reaction in which a suitable material is bombarded with alpha particles and, as a reaction product, neutrons are obtained. An example of a neutron source using this approach is $^{241}Am/Be$.[2]

Protons

Protons are positively charged particles with a mass very similar to neutrons one (1.673 x 10^{-27} kg). They can be produced by ionizing Hydrogen atoms and they can be accelerated with a cyclotron or synchrotron to reach the desired energy. Depending on the power of the accelerator, protons can reach energies up to hundreds of MeV. Since they are charged particles their interaction with matter is very different from the one of photons and neutrons. They interact strongly with matter and their energy release profile is very peculiar with the highest release (called Bragg peak) in a limited region of space. For this reason, protons are used in hadrontherapy for cancer treatment. The medical applications of protons will further discuss in the next section.

β-particles

β-particles are fast electrons emitted by unstable nuclei undergoing a β-decay. An atom with atomic number Z transforms into a heavier element, with atomic number Z+1, as a result of a neutron transforming into a proton. The transformation produces one electron and an antineutrino. Contrary to other nuclear processes producing gamma-rays, β-particles are not monochromatic since the reaction involves an antineutrino that can share the energy with. The maximum energy of the electrons produced by the

decay is called Q-value and it is equal to the energy difference between the initial and final state. Another method used to produce electron beams is to use the thermionic effect already mentioned earlier. A filament is heated by an electric current. The thermal energy of electrons is sufficient to eject the charged particles outside the material of the filament. The electrons can then be accelerated by a potential difference. By changing the accelerating voltage, the energy of the electron can be changed. The most used material for the generation of electron beams is lanthanum hexaboride (LaB6) for its high brilliance. This is the technique used in scanning and transmission electron microscopes (SEM and TEM) to obtain the electron beam.

α-particles

When the repulsion of charged protons inside the nucleus of a heavy element became too strong the nucleus undergoes a decay emitting an α-particle. α-particles are composed of 2 protons and 2 neutrons, a nucleus of helium. The general nuclear reaction is the following:

$$ {}^{A}_{Z}X \rightarrow {}^{A-4}_{Z-2}Y + {}^{4}_{2}\alpha $$

Where X and Y are the initial and final atomic species respectively. If there is only one final energy state the energy of the transition (*Q-value*) is shared between the alpha particle and the recoil nucleus. The alpha particles energy is fixed by $Q(A-4)/A$. So, the alpha radiation can be considered monoenergetic. The energy of practically suitable alpha particle sources ranges between 4 and 6MeV.[2] Their interaction with matter is similar to the protons; they are both positively charged particles but α-particles have higher mass, thus they interact more with materials.

1.2 Application in modern society

Ionizing radiations are broadly used for several applications, in this section, the focus is on medical applications. The energy involved, the penetration power and the interaction mechanisms with matter make ionizing radiation very interesting because they allow to see the invisible. In medicine they are used for both diagnostic and therapy, below are reported some examples of applications for different types of ionizing radiations. Although the purpose of this thesis is not the fabrication of an imager, I have included in this section the most common medical imaging techniques to highlight the importance of ionizing radiation.

1.2.1 Radiography and CT

Radiography uses X-ray to generate an image of the inside of the human body. X-rays are high energy photons and, as better explained in section 1.2.1, they interact differently than visible photons. Low energy photons immediately interact with the human skin and get absorbed. What the human eyes see is the visible part of the electromagnetic spectrum reflected by the skin. Instead, X-rays have a lower interaction cross section and can penetrate more deeply into the body. At fixed X-ray energy the cross section of interaction depends on the atomic number of the atoms in the material of interest. Therefore, the attenuation of the radiation when passing through a material depends on its atomic composition and its density: high density materials have higher interaction with X-rays. That is why lead is used for screening and protection. This is exactly the concept behind the generation of an X-ray image. Tissues in our body have

different densities: some of them absorb more X-ray photons and transmit less (e.g. bones); while low density tissues absorb fewer X-rays and transmit more (muscles). The result is a spatial modulation of X-ray intensity that can be acquired with a sensor sensible to X-rays.

In a planar X-ray image, the object (or patient) is placed between the X-ray source (normally an X-ray tube) and the detector which are placed at a 180° angle. The X-rays pass through the object and depending on the local density an image is transmitted to the detector. Computed Tomography (CT) is the evolution of planar radiography, it allows to obtain a 3D image by combining different images taken from different orientations of the X-ray source and detector. In order to recreate a 3D image of the body, several images from different angles are needed. The X-ray tube and detector are mounted on a circular rail that runs around the object. The detector and source are moved around to take hundreds of images needed for the reconstruction. When CT is performed on a human body, the patient lies down in a motorized bed and is moved inside the circular rail, see Figure 1.2d. With just one scan (one circle of the rail) what can be obtained is just a small slice of the body, usually between 0.1 mm to 1 cm in thickness. The patient is moved perpendicularly to the ring and multiple slices are acquired. There are machines that employ multiple X-ray sources and detectors to make the scan even faster. Sometimes to highlight some tissue a contrast agent is used. A contrast agent is an atom bound to a drug that has a higher X-ray absorption coefficient than the typical tissues. The contrast agent accumulates in the organ/tissue under test creating higher contrast in the final image. CT is one of the most prevalent diagnostic tools in terms of frequency of use and hospital availability. The use of CT is increasing, and the number of clinical CT scanners in operation worldwide is estimated at over 45 000. Today, over 70 million clinical CT scans are performed yearly in the United States alone.[3]

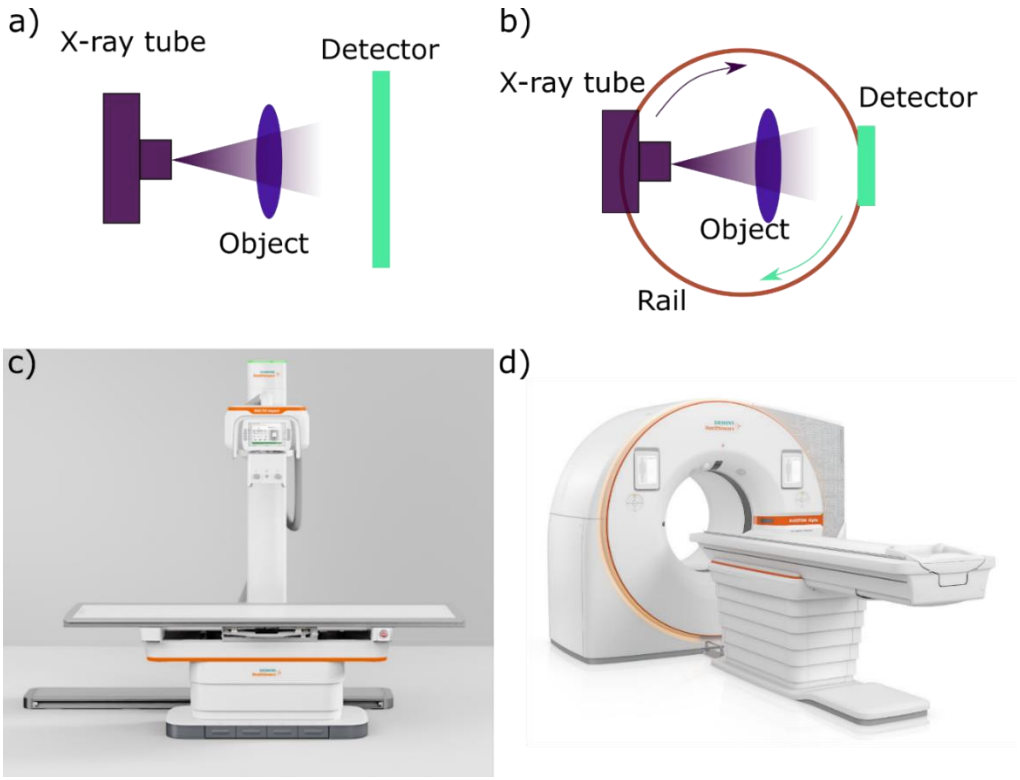

Figure 1.1: X-ray radiography and CT. a) Scheme of the setup for acquiring a radiographic image of an object. It is composed of the X-ray source and the detector positioned at 180° with the object in between. b) CT scan scheme. The source and detector are mounted on a circular rail and they are rotated to acquire several images from different angles respect to the object in the middle. c, d) Example of X-ray machine and CT scan machine from one of the major brands.

1.2.2 PET and SPECT

There are useful diagnostic techniques using gamma-rays to picture the inside of our body. Those techniques are in nuclear medicine. In particular, PET stands for Positron Emission Tomography and allows to obtain morphological and functional information about organs and tissues. It combines a positron source as contrast agent and tomography to map the position of the radiotracer. The most used contrast agent in PET is fluorodeoxyglucose (^{18}F-FDG), see the chemical structure reported in Figure 1.2b. The molecule is very similar to the one of glucose with a radioactive fluorine atom attached. Thanks to his similarity, ^{18}F-FDG is recognized as glucose from the

human body. Once inside the bloodstream, it accumulates in regions where there is a high intake of glucose like the brain and cancer cells. Due to their uncontrolled growth, they require a higher quantity of glucose than healthy cells. Therefore, tumours appear in PET images as regions with higher signal intensity. ^{18}F-FDG gets metabolized by the body once the florin has decayed. The unstable isotope of fluoride as a half-life time of about 110 min and decays following the reaction:

$$^{18}_{9}F \rightarrow {}^{18}_{8}O + \nu_e + e^+$$

The fluorine atom decay in oxygen emitting a neutrino and a positron. The positron travels a few microns in the human tissues and then annihilates with an electron producing two 511 keV gamma-rays travelling in space in opposite directions. The high energy allows the photons to escape the body and they can be detected, see figure 1.2c. Around the patient, there is a ring very similar to the one employed in CT machines, but in PET machines the ring is filled with gamma detectors. The location of the tracer is found by looking at the coincidence events. Since the peculiar gamma emission, if one detector measures a gamma photon, the opposite detector in the ring should measure a signal in a defined time widow. A short time window is necessary to eliminate as many possible spurious events that can trigger the detectors. In the same voxel, 3D corresponding to a pixel, there are more fluorine atoms that emit gamma-ray pairs in different directions. By intersecting all the coincident lines is possible to reconstruct the spatial distribution of ^{18}F-FDG. As for CT the patient is moved perpendicularly to the detector ring to obtain a 3D image of the region of interest. Nowadays, Time of Flight PET is also available. By using very fast detectors and readout electronics it is possible to determine the different times, needed to reach the detectors, between two photons coming from one single event. The time difference tells also the position along the coincidence line where the positron annihilated. This increases the signal-to-noise ratio for better image quality. Apart from tumour location and tissue morphology, PET can be used also for the diagnosis of brain diseases like Alzheimer's. Single Photon

Emission Computed Tomography (SPECT) differs from the PET for the radiotracer used: ^{99m}Tc. It is a metastable isotope obtained by bombarding molybdenum in a cyclotron. ^{99m}Tc can be attached to different drugs depending on the target organ. The decay produces gamma-rays at low energy (140 keV) easy to detect. In SPECT there is a single imaging sensor that is moved around the patient to obtain images from different angles for the tomography reconstruction.

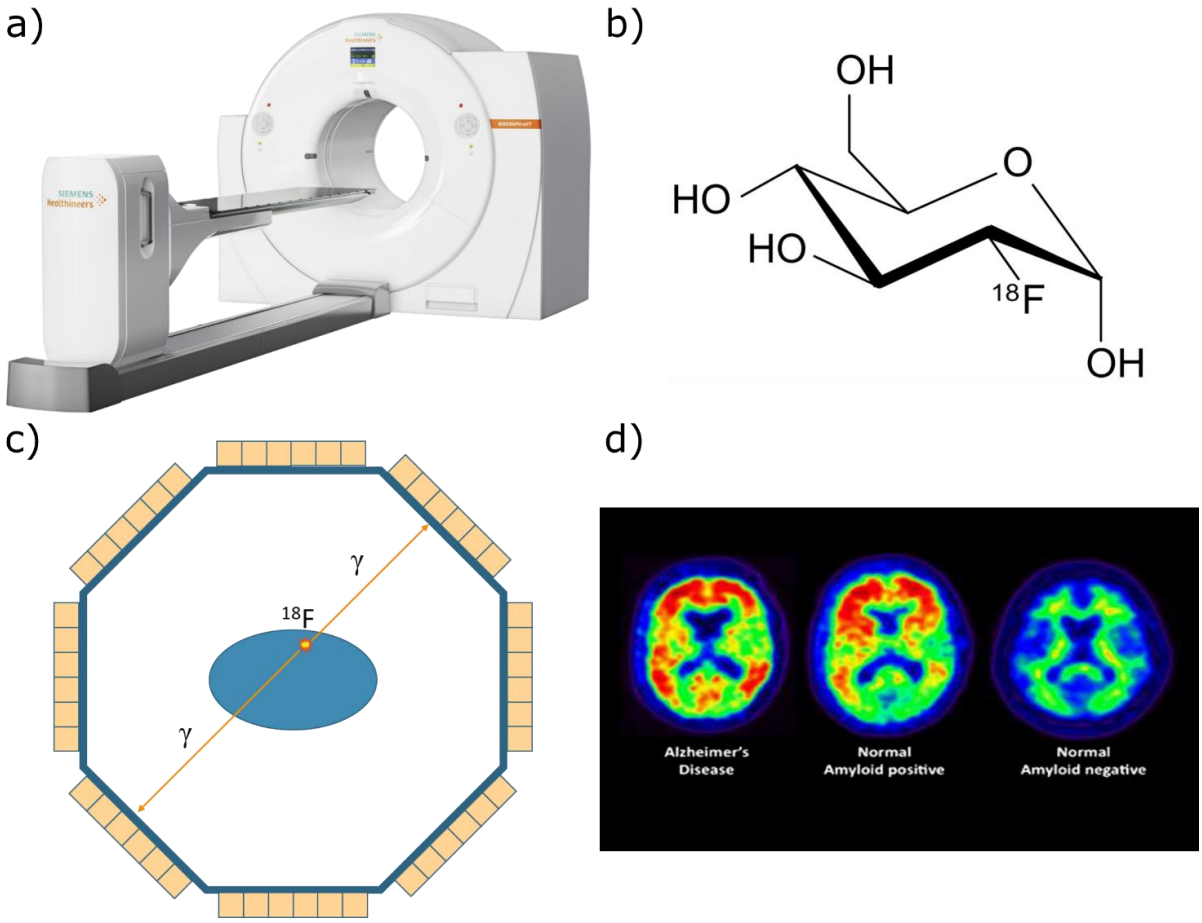

Figure 1.2: PET. a) Complete PET system, the shape is very similar to CT machine. b) Chemical formula of ^{18}F-FDG. c) Scheme of the PET working principle: inside the body, a radioactive tracer emits two gamma-rays in opposite directions as a consequence of electron-positron annihilation. The event is then measured by two opposite detectors in the detector ring. d) PET images of a sick and healthy brain.

1.2.3 Radiotherapy

Ionizing radiations are not applied only for diagnostics, but they are also used for therapy to treat cancer. In this case, the radiation serves as means to transport the energy to the tumour cells, the energy released can cause irreparable damage to the tumour cells' DNA stopping their reproduction. For this purpose, different methods, with different ionizing radiations, can be used. When the therapy involves electrons or photons is called radiotherapy, when instead uses protons, neutrons or ions is called hadrontherapy, see next paragraph. Since the beginning of 1900, after the discovery of Ra, scientists used radioactive compounds to treat skin infections. In 1934 Henry Coutard invented the fractional method, which is now the basis of modern radiotherapy. A tumour is a mutated cell that reproduces itself indefinitely in a disordered way. Some tumour cells can also migrate and form metastases. The final goal of radiotherapy is to prevent the proliferation of tumour cells; it is not necessary to kill the tumour cell, it is enough to damage the DNA so that the cell loses its ability to reproduce. A cell that cannot reproduce is considered dead. There are two ways of damaging the DNA: direct and indirect. In the direct way, the ionizing radiation energy directly ionizes the nucleotides in DNA. Instead, the indirect way consists in the formation of free radicals, neutral very reactive molecules, that can react with the DNA damaging it. However, the DNA is able to self-repair. In the double helix configuration, the two phosphate-deoxyribose backbones are bonded together by the four bases: adenine, thymine, cytosine and guanine. Adenine is always chemically bonded to thymine and cytosine to guanine. If one of the bases gets damaged, the cell knows how to repair the DNA because the base on the other side of the helix tells exactly what base is missing. When the energy released by the ionizing radiation breaks only one base the event is called a single strand break. In order to permanently damage the DNA a double strand break is necessary. When two bases in the same position of the

helix are broken then the cell cannot repair its DNA structure. If the DNA chain is interrupted the replication of the cell is forbidden. Therefore, the aim of radiotherapy is to release energy in a small region of space to induce double strand brake in the DNA chain of tumour cells. However, around cancer cells there are also healthy tissues and if the radiation damages also them, the probability of collateral effects increases. Damaging the DNA of healthy cells can be dangerous and could lead to the formation of new tumours. Radiotherapy must find the right balance between killing cancer and not creating a new one. The tumour control probability (TCP) and normal tissue complication probability (NTCP) are the two parameters to be properly tuned. Luckily, healthy cells have higher recovery capabilities than tumour cells. Before going further in the explanation, a small parenthesis on the dose. The dose is defined as the energy in Joule deposited in one kilogram of matter. It is measured in Gray (Gy) and 1 Gy = 1 J / 1 kg. It is used to measure the energy released in materials by ionizing radiations, see section 3.2.3.

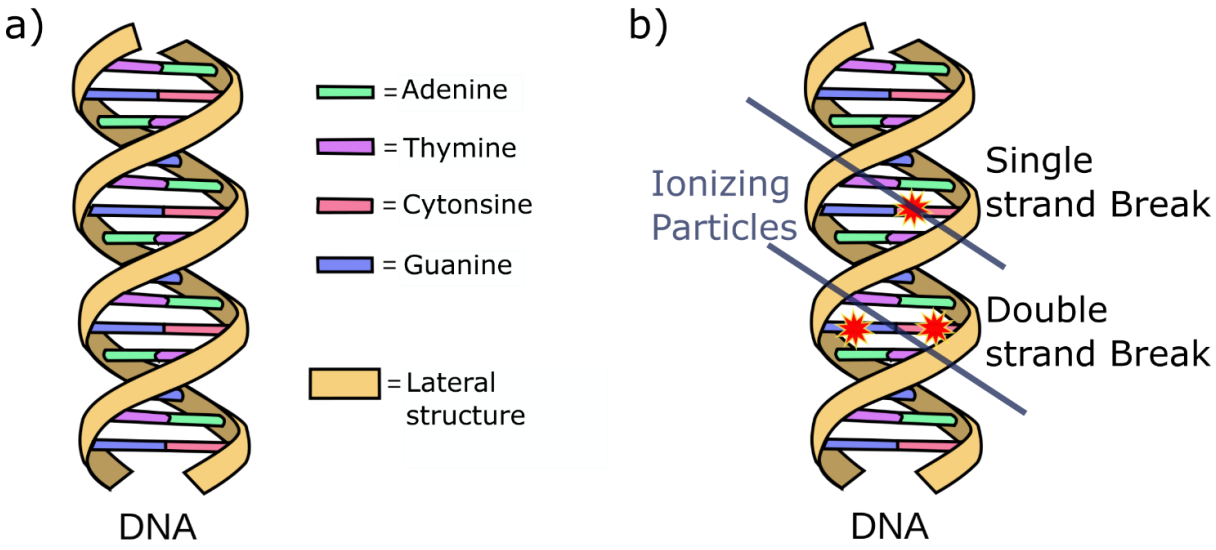

Figure 1.3: DNA damage. a) Simplified structure of the DNA chain with the four bases. b) Single strand break in comparison with the double strand break.

In cancer treatment there is a range of dose values that maximize TCP and minimize NTCP; typical total absorbed dose values delivered during therapy are between 20 and 80 Gy, see graph in Figure 1.4. Considering that 1-2 Gy received in all the body is deadly, the doses delivered during treatment are really high. That is why dose fractionation is important. In radiotherapy, the total dose necessary to control the proliferation of tumours is fractioned in multiple sessions. This method has several advantages:

Healthy tissues recover the radiation damage. Between one session and the next one, the healthy tissues have the time to recover the damage while the tumour cells do not.

During the life cycle of a cell there are more radio-resistive phases and others in which the radio sensitivity is higher. Dose fractioning allows bombarding the cells in different phases of their life.

Avoid the danger of delivering a big dose all in one shot.

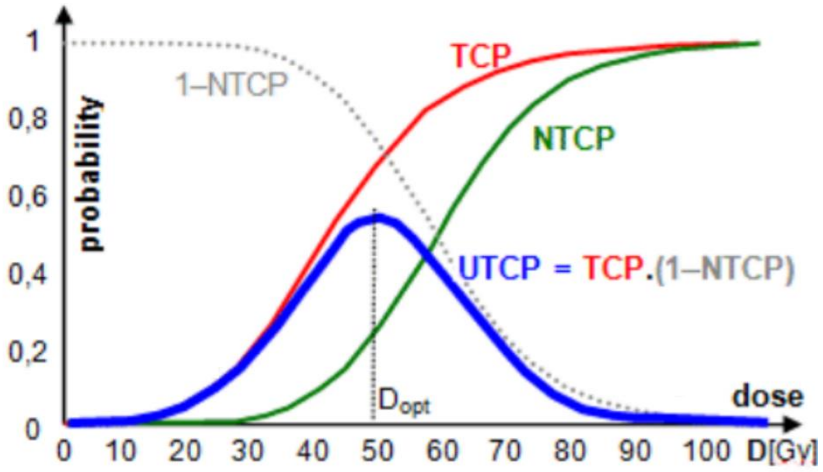

Figure 1.4: TCP and NTCP. Probability of tumour control and probability of healthy cells damage as a function of total dose.

There are two main categories of radiotherapy: external and internal. In external radiotherapy, an X-ray beam, usually generated by a linear accelerator (LINAC), with

an energy between 5 to 10 MeV is focused on the region of interest. Instead, in internal radiotherapy, a sealed radioactive source is placed inside the body near the tumour. Another way used to treat cancer with ionizing radiation is with systemic therapy, where the radioisotope atoms are bonded to a drug and spread in the body trying to target the tumour. An example of a radioisotope used for systemic therapy is ^{177}Lu. It is a pure β emitter with a Q-value of 478 keV used for the treatment of prostate cancer.[4,5]

1.2.4 Hadrontherapy

Hadrontherapy is a development of radiotherapy in which, instead of photons, hadrons are used to deliver the energy to the tumour spots. It takes advantage of the different interactions charged and massive particles have with the matter. Briefly, charged particles interact with the charged nuclei and electrons clouds of atoms leading to higher cross section of interaction than photons. The result of the peculiar interaction charged particles have in materials is a peaked energy released profile. In comparison to photons, the energy can be released in a smaller region meaning more precise delivery of the dose to the patient's tumour. Thus, less probability of undesired effects on the healthy cells around the tumour. In hadrontherapy protons or even light ions like ^{12}C are accelerated and used as a projectile on the patient. In Figure 1.5a is reported a simulation of the deposited dose of different ionizing radiation as a function of the penetration depth in water. While gamma-rays present a broad energy release profile with a broad peak after a few centimetres, hadrons show a pronounced and narrow maximum of Linear Energy Transfer (LET), the so-called Bragg peak. As the charged particles penetrate into the material, they lose energy and speed. When the speed decreases enough, charged particles release all the energy left in a very limited region of space. What determines the depth of the Bragg peak is the initial energy of the

particles and the mass. Higher energy corresponds to higher penetration depth. Heavier particles travel less in materials at the same energy. Ions have a sharper Bragg peak and their energy loss rate before the Bragg peak is lower than protons. The situation is different after the peak. While the effect of protons after the peak is negligible, light ions can still deposit some energy for few centimetres.

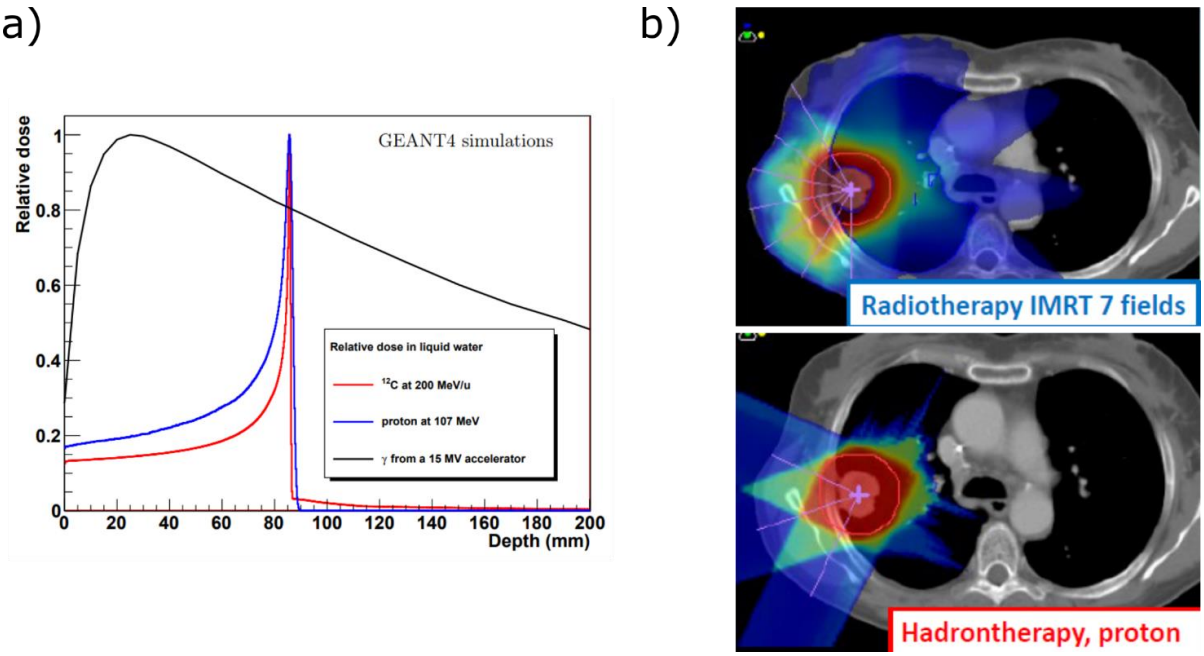

Figure 1.5: Hadrontherapy vs Radiotherapy. a) Released dose profile in water for different ionizing radiations. b) Simulations of the spatial distribution of the dose delivered to the tumour.

Figure 1.5b shows the comparison between radiotherapy and hadrontherapy for what concerns the special distribution of dose. It is clear that hadrontherapy allows a more targeted dose delivery which translates in a higher probability of damaging the tumour DNA and a lower probability of complications in healthy tissues. Although the big advantage of hadrontherapy the high building cost of the accelerators is limiting the application and spreading of facilities. In Italy there are three centre for therapy: TIFPA a cyclotron accelerating protons located in Trento, in Catania there is a cyclotron for eye tumour therapy and located in Pavia, CNAO offers proton and carbon beams.[6]

Medical diagnostics and therapy are not the only application in the society of ionizing radiations. In hospitals, radiation detectors are needed to measure the dose received by technicians and doctors while there are using X-ray machines or manipulating radioactive tracers. Indeed, one of the professionals receiving the higher dose are surgeons. A lot of surgery nowadays are X-ray guided. Furthermore, public security is an important application where ionizing radiations play a crucial role: every time at the airport our baggage passes through an X-ray scan and the image obtained is controlled by the operator. Ionizing radiation sensors are used to monitor environments with high radiation risks like nuclear power plant or nuclear accident sites. Another important application field for ionizing radiation is scientific research. X-rays are used to study the atomic structure and element composition of materials. Electrons allow to see at the nanoscale level and even more. Tens of large facilities, founded by multiple countries, were built and constantly updated in Europe and all around the world, to provide the highest performing radiation source to study materials, biological structures and more. Examples are the European Synchrotron Radiation Facility (ESRF) in Grenoble, Deutsches Elektronen Synchrotron (DESY) in Hamburg and the Stanford Linear Accelerator Center (SLAC) in the US. X-rays and gamma-rays are keys to understand the mysteries of the Universe. Detectors are important for future space missions where astronauts are exposed for prolonged periods to cosmic rays and other ionizing radiations coming from outer space.

This first part of this work wanted to stress the importance of developing new technology in the field of ionizing radiation detectors.

1.3 Detecting Ionizing Radiations

Ionizing radiations are invisible to human eyes, and their effects are evident only after a long time. Therefore, for all the important applications discussed before a detector that can measure the ionizing radiation is essential. For diagnostic techniques, the detector is the active part that produces the image, in therapy techniques a detector measuring the dose delivered to the patient is needed. Depending on the energy, the fluxes and the type of radiation involved one needs to choose the proper detector. In the following, the working principles of traditional detectors are discussed. In general, a detector is an object that absorbs the radiation, transforms the energy deposited by the radiation inside the active material and converts it into another measurable physical quantity (i.e an electrical signal, chemical modification, colour change, etc…). For example, there are polymeric films that change colour after radiation exposure (Gafchromic)[7] or materials that change their optical properties (Thermoluminescence Dosimeter, TLDs)[8]. However, in those cases, a real-time evaluation of ionizing radiation is impossible since those methods require post-processing. Real-time detectors have an electrical signal as output that can be read by readout electronics and give the possibility to easily digitalize and analyse the data. Before understanding how a detector works, it is important to describe the main processes of ionizing radiations interaction with matter.

1.3.1 Radiation-Matter interaction

As already mentioned, the ionizing radiations interaction mechanism with matter strongly depends on the type of radiation, so in the following different ionizing radiations will be treated separately.

γ and X-ray photons

The behaviour of high energy photons in materials is in net contrast with the behaviour of charged particles. Charged particles continuously lose their energy during their track inside the absorber. The photons, instead, can disappear in one single interaction or they can scatter at a significant angle. X and gamma photons interact with matter in three different ways: photoelectric absorption, Compton scattering, and pair production. All three processes deposit energy inside the detector contributing to the final signal, the relative importance depends on the atomic number of the absorber and the energy of the impinging photons. In Figure 1.6 is reported, for a generic material, the typical graph of the attenuation coefficient as a function of the photon energy with the relative contribution of the different interaction mechanisms. The attenuation coefficient represents the radiation intensity attenuation after the interaction with a material of a defined thickness. In the lower energy range (X-rays) the predominant effect is the photoelectric effect, while at energies above 1 MeV the Compton scattering becomes the most important one. At energies higher than 100 MeV pair production is the most relevant.

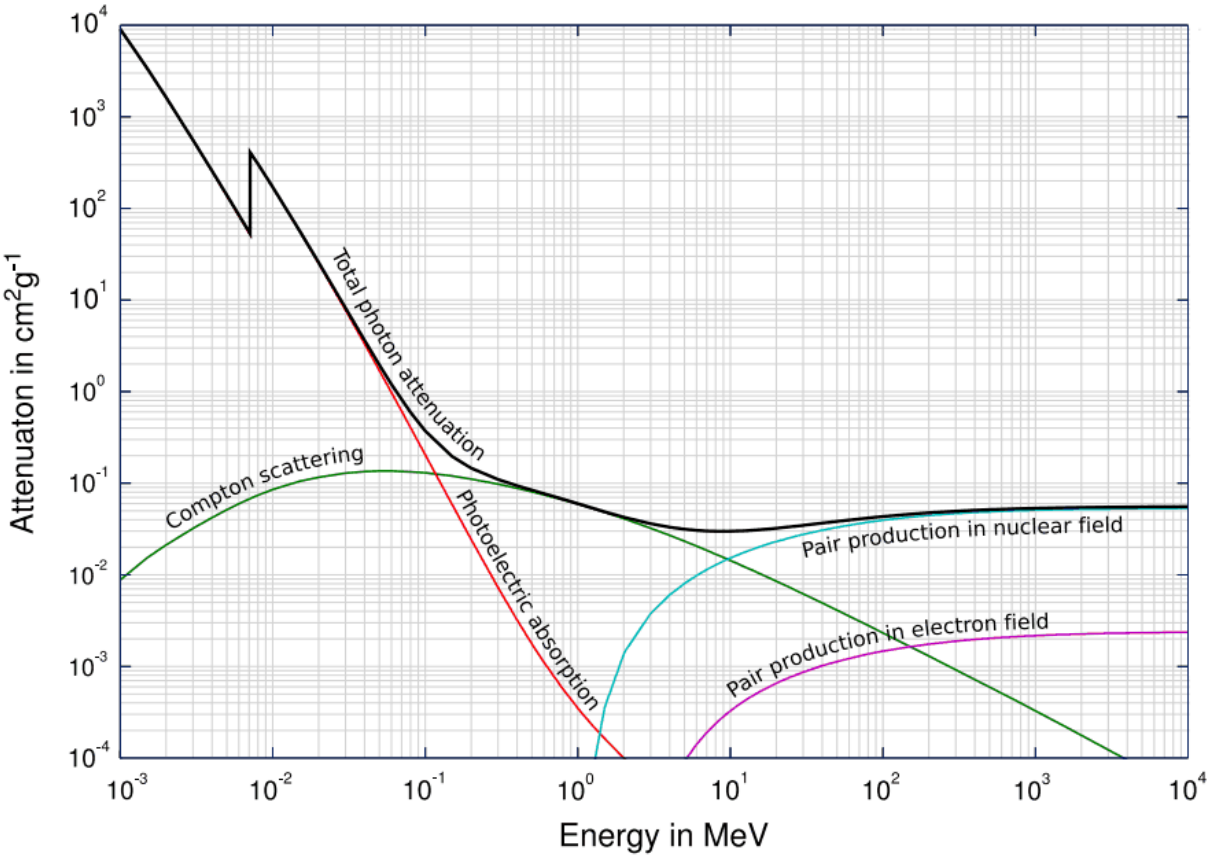

Figure 1.6: Attenuation coefficient. Relative contribution to the attenuation coefficient of the different photons-matter interaction mechanisms.

The photoelectric effect consists of the energy transfer of all the photon energy to an electron. After the interaction, the photon disappears, and the electron involved is now in an excited state. In the photoelectric effect is implied that the photon as enough energy to eject the electron from the atom with final energy equal to:

$$E_e = h\nu - E_b \qquad (1.1)$$

For the conservation of energy, the energy of the electron, called photoelectron, is equal to the difference between the photon energy and the electron binding energy in its shell. For the energy range of X-rays and gamma-rays, the most probable origin of the photoelectron is the K-shell of the absorber atoms. This interaction produces a vacancy in the electron shell. This vacancy is quickly filled by a free electron or with the

rearrangement of other shells. Therefore, one or more characteristic X-ray photons may be generated. The secondary X-rays produced in this process are usually absorbed near the interaction site from electrons with lower binding energy. However, if the absorption of the external radiation and subsequent emission of characteristic X-ray photons, takes place near the surface of the absorber, the photons can escape from the material. If this happens, the energy of the initial photon is converted only partially in the detector signal. Sometimes the emission of Auger electrons can substitute the secondary X-ray emission. Auger electrons are electrons that absorb the secondary photon emitted. Since the low energy of Auger electrons is harder for them to escape the absorber. There is no single analytic expression for the probability of photoelectric absorption valid for all the energy ranges, but a rough approximation is:2

$$\tau \cong A\frac{Z^n}{E_{ph}^{3.5}} \qquad (1.2)$$

Where A is a constant, n varies between 4 and 5 over the photon energy (E_{ph}) range. The materials with high atomic number have higher probability to absorb photons via the photoelectric mechanism. The strong dependence on Z is the primary reason for the use of lead as shields. Discontinuities in the cross section behaviour are present in the low energy range of the plots, see Figure 1.6. The discontinuities appear at energy values equal to the binding energy of electron shells. The plot in Figure 1.7 reports the interaction cross section for the low energy range for different elements. The K-edges are clearly visible in the interaction probability curve. X-rays with energy lower than the binding energy of electrons in the K-shell cannot excite the electrons in the inner core. Thus, the photoelectric cross section decreases with the increase in energy, but when the photons have the right energy to excite the electron in the K-shell a sudden increase in the interaction probability is observed. The heavier is the element the more discontinuities are visible. Each of them corresponds to an electron shell, the

one at higher energy is the K-shell because is the electron shell with the higher binding energy.

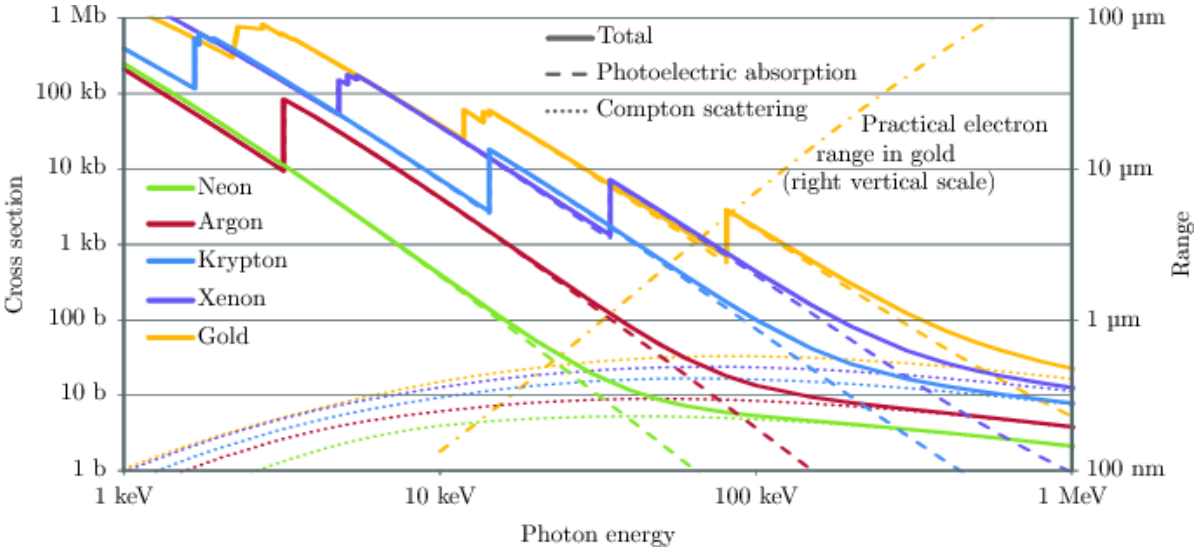

Figure 1.7: Photoelectric effect cross section. Cross section expressed in barn (1 barn = 10^{-24} cm^2) for the photoelectric effect in different materials.

The Compton scattering describes the inelastic scattering between an electron and a photon. In this interaction, only a part of the photon energy is transferred to an electron of the absorber atom, called the recoil electron. So, the photon doesn't disappear during the process, but after the scattering it continues its path inside the material with a different energy (Compton shift). The Compton scattering is the most relevant absorption process for gamma-ray energies typical of radioisotope sources. The mathematical expression for the final photon and electron energies can be easily derived considering the electron at rest. The electron can be considered at rest because of the high energy difference between the bound electron and gamma-ray photon. From the law of energy and momentum conservation, one can obtain:

$$E'_\gamma = \frac{E_\gamma}{1 + \left(\frac{E_\gamma}{m_e c^2}\right) + (1 - \cos\theta)} \qquad (1.3)$$

where E_γ and E'_γ are the initial and final photon energies, m_e is the rest-mass of the electron (0.511 MeV) and θ is the scattering angle with respect to the initial photon direction. For the electron the final energy is:

$$E'_e = \frac{\left(\frac{E_\gamma^2}{m_e c^2}\right)(1-\cos\theta)}{1+\left(\frac{E_\gamma}{m_e c^2}\right)+(1-\cos\theta)} \qquad (1.4)$$

The scattering angle has no forbidden values, the formulas admit every angle between 0 and π. There are two limit cases. When the angle is equal to zero (forward scattering) the energy of the photons doesn't change in the interaction. Instead, in the case of $\theta=\pi$ (backwards scattering) the kinetic energy of the electron after the collision is the maximum.

When the energy of the photons composing the ionizing radiation becomes higher than 1.02MeV (the sum of two electrons' rest masses), a third interaction can occur. High energy gamma-rays can exceed this value, and the process of pair production is energetically possible. Pair production consists of the coupling of a photon with the nuclear or electronic field of an atom creating an electron-positron pair. The photon disappears in the process and its energy is fully converted into the pair. The pair production cross section becomes significant for gamma photons with energies of several MeV. The excess energy is transformed into kinetic energy shared by the electron and positron. As a secondary effect of this interaction mechanism, two annihilation photons are produced by the positron which, after being slowed down, it annihilates with an electron of the absorber.

In summary, the interaction of X or gamma-ray photon beams with an absorber material results in a combination of all the interactions and the interaction of the secondary product. As a consequence of the interaction at the atomic scale, some photons are fully absorbed and other lose energy, thus the intensity of the initial beam decreases. The intensity attenuation after the interaction with a material of defined thickness is

described by the attenuation coefficient. When a monoenergetic photons beam hits an absorber, the photons interact with the absorber atoms, some of them get scattered others get absorbed. If one measures the intensity of the beam after it has crossed all the absorber thickness, an exponential decrease as a function of the absorber thickness would be observed. The attenuation depends on the material because on the material depends the probability of the interaction. If material and density are fixed (state of absorber fixed) the intensity of the outgoing beam depends on the thickness of the absorber. The larger the thickness of the absorber the larger the time spent by the photons near electrons or nuclei, thus the number of interactions is higher. The linear attenuation coefficient μ is the probability that a photon is removed by some interaction from the initial beam per path length unit. And it is simply equal to the sum of all interaction probabilities:

$$\mu = \tau_{Photoelectric} + \sigma_{Compton} + k_{Pair} \qquad (1.5)$$

The exponential decay describing the intensity attenuation can be written by the Beer-Lampert law:

$$\frac{I(d)}{I_0} = e^{-\mu d} \qquad (1.6)$$

Where I_0 is the initial beam intensity and $I(d)$ is the intensity of the beam after crossing an absorber of thickness d. More often the mass attenuation coefficient is used. It is defined as the ratio between the attenuation coefficient and the material density ($\mu_m = \mu/\rho$). As defined the mass attenuation coefficient depends only on the atomic composition of the material and not on its state. For example, water and ice have different attenuation coefficients since their density is different but the same mass attenuation coefficient.

Heavy charged particles

The main interaction of heavy charged particles, such as protons and alpha particles, is through electrostatic forces between their electric charge and the electrons cloud of the absorber. Interactions with nuclei like Rutherford scattering or alpha-induced reaction are also possible. However, the probability of such interactions is small and their contribution to the final detector signal is insignificant. As soon as the charged particle enters the absorbing materials, it interacts with many electrons. For each interaction the highly energetic external particle exchanges energy with the electron of the absorber. The absorbed energy can excite the electrons in a higher orbit or, if it is sufficient, even ionize the atoms of the absorber. As a result of the interaction the energy of the charged particle must decrease for energy conservation. In each interaction, the external particle decreases its velocity until eventually, it stops. A detector of heavy charged particles can detect their presence by measuring the charge carriers created inside the absorber thanks to the energy released by the radiation. In fact, the charged particles create ions in their path inside the material, but this state is unstable, thus they tend to recombine to return to the neutral state. Since the external charged particle interacts with many electrons simultaneously in all directions, the path inside the absorber is straight except at the very end when the energy is low. With this statement, it is possible to mathematically define the stopping power of a specific material. The linear stopping power S for charged particles, in a given absorber, is defined as the differential energy loss of the particle in the material divided by the corresponding differential path:

$$S = -\frac{dE}{dx} \qquad (1.7)$$

The value S is also called specific energy loss along the particle track. For a particle with a given charge state, the stopping power increases as the particle velocity

decreases. The mathematical expression for the specific energy loss is given by the Bethe formula:

$$-\frac{dE}{dx} = \frac{4\pi e^4 z^2}{m_0 v^2} NB \qquad (1.8)$$

Where B is defined as:

$$B = Z\left[ln\frac{2m_0 v^2}{I} - ln\left(1 - \frac{v^2}{c^2}\right) - \left(\frac{v^2}{c^2}\right)\right] \qquad (1.9)$$

The stopping power depends on the velocity of the particle (v), the charge (ze), the number density (N) and the atomic number (Z). The rest mass, the charge of the electrons and the ratio between velocity and light velocity are also considered in the formula. The parameter I is the average excitation and ionization potential of the absorber. For a non-relativistic particle (v << c) the expression for B varies slowly with the particle energy, therefore the trend of specific energy loss in function of the energy can be ascribed to the initial multiplicative factor. The value of dE/dx is inversely proportional to the energy of the particle through $1/v^2$. This can be explained intuitively by considering that the smaller is the velocity, the longer is the time the particle spends near the electrons transferring more energy to them. In the comparison between two particles with the same velocity, the only important factor is the charge which appears at the numerator (z^2). Therefore, the higher the charge the higher the interaction with the electron clouds resulting in higher stopping power. The properties of the absorber material appear in the expression with the product NZ representing the electron density. Higher atomic number, higher density materials stop better the external charged particles.

Fast electrons

Compared to heavy charged particles, fast electrons lose their energy at a lower rate and follow a more complex and tortuous path in the absorber. Deviations from the straight trajectory are possible because the mass of the interacting particles are equal.

Therefore, in one single interaction, the amount of energy exchanged between the two is much larger. Moreover, interaction with nuclei can also occur. Electrons differ from heavy particles also for the bremsstrahlung radiation. Electrons lose their energy by irradiating photons. The total linear stopping power for electrons is the sum of the collisional and radiative losses:

$$-\left(\frac{dE}{dx}\right)_c - \left(\frac{dE}{dx}\right)_r \qquad (1.10)$$

The ratio between the two specific energy losses is approximately given by:

$$\frac{(dE/dx)_r}{(dE/dx)_c} \cong \frac{EZ}{700} \qquad (1.11)$$

where E is in units of MeV. Typical energies for beta particles or secondary electron from gamma-ray interaction are less than few MeV. The radiative part become important only for heavy atoms.

Neutrons

Neutrons are heavy particles that do not carry any electric charge. Therefore, they do not interact through coulomb forces. They cannot couple with the electromagnetic field as photons do. As result, a neutron can travel centimetres of matter without any type of interaction. Neutrons can interact only with the nuclei of the absorber, and they can either disappear, transferring all the energy to the nucleus, or their energy and propagation direction can change significantly. For slow neutrons (energy lower than 0.5 eV), the main mechanism of interaction is neutron-induced nuclear reactions. Neutrons can be indirectly detected thanks to the secondary products of the interaction. For example, neutron collision with a nucleus can create alpha particles, protons or it can cause fission. All these products can be easily stopped and detected. The probability of such nuclear reactions decreases with the increase of neutron energy. For fast neutrons (energy up to MeV) the most relevant interaction is the elastic or inelastic

if the energy is high enough scattering; because in one single event neutrons can exchange a great amount of energy with the nucleus. Materials able to slow down neutrons are called moderators (they moderate the neutron velocity). The most efficient moderator is hydrogen, in a single interaction, neutrons can lose up to all the energy with a hydrogen nucleus. Inelastic scattering is also possible, in this process a neutron excites the nucleus of the absorber which then emits gamma-ray in the de-excitement process.

1.3.2 Detection mechanisms in solid state absorbers

In solid state absorbers, the energy deposited by the ionizing radiation is converted into free charges that can be collected if an electric field is applied. The energy deposited by ionizing radiation particles inside an absorber can be detected in two ways: direct and indirect detection; the mechanism schemes are reported in Figure 1.8. In the first case, the detection of the incoming photons is divided into two steps: the absorption and conversion of high energy photons into UV or visible photons easier to detect; second the creation of charges with the UV-vis photon. The material used for absorption is called a scintillator. A large variety of materials, inorganic, organic and even plastics, are used as scintillators. In the direct mode of operation, a proper absorber is used to generate directly free charges from the X or gamma-ray photons. In this type of detector, semiconductors are used. This work is focused on the direct detection of ionizing radiation but in the following, a brief overview of the indirect method will be also given.

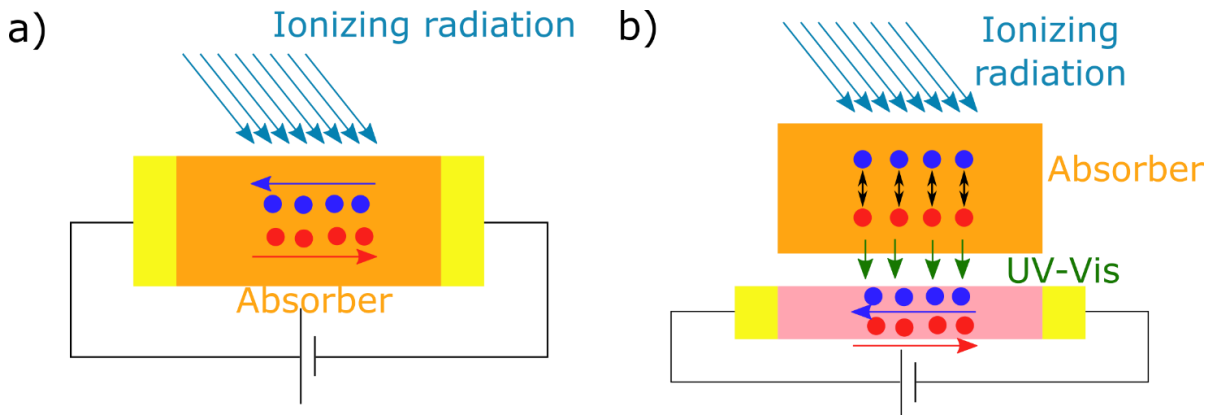

Figure 1.8: Direct and indirect detection mechanism. a) Direct detection method: ionizing radiation is absorbed in the active material which is called absorber and the energy deposited creates free moving charges. If an electric field is applied to the absorber the charges can move creating an electrical current. b) In the indirect method the absorber is a scintillating material in which the charges created by the incoming radiation recombine emitting UV-Vis photons then detected by a UV-Vis detector.

Direct detection

Ionizing radiation interaction with semiconductor materials produces the creation of electron-hole pairs that can be detected as an electric signal. The average energy needed to create an electron-hole pair, called ionization energy, depends on the absorbing semiconductor. For most inorganic semiconductor it is given by the empirical Klein's rule:[9]

$$W_{\pm}^{0} \approx 2.2E_g + E_{Phonon} \qquad (1.12)$$

Where E_g is the band gap energy of the semiconductor and E_{Phonon} is a phonon energy term. In silicon and germanium, the energy required to create an electron-hole pair is 3.69 and 2.62 eV respectively.[10] This is a low value compared to the one of traditional gas detectors (like Geiger counter) which is about 50 eV. In amorphous selenium (α-Se) is known the following behaviour of the ionization energy:

$$W_{\pm} \approx W_{\pm}^{0} + \frac{B(E)}{F^n} \qquad (1.13)$$

It presents a weak dependence on the photon energy through the term $B(E)$, a constant that decreases with the increase of the radiation energy. F is the external electric field

applied to extract the charges and n varies between 0.7 and 1. $W_{\pm}^{0}$ for selenium is expected to be around 5 eV. $W_{\pm}$ can reach 45 eV at the operating bias conditions.[9] The number of free charge carriers created inside the semiconductor can be calculated by:

$$N = \frac{\Delta E}{W_{\pm}} \qquad (1.14)$$

ΔE is the energy deposited in the active material.

In the following will be listed the properties of an ideal semiconducting material to be a good semiconductor for direct ionizing radiation detectors:[9]

- Most of the incident ionizing radiation should be absorbed within a practical semiconductor layer thickness. That means the interaction between the absorber and the radiation is strong enough to stop most of the radiation inside the detector with minimal radiation losses. At fixed radiation, the detector absorption depends on the attenuation coefficient of the semiconductor used and on its thickness.
- The semiconductor should have high intrinsic sensitivity. Sensitivity is defined as the total charge collected by the detector for a unit of radiation exposure. This quantity is representative of the whole detection process. The generation of charges inside the semiconductor depends on the absorbed energy and the ionization energy of the material ($W_{\pm}$). The collected charges are only the ones able to reach the electrodes, therefore sensitivity also accounts for charge transport in the semiconducting layer. The theoretical sensitivity (S) can be defined as:

$$S = S_0 \eta_X \eta_m \eta_{CC} \qquad (1.15)$$

Where S_0 is a constant that depends on the incident photon energy. η_X is the attenuated fraction, η_m is the number of electron-hole pairs generated by each single photon and finally η_{CC} is the charge collection efficiency representing the fraction of

charges collected. Usually, the sensitivity is reported per unit of area. 200 µm thick α-Se and 300 µm CZT have sensitivity, for 20 keV photons, of 24 µC Gy^{-1} cm^{-2} and 255 µC Gy^{-1} cm^{-2} respectively.[9]

- The output signal in a direct detector is an electrical current that is proportional to the charges collected. To have the higher output signal possible the bulk recombination of electrons and holes generated by the incoming radiation must be the minimum.
- There should be minimum deep trapping of holes and electrons. When an external electric field is applied the drift length of electrons and holes is equal to $D = \mu\tau F$; where μ is the mobility, τ is the charges lifetime and F the electric field. In order for the carriers to reach the electrodes and generate the output signal, the drift length should be higher than the distance between the electrodes. Semiconductors with high mobility (intuitively the velocity of charge carriers inside the material) and high lifetime (average time after which the charge carriers become useless for conduction) are desired.
- Diffusion of charge carrier should be negligible with respect to the drift. Charges can diffuse in unwanted directions due for example to a concentration gradient. However, this effect should be minimum to ensure in a pixelated detector good spatial resolution.
- The dark current (I_{dark}) in the detector should be as small as possible. When a potential difference is applied to a semiconductor a current is measured even when no radiation is present. This current is called dark current. In semiconductors, the thermal energy is sufficient to excite some electrons, following the Boltzmann distribution, in the conduction band generating free charges that can move generating a base current. The dark current is a source of noise, with high dark current is impossible to detect the small fluxes of ionizing radiations. The dark current mainly depends on the band gap of the

material. The smaller the band gap the higher are the free charges thermally excited. The presence of trap states can also increase the dark current. Kabir and Kasap report an ideal dark current density of 0.1 – 1 nA cm^{-2} and commercially available detectors have dark current below 50 nA cm^{-2}.[9,11]

- Another important parameter is the limit of detection (LoD). The LoD is defined as the lowest detectable dose rate and it is very important to determine if a detector is applicable for a specific application. For medical diagnostics, a limit of detection below 5.5 µGy s^{-1} is desired. For CT scans pulses below 1 µGy s^{-1} are used.
- The response time of the material to the impinging radiation should be also considered when evaluating the application of a detector. The current pulse generated inside the semiconductor is characterized by a rise and fall times. Both should be considered if the application employs a train of radiation pulses.
- The detector should be radiation hard, meaning that the properties of the semiconducting material should not change during and after the ionizing radiation exposure. The high energy of ionizing radiation can cause damage to the semiconducting material creating defects and trap states. Defects induced by the radiation can degrade the performance of the detector.
- The properties of the material must be uniform all over the active area of the detector.

Two points in the above list are in contrast. The band gap choice is a trade-off between the intrinsic sensitivity and the dark current value. For low and stable dark current, a high band gap semiconductor is desired; but the higher the band gap is, the lower the number of electron-hole pairs generated by the incoming radiation is. To overcome the problem of high dark current, a common strategy for direct detectors adopts a p-n junction to reduce the dark current. It consists of a highly doped p region in contact with a highly doped n layer. A charge depleted region occurs at the interface of the n-

and p-type regions. This region, depleted from the charges, is created as a result of both electrons diffusion from the n-type material into the p-type one and holes diffusion from p-type to n-type material. Therefore concentration-driven diffusion is responsible for the existence of a space charge region. This region is composed of two zones: a first zone made of filled electron acceptor sites not compensated by holes and a second zone made of positively charged empty donor sites not compensated by electrons. The space charge creates an electrical field that reduces further diffusion. At equilibrium, the field is strong enough to prevent additional net diffusion across the junction, a steady state charge distribution is obtained. Therefore, the depletion region acts like a high resistivity parallel plate ionization chamber, making it feasible to use a diode junction for radiation detection. Due to the electric field created inside the semiconductor, electron-hole pairs produced within the depletion region migrate out and their motion gives rise to an electrical signal. For this reason, the depletion region represents the sensitive volume of the semiconductor detectors.

The performance of the junction is improved by applying a reverse bias, meaning the n-type region is connected to the high potential output and the p-type region is connected to the low potential output of an external generator. As the reverse bias increase, both the width of the depletion region and the electric field increase thus leading to better performance. In modern detectors an intrinsic semiconductor layer is interposed between the p and n regions, creating a p-i-n photodiode. The intrinsic layer acts as the absorbing region while the p and n layers act as the charge extraction and transport layers.

Indirect detection

In indirect detectors, the detection of ionizing radiation is accomplished in two steps involving two different devices. Indirect detectors use a scintillating material to convert the high energy deposited by ionizing radiation into low energy photons. The low

energy photons (UV-Vis) can be easily detected by a photomultiplier tube or a photodetector. In other words, the scintillator converts difficult to detect photons or particles into more detectable photons. As for the direct detector, the scintillating layer has to stop the ionizing radiation in order to generate electron-hole pairs. In this case, they are not collected by an electrical field, they recombine releasing photons in the UV-Vis range. Two are the possible mechanisms reported in Figure 1.9. In the intrinsic case, the electrons excited to the conduction band recombine directly with the holes in the valence band, or, if an exciton is formed the recombination takes place between the valence band and the exciton band. Instead, when defects are present in the material and introduce energy levels inside the band gap the recombination can be a trap mediated one. Scintillators can be organic or inorganic and they can be doped to obtain the desired emission. In order for a scintillator to work properly the Stoke shift is important. A big Stoke shift is important to avoid self-absorption of the scintillating light. The material has to emit photons which have significantly lower energy than the band gap, otherwise the emitted light is absorbed by the scintillator itself and the transmitted one is weak. For this purpose, defects can be inserted in the material to create recombination centres specifically designed to emit a photon that can be transmitted by the scintillator. The self-absorption effect becomes important for high energy photon because centimetres thick scintillator is needed to stop the radiation. As for the direct detectors unwanted defects can degrade the performance of the scintillating materials by introducing non-radiative recombination centres. The most important parameter for a scintillator is the light yield: the number of photons emitted per unit of deposited energy.

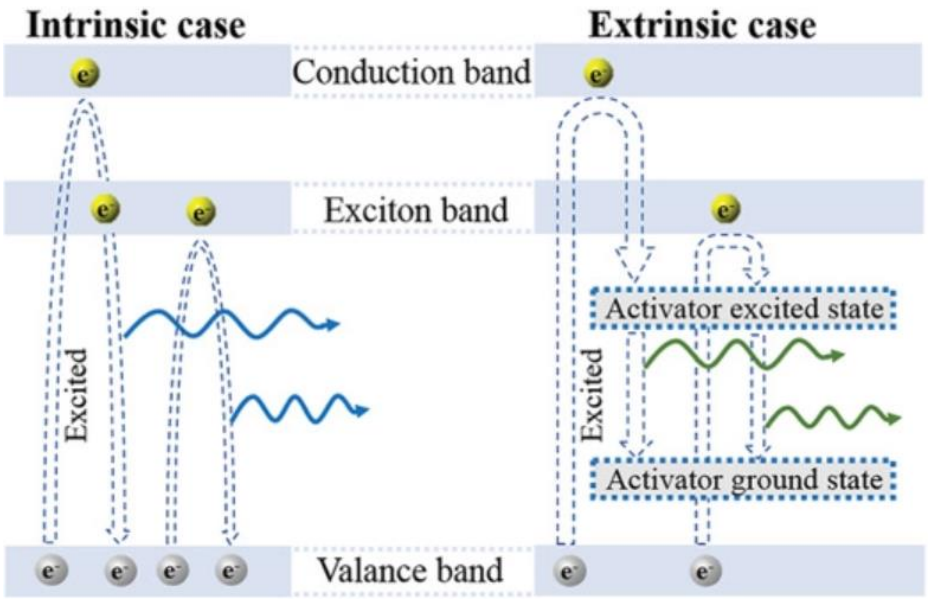

Figure 1.9: Scintillators. Intrinsic and extrinsic scintillating mechanisms.[12]

The scintillating material needs then to be coupled to a UV-Vis detector able to measure the photons emitted. This step is critical because the proper match between the emission spectra of the scintillator and the spectral response of the detector have to be accomplished.

1.3.3 State-of-the-art of solid-state ionizing radiation detectors

Solid state ionizing radiation detectors can operate mainly in two different ways depending on the application: current mode or pulse mode. The current mode is used in high fluxes applications, for example in X-ray imaging techniques. In current mode, the integral of the charges created inside the semiconducting material per unit of time, i.e. the electrical current, is measured.

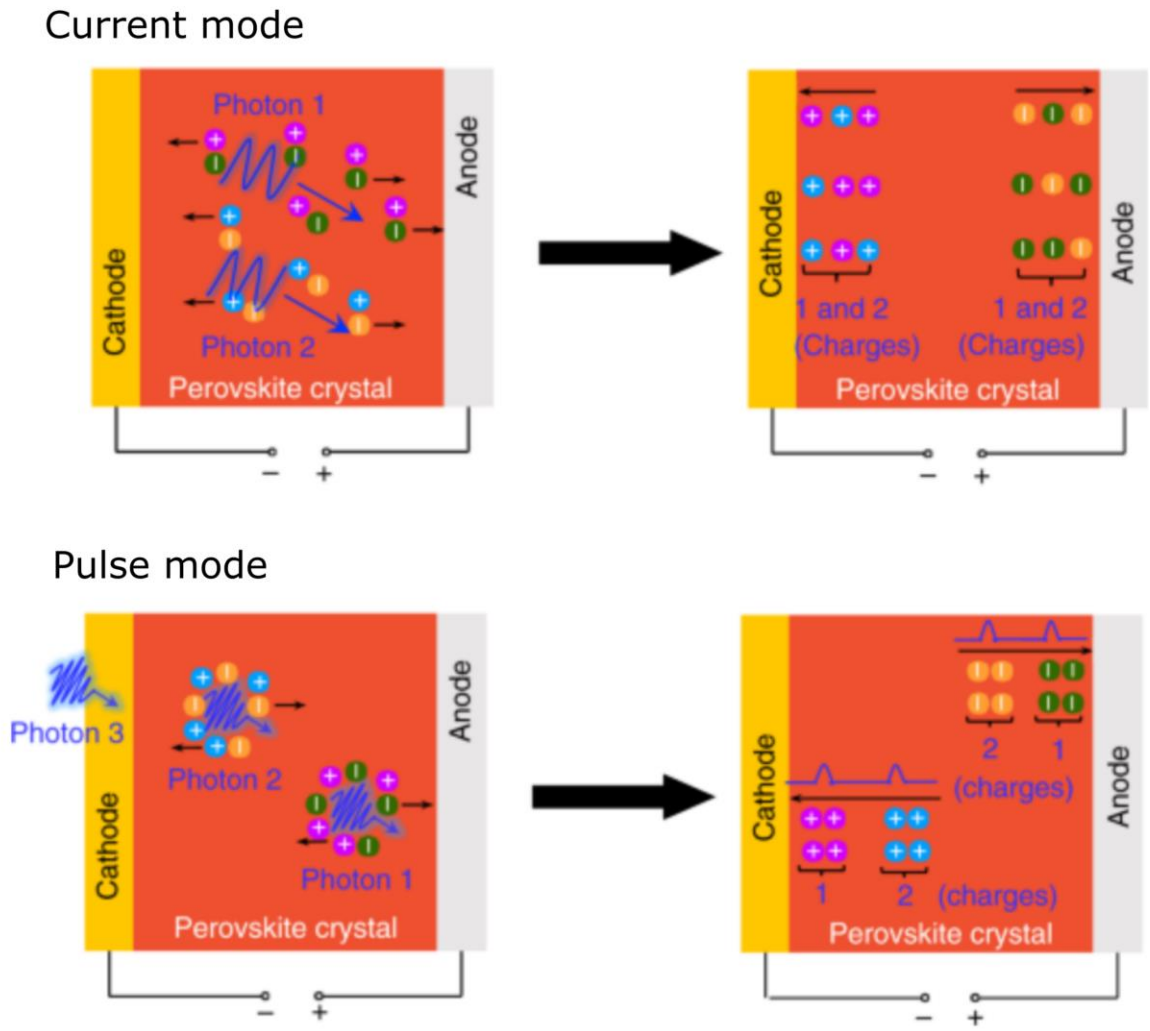

Figure 1.10: Current and pulse mode. In current mode the detector collects the charges independently from the events. In pulse mode the charge generated from every single event is collected is separate times creating current pulses.[13]

Each ionizing particle interacting with the active material releasing energy is called *event*. Since, in general, the response time of the detector is slower than the time between two events, especially in high fluxes conditions, the measured current is equal to the average charge deposited by the radiation per unit of time. A detector operating in pulse mode instead measures the charge deposited by a single radiation event. Since the charge deposited inside the semiconductor is proportional to the energy of the radiation if the detector and the read-out electronics are able to measure single events,

it is possible to establish the energy of the incident radiation. This technique is called charge spectroscopy and it is used in many fields of scientific research.

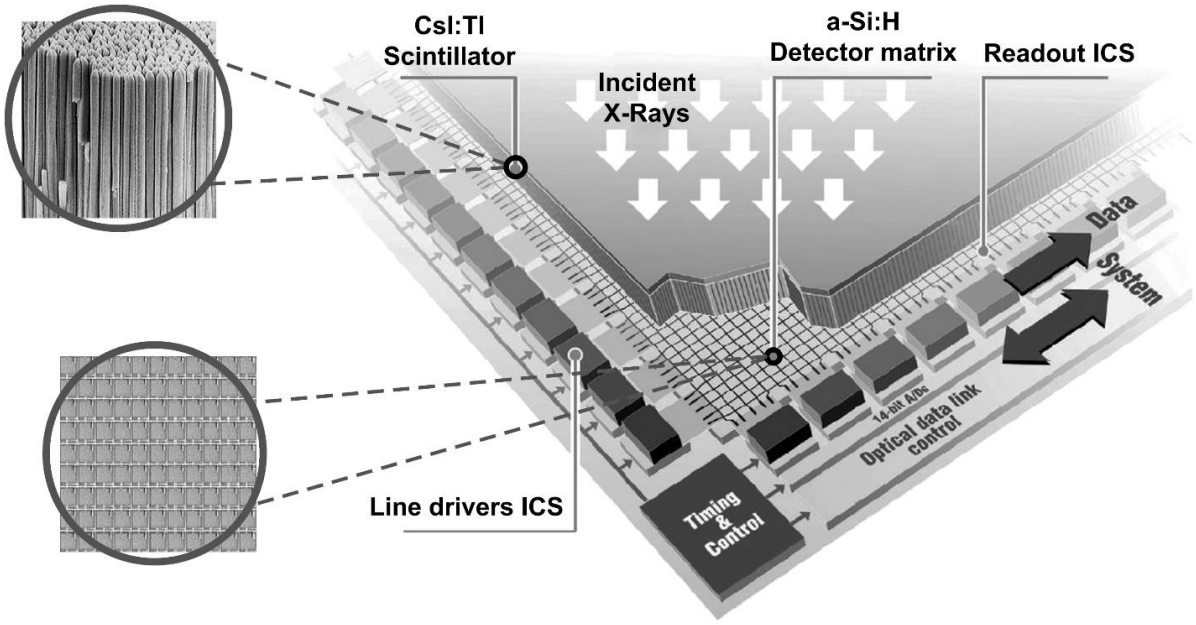

Figure 1.11: Si flat panel. Scheme of amorphous silicon based flat panel for imaging applications. The scintillators are patterned to increase the spatial resolution. Below the scintillator there is the matrix of silicon photodiodes with switches for the readout.[14]

For imaging applications detectors work in current mode. For this application, the energy determination of the radiation is not crucial but it is important to measure the photon flux (or dose) of the radiation impinging on the detector. To obtain the final image, the spatial information is also needed; usually this is obtained which a pixelated detector. When speaking about imaging detectors used in medical applications the word often used to identify the detector is flat panel due to the final shape of the device. The leading market material for flat-panel X-ray detectors is amorphous silicon (α-Si).[15]

In this case, a matrix of silicon photodiodes is coupled with a scintillating material making an indirect detector, see Figure 1.11. Indirect detectors suffer from low spatial resolution and are difficult to fabricate since the coupling of the scintillating material and the photodetector is a difficult task.[2,16] The low spatial resolution is due to the

presence of the scintillators and the possible spreading in nearby pixels of the emitted light. The issue is partially overcome by patterning the scintillating layer in pillars or equivalent vertical structures. In this way, a wave guiding effect is obtained containing the light emitted in the pixel where the event occurred. On the other hand, the most used semiconductor for direct detection in flat-panel is amorphous selenium (α-Se).

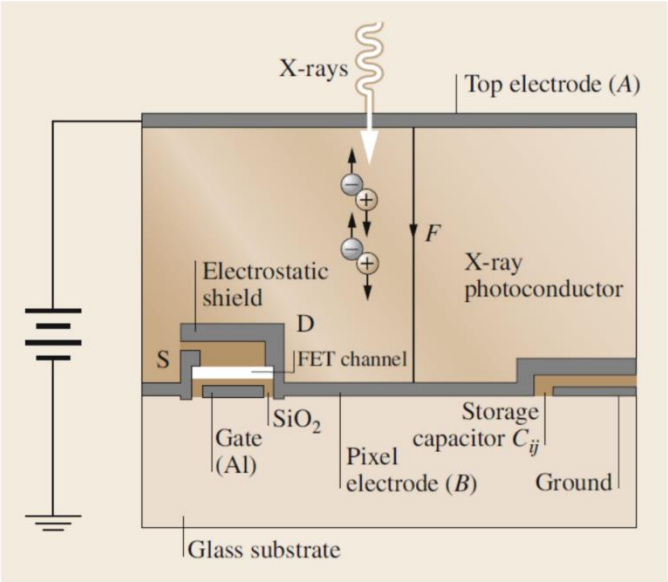

Figure 1.12: α-Se flat panel. A pixel of a direct flat panel detector. The active layer (X-ray photoconductor) is deposited on top of a TFT matric for the readout.[9]

Millions of individual pixels are connected in a matrix similarly to the case of silicon photodiodes. Each pixel has its own thin-film transistor (TFT) switch and storage capacitor to store image charges, Figure 1.12. The charges produced by the radiation inside the active layer are stored in the capacitor and the TFTs allow to read the stored charge in each pixel one at the time. Although superior spatial resolution has been demonstrated,[17] α-Se has a low mobility-lifetime product ($\mu\tau$) which limits its performance at low bias, thus requiring an electric field of 80V/μm (operative bias around 1 kV) to operate efficiently.[18,19] Polycrystalline cadmium zinc telluride (CZT) is an interesting alternative thanks to its high effective atomic number and good transport properties. However, like α-Se, CZT films are obtained through thermal

deposition techniques requiring high vacuum and high temperature to be performed, thus reducing the scalability of the technology.[20] Moreover, α-Si, α-Se and CZT are intrinsically stiff materials and the high-temperature fabrication techniques make it impossible to fabricate them on top of flexible plastic substrates.

2. Perovskites as novel materials for ionizing radiation detection

As an alternative to the traditional semiconductors for radiation detection, organic semiconductor based detectors with high performance have been developed.[21,22] Organic semiconductors are carbon based molecules with a particular chemical bonds configuration. In inorganic semiconductors, the band structure formation is due to the orbitals interaction of large number of atoms. In organic molecules, the semiconducting properties are created by a delocalization of the electrons in the molecule caused by an interaction of $2p_z$ orbitals of the carbon atoms. Usually organic semiconductors are made of conjugated molecules in which the electrons are delocalized and free to move. The particular chemical bonds arrangement creates an energy levels structure characterized by the highest occupied molecular orbital (HOMO) and the lowest unoccupied molecular orbital (LUMO). In analogy to inorganic semiconductors, the HOMO and LUMO level correspond to the valence and conduction band edges respectively; the energy difference represents the band gap of the material. Organic

semiconductors can be deposited from solution at low temperature by printing techniques over rigid and flexible substrates. Since they are mainly composed of C, H and O, the absorption of high energy radiation is very small (<< 1% under 35 keV X-rays). The efficient detection relies on the photoconductive gain mechanism: the minority carrier once generated by the radiation is trapped creating an unbalanced charge inside the material. To keep charge neutrality another charge is injected. If the detrapping time is long enough, multiple majority carriers are injected for one trapped minority carrier, thus creating a gain. Since is a trap mediated effect, the electrical response is slow (in the order of seconds). Hybrid perovskites combines high absorption, very good transport properties and solution processability making them the bridge between organic and inorganic semiconductors.

2.1 History of halide perovskite

The mineral $CaTiO_3$ discovered in Achmatovskaja in the Urali mountains (Russia) by german mineralogist Gustav Rose (Berlin March 18, 1798 - Berlin July 15, 1873) in 1839 is the "father" of all perovskite materials. The name Perovskite was chosen by Rose for his findings in honour of Count Lev Aleksevich von Perovski (9 September 1792, Počep - 21 November 1856, St. Petersburg). He was a Russian nobleman and mineralogist who also served as Minister of Internal Affairs under Nicholas I of Russia. The crystal structure was then described for the first time by Victor Moritz Goldshmidt (January 27, 1888, in Zürich - March 20, 1947, in Oslo) in 1926, a Norwegian mineralogist who introduced the so-called Goldshmidt tolerance factor.[23] The exact

atomic structure was revealed by Helen Dick Megaw (1 June 1907, Dublin - 26 February 2002, Ballycastle) after the development of X-ray crystallography. She studied the diffraction of X-ray on barium titanate $BaTi0_3$ sample which has the same crystal structure as the mineral found by Rose.[24] The name Perovskite was adopted to identify a class of materials with the same structure as calcium and barium titanate. This family of materials have the chemical formula ABX_3, with A and B being cations and X an anion. Historically, oxide-based perovskites have been the most studied due to their ferromagnetic, magnetic and superconductive properties. The first halide perovskite was observed by Moller 1958, $CsPbX_3$, in which X can be Cl, Br or I. In this kind of perovskites, photoconductivity was discovered. The first hybrid perovskite with methylammonium (MA) as the organic cation was studied by Weber in 1978. Demonstrations of possible application in thin-film transistors and LEDs were proved by Mitzi and coworkers in 1999.[25] Indeed, in 2006 Miyasaka used $CH_3NH_3PbBr_3$ (MABr) as a sensitizer in dye-sensitized solar cells (DSSC) showing a power conversion efficiency of 2.2%.[26] Nowadays, heterostructured perovskite solar cells (PSC) have reached 25.2% certified efficiency.[27] Up to now, it is the fastest-growing solar cell technology.

The excellent optoelectronic properties of halide perovskites combined with the high effective atomic number (presence in the structure of heavy elements) make this new class of materials very attractive also for ionizing radiation detection applications. The first proof of direct electrical response for inorganic lead halide perovskites under X-rays was given by Stumpous and colleagues in 2013.[28] Since then perovskites have attracted increasing attention in the detector research community; the number of publications about perovskite X-ray detectors increased reaching more than 25 publication per year in 2020.[29] For gamma-ray detection the number of publications is lower but increasing year by year. In Figure 2.1 are reported the number of

publications and citations in the last years for X-ray and gamma-ray detectors based on perovskite semiconductors.

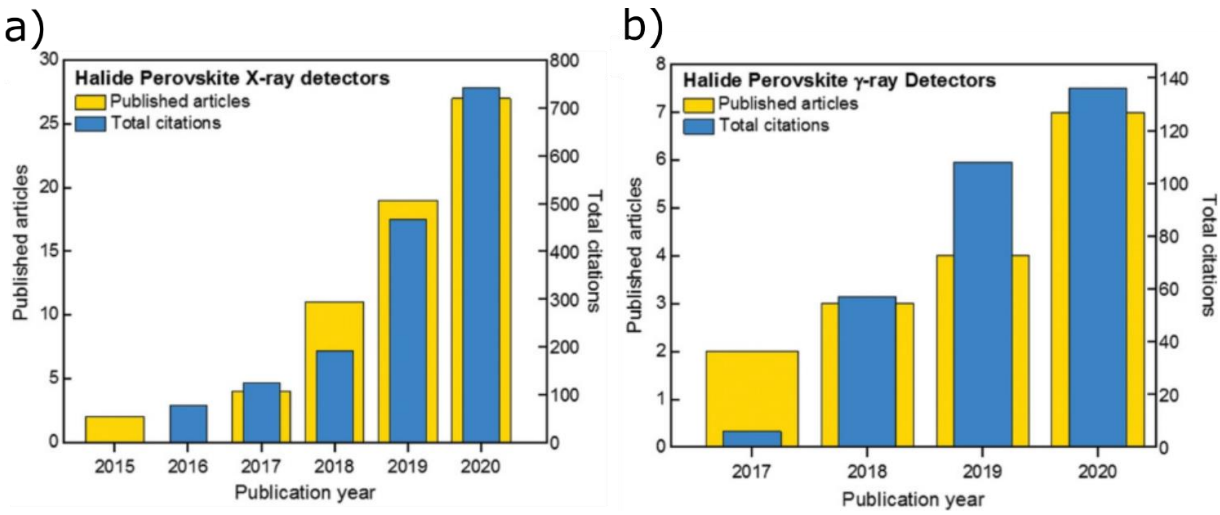

Figure 2.1: Published article ad citations. Published articles about perovskite for X-ray (a) and gamma (b) detection with relative citations number per year.[29]

2.2 Perovskite structure

A common classification of perovskite structures is based on the spatial dimensionality of the atomic structure.

2.2.1 3D perovskite structure

In the perovskite family, the ones of major interest for optoelectronic applications are the halide perovskites.

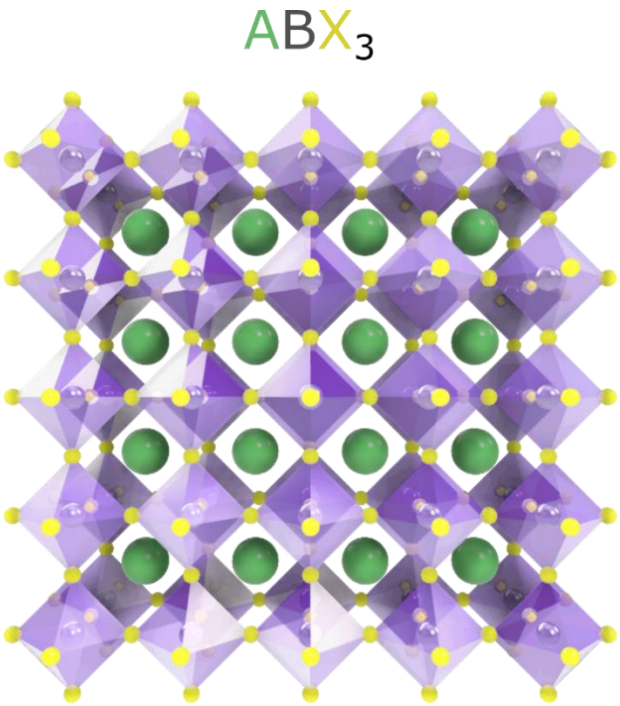

Figure 2.2: Perovskite structure. Representation of the perovskite structure: in green the cation A, in grey the metal B and in yellow the halide atoms. The purple colour indicates the BX_6 octahedra. the cation A sits in the cavity formed by 8 octahedra.

The general chemical formula for perovskites is ABX_3, where A is a cation in the cubo-octahedral interstitial site formed by the BX_6 octahedra net. Cubic symmetry is the ideal case for perovskite, corresponding to a *Pm3m* space group with 12-fold coordination of cation A and 6-fold coordination for cation B. The perovskite atomic structure is reported below in Figure 2.2. In most cases, perovskites present a deviation from the cubic symmetry. The most significant factors are the size effects, described by the tolerance factor and the octahedral factor. The tolerance factor developed by Goldschmidt (t factor) is used to describe the perovskite structure, based on the radius size of the elements in such a structure. It is defined as:

$$t = \frac{R_A + R_X}{\sqrt{2}(R_A + R_B)} \qquad (2.1)$$

where R_A, R_B and R_X are the ionic radii of A, B and X respectively. For an ideal cubic crystal structure, this value is equal to 1. The sum of the ionic radii on the edge of the cube is equal to the sum of the radii on the diagonal divided by the square root of two. Cubic structure in oxide perovskite is found for $0.89 < t < 1$ and in halide perovskite for $0.85 < t < 1.11$. Deviation from this range due to a mismatch of crystal components results in a deformation of the crystal structure. If $t < 1$ the tensions on the bounds result in the tilting of the octahedra reducing the symmetry of the system, thus tetragonal or orthorhombic structure. Instead, with $t >> 1$, meaning cation A is bigger than cation B, the 3D structure of the perovskite can be compromised. Indeed, if the radius of A is too big may not fit anymore in the interstitial site resulting in a low dimensionality perovskite. To describe better the perovskite structures another factor must be taken into consideration. μ represents the octahedral factor and it is defined by the ratio between the two ionic radii of the atoms composing the octahedron.

$$\mu = \frac{R_B}{R_X} \qquad (2.2)$$

For halide perovskites is necessary to have $\mu > 0.442$ otherwise the octahedra net will be unstable and the perovskite structure does not form. These two factors are very helpful, however, there are other external factors, such as the temperature or the chemical environment, which can modify the structure from the ideal one predicted by the Goldschmidt and octahedral factors. In general, the perovskite structure symmetry increases with temperature. $MAPbCl_3$ and $MAPbBr_3$ are in the cubic phase at room temperature and undergo phase transformation to tetragonal and then orthorhombic decreasing the temperature. Methylammonium lead iodide, $MAPbI_3$, is in the tetragonal phase at room temperature and it forms a pseudo-cubic phase by increasing the temperature to 400 K. In the last years, several combinations of elements have been studied for the creation of new perovskite materials. This research was meanly carried out for the development of photovoltaic cells. In the following, the elements used for each site of the crystal structure will be presented.

A site

The A cation does not show a direct contribution to the electronic properties of the perovskite, but as already mentioned the size of the ion in this site is important. Since the electronic properties are strictly related to the crystal structure, cation A can influence indirectly the properties by deformation of the atomic structure. The most widely used organic cation for the A site is methylammonium (MA; $CH_3NH_3^+$) with an ionic radius of 1.81 Å. This value is too small to form the cubic structure, leading instead to the tetragonal lattice at room temperature for $MAPbI_3$. Since the weak compact structure, the bandgap of methylammonium lead iodide is 1.51 - 1.55 eV. Researchers studied the formamidinium cation (FA; $HC(NH_2)_2^+$) with an ionic radius 1.9 – 2.2 Å. $FAPbI_3$ perovskite should have a cubic structure, nevertheless, the asymmetric nature of FA leads to nonhomogeneous interaction with the iodine; thus, resulting in a displacement of the cation in the interstitial site. This non-centered position of formamidinium brings the system to adopt the trigonal structure with band gap values of 1.43 – 1.48 eV. Smaller radius cations have also been investigated, Cs^+ with 1.67 Å results in a smaller symmetry structure with a larger bandgap (1.73 eV). A great advantage of perovskite materials is the possibility to easily create double or triple cation "alloys". It is possible to create mixed cations perovskite as $(MA)_x(FA)_{1-x}PbI_3$ creating the possibility to tune the properties by varying the relative amount of the two (or three) cations in the structure.

B site

In hybrid perovskite, the B site is occupied by metals of the *IVA* group of the periodic table, Ge, Sn, and Pb in their divalent oxidation state. The most stable and performing perovskites devices are the ones with lead as B cation. For this reason, lead-based perovskites are the most studied for optoelectronic applications. Proceeding along the *IVA* group the stability of the divalent state decreases, in fact, germanium based hybrid

perovskites are very unstable and difficult to fabricate.[30] The structure of Sn-based perovskite has been studied by Stoumpos et al.[31] ; they showed a tetragonal structure for $MASnI_3$ at ambient conditions similar to the one of $MAPbI_3$ but with a higher symmetry phase. They also investigated the possibility to create mixed B cation perovskites. They managed to produce $MASn_{1-x}Pb_xI_3$ binary metal perovskite demonstrating the possibility to tune the band gap by varying the ratio between tin and lead. For Sn-rich perovskite up to x = 0.5 a pseudocubic tetragonal *P4mm* structure similar to the one of pure $MASnI_3$ is obtained. For higher concentrations of Sn the structure changes to a tetragonal *I4cm* structure. Higher Sn:Pb ratio corresponds to a lower band gap as expected since $MASnI_3$ has a band gap of 1.1 – 1.4 eV. The $MASnX_3$ perovskites should be better as solar cell performance than lead-based ones but their marked instability is still a big problem to solve.[32]

X site

In the organometallic lead-halide perovskites, the X site is occupied by a halide atom, the *VIIA* group of the periodic table (Cl, Br, I). The halide component has been the most effectively varied for tuning the properties of perovskites. Proceeding along with the halide group from chlorine to iodine, the atomic radius increases, and the electronegativity decreases for a better match with the one of lead. In this way, the covalent character increases resulting in a lower energy band gap. The most used halide is iodine. Thanks to its similarities with the lead cation, it creates the most stable structure. It is found that the addition of a small amount of chlorine to $MAPbI_3$ improves the carrier diffusion lengths and carrier lifetimes. Interestingly, the Cl incorporation leaves the band gap almost the same, because of low miscibility with iodine. $MAPbCl_3$ adopts a cubic structure at room temperature, however, $MAPbI_{3-x}Cl_x$ have shown to produce highly oriented crystalline structures in a tetragonal phase. There was a large debate on the role of chlorine in mixed halide perovskite. Hui et al.[33] investigated the role of chlorine during the formation of the perovskite phase. They

showed with EDX and XPS analysis that only a negligible amount of chlorine atoms exists in the mixed halide perovskite $MAPbI_{3-x}Cl_x$. The Cl affects the formation of the crystals by removing the excess $CH_3NH_3^+$ precursor as volatile CH_3NH_3Cl. The presence of excess precursor is important to slow down the formation of the crystals thus the formation of higher quality crystals. On the contrary, the inclusion of Br in the perovskite structure leads to a change in the structure so in the band gap value. The difference in atomic radius results in a compression of the Pb-I bonds causing structural distortion that leads to an increase of the band gap. Snaith and co-workers studied the effect of I:Br ratio in $FAPbI_{3-x}Br_x$ perovskite tuning the band gap between 1.48 and 2.23 eV.[34] Although iodine based perovskite have a major role in the solar cell community, bromine based on the other hand are largely used for ionizing radiation detection since the larger band gap decreases the dark current.

Perovskites are further classified based on their dimensionality. The structure described so far is called 3D perovskite structure and it is the one of barium titanate. When in the A site a large cation is inserted the inorganic octahedra structure falls apart and separates in layers or even in island. The most studied low dimensional perovskite systems are the, so called, 2D perovskites.

2.2.2 2D perovskite structure

Layered two-dimensional (2D) halide perovskites have recently emerged as a more stable and more versatile family of materials than three-dimensional (3D) perovskite solar cell absorbers and other applications. 2D perovskites are a vast family of materials that allow a greater diversity of compositions and properties. They can be seen as the dimensional reduction of the 3D perovskite lattice, with the general formula $(A')_mA_{n-1}B_nX_{3n+1}$, where A' can be a monovalent (m=2) or divalent (m=1) cation that fits between the inorganic $A_{n-1}B_nX3_{n+1}$ two-dimensional sheets. When m=2 the 2D

perovskites form in the Ruddlesden-Popper phase (RP) where the octahedra within two inorganic layer are shifted, while with m=1 they are found in the Dion-Jacobson phase (DJ), in which the octahedra are aligned. The number n can be seen as the number of octahedrons one over the other between two A' molecules, or improperly as the inorganic layer thickness. The most notably A' molecules are butylammonium (BA) and phenethylammonium (PEA). The atomic structure is reported in Figure 2.3a. Although the width of the A' cation is approximately restricted to the area of a square with a side equivalent to the A-X-A distance, the length of the molecule is virtually unrestricted. Long and narrow molecules are favoured over molecules with a large cross-sectional area. Besides the size and shape of the organic molecule, interactions between the organic groups can either stabilize or destabilize the perovskite structure. These interactions may include hydrogen and halogen bonds as well as p-p and van der Waals interactions. While many of these interactions are weak, in more complex organic molecules with multiple functional groups the effects of the interactions along the longitudinal axis of the molecule are additive and, therefore, can play a crucial structure-directing role. Importantly, the perovskite framework is highly tolerant of organic functional groups such as thiol, carboxyl, alkenyl, alkynyl, diyn, and many others.[35] The tolerance for such a wide variety of sizes and functional groups in the organic cations, along with the possibility to change the metal, halides, and thickness of the inorganic sheets (n value), make the possible 2D hybrid perovskites virtually infinite, and yet only a few hundred perovskite structures have been reported. Similar to 3D perovskites, 2D perovskites exhibit a valence band made up predominantly of halide p-orbitals hybridized with some metal s orbitals and a conduction band where metal p-orbitals dominate. Compared with 3D halide perovskites, 2D perovskites have enhanced exciton binding energies due to a dielectric confinement effect in the layers and thus the excited electrons are strongly attracted to the holes having then a higher E_b. This can also be explained when considering that E_b is proportional to the effective

mass of the charge carriers and dielectric constant (ε). Binding energies for 3D perovskites are in the range of 10 to 60 meV depending on the perovskite and crystal phase,[36] while 2D perovskite can reach binding energy of 480 meV.[37] Thus, a dielectric confinement effect originates from the alternation of low ε of the organic molecules and a high ε of the lead-halide layers, see Figure 2.3b. This layered structure brings the 2D perovskite to an anisotropic conductivity. The charge carrier mobility is found to be higher in the direction parallel to the octahedra sheets. While is lower along the perpendicular direction due to the insulating barrier.

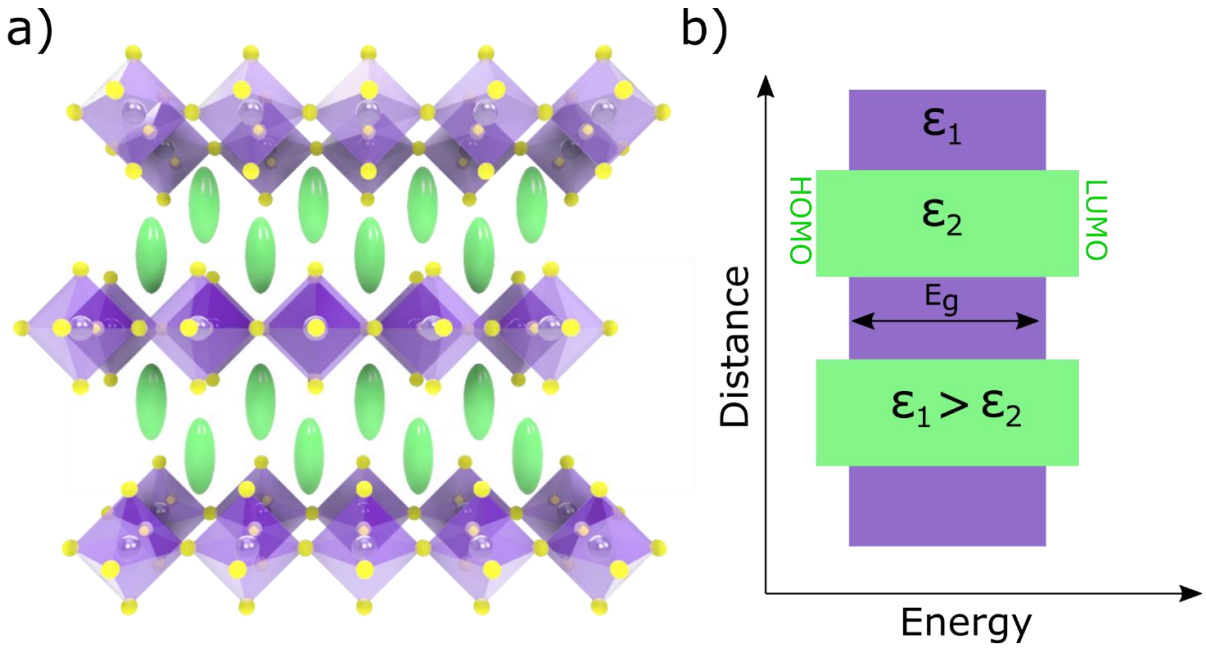

Figure 2.3: 2D perovskite structure. a) Atomic structure of 2D perovskite: the inorganic layer formed the octahedra are separated by the A cation in green creating a layered structure. b) Energy level scheme of the structure. The band gap is determined by the inorganic part and the lower dielectric constant of the organic layer creates a confined effect building a natural multi quantum well.

The large organic molecules donate an important advantage to 2D perovskite. Although 3D perovskites have better transport properties, they suffer from high environmental instability. Instead, 2D perovskites possess high environmental stability because of the enhanced hydrophobicity given by the tail of the organic molecule. The organic cation

tends to cover the grain boundaries surfaces of perovskite forming a repulsive barrier to water.

2.3 Synthesis and Growth

Compared to traditional semiconductors, halide perovskites can be synthetized and grown in different ways making them very versatile semiconductor materials. Traditional semiconductors like silicon and germanium are produced with slow and expensive techniques creating crystalline ingots from the melt at high temperatures. The fabrication of ultrapure wafers is obtained with the Czochralski method. In this process, a high temperature melt of the semiconductor is obtained. For silicon the melting temperature is above 1400 °C while for germanium is 937 °C. A crystal seed is placed at the liquid interface and it is slowly pulled out. The melt solidifies at the interface creating a single crystal ingot that can be then sliced down for the specific application. It is a very highly energy consuming and slow process and the dimensions of the final wafer are limited by the complexity of the fabrication method. Nowadays, the largest wafers have a diameter of 12 inch (30 cm) but going further is a challenge.[38] Moreover, the high temperature involved in the process does not allow the direct deposition of these semiconductors above TFT matrices for the fabrication of imagers. Medical application of ionizing radiation detectors would greatly benefit from large-area low-cost materials deposition techniques. For some medical applications, like dose monitoring, flexible detectors are desirable since they could be conformed to the shape of the body for direct measurements on the patient. With traditional semiconductors, the fabrication of flexible device is impossible due to their intrinsic stiffness and their high processing temperature makes impossible their deposition on plastic substrates.

Contrary to traditional semiconductors, perovskites can be processed at low temperature from solution making them a possible low-cost alternative. In the following the most used synthesis and deposition technique for the creation of perovskite based ionizing detectors are given. In general halide perovskites are prepared starting form powder precursors. For a common perovskite, like methylammonium lead iodide ($MAPbI_3$), the synthesis starts with methylammonium iodide (MAI) and lead iodide (PbI_2). The powders in the right stoichiometry can be melted or dissolved in a strong polar organic solvent like dimethyl sulfoxide ($(CH_3)_2SO$; DMSO) or N,N-dimethylformamide (C_3H_7NO; DMF). Once the powders are combined the growth process can start.

2.3.1 Bridgman growth method

This method allows the growth of big single crystals starting from melted perovskite precursors. Following the scheme reported in Figure 2.4, the precursors' powders are positioned in a crucible that is inserted in a furnace with a lowering mechanism. The vertical furnace with temperature control is divided into two parts at different temperatures. The upper part is heated above the perovskite melting point while the lower part is kept at a temperature below the perovskite melting point. In the middle of the furnace, a temperature gradient is formed. The crucible with the melted perovskite is slowly lowered into the furnace and the solidification of the melt takes place. This method is used to produce high quality single crystals of inorganic halide perovskite like $CsPbBr_3$. The Bridgman method has been used by Kanatzidis's group to fabricate high performance X-ray, gamma and alpha particle detectors.[28,39,40] Despite the good material quality obtained with this method, the Bridgman growth has the same problems discussed before for traditional semiconductors: high temperature process, limited dimensions and it requires a long time for cooling. The process is also

very challenging since temperature, lowering speed and cooling time need to be carefully controlled in order to avoid crystal cracking and defects formation.

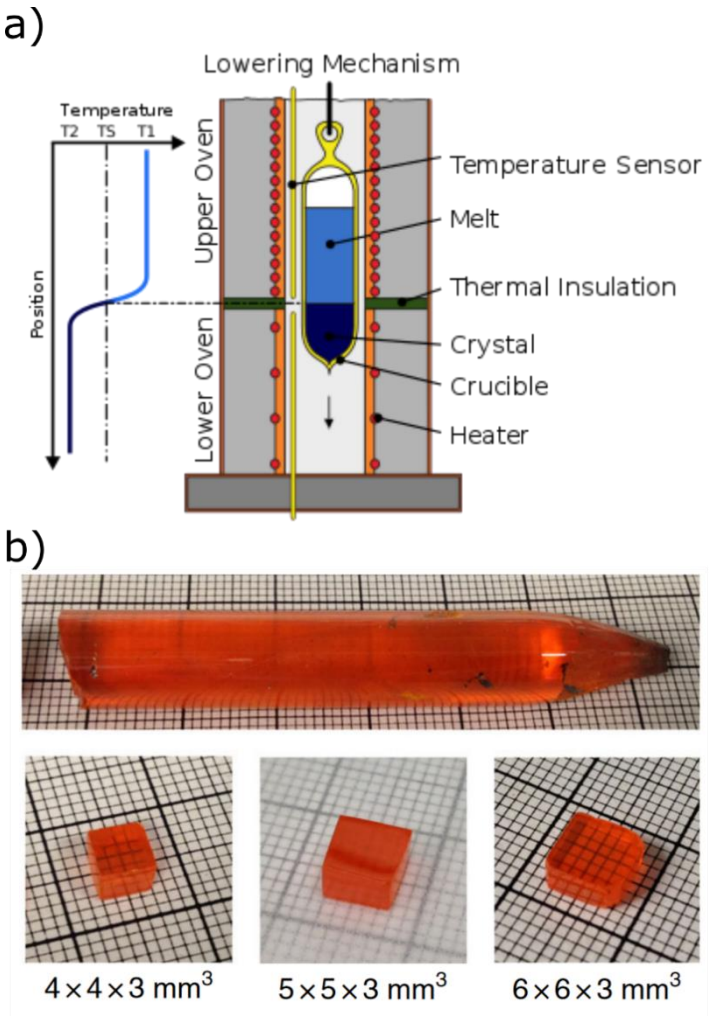

Figure 2.4: Bridgman growth method. a) Vertical Bridgman furnace. The semiconductor melt is placed in a crucible inside a furnace. In the furnace a temperature gradient is present and the crucible is slowly moved along the gradient causing the solidification of the melt. b) Example of a single crystal obtain with the Bridgman method. The big crystal has been cut out for a specific application: gamma-ray detection.[39]

2.3.2 Perovskite melting

Precursors' melt can also be used to fabricate thick perovskite film on rigid substrates. Matt et al.[41] used a melt processing directly on a glass substrate coated with fluorine doped tin oxide (FTO) for the fabrication of X-ray detectors. In their process, the

precursors were dispersed in two different solvents and then mixed causing the precipitation of $CsPbBr_3$ perovskite crystals with sizes between 1 and 10 µm in diameter. The perovskite crystals were filtered and dried. The substrates were then coated with perovskite powder and heated to 575 °C. They initiated the crystallization by cooling the samples to 560 °C with a fixed cooling rate. After the crystallization was completed, the samples were cooled to ambient temperature with a ramp of 1 °C min^{-1}. In Figure 2.5a are reported pictures of different perovskite films obtained with different cooling rates. It is clearly visible the correlation between cooling rate and crystal grain dimensions with larger domains for slower cooling rates. By performing XRD measurement they observed a preferred in-plane orientation in the domains of $CsPbBr_3$. With the melting process, they were able to obtain 250 µm thick film with a hole mobility of 18 cm^2 V^{-1} s^{-1}.

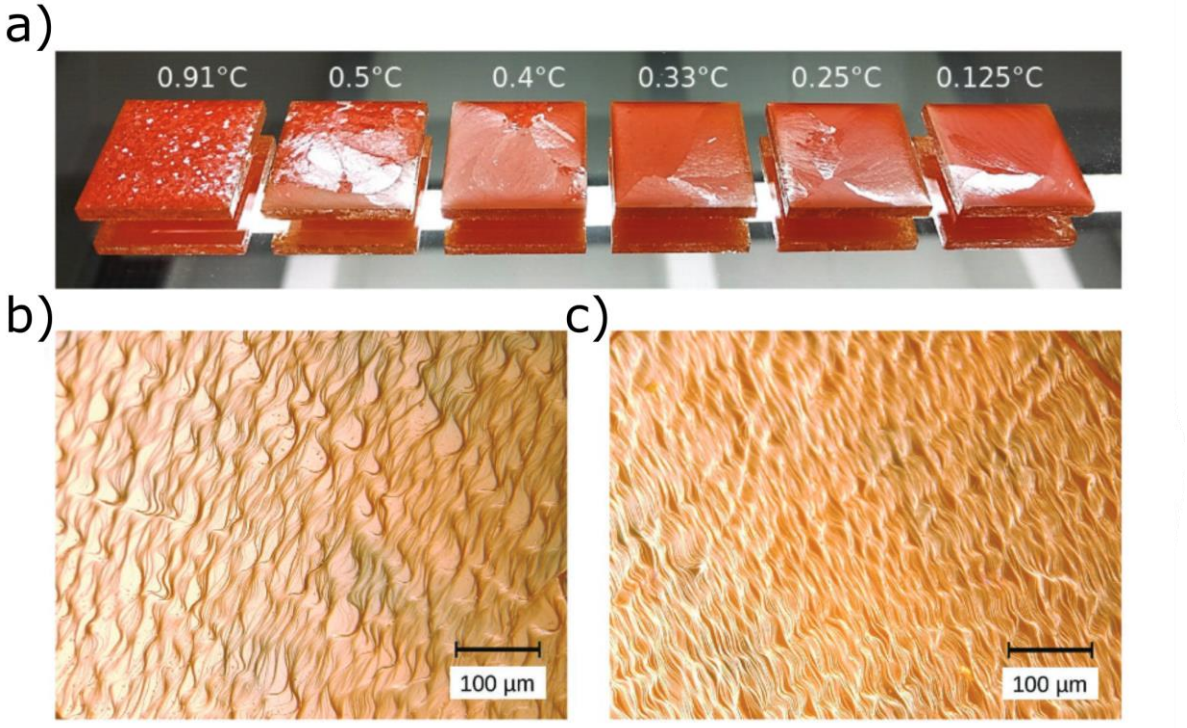

Figure 2.5: Melt processing of $CsPbBr_3$ films. a) Perovskite films on FTO obtained from melted precursors cooled with cooling rates from 0.91 °C min^{-1} to 0.125 °C min^{-1}.[41] b, c) Surface topography of two different crystal domains.[41]

A slightly different approach was used by Pan and his co-workers.[42] The process used for the fabrication of an X-ray detector active layer with the hot-pressed method is reported in Figure 2.6. The perovskite powder is placed on the FTO substrates and inserted in a furnace. The environment is heated up to 600 °C. The samples were kept in this state for a few minutes to reach a fully melted state and to give time at the molten perovskite to spread on the glass. A pre-heated quartz glass is placed on top of the perovskite to force the formation of a uniform layer. The temperature is decreased to initiate perovskite crystallization. The researchers found cracks in the crystal grains subjected to fast cooling (10 °C min^{-1}). They measured the carrier mobility for films created at different cooling rates and they found 38 $cm^2 V^{-1} s^{-1}$ and 12 $cm^2 V^{-1} s^{-1}$ for the fast and slow cooled respectively.

Although these processes are more scalable than the Bridgman method they require high temperatures which limits their application.

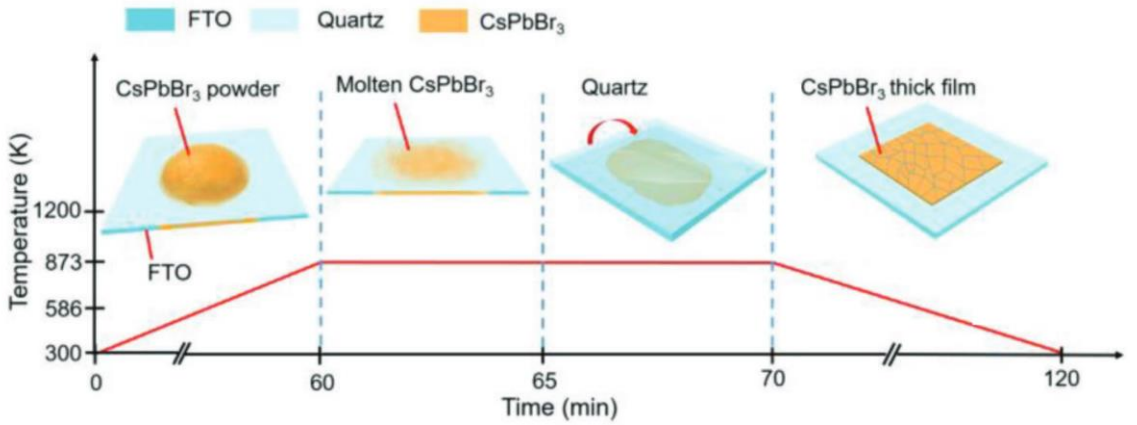

Figure 2.6: Hot-pressed $CsPbBr_3$. The perovskite powder is positioned on a FTO substrate. The powder is melted and it spreads uniformly on the substrate. A pre-heated quartz glass is placed on top of the melt to force the formation of a uniform perovskite layer. Then the temperature is decreased to achieve perovskite crystallization.[42]

2.3.3 Inverse Temperature Crystallization (ITC)

The processes described above are not suitable for hybrid perovskite containing an organic cation. In fact, hybrid perovskites are unstable at high temperature because the organic cation sublimates and leaves the perovskite structure causing a degradation of the material before the melting point.[43] For the fabrication of hybrid perovskite single crystals and films solution processes are used which provide a great advantage over traditional semiconductors. Inverse Temperature Crystallization (ITC) was used the first time with halide perovskite by Saidaminov et al.[44] for the fabrication of hybrid perovskite single crystals. This method takes advantage of the abnormal solubility behaviour of perovskite in some organic solvents. For some combinations of perovskite and solvents, for example $MAPbBr_3$ in DMF, the solubility decreases with increasing solution temperature above a certain temperature. This regime is called the retrograde solubility regime. To perform ITC the perovskite solution is heated in a closed vial positioned in an oil bath for better temperature control. For $MAPbBr_3$ in DMF a drop in the solubility is observed at 80 °C; by keeping the solution at the same temperature perovskite crystals start to grow. To avoid multiple small crystals formation a seed can be introduced in the solution to drive the crystallization. The technique allows to grow large high-quality single crystals within a few hours. ITC has been used by different research groups to grow high quality single crystals for X-ray and gamma-ray detection. Single crystals of $MAPbI_3$,[45,46] $MAPbBr_3$,[47] and even inorganic $CsPbBr_3$ perovskite.[48] ITC has also been used for growing more complex perovskite containing mixed halide or mixed cations. For example: $MAPbBr_{3-x}Cl_x$,[49] and $FA_{0.85}MA_{0.1}Cs_{0.05}PbI_{2.55}Br_{0.45}$.[50] Interestingly this technique has been used to fuse multiple perovskite single crystals together until a 3.3 kg perovskite cube was obtained.[51]

2.3.4 Anti-Solvent Vapour-assisted Crystallization (AVC)

The Anti-solvent Vapour-assisted Crystallization (AVC) method exploits the different solubility of perovskite in different solvents for crystal growth. This method is generally applicable to those cases where the raw material has a large solubility in one solvent, and poor solubility in another solvent, and the two solvents are mutually soluble. During the growth process, the perovskite solution inside a vial is placed in a closed space containing the antisolvent. The perovskite vial is provided with a porous cap so that the antisolvent vapour can penetrate the perovskite solution. The presence of the antisolvent decreases the perovskite solubility which starts to crystalize. To speed up the process the antisolvent can be heated generating an antisolvent-rich environment. With this process, the first ionizing radiation detector based on solution processed perovskite single crystal was fabricated.[52]

2.3.5 Slow temperature reduction technique

In this technique, a saturated perovskite solution is obtained at a high temperature. The temperature is then slowly decreased to reach the supersaturation regime. In this condition, the perovskite starts to crystalize. With this technique, 2D perovskite single crystals can be obtained.[53,54]

2.3.6 Sintering

Sintering is a process where solid particles are joined together with heat or pressure without reaching the melting point of the material. Powders can be compacted in the

desired shape. When pressure or heat is applied, atoms composing a particle diffuse into the next particle across the boundaries joining the two particles. An easily overlooked property of ionic crystals is their plasticity, which results in pressure-induced flow processes. Although halide perovskites are not pure ionic crystals, these materials do exhibit pressure-induced agglomeration effects. Shrestha et al. used a pressure of 0.3 GPa on $MAPbI_3$ powder creating a solid wafer, than used it as X-ray detector,[55] see Figure 2.7b. They obtained good quality polycrystalline wafers presenting ambipolar charge transport with holes mobility in the range 0.53 – 0.70 $cm^2 V^{-1} s^{-1}$ and electrons mobility between 0.50 – 0.56 $cm^2 V^{-1} s^{-1}$. Recently, sintering has been used also for the fabrication of lead-free double perovskite $Cs_3Bi_2Br_3I_6$ wafers.[56] A different approach was used by Frank Liu's group for the fabrication of shape-controlled perovskite wafers.[57] They started with the precursors' powders grinded to small particle dimensions. They applied 10 MPa pressure while heating at 150 °C to sinter the grinded powder in the mold shape. Thanks to pressure and heat the formation of the perovskite structure happens during the wafer formation.

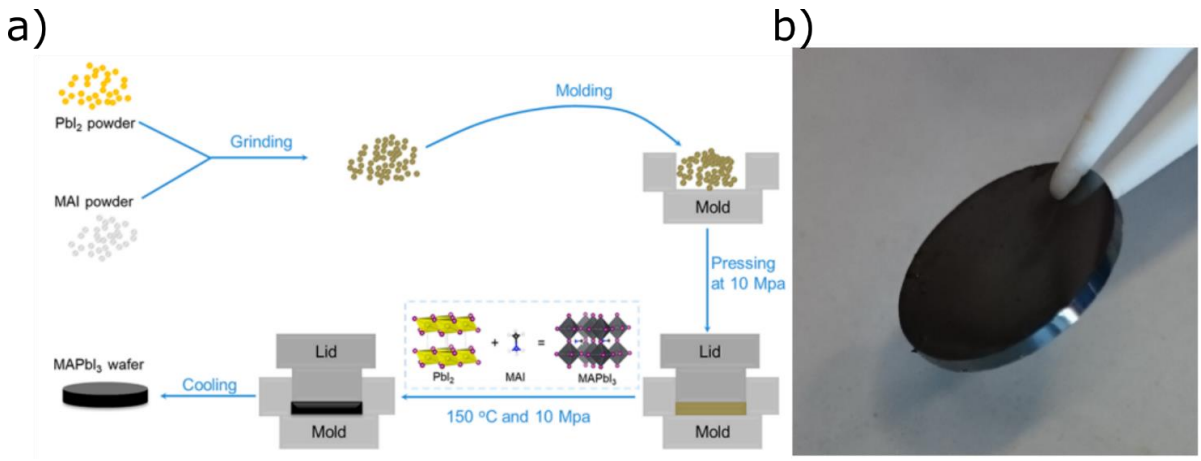

Figure 2.7: Perovskite sintering.[55] a) Reactive wafer production, the precursors' powders are grinded together and place in a mold.[55] Pressure and heat are applied to create a perovskite wafer.[57] b) Picture of a $MAPbI_3$ wafer obtained by sintering.

2.3.7 Film coating techniques

The solution processability of perovskite can be fully exploited using film coating and printing techniques. Those methods allow the fabrication of uniform films onto a large variety of substrates with controlled thicknesses. Moreover, they are the most scalable and less energy consuming techniques. Since perovskite can be deposited by solution, those techniques are the most used for the fabrication of perovskite solar cells and also of perovskite X-ray detectors. On a laboratory scale, the most used coating technique is spin coating. Spin coating exploits centrifugal forces applied to a substrate in which ink has been deposited on top. By rotating the substrate at high rotating speed (1000 - 5000 rpm) the liquid ink spreads on all the available area on the substrate creating a film. During the rotation, the solvent evaporates and the crystallization of the material starts. Depending on the solution and materials used an annealing on a hot plate could be useful to remove completely the solvent and complete the crystallization. The final film thickness and uniformity depend on the solution viscosity, amount of solution on the substrate before spinning, evaporation rate, the total area of the substrate and interaction of the solution with the substrate itself. Perovskite X-ray detectors fabricated by spin coating have been demonstrated for the first time by Yakunin et al.[58]. Basiricò et al. [59] showed the possibility to obtain a thin-film X-ray detector with a triple cation perovskite layer by spin coating with a $\mu\tau$ product of (2.0 ± 0.4) 10^{-5} cm^2 V^{-1}. Spin-coating has also been used to fabricate 2D perovskite based X-ray detectors.[60]

Blade coating is a large area coating technique used by researchers to test the scalability of materials or inks. It used a moving blade to coat a substrate with the desired ink. With this technique is possible to obtain thick film suitable for X-ray detection. Blade coated $MAPbI_3$ based ink was used for the realization of the first imager reported in

perovskite X-ray detector literature.[61] They used a two-step solvothermal process with the addition of α-terpineol in a $MAPbI_3$ dispersion in γ-butyrolactone to obtain a viscous ink to be used in the coating process. They obtained a 400 µm thick perovskite layer over a 10 x 10 cm^2 area and they used a TFT backplane for the signal readout.

Spray coating involves the use of a carrier inert gas at high pressure to create an aerosol for then being deposited on a substrate. This technique can coat large areas faster than spin coating and blade coating. It has been used for the preparation of different perovskite films with variable thicknesses.[62]

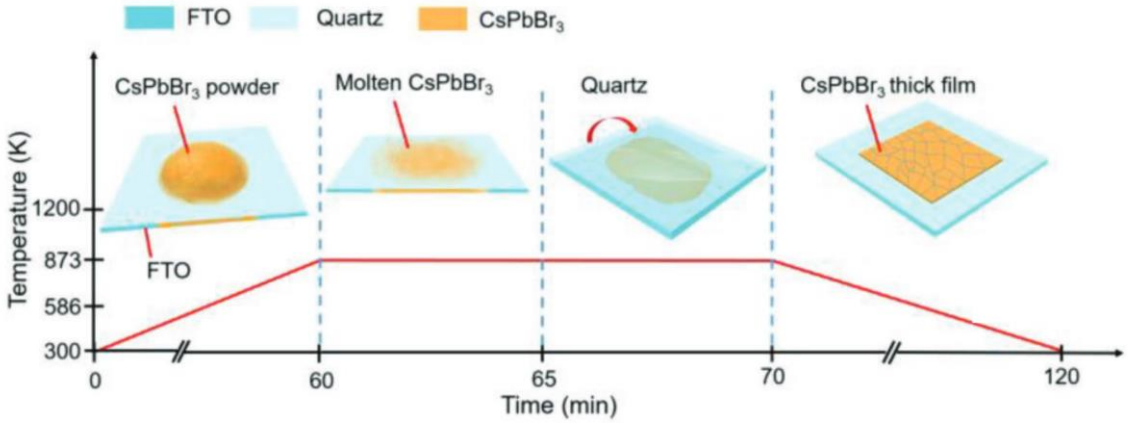

2.3.8 Recrystallization

Gou et al. proposed a new method for the fabrication of thick perovskite films.[63] They positioned the substrate to be covered inside a beaker containing the perovskite solution. They made the perovskite precipitate on top of the substrate by adding an antisolvent to the solution. The substrate is then annealed at 150 °C. On top of the obtained film, they dropped perovskite solution multiple times. This process allows the dissolution and recrystallization of the perovskite film improving its quality.

2.3.9 Printing techniques

Printing techniques allow the controlled deposition of ink on a substrate. The perovskite solution can be designed to be printed with different techniques. Inkjet printing is a versatile method for fabricating functional layers from homogeneous or colloidal liquid phase inks. Drop-on-demand inkjet printing is a specific type of inkjet printing technique. It enables the generation of a single drop when required, limiting the material used. In such a system the printing head or the substrate plate moves to the desired location. The ejection of printing materials is related to a regular pressure pulse in the printing nozzles that is generated by a sudden contraction in the chamber volume, which forces the ink out of the nozzles. The common way to generate pressure pulses is with a piezoelectric transducer. An impulse current is applied to a piezoelectric transducer, resulting in its cyclic deformation, which causes droplets to be ejected from the nozzle. Piezoelectric inkjet printing system allows control over drop size and the velocity of any fluid through the simple adjustment of the electric pulse.[64] Inkjet printing has been used to fabricate inorganic perovskite quantum dot based X-ray detector,[65] and to print a triple cation hybrid perovskite used as absorbing layer in a stacked X-ray detector architecture.[66] Aerosol-jet printing is an air based deposition process of additive manufacturing.[67] It is mainly used for electronic applications thanks to the possibility of making very small features. This technique requires the creation of aerosol and its subsequent deposition on a given substrate. An aerosol is a mixture of a solid or liquid in a gas medium called carrier. In Figure 2.8b is reported a scheme of the technique used for depositing perovskite solution. The first component where the perovskite solution is placed is called atomizer. The carrier, or atomizing gas, is injected through a specific component in the atomizer designed for creating the aerosol. The aerosol travels along a pipe but before reaching the nozzle it passes through the virtual impactor. This device is represented in the scheme with a T connection with the main pipe.

The virtual impactor partially removes the carrier gas increasing the concentration of ink in the aerosol. By doing this, it removes also the smaller particle in the aerosol and decreases the gas velocity. If the gas velocity decrease, the bigger particle cannot be transported anymore. The virtual impactor has then the role of controlling the size uniformity and concentration of the droplets inside the aerosol before the deposition takes place. The aerosol is transported and deposited on the substrate with a sheath gas. The sheath gas is injected coaxially to the nozzle and ensures the correct transportation of the aerosol on the substrate [67]. In the perovskite case, a solution of perovskite in DMF is placed in the atomizer. The carrier gas used is nitrogen. Glushkova et al.[68] used this technique to fabricate high aspect ratio MAPbI3 pillars, Figure 2.8c to be used as an X-ray detector.

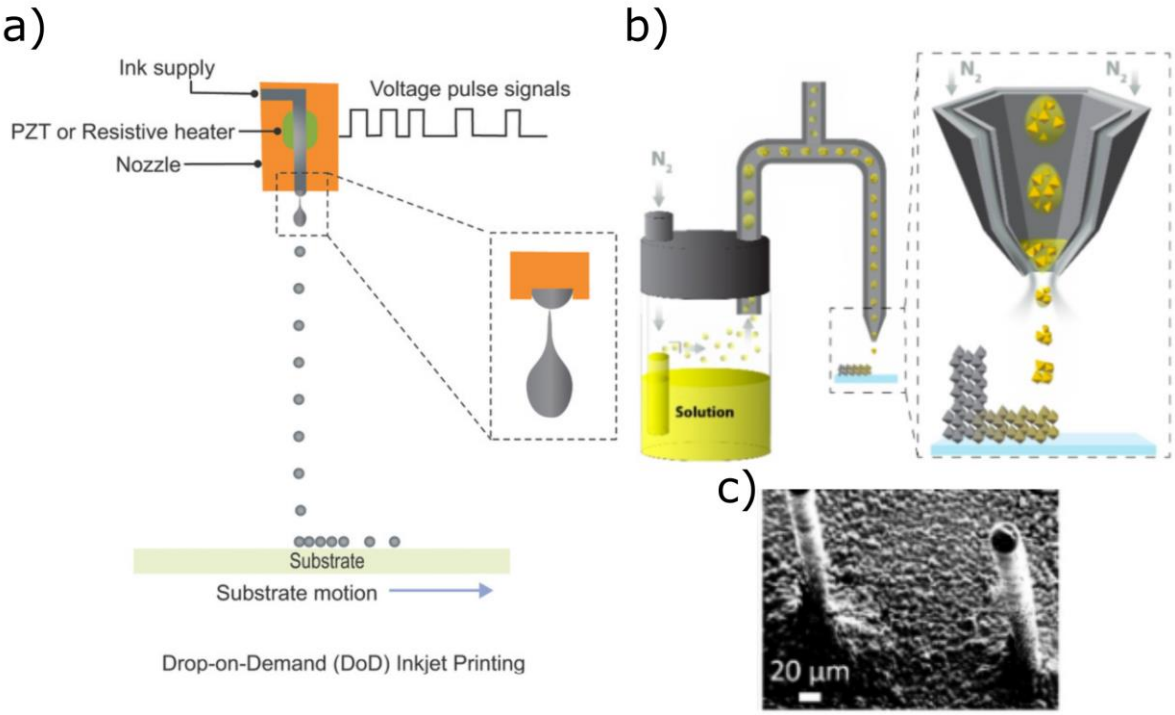

Figure 2.8: Perovskite printing. a) Drop-on-Demand inkjet printing apparatus. An electric pulse is sent to a piezoelectric transducer (PZT); it vibrates creating pressure pulses on the nozzle forcing the expulsion of the ink in small droplets.[64] b) Aerosol jet printing. A carrier gas nebulizes the ink and transports it to a nozzle for the controlled deposition on a substrate. c) Perovskite pillars created with aerosol jet printing.[68]

2.4 Perovskites optoelectronic properties

Besides the large variety of fabrication methods available for perovskite they also have very interesting optoelectronic properties. In this section, an overlook of the halide perovskite properties for ionizing radiation detection is given.

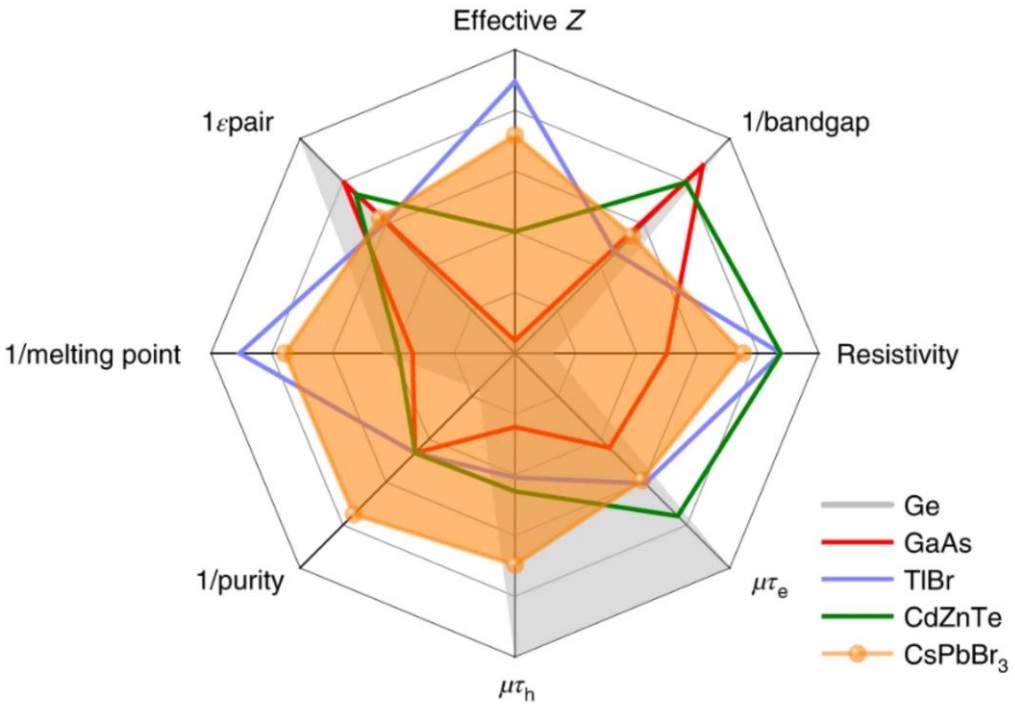

Figure 2.9: Overview of semiconductors properties. Radar plot of semiconductor properties for a good ionizing radiation detector.[69]

In the radar plot reported above the researcher tried to give a general overview of the inorganic perovskite $CsPbBr_3$ properties with respect so other semiconductors used for ionizing radiation detection. From the graph is clear that, even if more work is needed to increase the resistivity and increase purity, perovskites are promising materials for radiation detection.[69]

2.4.1 Ionizing radiation absorption

One of the most important characteristics of an efficient ionizing radiation absorber is the ability to stop and absorb the energy of the impinging radiation. Halide perovskites, especially lead-halide perovskites, have high effective atomic numbers since the presence of heavy elements inside the structure. The perovskites used as active layer for ionizing radiation detectors contain Pb or Bi, in the case of double perovskite, with atomic number 82 and 83 respectively. The most used halides are I (Z = 53) and Br (Z = 35). Inorganic perovskites often contain Cs with atomic number 55. The interaction probability is higher for higher effective atomic number for both photons and charged particles according to equations (1. 8), (1. 11) and(1. 2). The effective atomic number (Z_{eff}) is defined as the fictitious atomic number which is possible to describe a compound concerning ionizing radiation attenuation.[70] It can be calculated as follows:

$$Z_{eff} = \sqrt[2.94]{\sum_i f_i Z^{2.94}} \qquad (2.\ 3)$$

Where 2.94 is an empirical factor, f_i is the electron fraction of the i^{th} element in the mixture. For CZT the effective atomic number is roughly 50,[71] it can slightly vary based on the exact composition. For $MAPbI_3$ the effective atomic number is 64, higher than the one of CZT. The other parameter to consider is the material density. 3D

perovskites have densities between 3.5 and 4 g cm^{-3} while CZT has a density of 5.8 g cm^{-3}. In Figure 2.10, the attenuation coefficient as a function of energy for different traditional semiconductors and perovskites. Perovskites have attenuation coefficients comparable to the ones of CZT. In the energy range used for medical applications 20 – 511 keV, perovskites have attenuation coefficients 1 – 2 orders of magnitude higher than silicon and even higher than the one of selenium and germanium. 2D perovskites have Z_{eff} very similar to the 3D perovskite ones, but given their layered structure and the presence of a larger organic part the density is reduced, thus lower attenuation coefficient than 3D perovskites.

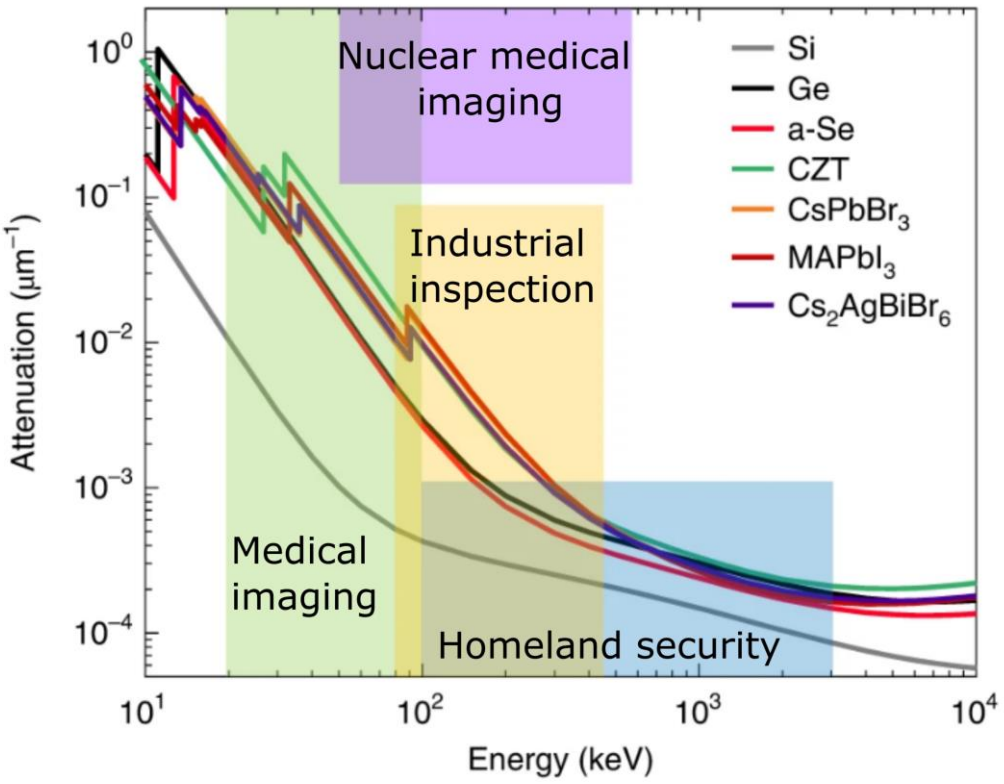

Figure 2.10: High energy photons attenuation coefficient. Attenuation coefficient μ as a function of energy for traditional semiconductors and halide perovskites. The coloured areas refer to different applications energy ranges. In green (20 – 100 keV) medical imaging, purple (50 – 511 keV) nuclear medical imaging, orange (80 – 450 keV) industrial inspection and blue (100 keV – 3 MeV) homeland security.[69]

The presence of lead and the fast development of lead-halide perovskites have raised an important debate in the literature: whether the presence of lead would compromise their commercialization. Since lead is considered a highly toxic element, researchers working on perovskite solar cells are trying the substitute lead with Sn with promising results but with lower performance with respect to Pb based perovskites.[72] Moreover, tin is less abundant on Earth's crust, more expensive and the extraction process has higher environmental impact than the one of Pb.[73] Especially for thin-film technologies, the presence of lead, is not a real concern. In fact, lead is present in a small fraction, 0.001 %wt, well below the RoHS limit (0.1%wt). In perovskite ionizing radiation detectors, the substitution of Pb with Sn would decrease the effective atomic number. The lead-free perovskite versions for this application are often double perovskites or lower dimensionality structures containing bismuth. Although the stopping power remains the same or even enhanced, the mobility is reduced.

2.4.2 Transport properties

For efficient detection, the charges generated inside the absorber should reach the electrodes without recombining during the process. Recombination of charge carriers represent a loss decreasing the signal to noise ratio. The transport properties of perovskites are strongly influenced by the soft nature of the crystalline lattice. The interconnected corner-sharing BX_6 octahedra can easily tilt conferring to the structure a dynamic distortion behaviour. This motion of the lattice produces anharmonic and liquid-like fluctuation behaviour.[74] Recently, polarons have been proposed, where the carrier scattering could be screened by the strong electron-phonon coupling in these materials.[74–76] For MAPbI3 a radius of 60 Å is predicted. The polaron equilibrium radius is larger than the unit cell; such a large radius is quite unique among semiconductors. These features are believed to define the excellent transport properties of perovskites.

As already mentioned, the A cation influences the octahedra connectivity, thus influencing the perovskites transport properties. In 3D perovskites, where there is no spacer, the reported carrier mobility spans between 10 to hundreds of $cm^2\ V^{-1}\ s^{-1}$ for single crystals,[69] and in the order of few tens of $cm^2\ V^{-1}\ s^{-1}$ for polycrystalline films.[77] Interestingly, balanced electron and hole mobility is found in 3D perovskites, consistent with their electron band structure indicating similar electrons and holes effective masses.[77] Those values are 1 – 2 orders of magnitude lower than the electron mobility of CZT and 2 orders of magnitude higher than high mobility organic semiconductors.[22] The carrier lifetimes are in the rage of 1 to tens of μs comparable to the holes lifetime in CZT. These interesting features allow having long carrier diffusion length, exceeding 1 μm even in polycrystalline film.[78] When increasing the dimension of the A cation, the dimensionality of the perovskite structure is reduced. 2D perovskites have mobility between 0.1 to 10 $cm^2\ V^{-1}\ s^{-1}$, quite lower compared to the 3D ones.

2.4.3 Defects

Perovskites are considered to be defect tolerant materials. In the perovskite structure, the defects are the one depicted in Figure 2.11. The tolerance to defects arises from two properties of the perovskite structure. First, the formation of deep traps, detrimental to the transport properties, are predicted to be high,[79] thus making the formation of those defects less probable. The absence of deep traps could explain the long carrier diffusion in polycrystalline films. Second, the dynamic nature of the crystal lattice and its dynamic disorder, as confirmed by Raman spectra. Schilcher et al.[80] measured phonon spectra in perovskites demonstrating the absence of clear phonon mode above 150 K. This supports the theory in which the perovskite crystal lattice is in continuous movement. The dynamic disorder could lead to a self-annealing of the bulk perovskite structure and a migration of the point defects at the surface of the

material. The Huang's group at the University of North Carolina studied the trap density profiles in perovskite based solar cells. They used Drive-Level Capacitance Profiling (DLCP) on stacked architectures with single crystal or polycrystalline perovskite as active layer. They found a deep trap concentration of 10^{10} – 10^{12} cm^{-3} in single crystals bulk. While for thin polycrystalline films the trap concentration found was 10^{14} - 10^{15} cm^{-3}. The defects concentrations of polycrystalline perovskite films are comparable to the one of GaAs grown with metal organic chemical vapour deposition for multijunction solar cells.[81] Perovskite single crystals and films have different interfaces. Depending on the interface, researchers have found trap concentrations between 10^{16} - 10^{17} cm^{-3}. Those results are consistent with the dynamic disorder vision of the perovskite lattice, where the bulk would be defects free and the traps located at the interfaces.

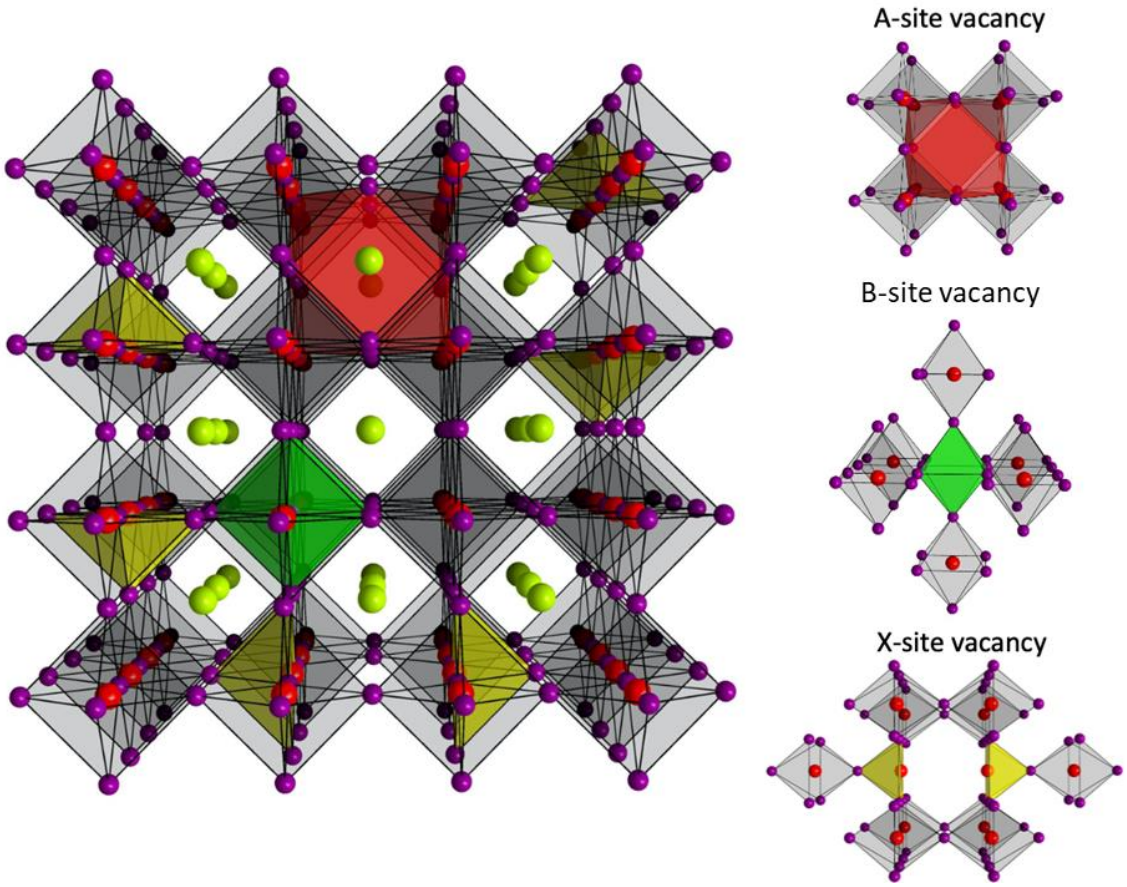

Figure 2.11: Vacancy defects in perovskites. Representation of the vacancy defect of the perovskite structure.

2.4.4 Ion migration

In Figure 2.12a is reported a typical current density versus bias plot of a perovskite based solar cell under illumination. The shape of the curve is strongly dependent on the direction of the bias-ramp during the data acquisition. Snaith propose ion migration as the cause of this phenomenon. Since then, the ion migration in perovskite gained more and more attention from the solar cell and ionizing radiation detection communities. In hybrid halide perovskite the species associated with ion migration are I^- or Br^- and the MA cations, see Figure 2.12b.[82–84] Since this effect is driven by the bias applied to the material for ionizing radiation detectors is a critical aspect. In fact, detectors need to be biased, often at high voltages, to operate efficiently. Moving ions in the crystal structure lead to unstable dark current, higher noise and high electrode degradation, reducing the efficiency of the detector.

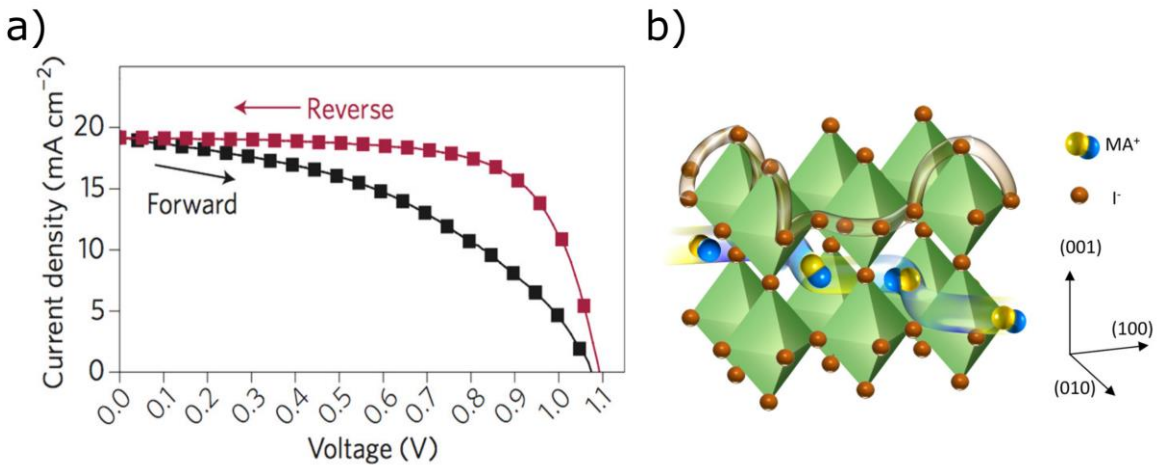

Figure 2.12: Ion migration. a) Typical J-V curve of a perovskite solar cell shoving an important hysteresis effect.[85] In black and red the forward and backward scans respectively. b) Scheme of the migration pathway for iodine and methylammonium in $MAPbI_3$.[82]

2.5 Perovskites degradation mechanisms

Despite the very good optoelectronic properties of halide perovskites, this class of semiconductors has still low environmental stability. In the following the main degradation mechanisms for perovskite are described.

Humidity

Moisture resistance is considered one of the biggest challenges. The moisture instability originates due to the hygroscopic nature of amine salts. For instance, $MAPbI_3$ endures moisture assisted degradation process in which the methylamine group is lost via sublimation and PbI_2 is formed. The highly hydrophilic properties of perovskite lead to water absorption from the surrounding environment and induce the formation of hydrate products similar to $(CH_3NH_3)_4Pb_6 \cdot {}_2H_2O$. The most observed degradation pathway of perovskite in a moisture-rich environment follows the reported reactions:[86]

$$CH_3CH_2PbI_3(s) + H_2O(g) \leftrightarrow CH_3CH_2I(aq) + PbI_2(s)$$

The tendency of methylammonium lead iodide to decompose is caused by the hydrogen bonds between the organic and inorganic part, these bonds are strongly influenced by the polarity of water molecules. Both, sublimation and the reaction previously reported lead to a complete change in the material destroying the electrical and optical properties.[87]

UV degradation

Besides the moisture instability, another important source of degradation in perovskite materials is the UV light exposure. When perovskites are subjected to both light and

dry air they decompose into the organic part, PbI_2, and I_2 as reaction products. The photogenerated electrons on the perovskite reacted with molecular oxygen to form superoxide, which further reacts with the organic component of the perovskite absorber.[87]

Thermal degradation

Hybrid halide perovskite are subjected to thermal degradation. Since the volatile nature of the organic part, at temperature above 300 °C the organic cation can escape from the perovskite structure.[43] But for MAPbI3 based solar cells degradation at temperature above 100 °C has been reported.[87]

2.6 Perovskite single crystals for Direct X-ray and Gamma-ray detection

Perovskite single crystals have demonstrated superior performance with very high sensitivity and low limit of detection. In this section, an overlook to the most important results reported in literature about perovskite single crystals are given. In 2016 Wei et al. reported about the first hybrid lead-halide perovskite single crystal for X-ray detection.[52] They perovskite precursor were dissolved in DMF and dichloromethane was used as the antisolvent for the AVC growth method. By tuning the molar concentration of the precursor in solution they were able to obtain clear crystals with a surface area of 25 cm^2 and 2 mm thick with very high $\mu\tau$ product of 1.2×10^{-2} cm^2 V^{-1}. To realize the detector, they thermally evaporated gold electrode from one side,

and an organic interlayers with silver metal contact on the other side of the crystals (Figure 2.13a). At 0.1V bias the detector showed a current density of 25 nA cm^{-2} resulting in 1.7 × 10^7 Ω cm bulk resistance. In Figure 2.13b is reported a typical dynamic response to an X-ray pulse. The detector showed a box-like response under X-rays with 50 keV maximum energy. They report an X-ray sensitivity of 80 μC Gy^{-1} cm^{-2} and a limit of detection of 0.5 μGy s^{-1}. The sensitivity value is higher than the one of α-Se and the limit of detection is good enough for medical application. An example on how the properties of halide perovskite can be tuned by changing the relative amount of components inside the structure was given by the Jinsong Huang group in 2017.[49] With the ITC growth technique they manage to obtain crystals of mixed halide perovskite $MAPbBr_{3-x}Cl_x$. Lead-halide perovskite suffer from intrinsic doping due to the presence of defects. Unintentional doping increases the dark current inside the material decreasing the device performances. $MAPbBr_3$ is normally a p-type semiconductor, while $MAPbCl_3$ is an n-type semiconductor. Mixing the two materials leads to a doping compensation improving the properties of the final material. In Figure 2.13c are reported the IV curves for different amount of chlorine. The perovskite with x = 0.06 presented a reduction of one order of magnitude of current density, reaching a resistivity of 3.6 × 10^9 Ω cm. The introduction of Chlorine also improved the charge transport properties increasing electrons and holes mobility. The electrons mobility of $MAPbBr_3$ single crystal is roughly 140 ± 17 cm^2 V^{-1} s^{-1}, and increases to 340 ± 20 cm^2 V^{-1} s^{-1} for crystals with 2.0% Cl. While the holes mobility of the $MAPbBr_3$ single crystal is about 220±20 cm^2 V^{-1} s^{-1} at room temperature. The addition of 2.0% Cl into $MAPbBr_3$ dramatically increased the hole mobility to 560 ± 46 cm2 V^{-1} s^{-1}. The X-ray detector fabricated with this material reached a sensitivity of 8 x 10^4 μC Gy^{-1} cm^{-2} and an impressive LoD down to 7.6 nGy s^{-1} under 8 kVp X-ray. This example gives an idea of the great advantage of perovskite properties tunability. A great advantage of lead-halide perovskites is their solution processability. Wei et al.

demonstrated the possibility to grow perovskite single crystals on Si substrates.[47] Polished and precleaned Si (p-type) wafer was treated with a mixture of dichlorobenzene and (3-aminopropyl)triethoxysilane (APTES) to obtain NH_2-terminated molecules on the surface. The wafer was then treated with HBr (aq.) to convert the amino groups into $-NH_3Br$ groups. This allows a good mechanical and electrical connection between the $MAPbBr_3$ layer and the silicon surface. For the perovskite crystal growth, a seed is positioned on the silicon surface and the growth is performed through ITC method. In Figure 2.13d is reported the SEM picture of the perovskite/silicon interface. They grew an integrated crystal of 5.8 x 5.8 mm^2 that could resist to a tensile pressure of 3.5 kPa. The interface generated using silicon as p-type layer allowed a dark current suppression down to 23 nA cm^2. The presence of silicon also increased the sensitivity with respect to a control device featuring Au/$MAPbBr_3$ interface, with a top value of 322 µC Gy^{-1} cm^{-2} at -1 V bias obtained for a 2.0-mm-thick device under 50 kVp X-rays. They observed a huge increase in the sensitivity when the bias is applied, reaching 2.4 x 10^4 µC Gy^{-1} cm^{-2} at -7 V. By patterning the metal contact on the top of the crystal they realized a linear array for the acquisition of X-ray images, an example is reported in Figure 2.13e. Very recently Liu et al. demonstrated the possibility to grow high performance single crystals with a triple cation mixed halide perovskite.[50] They demonstrated superior performance in comparison to $MAPbI_3$ and $FAPbI_3$ in terms of sensitivity, limit of detection and operational stability of the device. In Figure 2.13f the estimation of the LoD for the three materials is reported. The triple cation single crystals, in an asymmetric configuration employing C_{60} and bathocuproine (BCP) as electron transport layer and spiroTTB as hole transport material, reached a top sensitivity of 3.5 ± 0.2 × 10^6 µC Gy^{-1} cm^{-2} at -60 V bias three orders of magnitude higher than the other crystals explored. The triple cation perovskite demonstrated superior stability retaining 91 % of the initial sensitivity after 45 days, while MAPbI3 crystal only 68 %.

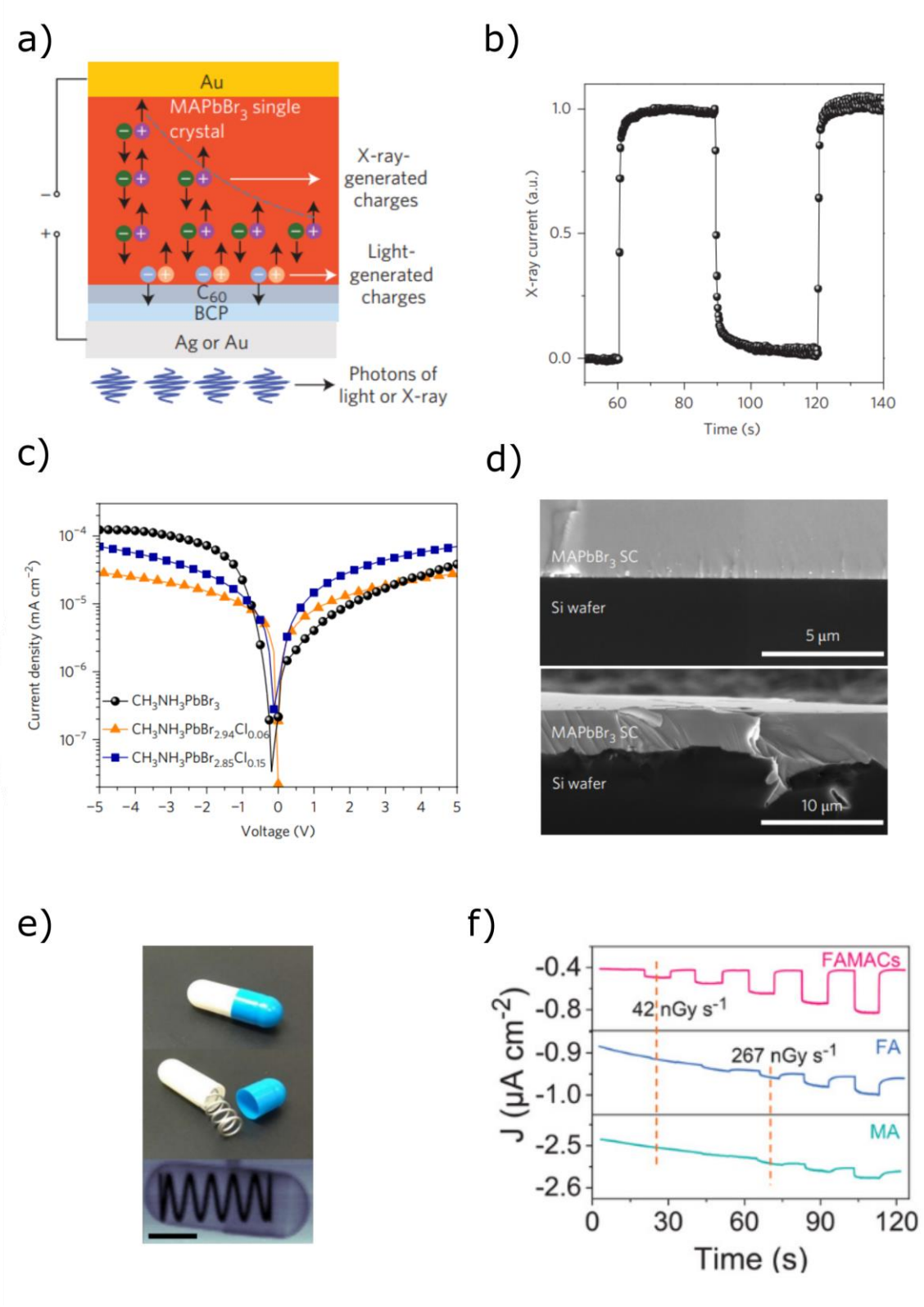

Figure 2.13: 3D perovskite single crystal for direct X-ray detection. a) Example of a typical detector configuration based on perovskite single crystal.[52] b) Dynamic response to an X-ray beam showing fast, repeatable and box-like response.[52] c) J-V curves acquired in dark for different perovskite single crystal compositions. The introduction of chlorine decreases the dark current of the device.[49] d) SEM images of $MAPbBr_3$ single crystal integration on a silicon

substrate.[47] e) X-ray image of a metal spring obtained with a perovskite line matrix array.[47] f) Dynamic response to low dose rate irradiation of a triple cation single crystal compared to single cation perovskites.[50]

Lead-halide perovskite single crystals have been successfully used also for the detection of gamma-rays.

Very recently Liu et al. demonstrated the possibility to grow high performance single crystals with a triple cation mixed halide perovskite.[50] They demonstrated superior performance in comparison to $MAPbI_3$ and $FAPbI_3$ in terms of sensitivity, limit of detection and operational stability of the device. In Figure 2.13f the estimation of the LoD for the three materials is reported. The triple cation single crystals, in an asymmetric configuration employing C_{60} and bathocuproine (BCP) as electron transport layer and spiroTTB as hole transport material, reached a top sensitivity of $3.5 \pm 0.2 \times 10^6$ μC Gy^{-1} cm^{-2} at -60 V bias three orders of magnitude higher than the other crystals explored. The triple cation perovskite demonstrated superior stability retaining 91 % of the initial sensitivity after 45 days, while MAPbI3 crystal only 68 %. Lead-halide perovskite single crystals have been successfully used also for the detection of gamma-rays. With $MAPbI_3$ single crystal, a device able to detect the flow of a radioactive tracer inside a glass capillary was made. The setup used by researchers is reported in Figure 2.14a. The radioactive element contained in the drug was ^{18}F used in Positron Emission Tomography (PET) analysis. The perovskite detector was able to detect 511 keV photons, emitted by ^{18}F, in a very similar way to a commercial GABI detector, Figure 2.14b. The same research group demonstrated for the first time energy resolved spectra with a 3 mm thick $FAPbI_3$ single crystal. The energy resolved spectrum, acquired with a $FAPbI_3$ single crystal, of ^{241}Am is reported in Figure 2.14c. ^{241}Am emits alpha particles with an energy of 5.48 MeV and gamma-rays with an energy of 59.5 keV. They were able to resolve the gamma peak with a full with half maximum resolution (FWHM) of 35%. The spectral resolution of a gamma detector is correlated

to the charge carrier transport properties. Since the photon energy involved, researchers have focused their attention to thick single crystals in which the electrodes are 2 – 3 mm apart.

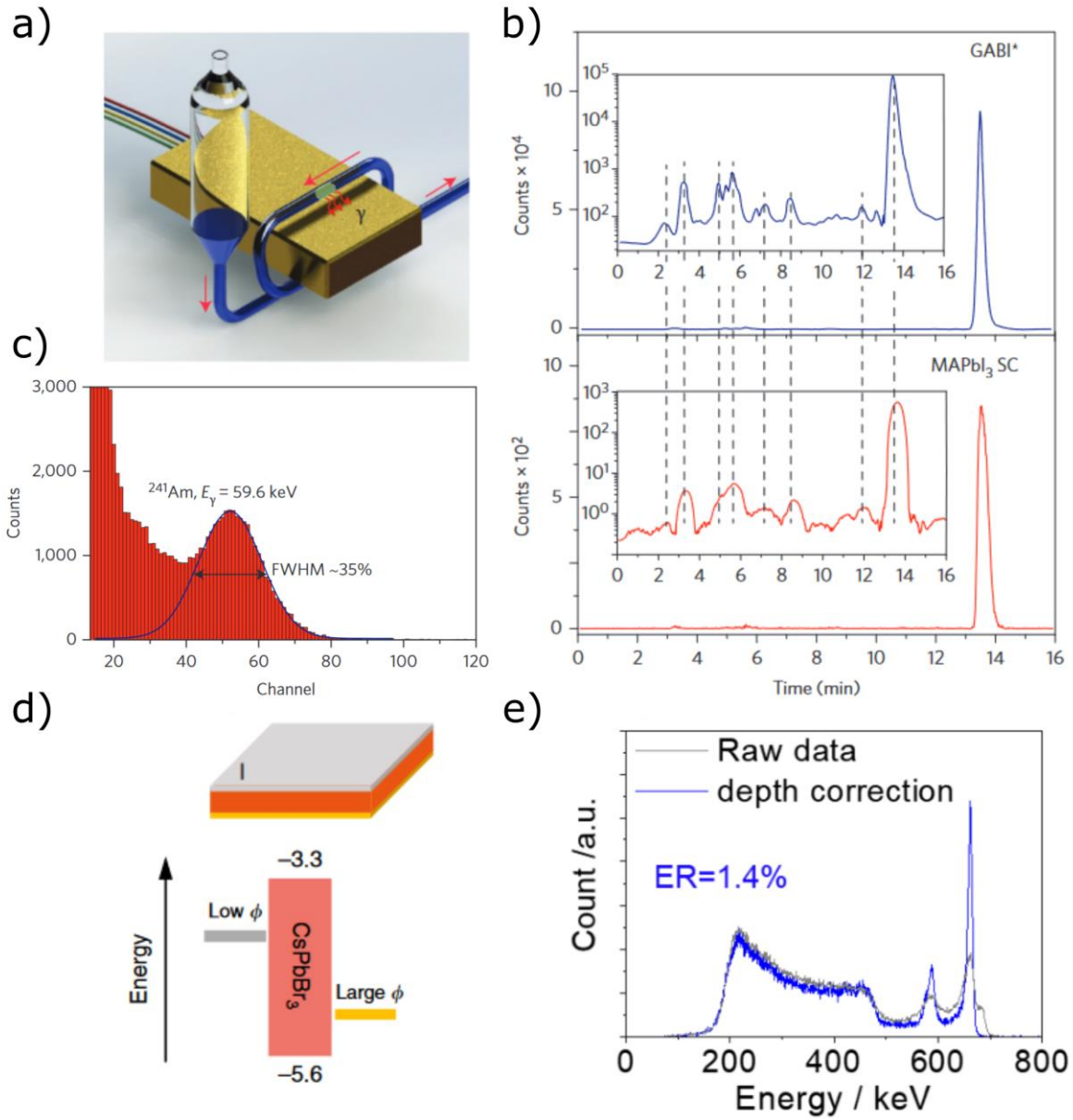

Figure 2.14: Gamma-ray perovskite single crystal detectors. a) Apparatus used to measure a radioactive drug passing in a capillary close to the detector.[45] b) Comparison of the signal of the radiotracer measured with a commercial GABI detector and a $MAPbI_3$ single crystal.[45] c) Spectra of a ^{241}Am source obtained with a $FAPbI_3$ single crystal based detector.[45] d) Energy diagram of photodiode containing $CsPbBr_3$ as active layer in the middle of two metal contacts with different work functions.[39] e) Current resolution record for perovskite gamma detectors. The spectra of ^{137}Cs was obtained with a $CsPbBr_3$ single crystal between EGaIn and Au contacts.[88]

To achieve efficient charge collection, it is necessary to increase the bias applied to the device, but this increases the dark current reducing the signal to noise ratio. Diode structures, instead, allow to apply strong reverse bias while keeping the dark current low. He et al. managed to build a diode structure with $CsPbBr_3$ as absorbing layer, gold as bottom metal contact and gallium as the top metal contact.[39] The structure and energy levels alignment are reported in Figure 2.14d. In this configuration, high injection Schottky barrier is formed at the interfaces decreasing the dark current of 4 orders of magnitude respect to a symmetric device. The $Au/CsPbBr_3/Au$ symmetric device showed a dark current density of 1.1×10^6 nA cm^{-2} with an electric field of 2000 V cm^{-1}. Under the same electric field, the rectifying device showed a stable dark current down to 83 nA cm^{-2}. The perovskite detector operated at -150V was able to resolve gamma emission from ^{57}Co at 122 keV and ^{137}Cs at 662 keV, with energy resolution of 4.3 % and 3.8 %, respectively. The same group, by improving the growth process and the contact design on top of the crystal, was able to resolve the ^{137}Cs gamma peak with a resolution of 1.4 %,[88] see Figure 2.14e. In 2017 a MAPbBr3 single crystal was used to successfully detect the alpha particle emission from ^{241}Am. The device was asymmetrical with Cr, C_{60}, BCP as contact layers. Although the energy of the alpha particles is constant, the peak measured by the detector showed a bias dependence. They stabilized the centroid by increasing the bias up to 550 V.[89]

Neutron detection has also been demonstrated for 3D lead-halide perovskite single crystals.[90] The device used for the experiment is schematized in Figure 2.15a. Also, in this case, a high work function metal (like Au) and a low work function material (like Ga2O3) were used, to obtain a high rectification factor. They employed a guard ring in the top metal contact design. The guard ring reduces hysteresis and improves diode performance by reducing crystal surface edge leakage current, resulting in reduced dark current. The JV characteristic is reported in Figure 2.15b. As thermal neutron source they used ^{252}Cf. The low interaction probability of thermal neutron

makes their detection challenging. To increase total capture cross section, a layer of ^{10}B was added on top of the perovskite layer. The Boron atom captures a neutron, decaying into ^{7}Li emitting an alpha particle with 1.4 MeV energy. Alpha particles are then absorbed and detected by the perovskite. In Figure 2.15d is clearly visible the enhancement effect of boron as conversion layer.

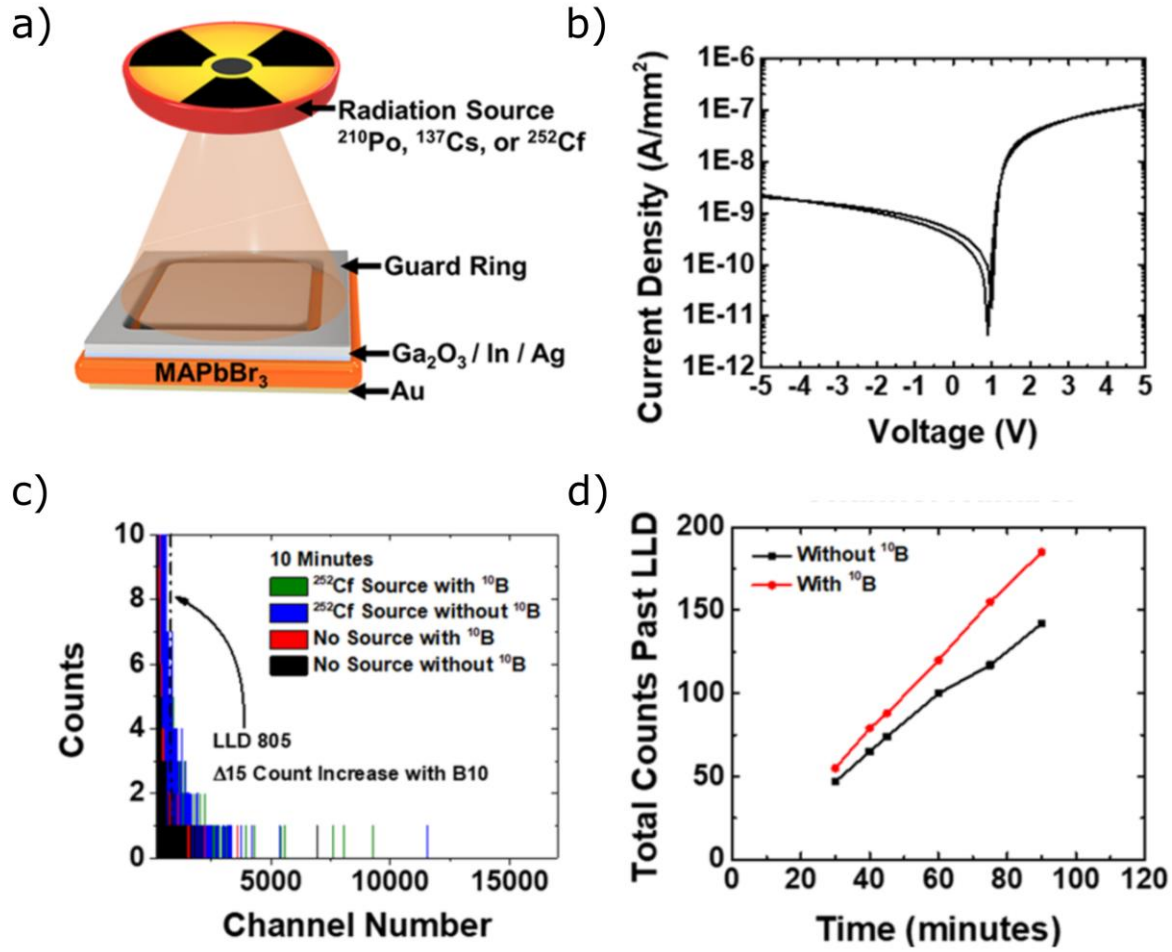

Figure 2.15: Perovskite single crystals for neutron detection.[90] a) Example of a diode structure with MAPbBr3 as active layer and a guard ring top contact. The device has been irradiated with different radiation sources. b) I-V characteristic of the diode acquired in dark conditions. c)^{252}Cf spectra obtained in different conditions. Adding a ^{10}B layer the neutron counts increase. d) Total counts with and without ^{10}B acquire at different exposure times.

In literature there are also examples of 2D perovskite single crystals successfully used as ionizing radiation detectors. Ji et al. used $BA_2EA_2Pb_3Br_{10}$, a n = 3 layered perovskite single crystal to detect X-rays.[54]

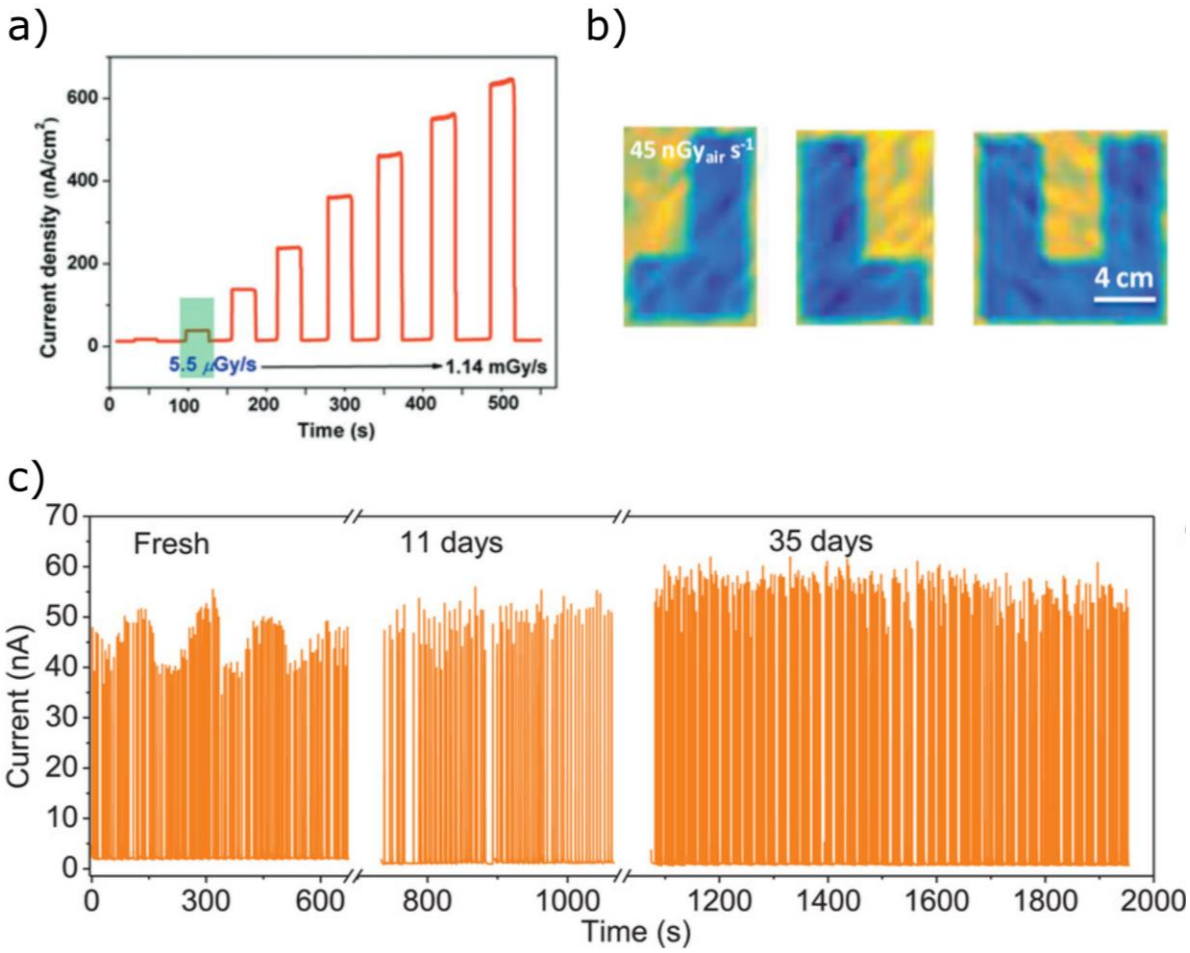

Figure 2.16: 2D perovskite single crystal X-ray detector. Dynamic responses under different dose rates[54] b) X-ray images of metal plates composing a logo acquired with a detector made out of F-PEA_2PbBr_4 single crystal. The Images have been acquired with a very low dose rate of 45 nGy s^{-1}.[53] c) Current stability of a 2D perovskite-based X-ray detector under pulsed 120 keVp X-ray beam.[53]

In Figure 2.16a are reported the dynamics response under 70 kVp X-rays with different incident dose rates showing fast and box-like response. The device, operated under a bias of 10 V, reached a sensitivity of 6.8 × 10^3 μC Gy^{-1} cm^{-2} and a detection limit of 5.5 μGy s^{-1}, comparable to the dose used in medical diagnostic. A n = 1 2D

perovskite single crystal for ionizing radiation application was grown from Li et al.[53] They used a slow cooling growth technique to obtain fluorophenethylammonium lead iodide (F-PEA_2PbI_4) single crystals. This material showed a remarkable high bulk resistivity of 1.36×10^{12} Ω cm, which enabled a low dark current and noise even under 200 V operative bias. The 2D perovskite detector showed a large sensitivity of 3402 µC Gy^{-1} cm^{-2} to 120 kVp hard X-rays, which is more practically useful for medical imaging. The large sensitivity and low device noise ensured the perovskite detector to resolve the lowest detectable X-ray dose rate of 23 nGy s^{-1}, and then acquire X-ray image at low dose rate, see Figure 2.16b. In Figure 2.16c is reported the operational stability under X-ray beam at 35 days after the fabrication.

2.7 Perovskite polycrystalline films for X-ray detection

Perovskite single crystals offer high performances in terms of sensitivity, LoD and stability. The sensitivity of perovskite single crystal detectors surpassed by far the sensitivity of traditional semiconductors. Despite the very good performances, perovskite single crystals do not exploit the peculiarity of solution grown techniques: large area scalability. Flexibility and conformability are appealing features for the new generation of ionizing radiation detectors, especially for medical and future space mission applications. A conformable detector can be placed directly on the patient's skin improving comfort and precision in dose determination. The direct fabrication of thin films on plastic substrate allows the creation of lightweight devices with low

payload cost for space launch. For these reasons, researchers have tried to develop the perovskite thin-film technology for radiation detection.

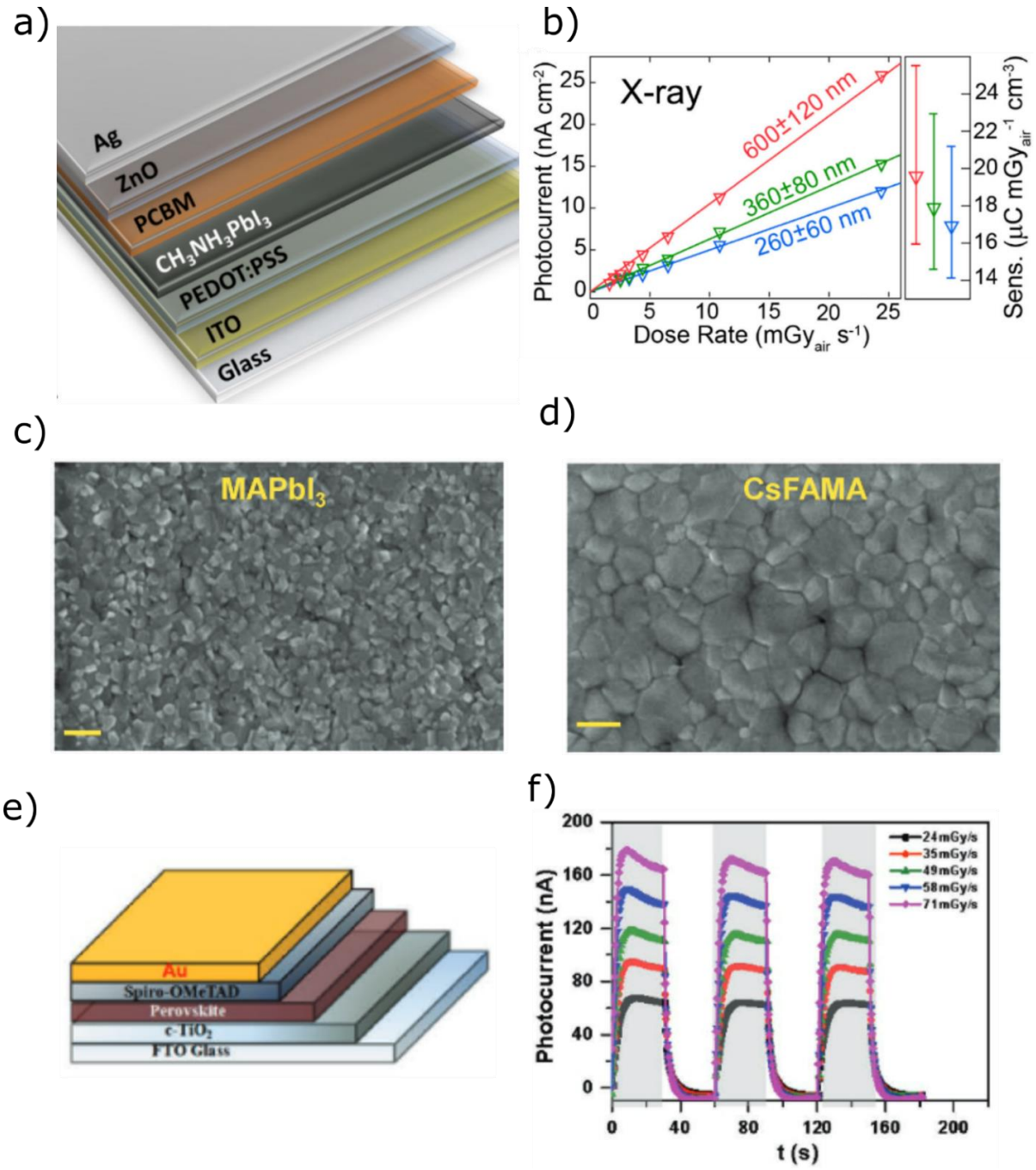

Figure 2.17: Thin-film perovskite X-ray detector. a) Structure of a perovskite photodiode interfaced with all organic interlayer.[58] b) X-ray detection performance for different perovskite layer thicknesses measured under 8 keV X-ray beam.[58] c) SEM picture of $MAPbI_3$ layer, scale bar 200 nm.[59] d) SEM image of a triple cation perovskite layer deposited by spin coating, scale bar 200 nm.[59] e) Another example of a perovskite photodiode architecture.[59] f) Dynamic response of a perovskite thin-film X-ray detector under 35 kV Mo target X-ray tube with -0.4 V bias applied to the sample.[59]

Thin-films offer several advantages: they can be deposited on top of flexible lightweight plastic substrates with low-cost large-area printing techniques easy to scale up; the device properties can be tuned by changing the ink/solution composition; thin-film requires low operating voltages compared to Si, Ge and CZT thick wavers, which require hundreds or thousands of Volts; the combination of thin-film properties allows the creation of wearable detectors. The first example of perovskite thin-film detector comes from Yakunin et al. in 2015.[58] They used $MAPbI_3$ as absorbing layer in an inverted p-i-n photodiode architecture visible in Figure 2.17a. They employed phenyl-C61-butyric acid methyl ester (PCBM) as electron transport layer (ETL) and poly(3,4-ethylenedioxythiophene) polystyrene sulfonate (PEDOT:PSS) as hole transport layer (HTL). They also inserted a ZnO buffer layer between the ETL and the top Ag metal contact, this layer is needed to increase the interface quality. The device layers are deposited by spin-coating on top of ITO covered glass, which is used as bottom contact. This structure allows good diode characteristics and excellent charge collection. The thickness of the perovskite layer used in this configuration was 300 nm. The electron-hole pairs generated inside the perovskite layer are separated by the internal or external electric field and then transported through the ETL and HTL to the metal contacts. With a thickness between 300 nm to 500 nm the internal quantum efficiency is close to unity. That means the lack of absorption due to the small thickness of the film is partially compensated by a very efficient charge collection. Figure 2.17b reports the photocurrent values for different perovskite layer thicknesses. They achieved a top sensitivity of 1.5 $\mu C\ Gy^{-1}\ cm^{-2}$ under 75 kVp X-ray beam without any external bias applied to the device. The researchers managed to acquire some X-ray images with a single pixel device moved by motors. Basiricò et al. in 2019 used a mixed cation perovskite in a different photodiode architecture achieving a top sensitivity of 3.7 ± 0.l $\mu C\ Gy^{-1}\ cm^{-2}$ at 0 V bias under a 35 kVp X-ray beam.[59] When the bias increased to -0.4 V the sensitivity increased up to 98 ± 1 $\mu C\ Gy^{-1}\ cm^{-2}$, higher than the sensitivity

value obtained with the first single $MAPbBr_3$ crystals.[52] In Figure 2.17b, c are reported the SEM images of a $MAPbI_3$ and $Cs_{0.05}FA_{0.79}MA_{0.16}Pb(I_{0.8}\ Br_{0.2})_3$. The mixed cation perovskites film presents better crystallization with larger grains. The photodiode structure used is a n-i-p architecture with mesoporous TiO_2 as ETL and Spiro-MeOTAD as hole transport layer. In this heterostructure, ambipolar transport has a positive effect on the performances. The researcher found a better ambipolar transport in the mixed cation mixed halide perovskite than in $MAPbI_3$. The dynamic response of the photodiode structure is reported in Figure 2.17f for different incident dose rates; noticeable the linear response to X-rays.

In 2017 Kim et al. realized the first perovskite based imager.[61] They created a suspension of $MAPbI_3$ nanocrystal in gamma butyrolactone (GBL) to be used as ink for blade coating over large area substrates. They also optimized the interlayers with different formulations of perovskites and polyimide to match the band alignment for the creation of a diode structure, Figure 2.18a. They printed the device over a TFT matrix 1,428 × 1,428 pixels (10 cm × 10 cm) with a pixel pitch of 70 μm, achieving a spatial uniform film with a thickness of 830 μm. A picture of the printed perovskite film is reported in Figure 2.18b. The $\mu\tau$ of the blade coated perovskite film was 1 x 10^{-4} cm^2 V^{-1}. In Figure 2.18c the device response to a train of 50 ms long 100 kVp X-rays pulses is shown. Electrical fields in the range 0.01 - 0.24 V μm^{-1} were applied to collect charges through the bottom ITO electrode and X-ray sensitivities in the range 1000 - 1100 $\mu C\ Gy^{-1}\ cm^{-2}$ were observed. Thanks to the perovskite integration onto a TFT matrix they acquired a high-resolution X-ray image of a phantom's hand irradiating the object for 5 ms with a dose rate of 5 mGy s^{-1}.

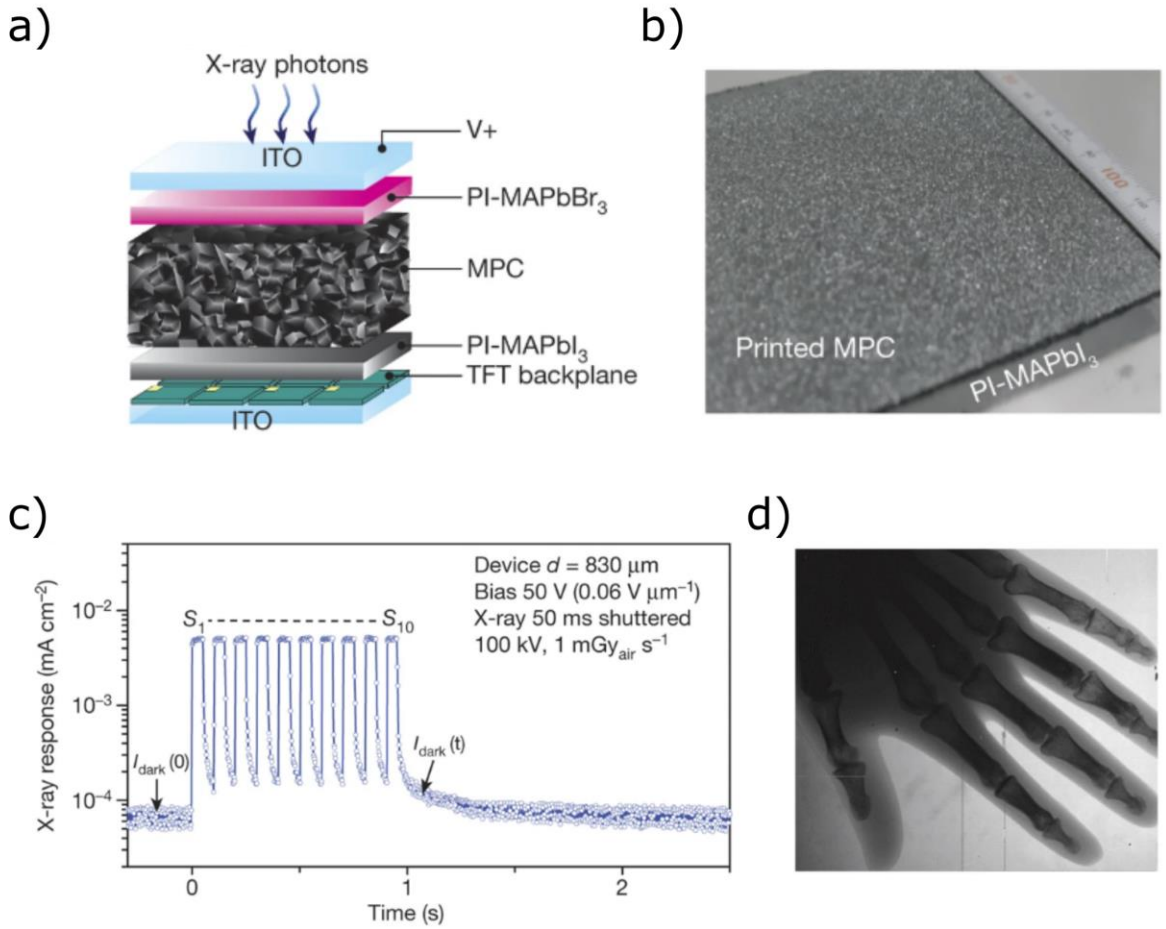

Figure 2.18: Printed thin film perovskite imager.[61] a) Device structure: a 830 µm thick $MAPbI_3$ perovskite layer (MPC) is placed between modified perovskite layer for charge extraction. Everything is deposited by blade coating on a TFT backplane for readout. The bias is applied through an ITO layer on top. b) Printed $MAPbI_3$ layer over an area > 10 x 10 cm^2. c) Detector response to a train of 50 ms X-ray pulses. d) X-ray picture of a phantom's hand acquired with the perovskite detector using 100 kVp and 5 mGy s^{-1} for 5 ms irradiation condition at 50 V bias.

Sarah Deumel et al. demonstrated another perovskite imager made with polycrystalline film.[91] In this case, they used a soft-sintered $MAPbI_3$ wafer integrated on a TFT backplane, the device structure is visible in Figure 2.19a. The bottom electrodes are of molybdenum-chromium alloy. On top of the backplane, a grid structure made of an approximately 10 µm thick photoresist is used as a mechanical anchoring structure for the thick absorber layer. Without the grid, the mechanical adhesion between $MAPbI_3$ and the backplane was found to be poor, indicated by the release of the wafer after a few days. However, with the grid, no spontaneous detachment are seen in several

months. Pull tests revealed a tensile strength of 100 kPa, 2 orders of magnitude higher than the monolithic integration of single crystal on silicon seen in the previous section.[47] With a perovskite layer as thick as 230 µm, the extremely low LoD was measured to be 0.22 nGy s^{-1} with an electric field of 0.03 V μm^{-1}. A high resolution of 6 lp mm^{-1} was found; the image used for the resolution test can be observed in Figure 2.19b. In Figure 2.19c a picture of the final encapsulated device is shown.

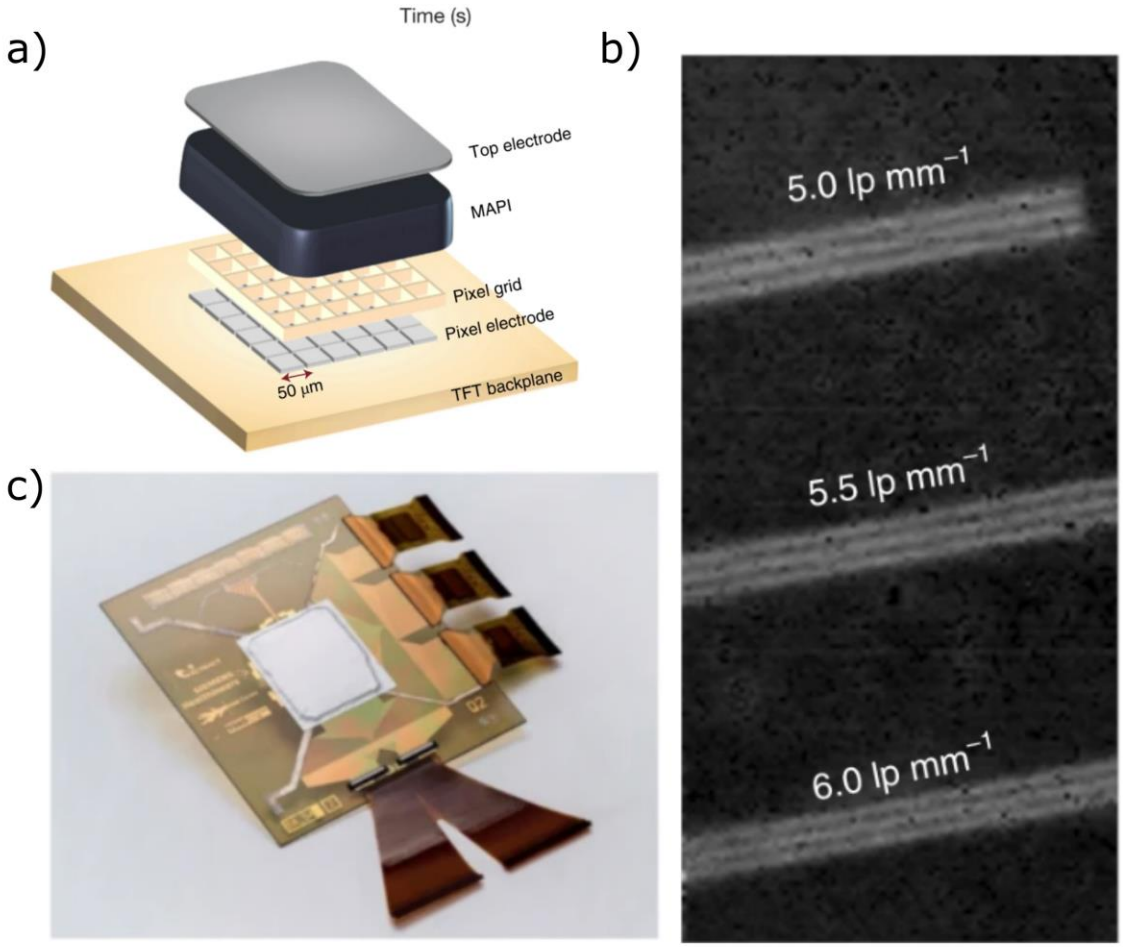

Figure 2.19: Sintered perovskite wafer for imaging.[91] a) Device structure with the TFT backplane on the bottom, the anchoring grid made of photoresist $MAPbI_3$ sintered wafer and the Cr top metal electrode. b) Test to establish the resolution of the imager. c) Picture of the final device.

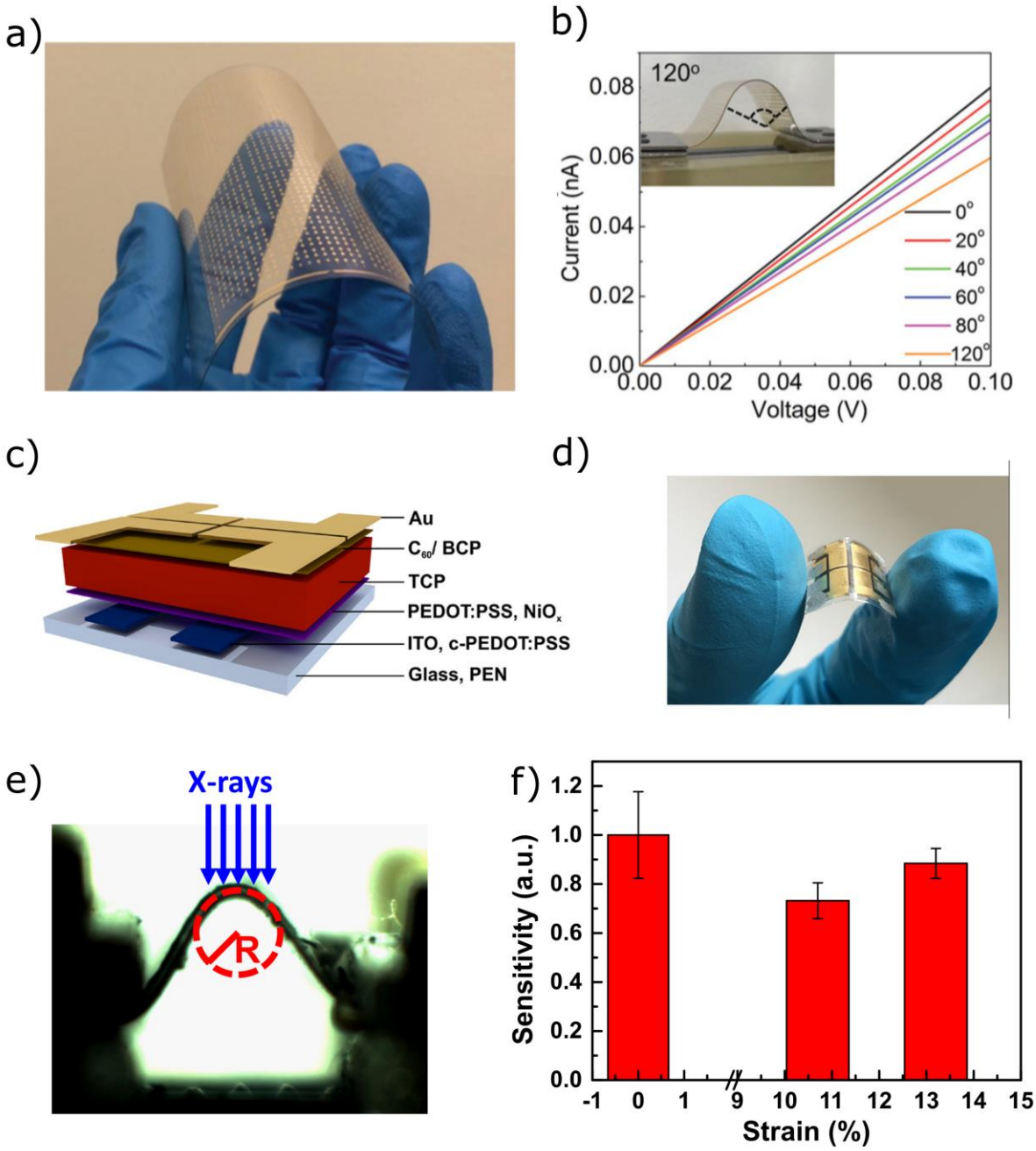

Figure 2.20: Flexible perovskite X-ray detectors. a) Inkjet printed perovskite quantum dots on patterned metal contacts.[65] b) IV characteristic of the device in a) under different banding conditions.[65] c) Flexible photodiode device with an inkjet printed triple cation perovskite active layer.[92] d) Picture of the device in c) bent by the researcher's fingers.[92] e) Blade-coated perovskite photoconductor under bending during X-ray exposure.[93] f) Sensitivity of the device in e) as a function of the device strain.[93]

Among all the papers published on thin or thick film perovskite X-ray detector only few of them reports about flexible devices. The first example is based on printed $CsPbBr_3$ quantum dots deposited on pre-patterned metal contacts.[65] A picture of the

flexible device is reported in Figure 2.20a. They used an inkjet printer to selectively deposit inorganic perovskite quantum dots dispersed in toluene. The deposition on PET resulted in 20 nm thick perovskite absorber in a channel between two Au metal contacts. They tested the detector under soft X-ray with energy below 2 keV in a synchrotron beamline reporting, for the flexible device, a sensitivity of 17.7 μC Gy^{-1} cm^{-2} and a high limit of detection (i.e. 17.2 μGy s^{-1}). The energy range and the LoD for this device are not suitable for medical applications but they showed the feasibility for flexible detectors through inkjet printing. They also tested the electric characteristic of the device under different bending configurations, see Figure 2.20b. The device could withstand a bending angle of 120° and 200 repetitions cycle without strong degradation of the performance. Another group used inkjet printing to deposit a triple cation perovskite layer in the middle of a flexible photodiode.[66] The device structure is shown in Figure 2.20c. The active material ($Cs_{0.1}(FA_{0.83}MA_{0.17})_{0.9}Pb(Br_{0.17}I_{0.83})_3$) with a thickness of around 3.7 μm is deposited on top of PEDOT:PSS layer working as HTL. As ETL C_{60} and BCP are used. The device is fabricated on 25 μm thick polyethylene naphthalate (PEN) substrates. A picture of the bent device is reported in Figure 2.20d. They tested the device under 70 kVp X-rays finding a top sensitivity of 59.9 μC Gy^{-1} cm^{-2} with 0.1 V applied, stable even after a total dose exposure of 4 Gy. The extracted LoD is equal to 12 μGy s^{-1}, quite high for medical applications. The device was exposed to X-ray under bending. It showed no degradation in the response when bent at 3 mm bending radius corresponding to a strain in the perovskite layer of 0.48 %. Ciavatti et al. fabricated a flexible perovskite X-ray detector by blade-coating. They used a cyclic approach to decrease the dimension of $MAPbI_3$ nanocrystal used, dispersed in isopropanol, as ink. The perovskite ink was deposited on top of interdigitated Au metal contact fabricated with standard photolithography. To boost the perovskite performance a layer of PCBM was added by drop-cast on top of the 10 μm perovskite. The flexible devices achieved a top sensitivity value of 494 μC Gy^{-1} cm^{-}

^{2} for 150 kVp X-rays, with a rise time of 52 ms. In Figure 2.20f the sensitivity as a function of the strain on the perovskite layer is shown. The sensitivity stays constant even at high strain, demonstrating the ability of polycrystalline perovskite films for the realization of flexible detectors.

A different approach was used by Zhao et al. in 2020, they used a flexible nylon membrane as a scaffold for the perovskite active layer.[94] The fabrication process is illustrated in Figure 2.21a. The saturated perovskite solution is infiltrated in the nylon membrane by creating vacuum on the opposite side. After infiltration, the membrane is annealed to crystalize the $MAPb(I_{0.9}Cl_{0.1})_3$ perovskite. To complete the device C_{60}/BCP and Cr contacts were evaporated on top of the device. The X-ray response of the devices was tested under X-rays with a peak energy of 60 keV, the 240 µm thick device biased at an electric field of 0.05 V µm^{-1} has a dark current density of 98.3 nA cm^{-2} and sensitivity of 2.204 µC Gy^{-1} cm^{-2}. They demonstrated a bending radius of 3 mm without degradation and a stable operation for a total dose of 377 Gy, the equivalent of 1.88 million of chest scan. They report also about the imaging properties of the device. They created a pixelated detector by masked metal evaporation. The imager was able to resolve up to 4 lp mm^{-1}. They showed a usage case in which the possibility of bending the device could improve the image quality. The object used is showed in Figure 2.21c, it consists of a pipe with a cross-shaped aperture on one side. By bending the device and placing it inside the pipe, they acquired an image of the aperture with higher image quality with respect to the standard flat device, Figure 2.21d.

A novel concept of X-ray detector has been recently published by Gao et al.[95] They call it heterojunction X-ray phototransistor (HXPT) and the working principle is schematized in Figure 2.22a.

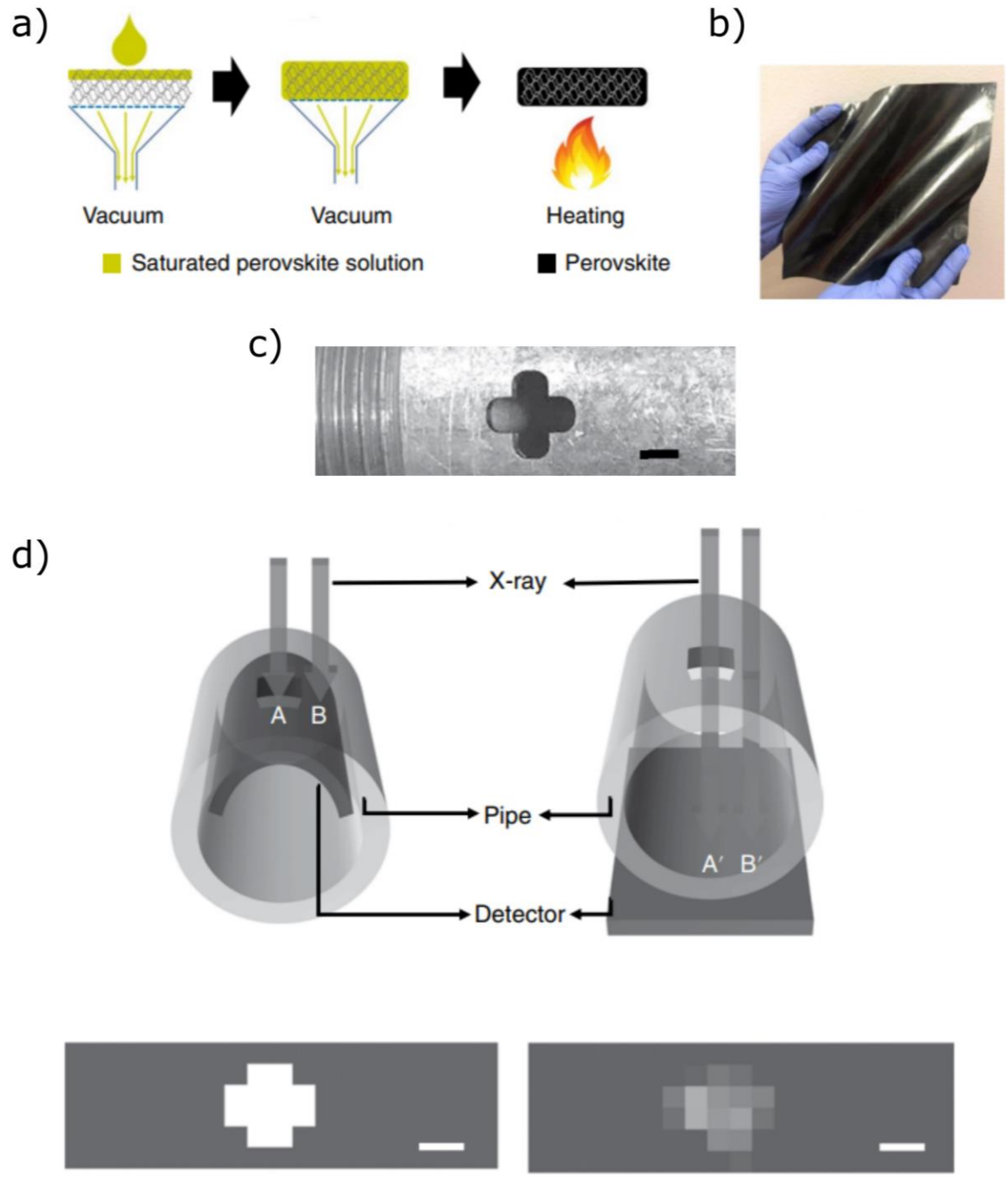

Figure 2.21: flexible perovskite X-ray detector based on nylon membrane.[94] a) Device fabrication: the perovskite solution is placed on top of the membrane, vacuum is created on the opposite side to help the solution permeate inside the nylon membrane. The membrane in then heated to crystalize the perovskite. b) Picture of the membrane (initially white) fill with perovskite crystals (black). c) A pipe with an aperture, scale bar 4 mm. d) Scheme of the imaging procedure used. The first take advantage of the flexibility of the device in order to take an image of the aperture. The second is the standard way which results in poor image quality. Scale bar 4 mm.

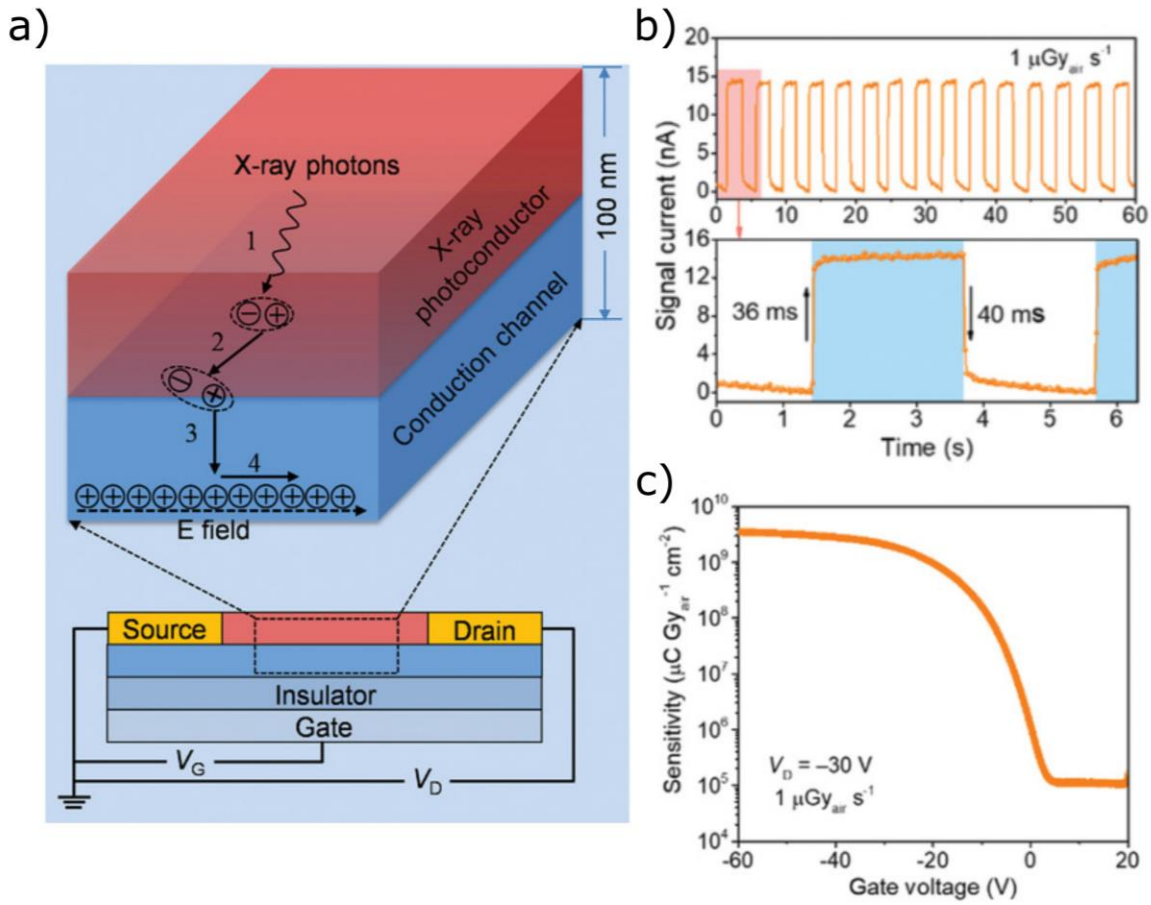

Figure 2.22: Heterojunction X-ray phototransistor.[95] a) Working mechanism of the device: X-rays are absorbed in the photoconductive layer, the charges are drive to the interface, the minority carrier gets trapped while the majority are injected in the transistor channel. The trapped electrons force the injection of holes in the conduction channel increasing the photocurrent. b) Dynamic response to 20 kVp modulated X-ray beam with an incident dose rate of 1 μGy s^{-1}. The detector showed a rise time of 36 ms and a slightly higher fall time of 40 ms. c) Modulation of the sensitivity as a function of the gate voltage applied to the transistor.

Under X-ray irradiation, charges are generated within the photoconductor layer and separated at the heterointerface owing to the energy offset and the internal electrical field created by the interface. The minority carriers are trapped and the majority carriers can be reinjected from the metal contacts and recirculated multiple times to maintain charge neutrality of the conduction channel. A large number of majority carriers are generated in the conduction channel and greatly boost the signal current. Such a process continues until the trapped minority carriers are released and recombined, thus producing high photoconductive gain. In this concept, the absorption

of ionizing radiation and photoconductive gain effect takes place in two different materials which can be optimized for the two purposes. The heterojunction consists of a p-type copolymer semiconductor PDPPBTT and $CsPbBrI_2$ perovskite serving as the conduction channel and the photoconductor layer, respectively. Thanks to the gain effect, the phototransistor achieved extremely high sensitivity up to ~10^7 μC Gy^{-1} cm^{-2} under 20 kVp X-ray beam for 100 nm thick photoconductor layer. Organic semiconductors are used for thin-film X-ray detector fabrication because of the high gain generating high current response under the beam. One of the drawbacks of organic semiconductors is the time response. The photoconductive gain is usually a slow process mediated by traps. Organic X-ray detectors have a rise time of several tens of seconds. Interestingly in the case of HXPT the response is quite fast, as visible in Figure 2.22b, with a rise time of 36 ms. The researcher could increase even more the device sensitivity by increasing the gate voltage, see Figure 2.22c.

2D perovskites have demonstrated to be a candidate also for thin-film X-ray detectors. Tsai et al. fabricated a p-i-n diode with an active layer made of $(BA)_2(MA)_2Pb_3I_{10}$ layered perovskite.[96] The device structure depicted in Figure 2.23a, the 470 nm perovskite layer is placed between poly[bis(4-phenyl)(2,4,6trimethylphenyl)amine] (PTAA), p-type contact and the n-type contact C_{60}. The diode quality was evaluated by measuring J-V characteristic in dark conditions. The results are reported in Figure 2.23b, where It is also reported a silicon diode characteristic for comparison. The perovskite-based device showed lower dark current (~1 nA cm^{-2}) and higher response under 10 keV X-rays. The device showed a top sensitivity value of 12.9 μC Gy^{-1} cm^{-2}. Even if the sensitivity is not very high, the 2D perovskite-based device demonstrated superior operational stability with no drift in photocurrent or dark current as visible in figure Figure 2.23c. This demonstrates that 2D perovskites are a good candidate for the fabrication of stable X-ray detectors.

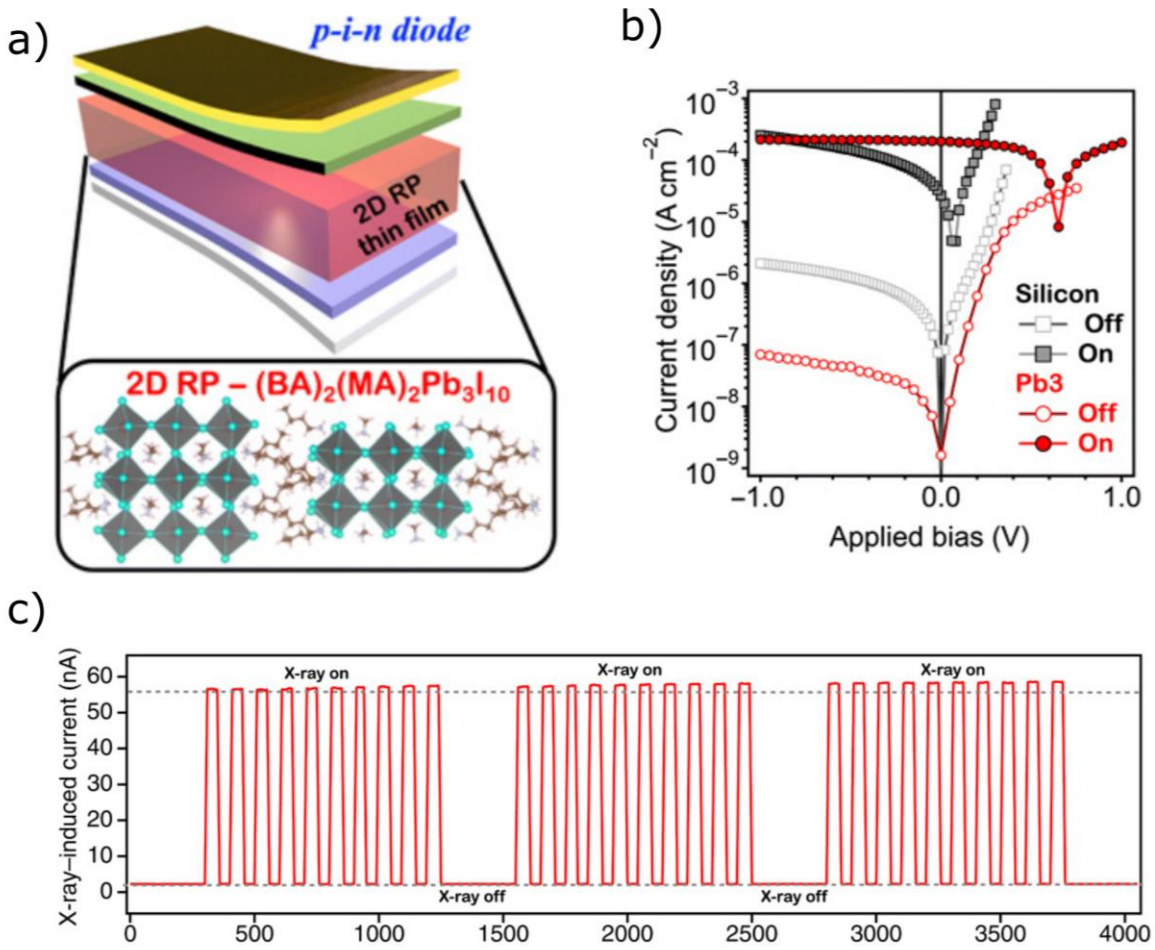

Figure 2.23: 2D perovskite thin-film X-ray detector.[96] a) Photodiode structure with the layered perovskite as absorbing layer. b) J-V characteristic of the perovskite photodiode (red) acquire in dark conditions and under 10 keV X-rays compared to a silicon photodiode (grey). c) Detector stability under operation

3. Experimental methods

In this work, different techniques were used to fabricate and characterized perovskites as novel materials for ionizing radiation detection. In this chapter, a description of the methods used is given, starting with the device fabrication; then the electrical, optoelectronic and morphological characterization; lastly, a description of large facilities, such as synchrotron beamlines, employed for the experiments.

3.1 Device fabrication

Here the fabrication techniques used for the fabrication of ionizing radiation detectors are described. At the end of the section, the device structures are presented.

3.1.1 Spin coating

The spin-coating technique is one of the most common solution-based film deposition techniques in research laboratories. The basic working principle is depicted in Figure 3.1. The substrate is placed on the sample holder able to spin and a certain amount of solution or ink containing the material to deposit is placed over the substrate through

a pipette or a syringe. The sample can be attached to the chuck (i.e. the spin-coater rotating platform) by mechanical connections or by vacuum. In the last case, a small pump is used to create an air depression region between the sample and the chuck. An electric motor starts to spin the substrate and the centrifugal force spreads the solution over the substrate surface; when the excess solution reaches the substrate edge it drops outside the substrate. At the end of the spinning process, the solvent is let evaporate on the spin-coater or usually onto a hot plate. The thin film is slowly created while the solvent evaporates. The process itself is fast and easy but the optimization of all the parameters to obtain the right film quality (uniformity) and thickness is not an easy task. The film formation depends on several factors. The hydrophobicity/hydrophilicity of the substrate, for example, is an important parameter: if the substrate is too hydrophobic, when the solution is rotated all the liquid escape from the substrate leaving not enough solution for the film formation. The type of solvent and viscosity, combined with spin velocity are important in determining the thickness and homogeneity of the final film. A mathematical description of the fluid dynamics of a liquid on top of a rotating disk was given by Emslie, Bonner, and Peck in 1958.[97] This model does not take into account the evaporation of the solvent while spinning. The final film thickness (h) can be expressed as follows:

$$h = \frac{h_0}{\left(1 + \frac{4\rho\omega^2}{3\eta} h_0^2 t\right)^{1/2}} \qquad (3.1)$$

Where h_0 is the initial liquid thickness on the rotating disk. ρ, η are the density and viscosity of the ink. The spinning time is represented by t. Operatively, researchers use a simplified relation:

$$h \propto \frac{1}{(\omega)^{1/2}} \qquad (3.2)$$

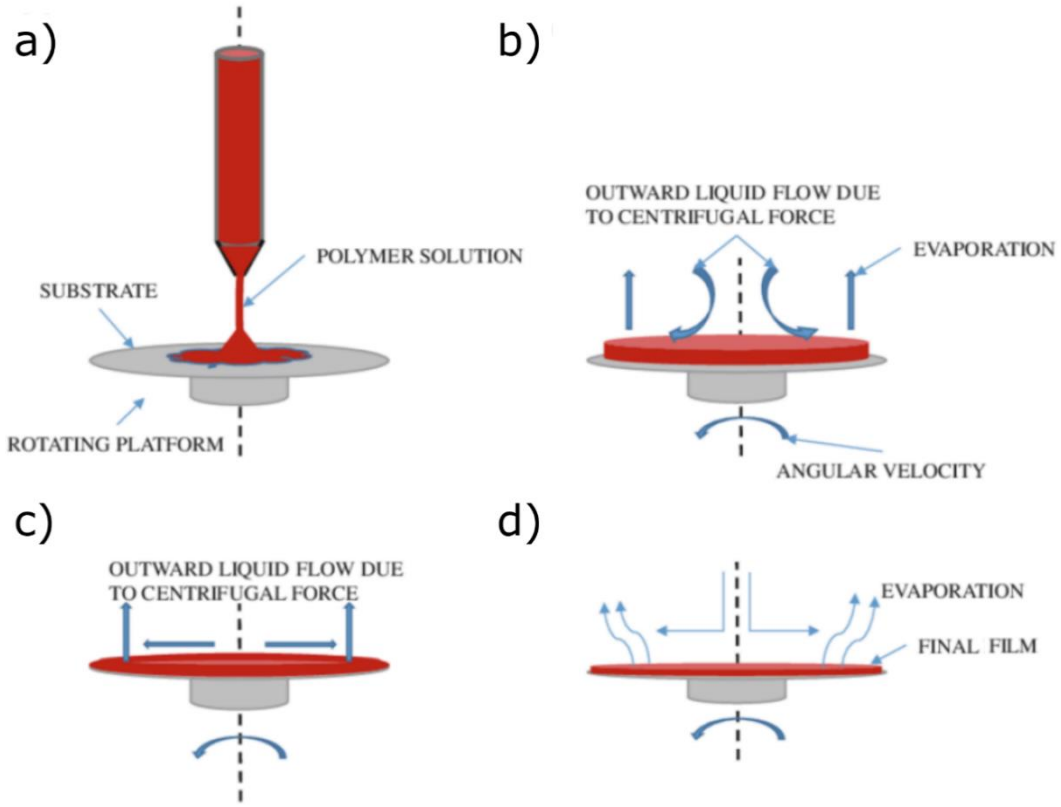

Figure 3.1: Spin coating process. a) The solution or ink is placed on top of the substrate. b) The spin-coater rotating platform starts to rotate and the solution is spread evenly on the substrate by the centrifugal force. c) The excess material gets ejected from the substrate by the centrifugal force and the liquid continues to spread until all the substrate is covered. d) The evaporation of the solvent leads to the final film formation.

With material and substrate fixed changing the velocity of the spin-coater changes the final thickness of the film, the higher the speed the lower the thickness. This is true but only in a limited range of thicknesses depending on the material, for perovskite is very difficult to make films with thicknesses higher than 5 µm. The procedure and the theory discussed above concern the easiest way to use spin coating where the film is formed by solvent evaporation. The most used strategy to obtain good quality 3D perovskite films is the antisolvent method. A solvent, in which the solute is insoluble, is used to increase the crystallization rate. While the sample is spinning, few drops of antisolvent are added onto the sample. When the drops reach the solution on the

substrate the solubility of the solute falls quickly causing the film formation. In this procedure, timing, type of antisolvent and quantity are very important for a successful material deposition. In this work, I used spin coating for the deposition of active perovskite layers and interlayers.

3.1.2 Photolithography

The word photolithography identifies processes that use light to transfer specific pattern with small features onto films, substrates or wafers. Photolithography employs photons, usually UV photons, and a shaped mask to expose a sensitive chemical called photoresist in some areas. I employed photolithography for the fabrication of the metal contact in the case of photoconductor samples, by making interdigitated electrodes geometry. These structures maximize the performance by dividing an area into small channels where the charges can flow, more detail in section 3.1.5. For this contact geometry, small features of a few microns are necessary, but is very hard to achieve it with machined metal or Kapton mask. The metal contact patterning process is illustrated in Figure 3.2. The process starts with the preparation of the desired substrate, glass or plastic. On the substrate, a photoresist layer of a few microns is deposited through spin-coating. A good film uniformity is needed to obtain a homogeneous exposure at the following step. Before the exposure, usually, a baking step on a hotplate is required to fully solidify the photoresist. The sample is then exposed to UV light through a mask that blocks the UV from going into unwanted regions of the photoresist. Photoresists are materials sensitive to UV radiation and their exposure to UV light changes their chemical properties. Photoresist are divided into two main categories: positive and negative resist. When positive photoresists absorb UV photons became soluble in the developer (a generic name used to indicate the chemical used in the developing step). On the contrary, the negative photoresist

after UV exposure becomes insoluble in the developer. After the exposure the sample is immersed in the developer, a chemical that removes or leaves the photoresist exposed to UV depending on the type of photoresist used. The metal evaporation is performed with physical vapour deposition, see section 3.1.3. The final step is the lift-off: here, the samples with the evaporated metal on top are placed in a solvent bath (usually acetone) to remove the excess photoresist and the metal with it. Therefore, in the case of positive photoresist the metal as the same shape as the projected mask on the substrate, while in the opposite case, the region without metal has the same shape as the mask.

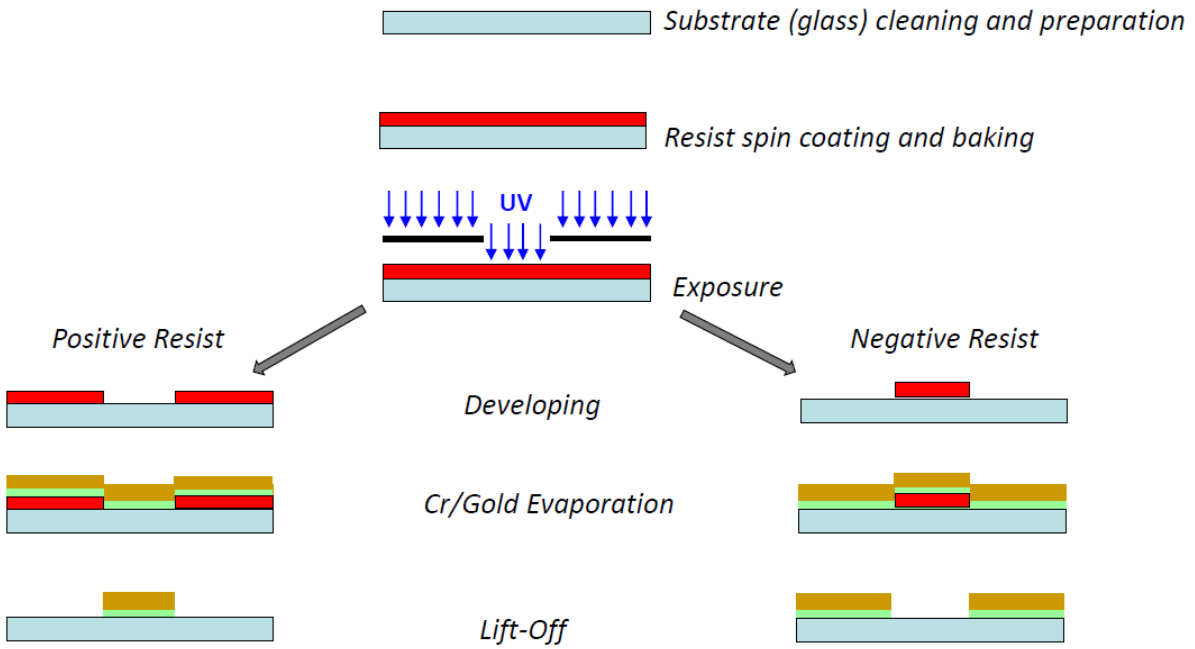

Figure 3.2: Photolithography for metal contact patterning. Scheme step by step for the preparation of patterned Cr/Au metal contact on glass substrates. The process starts with the substrate preparation and the deposition of the photoresist. The sample is exposed to UV light through a mask placed between the UV source and the sample. The developing step removes the resist exposed (not exposed in the case of negative photoresist) leavening it instead in the region where the UV light was blocked by the mask. After the metal evaporation the lift-off removes the excess photoresist leaving a patterned metal film on the substrate.

Photolithography is used in semiconductor industrial manufacturing for the fabrication of transistors and integrated chips at the basis of modern technology. The machine I

used for this work is the MicroWriter ML3 from Durham Magneto Optics, the picture is reported in Figure 3.3a. The Microwriter uses the concept of direct writing, i.e. it uses a digital mask created via software for the photoresist exposure instead of a physical mask. The digital mask guides the machine that exposes the sample only in the right regions. The MicroWriter is equipped with a precise sample positioning system in the x-y plane and a z stage with all the optics needed for the exposure. While the sample is moved the UV projection optics illuminates the photoresist only in the desired regions. This system provides extreme flexibility since the mask can be easily created with CAD software.

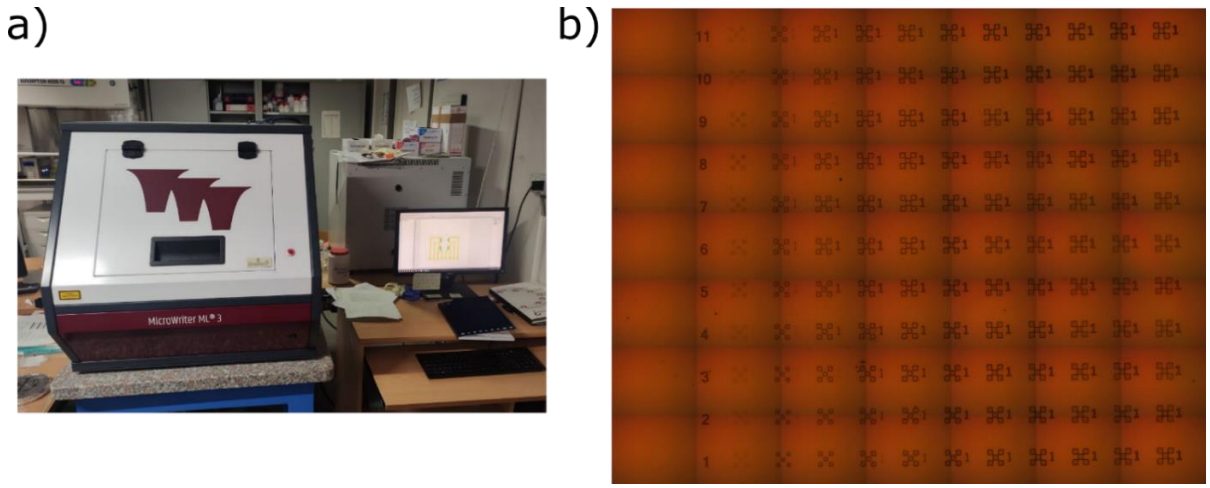

Figure 3.3: MicroWriter ML3. a) Picture of the MicroWriter ML3 from Durham Magneto Optics. The machine is placed on a heavy marble table for vibration damping. A computer next to the machine is used to control the process. b) Test to establish the best sensitivity value for the photoresist exposure.

For the patterning of interdigitated metal contacts, I used the MICROPOSIT S1818 positive photoresist. The photoresist was spin-coated on dried glass or PET substrates with a rotating speed of 3000 rpm for 60 s. Before the exposure, a soft baking at 110 °C was performed. To understand the UV light intensity to use for the exposure, I performed a test where a defined matrix of patterns with different UV intensities was written on the positive photoresist. A photoresist sensitivity between 230 – 260 mJ cm^{-2} gives the best results in terms of resolution.

3.1.3 Thermal evaporation

In Figure 3.4 is reported a scheme of the apparatus used for the deposition of metal contacts. Physical vapor deposition is a technique for depositing thin film (2 - 100 nm) of suitable materials. In device fabrication, the deposition of metals is commonly carried out with this technique, but the deposition of small organic molecules is possible too. It consists in the evaporation or sublimation of the material to deposit and the subsequent deposition onto a substrate. The materials to evaporate are placed in crucibles also called source boats, or baskets depending on the shape. The metal sources are connected to an external power supply providing electrical current through the crucible. The electrons flowing through the crucible heat up the source and the material inside. The material slowly starts to evaporate and goes towards the substrate placed above the sources at 30 – 50 cm. The hot atoms or molecules from the sources when hitting the cold substrate lose their kinetic energy and the film formation starts. A shutter is used to control the start and end of the evaporation procedure. If a patterned film is needed, it is possible to place a mask with the proper shape between the substrate and the source boats. The mask, usually in metal or kapton, blocks the hot atoms in unwanted regions of the substrates only letting pass the vapor in the right place. The mask is thin and must be placed close to the substrate to avoid shadow effects, moreover for a uniform deposition the substrate is kept in rotation. The layer thickness is controlled by a quartz crystal balance, properly calibrated, placed near the substrate. From the variation of the vibration frequency of the quartz resonator is possible to calculate the evaporation rate expressed in nm s^{-1} and from this, the total material thickness deposited onto the substrate. The evaporation rate is controlled by varying the current across the crucible. All the system is placed in a vacuum chamber kept under ultra-high vacuum (< 5 x 10^{-6} mbar) thanks to a turbomolecular pump connected directly to the chamber. The ultra-high vacuum (UHV) condition is needed

to increase the mean free path of gas molecules or atoms inside the chamber so that they can reach the substrate without scattering with other atoms.

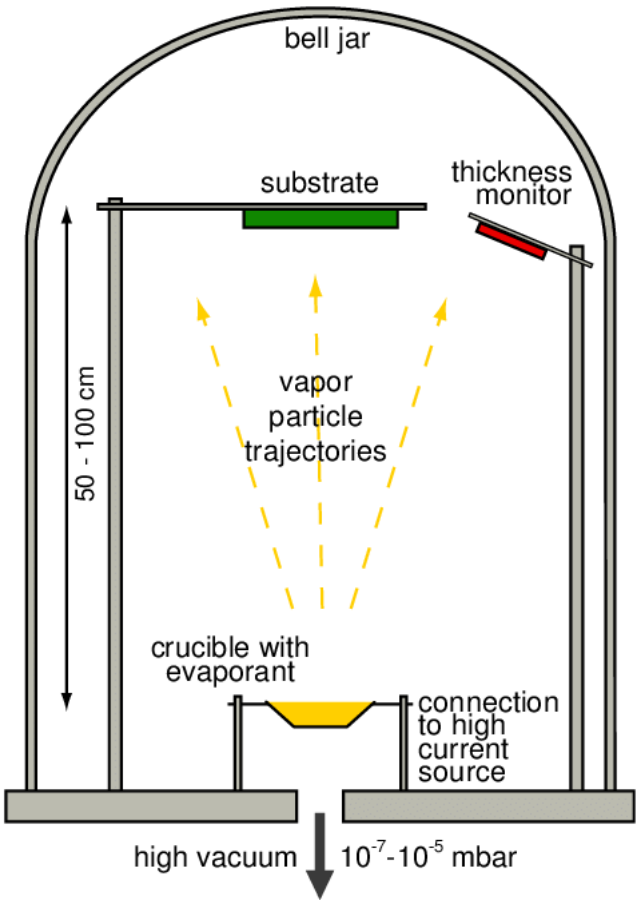

Figure 3.4: Thermal evaporation. The samples are placed on a sample holder facing the sources inside a metal or glass dome in high vacuum conditions. The metal to be evaporated is placed inside a crucible (usually made of tungsten) heated by a flowing electric current. A quartz-crystal balance is placed near the sample holder and monitors the thickness of the metal being evaporated.

3.1.4 Chemical Vapour Deposition (CVD)

Chemical Vapour Deposition (CVD) is a vacuum deposition technique for the deposition of films from a gaseous phase. With this technique a large variety of materials can be deposited, even materials difficult to obtain directly in gaseous phase. In fact, in CVD is possible to take advantage of chemical reactions happening in the

gaseous phase or on the substrate. For example, it is possible to deposit polycrystalline silicon via a volatile compound of silicon SiH_4 called silane. By introducing two or more chemical spices is possible to deposit a different compound by inducing a chemical reaction. For example, with CVD the deposition of SiO_2 is practicable by introducing silane and oxygen. Here, I used the CVD for the deposition of parylene-C as substrate for ultra-thin substrates. Parylene-C is used for his dielectric properties and moisture resistance. The parylene-C monomer is composed of a para-xylene ring where a hydrogen has been replaced by chlorine, the chemical structure is reported in Figure 3.6b. A CVD machine optimized for parylene deposition is often called parylene coater. The deposition process is reported in Figure 3.5.

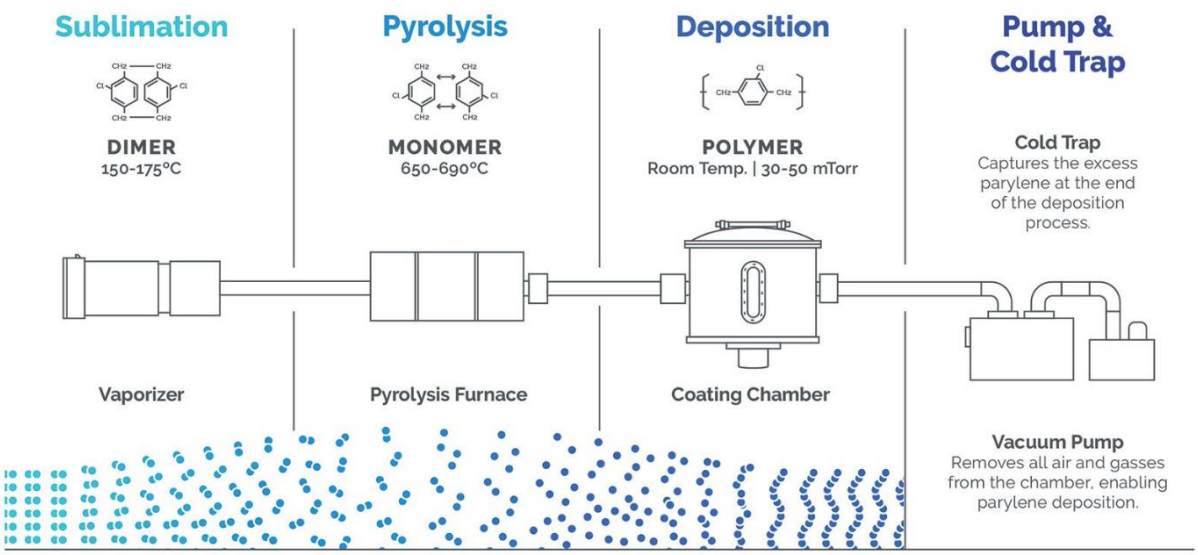

Figure 3.5: CVD process for parylene deposition. The deposition of parylene starts with the sublimation of the dimer (in powder form) in the vaporizer. The gaseous dimer goes in the pyrolysis chamber where the high temperature brakes the chemical bonds and forms the monomer. The gaseous monomer goes in the deposition chamber that is kept at ambient temperature. The monomers start to build the polymeric chain on top of the sample exposed surfaces. At the end of the deposition chamber there is a cold trap used to sublimate the excess parylene. To create the gas flow a rough pump is used at the end of the system.

The process starts with the insertion of the parylene dimer (usually in powder form) in the vaporizer, a region kept to a temperature between 150 - 175 °C. In the vaporizer, the dimer sublimates and follows the air flow created by a vacuum pump positioned at

the end of the system. The gaseous dimer enters the pyrolysis chamber, a high temperature region (600 – 700 °C) that has the purpose to separate the dimer in monomers. The monomers then arrive in the deposition chamber where the samples are placed. The temperature in this chamber is around the ambient temperature; the low temperature forces the monomer to aggregate on the sample surfaces into polymeric chains creating a layer of parylene. Following the gas stream, a cold trap is placed before the vacuum pump. The low temperature, obtained using liquid nitrogen, forces the solidification of the excess parylene. The system employed, Parylene P8 from Diener is visible in the picture reported in Figure 3.6. It is visible the vaporizer door on the left, the deposition chamber on the right with the top door and on far right the cold finger that extends outside the machine cover.

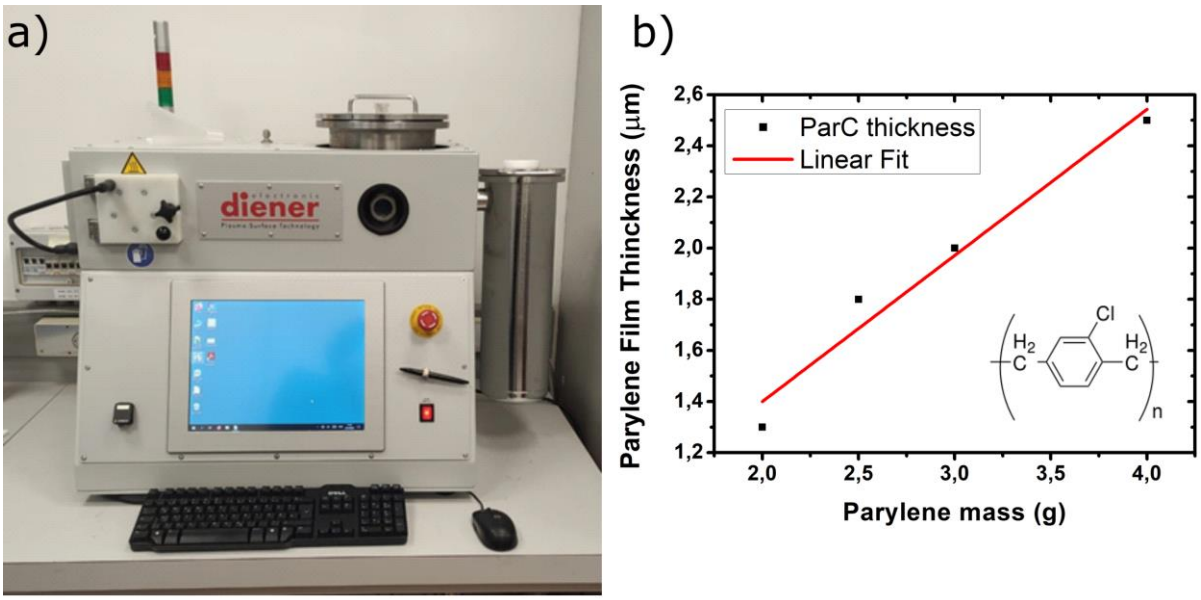

Figure 3.6: Parylene coater. a) Picture of the parylene coater used in the fabrication process of flexible photodiode. b) Calibration of the deposition process for parylene-C (the repeating unit is shown in the inset) on silane treated glass.

A calibration of the paryline coater has been performed to understand the relation between the mass of the precursor in the vaporizer and the final parylene thickness. For cleaned glass a value of 1 µm g^{-1} has been found. For free-standing flexible devices is useful to reduce the parylene adhesion on glass for better removal at the end of the

fabrication procedure. To do that, I used a chlorinated silane with a fluorinated carbon chain called Trichloro(1H,1H,2H,2H-perfluorooctyl)silane. It is a very volatile molecule and, on plasma treated glass, forms a self-assembled monolayer bond to the glass surface with the fluorinated tail pointing upwards. The fluorinated tail decreases the adhesion of parylene on the glass substrates. The linear relation between the precursor mass and parylene thickness on silane treated glass is reported in Figure 3.6b. From the slope of the linear fit I extracted a value of 0.57 μm g^{-1}, lower than the glass without silane treatment proving the decrease in adhesion.

3.1.5 Fabrication of photoconductors

The simplest detector geometry explored in this work is the photoconductor one. It consists of two planar metal electrodes with an interdigitated geometry, see Figure 3.7, with the perovskite layer deposited on top. By applying a bias to the electrodes an electric field is created inside the active material causing the charge carrier drift. The two electrodes are separated by a distance L called channel. The charges generated inside the channel are separated by the electric field and driven to the contacts. The width over which the charges are collected from each couple of fingers is indicated with the letter W. In the scheme, the pixel area used for response normalization is indicated with a green rectangle. This electrode configuration allows to optimize the charge collection in a given area. To fabricate photoconductors photolithography was used. Glasses 25 × 25 mm^2, 1 mm thick, were gleaned with ultrasounds and used as substrates for fabrication of rigid devices. The positive photoresist S1818 was spin-coated on clean glasses with 3000 rpm for 60 s. After a soft baking at 110 °C for 1 min, the samples were inserted in the MicroWriter ML 3 for UV exposure. The digital mask was designed using Clewin4 software. The exposure was divided into two parts: the conductive tracks and contact pad were exposed with 5 μm resolution; instead, the interdigitated part of

the pixels was exposed with 1 µm resolution. After the exposure, the samples were immersed in MF-319 for 45 s for the development and 45 s in distilled water for washing out the developer. The whole process was carried out in a yellow-light room to avoid degradation of the photoresist. The Cr/Au metal contacts were thermally evaporated on the sample. The lift-off was performed for 3 h in acetone. Next, the substrates were used for the deposition of the active perovskite layer.

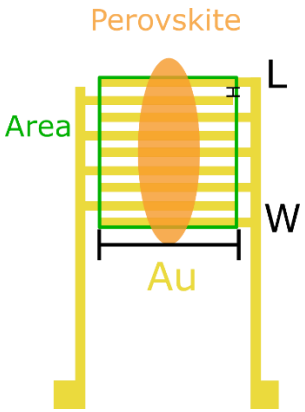

Figure 3.7: Photoconductor geometry. With photolithography an interdigitated metal contact is fabricated. Then it is covered with the perovskite active layer. In the scheme the perovskite covers only partially the fingers of the contacts, in reality the perovskite should cover all the interdigitated area. The distance between two fingers is called channel (L) and corresponds to the maximum distance the generated charges have to travel to be collected. The width of the channel is indicated with W. The pixel area used in normalization is indicated by a green rectangle.

3.1.6 Fabrication of photodiodes

A p-i-n photodiode is a p-n junction with the addition of an insulating layer between the doped regions (p-i-n). The layer in the middle is usually an intrinsic semiconductor, that is responsible for the absorption as already seen previously. In this thesis, I also studied photodiodes with perovskites absorbing layers. In the case of silicon photodiodes, the junctions are obtained with the same material (silicon) but with different types of doping and doping concentrations. In the case of perovskite, the strategy is different: the perovskite is sandwiched between organic or inorganic

materials with different purposes. In Figure 3.8a is reported a scheme of the general structure of a perovskite photodiode. Starting from the bottom, the device is made of the substrate with a conductive material applied (ITO or Au) and functions as bottom contact. The hole transport layer (HTL) is deposited on the bottom contact. The perovskite absorbing layer is in the middle of the structure, above the HTL. The Electron Transport Layer (ETL) is deposited on top of the perovskite and a buffer layer can be inserted before the metal contact to improve the interface. The structure is completed with the top metal contact.

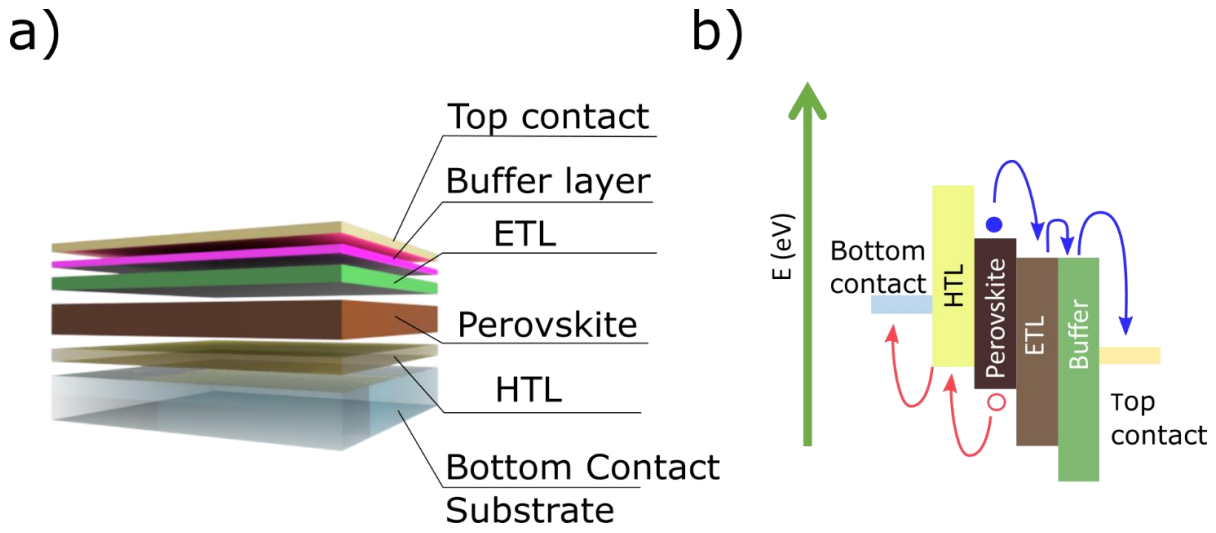

Figure 3.8: Photodiode structure. a) p-i-n photodiode architecture. The perovskite active layer is in the middle of the structure interfaced with the electron and hole transport layers. A buffer layer can be inserted to improve the interface with the metal contact. b) Energy level diagram of a perovskite based photodiode. In the p-i-n configuration holes are drifting towards the bottom contact and electrons are collected by the top metal contact.

The corresponding energy level diagram is reported in Figure 3.8b. When the perovskite layer absorbs the radiation, the generation of electron-hole pairs take place. The charges are separated by the action of the internal or external electric field. The hole and electron transport layers have the function of make the separation and extraction more efficient. The charges are then collected at the electrodes. In this work I used different interlayers and perovskite layers for the fabrication of photodiodes. In the following is reported a list of material used for each layer. The perovskite active

materials used will be described in the results chapter accordingly to the result presented.

Substrates

- *Glass/ITO.* For rigid devices ITO covered glasses (25 × 25 mm^2, 1 mm thick) are used as substrate and bottom contact for holes extraction. The glass must be cleaned with multiple solvents in an ultrasonic bath. The first step is in a solution of soap and distilled water followed by a step in water and IPA. A meticulous cleaning procedure is necessary for the fabrication of thin-film devices, any dust particles or imperfection on the substrate surface can compromise the fabrication.
- *Thin PET foil.* For the fabrication of ultra-flexible photodiode a 1.4 µm thick PET foil was used. Glass substrates (2.5 ×2.5 cm, 1 mm thick) were cut and cleaned in an ultrasonic bath with water, soap and IPA to be used as a carrier for the thin foil. Before used they were dried with N_2. A poly(dimethylsiloxane) (PDMS) solution was prepared by mixing 1:10 w/w of cross-linker to hardener and then diluting it 1:1 w/w with n-hexane. Then PDMS solution was spin-coated at 4000 rpm for 30 s on the glass and placed on a heat plate at 150 °C for 10 min to cross-link. The PDMS layer formed function as a glue for the PET foil thank to the strong electrostatic interactions. The 1.4 µm PET foil was carefully placed on the sample avoiding air bubbles and then transferred to a heating plate again at 110 °C for another 10 min. This step is useful to remove air between the PDMS and the PET. To make the substrate conductive, Cr/Au (10/100 nm) bottom contacts evaporated with thermal evaporation.
- *Parylene.* A 2 µm thick layer of parylene-C deposited by CVD was used as an alternative to the PET foil for ultraflexible devices. Cleaned glasses were treated by oxygen plasma (100 W, 10 min) to activate the glass surface with OH group. The glasses were quickly transferred inside a petri dish with some droplet of

Trichloro(1H,1H,2H,2H-perfluorooctyl)silane to functionalize the surface. After 30 min the glasses were cleaned in acetone to remove the excess silane. Then the substrates were positioned inside the parylene coater for the deposition. As in the previous case Cr/Au metal contact were evaporated.

Hole Transport Layer

- *PEDOT:PSS.* A PEDOT:PSS solution was prepared by mixing Clevios PH1000 solution with 5 vol% DMSO and 0.5 vol% Zonyl FS-300 (surfactant to improve the film quality), stirring at room temperature for an hour and keeping at 4 °C in the fridge overnight. Before spin-coating the solution was filtered through Minisart RC25 Syringe filter with 0.45 µm porous size to remove long polymeric chain agglomerate. The PEDOT:PSS was spin-coated at 1500 rpm for 45 s (ramp 2 s) followed by 1000 rpm for 2 s (ramp 1 s) on the PET or parylene substrates and annealed at 122 °C for 15 min. Then the film was washed by spin-coating isopropanol solution at 1500 rpm for 4 s followed by 4000 rpm for 12 s and annealed at 120 °C for 15 min. The gold metal contact on the PET where cleaned to have an access for contact the device.
- *NiO_x.* Nickel oxide was used as inorganic HTL. First, $NiCl_2 \cdot {}_6H_2O$ was dissolved in deionized water under stirring. Then, 10 M NaOH solution was added into the solution drop by drop until the pH value reached 10. The obtained solution was centrifuged, and the precipitation was washed with deionized water for two times, after which the powder was dried at 80 °C overnight and then annealed at different temperatures for 2 h. NiO_x nanoparticle solution was prepared by dispersing the NiO_x nanoparticles in deionized water with sonication. The resulted solution was filtered through a polytetrafluoroethylene (TPFE) filter (0.45 µm). The NiO_x film was obtained by spin-coating the dispersion at 4000 rpm for 15 s and then 5000 rpm for 15 s. Afterwards the film was annealed at 140 °C for 20 min.[98]

- *Poly-TPD.* Poly(N,N'-bis-4-butylphenyl-N,N'-bisphenyl)benzidine as organic alternative to PEDOT:PSS. This organic polymer improves the device stability thanks to higher hydrophobicity than PEDOT. After plasma treatment, a solution the poly-TPD HTL (1.5 mg/ml in CB) was deposited on glass/ITO by spin-coating at 4000 rpm for 60 s. The films were annealed at 110 °C for 30 min in air followed by UV treatment in air for 30 min to improve the poly-TPD wettability for the perovskite deposition step.

Electron Transport Layer

- *PCBM.* [6,6]-Phenyl C61 butyric acid methyl ester was employed as organic ETL. This molecule makes the fullerene soluble in organic solvents so that it can be deposited by spin-coating. The PCBM solution was prepared by dissolving 2 wt% PCBM in chlorobenzene and chloroform (1:1 volume ratio). The solution was spin-coated onto the samples at 1300 rpm for 16 s(ramp 2 s) followed by 2000 rpm for 15 s (ramp 2 s). No annealing is required and the buffer layer is deposited immediately on top.
- *PTCDI.* N,N′-dimethyl-3,4,9,10-perylentetracarboxylic diimide (PTCDI) is an small molecule n-type organic semiconductor. In this work was used as electron transport layer (100 nm). It was deposited onto sample via thermal evaporation at 0.5–2 nm s^{-1} rate and base pressure ≈1 × 10^{-6} mbar.

Buffer layer

- *BCP.* Bathocuproine BCP solution was prepared with a concentration of 0.5 mg mL^{-1} in isopropanol. BCP was spin-coated at 5000 rpm for 30 s on the PCBM layer.
- *TiO_x.* Diluted TiO_x sol–gel solution was spin-coated on top of PCBM at 4000 rpm for 30 s, followed by annealing at 110 °C for about 5 min in ambient air.

Top metal contacts

Cr, Au and Al were evaporated and used as top metal contact depending on the structure.

3.1.7 Rolled X-ray photodetector

In order to increase the detector performances, I took advantage of the extreme flexibility of the device fabricated by fabricating rolled perovskite-based X-ray detectors. I designed and 3D printed a rolling machine for perovskite devices see Figure 3.9. Two stepper motor are synchronized by an Arduino UNO board and fixed to the printed frame. To the motors a straight and cylindrical support is attached through two grabbers.

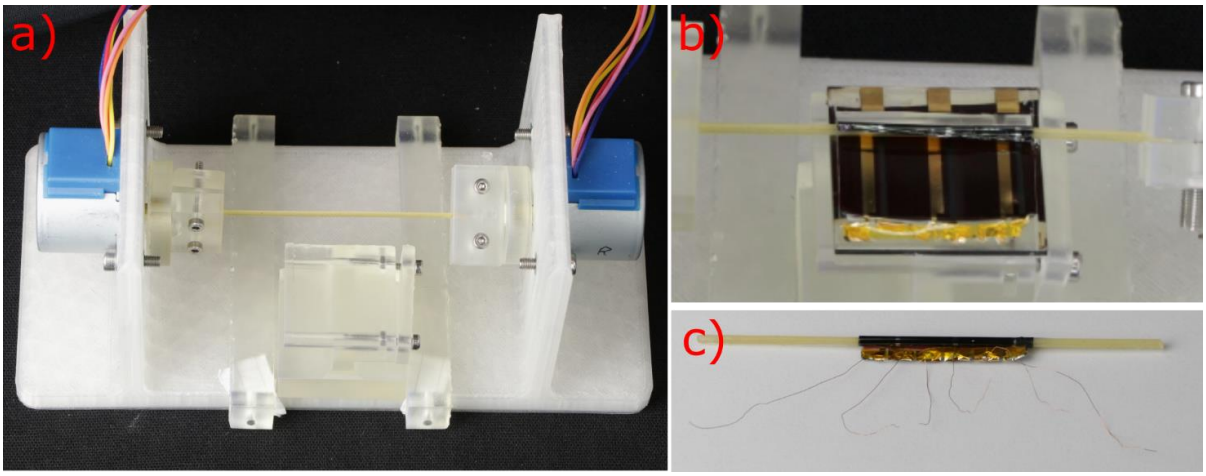

Figure 3.9: Rolled X-ray detectors. a) Rolling machine for photodiodes. Tow synchronized stepper motors slowly rotate a straight cylindrical support around which the device is rolled. b) A sample positioned in the machine, the device detaches form the substrate as it gets rolled up. c) Picture of a rolled X-ray detector with copper wire for electrical characterization.

The supports used are Cappelini n°1 spaghetti from Barilla. They provide a low atomic number, round and straight support around which the device can be rolled. To increase the adhesion of the devices, the spaghettis are covered with a layer of PDMS. The detector on the glass substrate is positioned below the support and slightly peeled off

from the glass. The spaghetti starts to rotate and the sample is gently detached from the glass. At the end of the rolling process some copper wires can be used to extract the signal from the detector.

3.2 Characterization

I characterized the perovskite-based photodetectors with different techniques investigating the optoelectronic properties of different perovskites and devices. I characterize the response of perovskite film detectors under different ionizing radiations. In this section, a description of the characterization techniques, procedures and data analysis performed is given.

3.2.1 Electrical characterization

For electrical characterizations, a customized probe station has been employed. The system is equipped with tungsten probe-tips and micro-manipulator under an optical microscope for positioning. The system is placed inside a metal box acting as Faraday shielding and protecting the sample from environmental light. The electrical characterizations have been conducted using a Keithley 2614B or a Keysight B2912 source meter units (SMU). I used the setup to acquire the current-voltage curves (i.e. I-V curves) of the planar and stacked devices. Combining the probe station with calibrated LEDs is also possible to characterize the device response under UV-Vis light. Due to the very low dark current of 2D perovskites in some cases, I used a Keithley 6517A Electrometer.

3.2.2 UV-VIS optoelectronic characterization

UV-Vis Photocurrent spectroscopy

In this experiment, a monochromatic light beam is shined on a semiconductor and the current flowing in the device is recorded as a function of the wavelength. I used the setup reported in Figure 3.10. As radiation source, a QTH (Quartz Tungsten Halogen) lamp (22 V, 150 W) or a Xe arc lamp were employed. Both sources produce a white spectrum, the Xe lamp is used with 2D perovskite because a higher emission in the blue-UV range is needed. The light beam passes through an optical chopper and is focused inside a Sciencetech 9055F monochromator. This is composed of two rotating diffraction grids with 1200 gr mm^{-1} and blaze wavelengths of 300 nm and 1000 nm. A mirrors system is used to guide the light on a focusing lens with a focal distance 10 cm that focuses the light on the sample. At the entrance and at the exit of the monochromator, two slits controlled by micrometre screws were used to collimate the light beam for the improvement of the intensity and sensitivity of the irradiation. The wavelength resolution is determined by the slid dimensions and the reciprocal linear dispersion coefficient (δ) of the monochromator equal to 3.3 nm mm^{-1}. The resolution ($\Delta\lambda$) can be calculated simply by:

$$\Delta\lambda = \delta d \qquad (3.3)$$

Where d is the slit aperture.

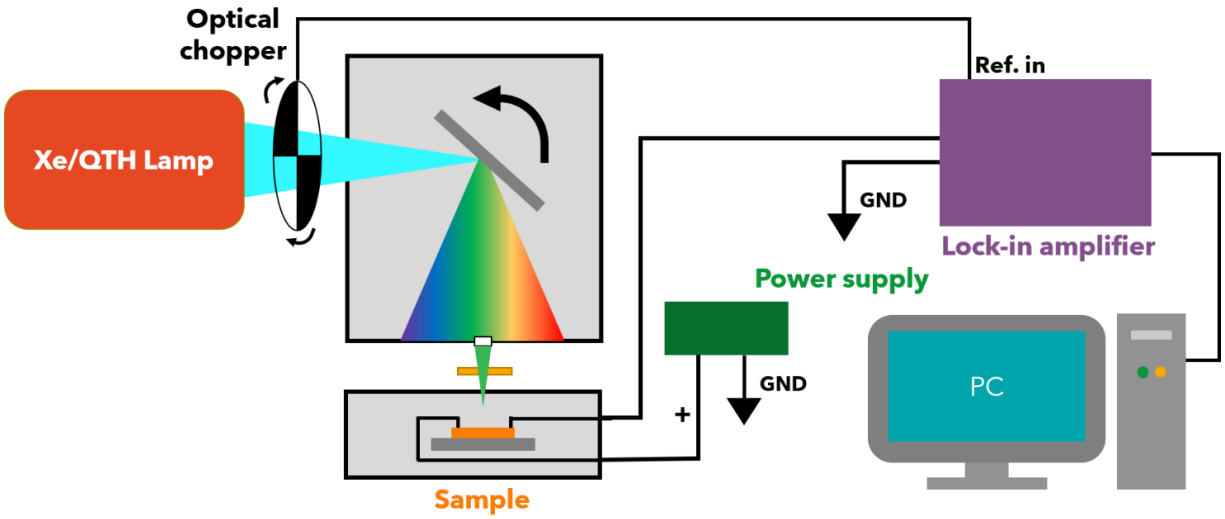

Figure 3.10: UV-Vis Photocurrent. Depending on the sample Xe lamp or a QTH lamp can be selected. The chopped light beam is focused on the monochromator grating through an adjustable slit. The monochromatic light exits through the second slit and passes through a filter if needed. The sample is placed in a metal box with an aperture on top. The sample is connected via micro-probe tips to a power supply, furnishing the bias, and to the lock-in amplifier used in current mode. Everything is controlled with a LabVIEW software.

In order to filter the photo-induced signal and discriminate it from the surrounding electrical noise, a chopper is coupled with a lock-in amplifier. The chopper is placed between the lamp and the monochromator and it transforms the incident continuous illumination in a modulated light at a set frequency. This reference frequency is sent to the Stanford Research 830 lock-in amplifier used in current mode. The sample is connected to the system with micro-probe tips and a power supply is used to provide the bias if needed. The wavelength is slowly changed and the current acquired obtaining a photo induced current spectrum. The spectrum is then normalized for the lamp spectrum (its photon flux) acquired with a Pyroelectric sensor (Scitec Instruments, LTQ2 Pyroelectric Single ElementDetector for Measurement Applications) kept in the same experimental conditions. This sensor provides a flat responsivity, independent of the light wavelength. The normalization was performed with the following:

$$Pc_N = \frac{Pc\, h\nu}{S_{py}} \qquad (3.4)$$

Where Pc_N is the normalized photocurrent spectrum, Pc the measured one and S_{py} the signal measured by the pyroelectric sensor.

From the normalized spectrum one parameter that can be extracted is the photocurrent onset, closely related to film bandgap. For non-crystalline materials and with the hypothesis of photocurrent proportional to absorption coefficient (at least close to photocurrent onset), the band-gap can be quantitatively extracted from the Tauc plot method.[99] The normalized signal times the photon energy squared is plotted as a function on the photon energy. In the band gap transition a linear fit can be performed for the extraction of the band gap.

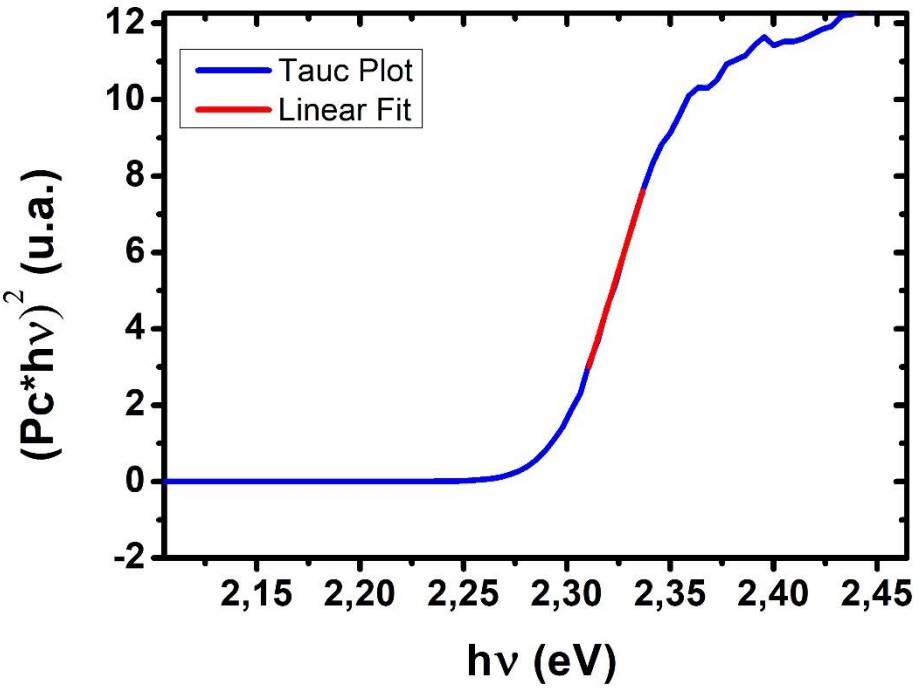

Figure 3.11: Example of a Tauc plot. On the y axis the measured signal times the photon energy squared is plotted versus the photon energy.

An example is reported in Figure 3.11. The Tauc method assumes that the energy-dependent absorption coefficient (in our case the photocurrent, that in the band gap transition is assumed to have the same behaviour.) can be expressed by the following equation:

$$(Pc\ h\upsilon)^{1/\gamma} = B(h\upsilon - E_g) \qquad (3.5)$$

where h is the Planck constant, υ is the photons' frequency, E_g is the band gap energy, and B is a constant. The γ factor depends on the nature of the electron transition and is equal to ½ for direct band semiconductors like the perovskite here studied. From the slope of the linear fit is possible to extract the band gap value.

Transient photocurrent measurement

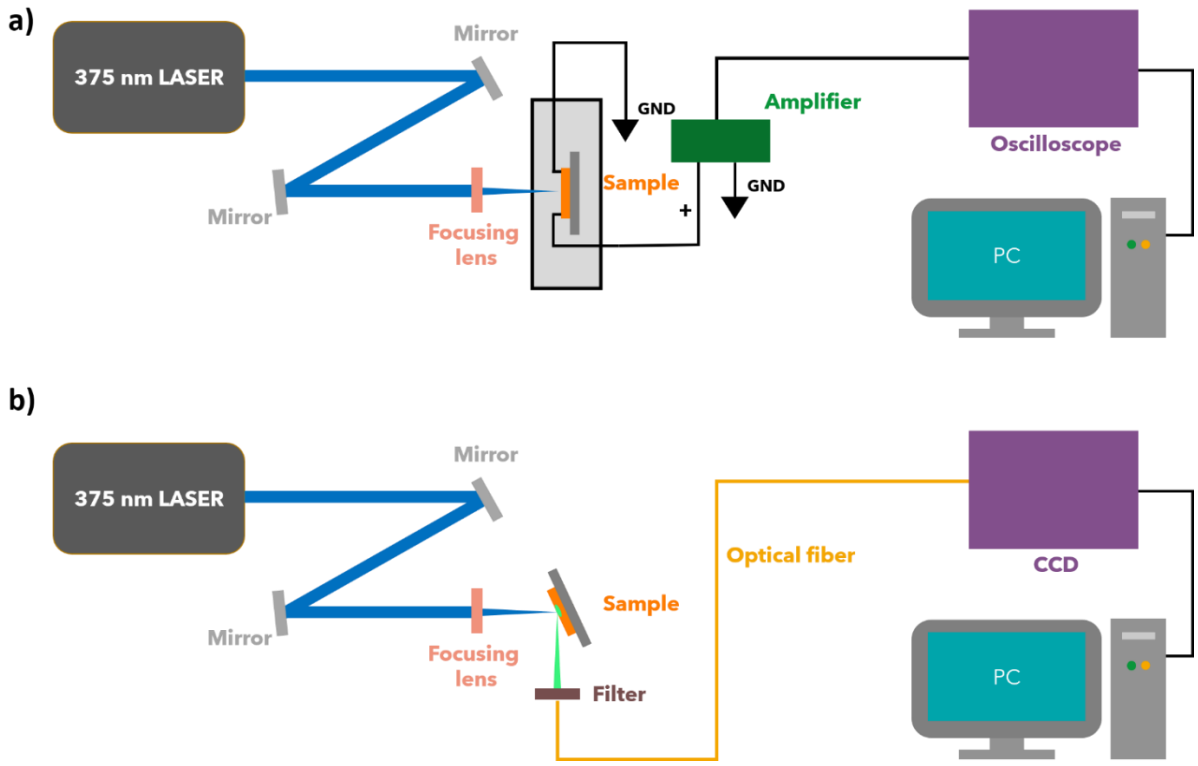

Figure 3.12: Transient photocurrent setup. A ps 375 nm LASER source is positioned on an optical board. Two mirrors are used to modify the direction of the beam. A focusing lens before the sample focuses the beam spot on the sample. a) The sample is positioned inside a faraday cage and connected to a current-voltage transimpedance amplifier used to amplify the signal. An oscilloscope measures the voltage pulse and acquires the data. b) The PL signal is collected in an optical fiber after filtering the reflected LASER beam. The spectrum is then collected with a CCD.

For this measurement, I used as fast excitation source a PicoQuant picosecond laser diode with narrow emission at 375 nm, and 40 ps pulse duration with adjustable power through the Taiko PDL M1 driver. Using built-in bunch mode, an arbitrary long laser

burst with 50% duty cycle can be obtained. In this operating mode, the laser shoots 40 ps pulses at a selected frequency. A longer wavelength square wave is used to modulate the power of the LASER creating separate bunch of pulses. The light-induced current signal is converted to voltage using a current amplifier FEMTO DHPCA-100 (bandwidth 1.8 MHz), then the signal was acquired with a Rohde & Schwarz RTB 2004 oscilloscope. Through the amplifier is possible to apply a 10 V bias to the sample. A picture of the set up used is reported in Figure 3.12a. Two mirrors are used to control the position of the beam, a lens is used to focus the beam spot on the sample surface. The sample is positioned in a metal box providing protection and shielding with the electrical connections. The time response is evaluated by calculating the time difference between the moments in which the response is 10 % and 90 % of the total photocurrent signal in the rising or falling dynamics.

Photoluminescence (PL)

A very similar setup can be also used to measure the photoluminescence spectra of the samples. The same diode LASER can be set in continuous mode. The peak wavelength is higher than the band gap energy thus perovskites absorb the light and electrons are excited to the conduction band. The electron-hole pairs, if not separated by an electric field, recombine emitting photons with energy equal to the energy difference of the levels involved in the transition. The PL emission on the sample surface is collected and guided with an optical fiber into a CCD compact spectrometer (ThorLabs CCS200). The optical fiber is positioned at 45° with respect to the incident laser beam and a 400 nm high pass filter is positioned before the optical fiber to cut the excitation source. The setup scheme is reported in Figure 3.12b

3.2.3 X-ray photocurrent measurement

X-ray photocurrent experiments are the routine characterization of the evaluation of performance of X-ray direct detectors. With this experiment is possible to extract the sensitivity and LoD measuring the current response of a device under X-ray beam. It is also important to define some physical quantities and unit of measure used in this work:

- Activity. It is used to describe how fast is the decay of a radioisotope source. It is defined as the number of nuclear decay, also called disintegration, per unit of time. The historical unit of measure is the curie (Ci) defined exactly as 3.7x 10^{10} disintegration per second. But it has been replaced by a more laboratory suitable unity of measure that is the becquerel (Bq) the S.I. units for activity.

$$1\ Bq = 2.703 \cdot 10^{-11} \qquad (3.6)$$

- Fluence. This quantity is important for the description of a radiation beam. If the photons beam is monochromatic the fluence can be defined as the number of photons through a unit area (equation 3.7). The fluence is strongly related to the distance between the source and the measurement point in space, in fact, it goes with the square of the distance. The distance between the source and the sample will determine the number of photons impinging on the active area of the device.

$$\Phi = \frac{dN}{dA}\ [cm^{-2}] \qquad (3.7)$$

- KERMA It is the acronym of Kinetic Energy Released per unit MAss in a material. It describes the first step in the interaction between the radiation and the material. It measures the energy transferred to the absorbing medium which

is then converted into excitation or ionization. The definition of KERMA is reported in the equation 3.15 where E_{tr} stand for transferred kinetic energy. KERMA can be related to thefluence of the source in that point of space by using the linear attenuation coefficient of the material, see equation 3.18. The radiation intensity in a specific point can be specified by the photon flux or the exposure, but it is often given in terms of AIR KERMA, which is the energy released in that point in a mass dm of air. In this work the incident dose reported in the measured is actually the air kerma dose at that specific distance from the source.

$$\mathrm{D} = \frac{dE_{tr}}{dm} \left[\frac{J}{kg} = Gy\right] \qquad (3.8)$$

X-ray tube

The X-ray tube is the most practical X-ray source for research laboratories. It is a vacuum tube with a cathode (negative pole) and an anode (positive pole), between the two an electron beam flow. The cathode is usually made of tungsten for its high melting point, it is heated by an electric current. Electrons are ejected from the filament due the thermionic effect. A metal cup, called focusing cap, positioned close to the cathode is negatively charged for focusing the electrons on the target. Between the cathode and the anode, a potential difference in the order of tens or hundreds of kV is applied. The potential drives the electrons toward the anode also called target. When the electrons collide with the anode they interact with the electron clouds of the target material. As described in the previous chapter, the electrons lose kinetic energy irradiating high energy photons. The radiation produced by decelerating electrons is called *bremsstrahlung* and it is a broad-spectrum emission with maximum energy equal to the maximum energy of the impinging electrons. Another effect take place if the electrons

energy is enough. When the electrons release energy inside the target, they can excite or ionize electrons in the core shells of the target atoms. If one electron gets removed from its core shell it leaves a hole, very soon the atom relaxes and an electron from the outer shells fills the void. By doing that it emits a photon with energy equal to the energy difference between the two levels. Since the transition involved are in the core shells, the energy of the emitted photon is in the keV range and the precise value depends on the target material. Typical target materials are: Ag, Cu, Mo and W.

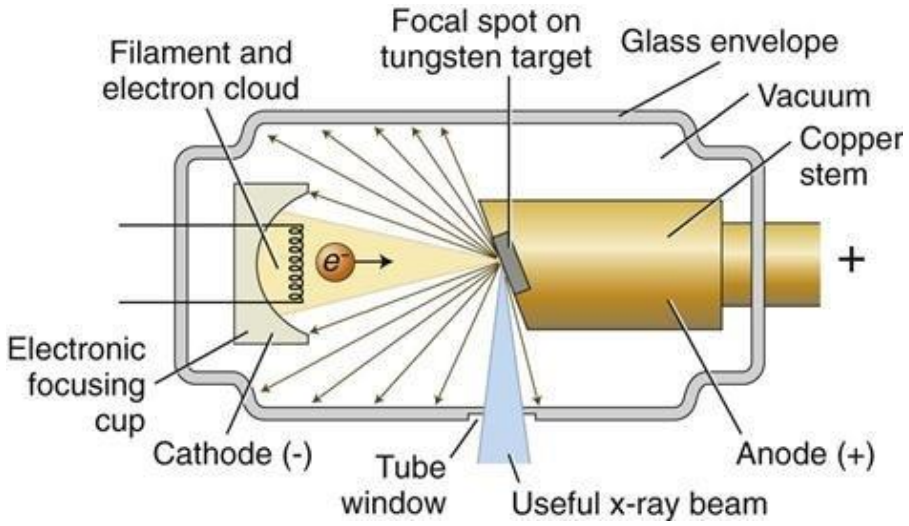

Figure 3.13: X-ray tube working principles. An electric current flow in a tungsten filament emitting electrons due to thermionic effect. The electrons are accelerated toward the anode where the target is placed. The interaction between electrons and target produces X-rays.

Depending on the target material the resulting X-ray spectrum changes because the emission line of the element is different. The emission lines are also called characteristic X-rays, they have high photon intensity, and they emerge from the bremsstrahlung broad emission. Therefore, an X-ray tube emission spectrum is always composed by two components, if the accelerating voltage is enough, one is continuous and the second is well defined in energy. The shape of the target metal determines the X-ray beam divergence and direction. The X-ray tubes are shielded to avoid the radiation to escape in unwanted directions, and Be is used to create a window for X-rays in a selected

direction. Beryllium is used for its low X-ray absorption due to the low atomic number. The target has to be cooled with water or air to dissipate the heat generated by the electron-target interaction. For device characterization, I used the Hamamatsu Microfocus L12161-07 X-ray source. It is a tungsten target X-ray rube with operating voltage up to 150 kVp and tube current between 10 to 500 µA. The tube has a 0.2 µm Be window and an X-ray beam aperture of 43°. The X-ray tube is air cooled with an external power supply that can be controlled with a PC via RS-232C interface. The simulated spectrum of the Hamamatsu tube at the two operating voltages used (40 and 150 kV) were obtained with the SpecCalk simulation software and reported in Figure 3.14a.[100–102] At 40 kVp only bremsstrahlung radiation is present with a mean energy of 15.2 keV. At 150 kVp the energy of the electrons is sufficient to excite the core levels of tungsten; in the spectra are present the K_α and K_β transitions emerging from the continuous emission. The resulting mean energy when operated at 150 kV is 47.4 keV.

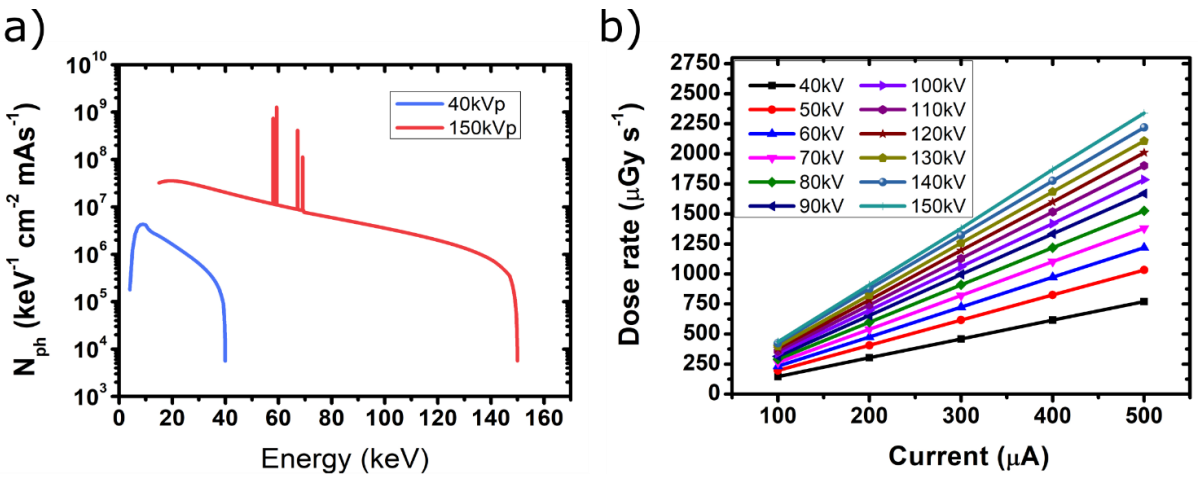

Figure 3.14: Tungsten target X-ray tube. a) Spectra of the tungsten target X-ray tube used at two different voltage: 40 kVp and 150 kVp. b) Dose rate calibration of the tube at different energies. The detector was placed at 50 cm from the source.

The dose calibration of the tube was performed with the commercial detector Barracuda (RTI Group, Sweden) inserted inside the same boxes used for the samples. The resulting dose rates (in air KERMA), at 50 cm from the tube, for different tube

voltages and tube current are reported in Figure 3.14b. The calibration was used to determine the incident X-ray dose rate on the sample under test.

Complete setup

The X-ray tube described above was used as radiation source in an experimental set up inside a shielded bunker. The setup is composed of the source, a lead shutter, a sample box and a source meter unit (SMU). The setup is schematized in Figure 3.15.

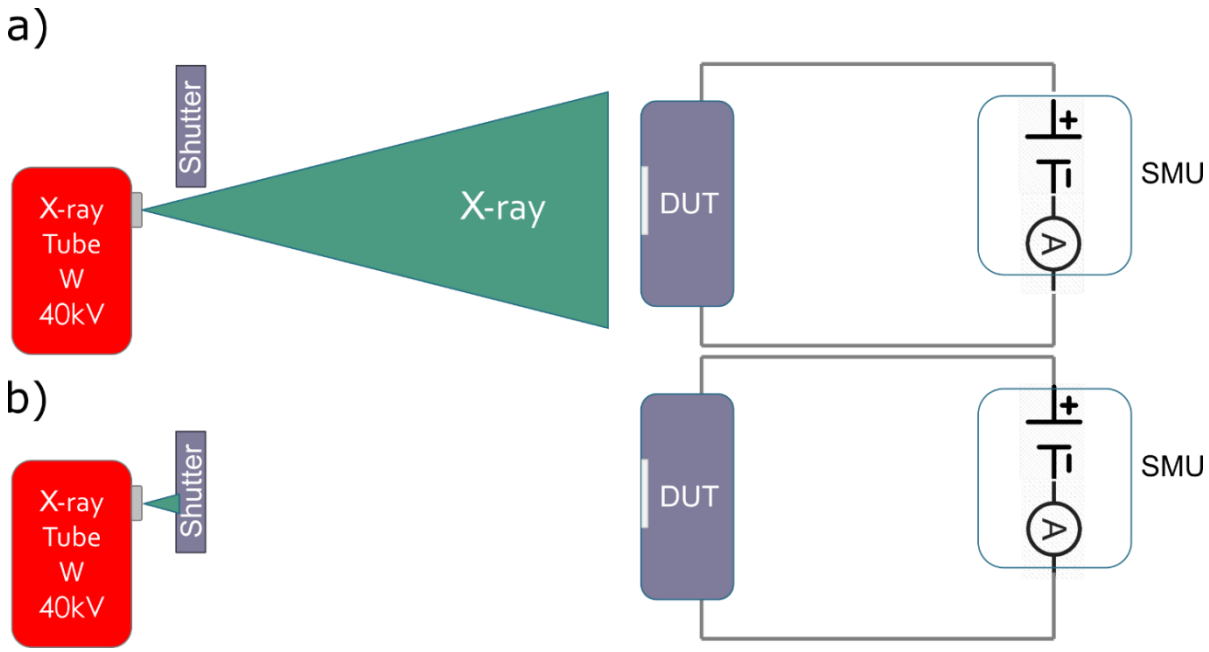

Figure 3.15: X-ray photocurrent experiment. The system is composed by the X-ray source, a lead shutter, the device under test and a source meter unit (SMU) electrically connected to the sample. The sample is placed inside a metal box with an aluminium window for light protection. The shutter is controlled to modulate the photon flux impinging on the sample. In a) the configuration with the shutter open, in b) when the shutter is closed blocking the X-rays.

The shutter (composed by 4mm of Pb) completely blocks the X-ray beam when closed. By opening and closing the shutter in front of the beryllium window a modulation of the beam is obtained. In this system, the opening and closing times of the shutter are ~50 ms. The sample is placed inside a metal box with a 70 µm Al window to protect it from environmental light and provides a faraday cage for noise reduction. Perovskites are very sensitive to light, I found essential to well isolate the samples from external

visible light to have the lowest dark current values. For some perovskite samples, that were very sensitive to atmospheric humidity and oxygen levels, I used a sealed metal box filled with nitrogen. The sample contacts are connected to the core of biaxial or triaxial connectors on the measurement box. To those connectors, biaxial or triaxial cables were used to connect the sample to the SMU that provides the bias and measure the current flowing in the devices. In this configuration the shields of the cables are connected to the box walls, providing a full signal shielding. The typical current output by the experiment is simplified in Figure 3.16a. When the shutter is closed the current measured from the SMU is the dark current. Instead, when the shutter opens and the X-rays reaches the sample the current should increase, ideally with a fast box-like response. The difference between the current with the shutter open (I_{on}) and the dark current (I_{off}) is called photocurrent (ΔI):

$$\Delta I = I_{on} - I_{off} \tag{3. 9}$$

For each photocurrent peak, the I_{off} and I_{on} values are obtained by averaging the experimental data when the shutter is closed or open respectively. To a give dose rate impinging on the sample the photocurrent is the average of the photocurrent value of each peak recorded. By adjusting the tube current the dose rate can be changed, the variation of the photocurrent as a function of the dose rate can be used for the sensitivity extraction. Operatively the sensitivity is defined as the derivative of the photocurrent versus dose rate curve:

$$S = \frac{\partial \Delta I}{\partial DR} \tag{3. 10}$$

In the case of a linear relation, like the example in Figure 3.16b, the sensitivity is simply the slope of the line that can be obtained by a linear fit the experimental data.

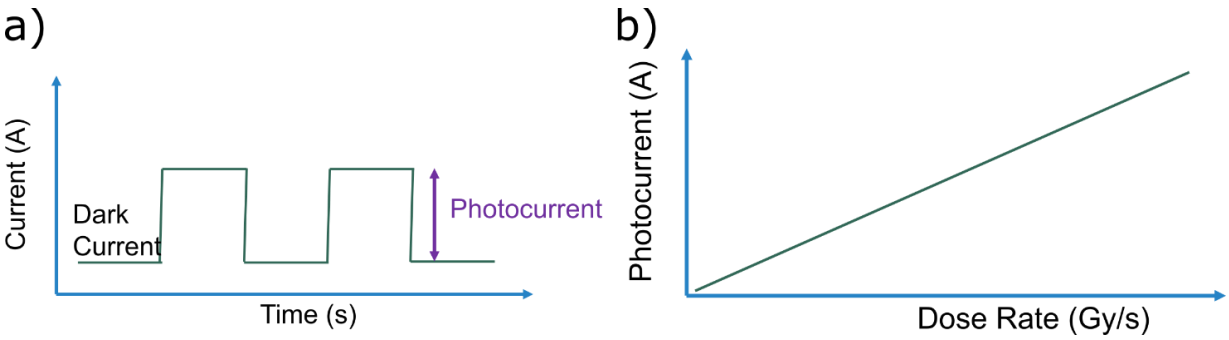

Figure 3.16: Output data. a) Typical shape of the current profile obtained in the experiment. The photocurrent is the difference between the dark current and the current flowing when the detector is irradiated. b) Example of a linear behaviour of the photocurrent as a function of the dose rate, for this type of plot the sensitivity can be extracted.

I evaluated the LoD according to the IUPAC definition: the input value in a detector that gives as output signal 3 times the noise value. The noise level is evaluated by calculating the standard deviation of the dark current ($3\sigma_{Dark}$), thus the LoD is calculated with the following relation valid for a linear behaviour of the photocurrent:

$$LoD = \frac{3\sigma_{Dark} - q}{S} \qquad (3.\ 11)$$

Where q is the intercept.

The tube current and voltage are set with a dedicated software, data acquisition and shutter control are performed by a LabVIEW software communicating with the instruments via USB connection.

3.2.4 Characterization with radio tracers

I also tested the detectors' responses to high energy gamma-rays emitted by radioactive tracers used in medical applications (^{18}F and ^{99m}Tc). The experiments were carried out at the IRCCS in Reggio Emilia. The system used to measure the device response is described in Figure 3.17

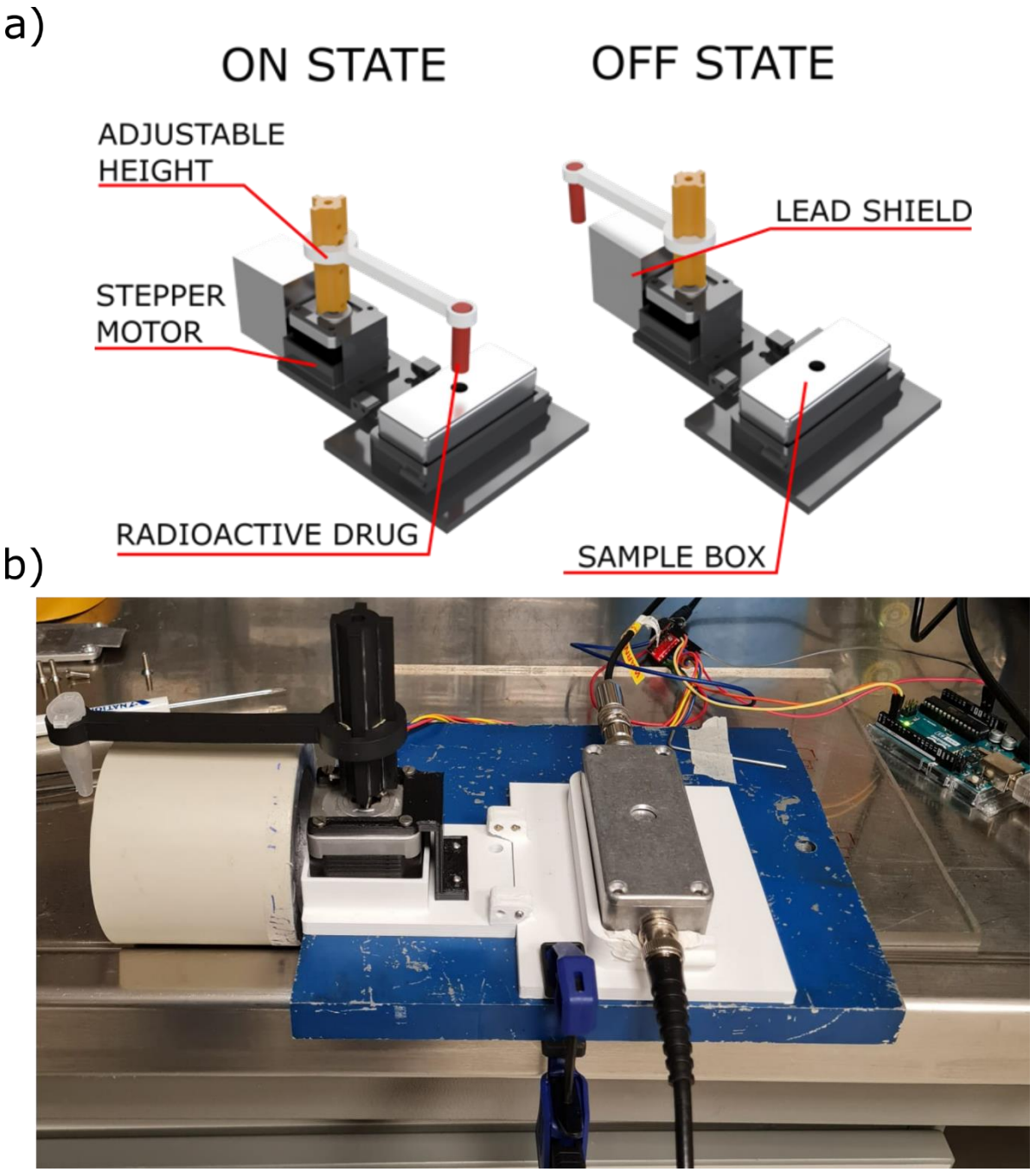

Figure 3.17: Shutter for high energy gamma rays. a) Scheme of the shutter system employed for the sensors characterization under high energy gamma ray emitted by radioactive drugs. A stepper motor is controlled by an Arduino UNO board. 3D printed holders keep the moto and sample box in place. The radioactive drug is contained in a vial hold by a custom support connected to the motor axis. A thick Pb cylinder is used to screen the sample from the radiation when the state is in the off position. In the on position the motor moves the gamma source on top of the sample. b) Picture of the setup used at the IRCCS in Reggio Emilia.

. I developed a 3D-printed frame that hold in place a stepper motor and the sample box. To the motor axis is connected a printed support for the vial in which the radioactive drug is contained. The motor is guided by an Arduino UNO board and an A4988 stepper motor driver. The Arduino is programmed to send a PWM signal to the driver; based on the pulse sequence the driver sends a specific current sequence to the motor coils. The motor moves the source by 180°, in the off state the source is > 15 cm from the sample. In the on state, the source is moved on top of the aluminium window of the metal box. An 8 cm thick lead shield is placed between the source and the sample when the system is in the off state. By moving the gamma source back and forth, is possible to acquire a dynamic response of the detector and the data can be analysed as in the case of X-ray irradiation. With this system, I measured the device response to ^{18}F and ^{99}Tc with activity between 1800 MBq and 94 MBq. The detector response was measured by a SMU connected to the sample box.

3.2.5 Characterization under proton beam

The mixed 3D-2D perovskite film-based detectors were characterized using a 5-MeV proton beam provided by the 3 MV Tandetron accelerator of the LABEC (Laboratorio di Tecniche Nucleari Applicate ai Beni Culturali) ion beam center (INFN Firenze, Italy). The proton beam is extracted into ambient pressure through a 200-nm-thick Si_3N_4 membrane; the sample has been installed 8 mm far from the extraction window. Proton beam currents used in this work are typically in the 0.1 pA to 100 pA range. The weak intensity of the extracted beam is monitored and quantitatively measured using a rotating chopper, placed between the silicon nitride window and the sample, that intercepts the beam; the chopper is a graphite vane covered with a thin nickel evaporated layer, and the Ni X-ray fluorescence is used as an indirect measurement of the beam current. To determine the actual energy of the protons impinging onto the

samples, the energy lost by the protons passing through the several layers interposed between the beam and the sensor has to be evaluated. The beam passes through 200 nm of Si_3N_4 for the beam extraction window, 8 mm of mixed air-He (50%-50%) atmosphere in the gap between the extraction window and the metal box, 14 µm of Al for sample box window, and 14 mm of air inside the box, has to be calculated. After passing through these layers, protons lose about 390 keV, as calculated with the SRIM Monte Carlo code.[103] As for the X-ray measurement. The samples were irradiated with proton flux in the range [10^5 – 10^9] H^+ cm^{-2} s^{-1} and 10 s time window. The spot of the proton beam has an area of 0.17 cm^2. Electrical response under proton beam irradiation was acquired by a Keithley 2614B precision SMU.

3.3 Synchrotron Beamlines

Synchrotron facilities provide high intensity X-rays and experimental setups for advanced material characterization. For this work I had the chance to perform two experiments with synchrotron sources. One took place at the European Synchrotron Radiation Facility (ESRF) in Grenoble (France), the other experiment was performed at ELETTRA Synchrotron facility in Trieste (Italy).

3.3.1 X-ray Nanoanalysis beamline at ESRF-EBS

X-ray nanoanalysis combines a nanosized beam with multiple techniques performed at the same time allowing the correlation of different material properties. In this thesis, I used X-ray fluorescence (XRF) and X-ray Beam Induced Current (XBIC) to correlate

elemental distribution and transport properties in perovskite thin-film X-ray detectors. The measurement were performed at the ID16B beamline at ESRF after the last upgrade (ESRF-EBS).[104] The X-rays are produced by a 2.5 m long undulator source with a period of 26 mm. The Figure 3.18 shows the optical layout of the beamline. While the primary beamline optics, double white beam mirror and double-crystal monochromator are placed as close to the source as possible (30 m and 35 m, respectively) to preserve the coherence of the beam and to minimize beam instabilities, the Kirkpatrick–Baez nanofocusing optics are located very close to the sample (10 cm) to obtain a high degree of demagnification.[105] The optical arrangement allows very small beam spot down to ~ 50 nm in diameter on the sample surface. The sample is positioned on a x-y stage, see Figure 3.19. The stage can move in the plane thanks to piezoelectric motors for fine movements or stepper when precision is not required. Closed to the sample are positioned two silicon drift peltier cooled detectors.

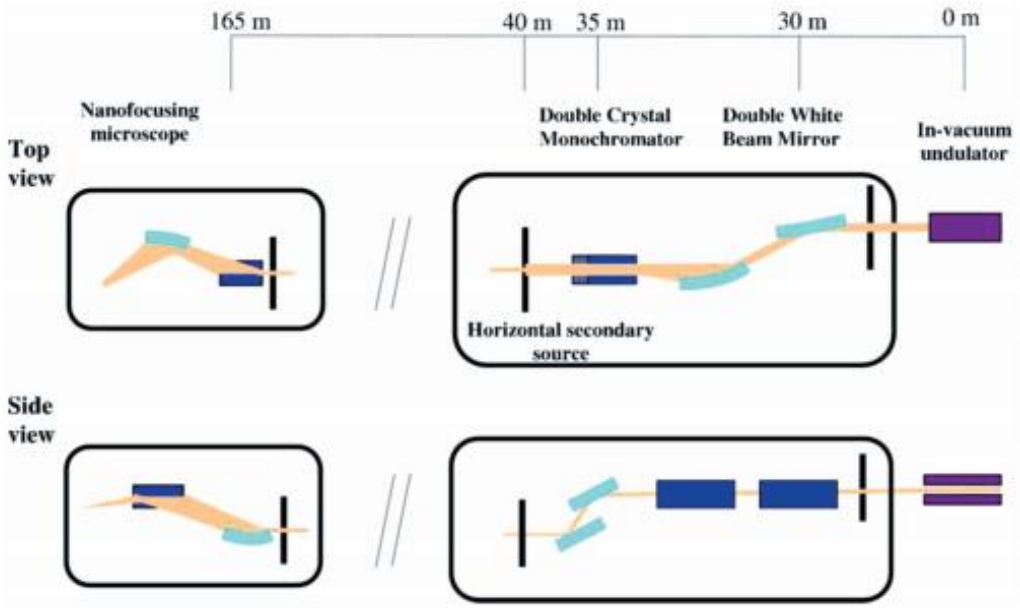

Figure 3.18: ID16B beamline at ESRF.[105] X-ray optics configuration for beam conditioning before the experimental cabin.

Those detectors were used to acquire the fluorescence signal coming from the sample under test. An optical microscope aligned with the X-ray beam is used for sample positioning. At the beamline XRF and XBIC were performed simultaneously using a 17.5 kV pink beam as excitation source. X-ray fluorescence allows to understand the elemental composition of the sample. The X-ray are used to excite the core electrons of the atoms in the sample. During the deexcitation an outer electron fills the void left from the photoelectron. As result an X-ray photon with energy equal to the energy difference between the two level is emitted. The emitted fluorescence spectrum can be measured by the detectors close to the sample. . Compared to standard EDX performed in a SEM setup, XRF offers several advantages:[106] the interaction volume of X-rays is smaller than the one of electron for improved spatial resolution; the deceleration of electron in materials produces bremsstrahlung backgroumd radiation which lower the resolution of the technique and allows also to measure weak M and L transitions. Using X-rays as a probe instead of electrons also has advantages when measuring the generated current since X-rays allow for higher spatial resolution and their low attenuation allows to probe the bulk.[106] To measure the current induced by the beam in the sample a chopper and a Stanford Research 830 lock-in amplifier were employed. The chopper frequency was set to 1017 Hz and a power supply was used to bias the sample. The motorized stage, the detectors and nanofocusing optics are positioned onto a 4.4 m long, 1.5 m wide and 0.3 m thick granite with passive damping system for vibrational insulation. The temperature inside the experimental cabin oscillates ±0.05 °C. By combining those two techniques with the moving x-y stage, elemental and current mapping can be obtained. The image obtained in this way contains multiple information in each pixel. In fact, in each of them is contained the XRF spectra and the current signal. The XRF spectra were analysed with the pyMCA software obtaining an intensity map for each element present in the sample.[107]

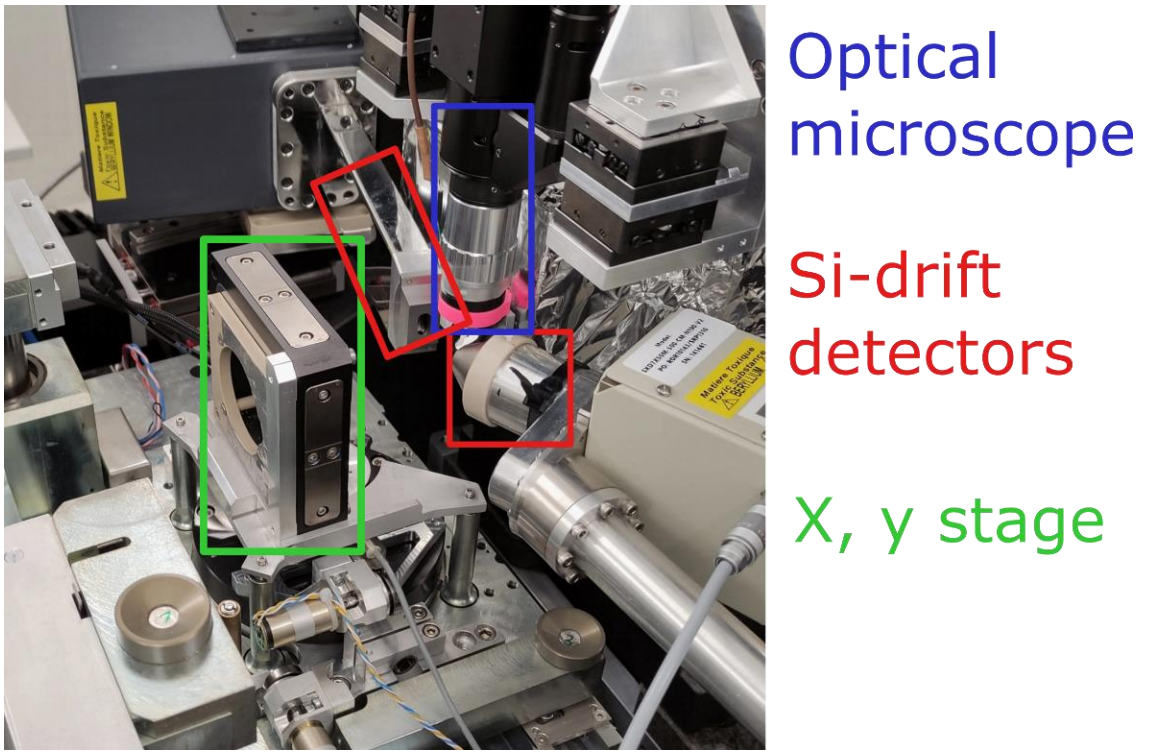

Figure 3.19: Nanoanalysis setup. The sample is placed on a vertical x, y stage moved in the plane perpendicular to the X-ray beam by piezoelectric motors. Two silicon drift detectors are placed near the sample surface to collect the XRF signal. An optical microscope is used for positioning.

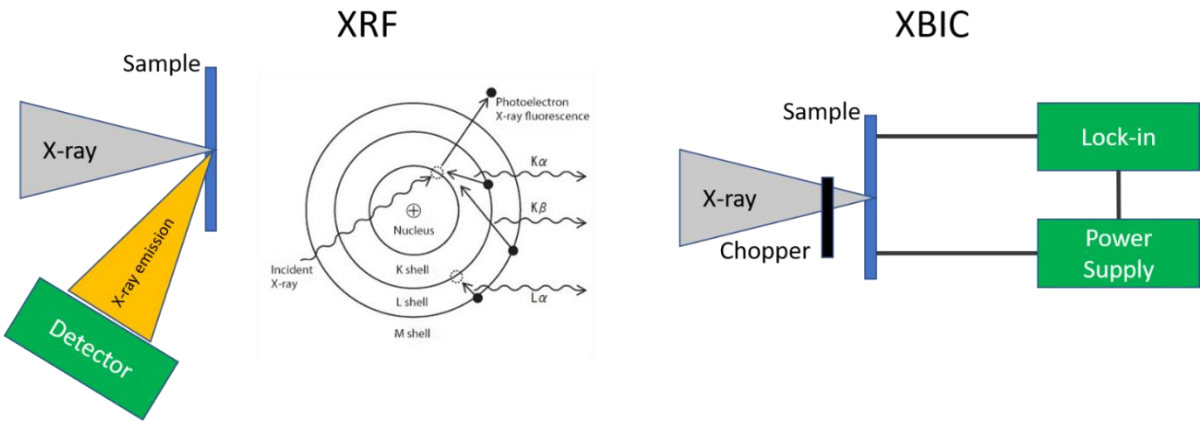

Figure 3.20: XRF and XBIC. In XRF the beam is used to excite core electrons of the atoms leaving a hole. An electron from an outer shell fills the hole and emit an X-ray photon with energy equal to the energy difference between the atomic levels. In XBIC the X-ray beam is used to generate charges inside the active layer. The sample is biased thanks to a power supply and a lock-in amplifier is used to measure the current in the device. The reference signal for the lock-in comes from a chopper positioned before the sample.

I wrote a python code to analyse the high quantity of images collected. The software allowed a fast comparison between the different images acquired thanks to an interactive dashboard. Moreover, to correlate the XRF and XBIC signals an overlap between the two maps was performed according to the RCG model. I obtained the overlaid images by summing pixel by pixel the RGB vectors of the XRF and XBIC maps. The RGB vector is composed by three integer number, between 0 and 255, representing the relative intensity of red, green and blue colour composing the final colour of the pixel. Since we attributed the purple to XRF maps and green to XBIC maps their respective RGB vector is as follows:

$$\overrightarrow{XRF_i} = \begin{pmatrix} x_i \\ 0 \\ x_i \end{pmatrix} \quad (3.\ 12)$$

$$\overrightarrow{XBIC_i} = \begin{pmatrix} 0 \\ y_i \\ 0 \end{pmatrix} \quad (3.\ 13)$$

Where in the case of XRF maps, the integers representing the intensity of red and blue are the same (x_i) in the ith pixel. While for XBIC maps red and blue are set to zero and the green depends on the intensity of the signal in that specific pixel. x_i and y_i are equal to zero when the signal is the minimum (resulting in black colour) and are set to 255 when the signal is the maximum. The sum of the two vectors can be expressed:

$$\overrightarrow{XRF_i} + \overrightarrow{XBIC_i} = \begin{pmatrix} x_i \\ 0 \\ x_i \end{pmatrix} + \begin{pmatrix} 0 \\ y_i \\ 0 \end{pmatrix} = \begin{pmatrix} x_i \\ y_i \\ x_i \end{pmatrix} \quad (3.\ 14)$$

The resulting vector contain the colour information of the overlaid image. The region where the XBIC signal is stronger than the XRF signal the pixels looks greener, on the contrary the pixels look more purple. Instead when the WRF XRF and XBIC signals are equal (same value in their relative scales) the resulting colour is a shade of grey, see **Figure 3.21**.

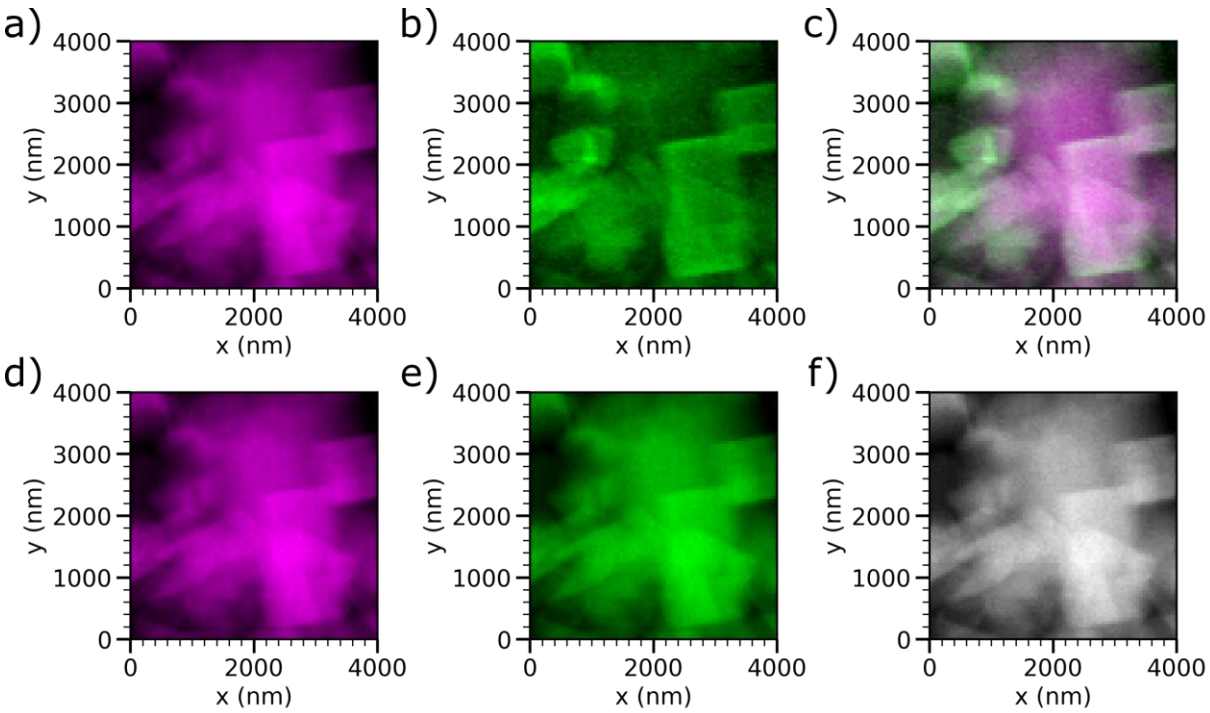

Figure 3.21: XRF and XBIC images overlapping. a) Pb fluorescence map and b) XBIC map of the same region. The overlay results in c). d) and e) Same Pb signal overlapped resulting in a shade of grey map f).

3.3.2 GIXRD

Grazing Incidence X-ray Diffraction (GIXRD) allows to study the crystal structure of the deposited perovskite thin-films. X-ray diffraction measurements of thin films (< 1 µm) using conventional $\theta/2\theta$ scanning methods generally produce a week signal from the film and an intense signal from the substrate. One of the ways to avoid intense signal from the substrate and get stronger signal from the film itself is to perform a 2θ scan with a fixed grazing angle of incidence, known as GIXRD. The fixed angle is generally chosen to be slightly above the critical angle for total reflection of the film material. The measurements were performed at the X-ray Diffraction beamline XRD1 bat the Synchrotron Radiation Facility Elettra in Trieste (Italy). The X-ray beam source is a wiggler on the Elettra 2 GeV electron storage ring. Before use it for diffraction experiment, the beam was monochromatized at 1.0 Å by a Si(111) double

crystal monochromator, focused on the sample and collimated by a double set of slits giving a spot size of 0.2 x 0.2 mm. Samples were oriented by means of a four-circle diffractometer with a motorized goniometric head. Once aligned, it was possible to rotate the sample around an axis perpendicular to the horizontal plane, to explore as much of the reciprocal space as possible, or, alternatively, vary the angle between the beam and the surface. Diffraction patterns were recorded with a 2M Pilatus silicon pixel X-ray detector (DECTRIS Ltd., Baden, Switzerland) positioned perpendicularly to the incident beam, at a distance of 150 mm from the sample. The incidence angles were kept close or slightly over 0.05°, the critical angle at the chosen wavelength. Uncertainty in the precise assessment of the incidence angle is estimated to be around 0.02°. Patterns were calibrated by means of a LaB6 powder standard from NIST by means of the software GIDVis31, which also allowed to represent the diffracted intensity as a function of reciprocal lattice vectors components q_{xy} and q_z and to project on the image predicted positions for the different phases present in the samples

4. 3D Perovskite for direct X-ray detection

Among hybrid lead-halide perovskites, 3D perovskites are the most studied for ionizing radiation detection thanks to their exceptional optoelectronic properties. In this chapter the results about 3D perovskite thin-film X-ray detector are reported

4.1 Designing Ultraflexible perovskite X-ray detector through interface engineering

Ultraflexible, low-cost, and highly sensitive ionizing radiation detectors are of great interest to the fields of medical diagnostics, treatment, dosimetry, industrial inspection,

public and land security. If the detector is very thin, light-weight and flexible it can be conformed around any object. High conformable X-ray detectors are appealing devices for astronauts, nuclear power plants, and laboratory workers, as well as for imagers used in structural inspection and cultural heritage preservation. For Example, these devices could be used directly on the skin patient for monitoring medical treatments or diagnostic procedures like a tattoo.[108,109] I realized an ultraflexible X-ray detector based on thin-film perovskite with a total thickness of ~ 3 μm, with extremely high conformability.[110] Ultraflexibility in electronics, refers to devices that can withstand bending radii below 1 mm. Indeed, ultrathin PET foil substrate grants these devices extreme flexibility and conformability. In Figure 4.1 are reported pictures of the device realized in this work placed on a laboratory glove. From the picture is possible to appreciate the high conformability of the device that is able to follow very small curvature radii. The key factor for fabricating ultraflexible devices is the substrate thickness, which defines the mechanical stress on the semiconducting material on top. The stress felt by a film (ε_f) on a substrate under bending is the following:

$$\varepsilon_f = \frac{t_f + t_s}{2R} \qquad (4.\ 1)$$

Where t_f and t_s are the film and substrate thicknesses respectively, R is the curvature radius. This relation is a simplification and it is valid only when the elastic moduli of film and substrate are equal. However, it is clear that the lower the substrate thickness the lower the stress on the semiconductor will be. Therefore, for high flexibility devices very thin substrates are needed. Another important concept for flexible stacked structure, as the one reported in this work, is the neutral mechanical plane, i.e. an ideal plane where due to the action of multiple layers the mechanical stress is equal to zero. Its location (n_p) can be identified with the following formula:

$$n_p = \frac{\sum_{i=1}^{n} \overline{E_i} h_i \left[\left(\sum_j^i h_j \right) - \frac{h_i}{2} \right]}{\sum_{i=1}^{n} \overline{E_i} h_i} \qquad (4.\ 2)$$

n_p is the distance between the neutral mechanical plane and the bottom of the photodiode structure described in the section 3.1.6. $\overline{E_i} = \frac{E_i}{1-\nu_i^2}$ is the plane Young's modulus, E the Young's modulus and ν the Poisson's ratio of the i-th layer of the structure. By playing with the layers thickness, the neutral mechanical plane can be positioned on the most fragile layer. Even if perovskite are quite soft materials (E = 16.5 GPa,[111] for $MAPbI_3$), the perovskite layer in the photodiode architecture is the most critical one. In fact, the interlayers are mostly organic/polymeric materials that can tolerate mechanical stresses. Therefore, the neural mechanical plane should be located in the perovskite layer.

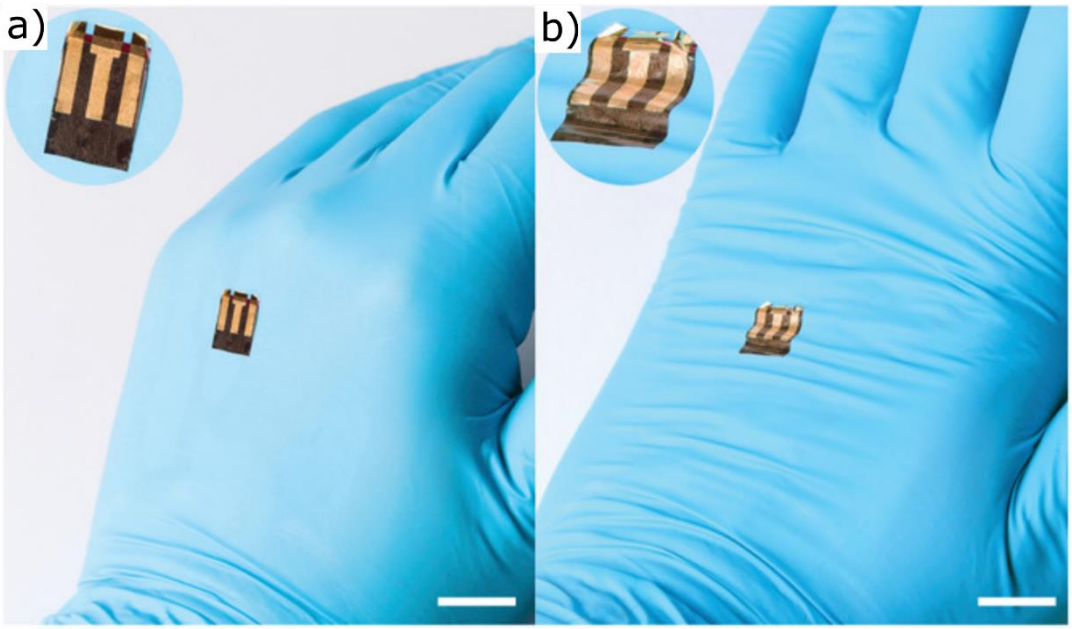

Figure 4.1: Ultraflexible detector.[110] a) Picture of an ultraflexible X-ray detector placed on a plain glove. b) Detector placed on a glove with wrinkles. Thanks to the extreme conformability, the detector can adapt itself to small curvature radii.

4.1.1 Perovskite interfaces and the effects on the X-ray detection performances

Ultraflexible X-ray detectors were fabricated using 500 nm mixed-cation mixed-halide perovskite composition ($Cs_{0.05}(FA_{0.83}MA_{0.17})_{0.95}PbI_{3-x}Br_x$) as a high energy photon absorption layer, in the middle of an inverted (p-i-n) photodiode configuration realized on 1.4 µm thick PET foil substrate. The perovskite layer deposition was carried out into N_2 glovebox. The precursor solution was deposited using the antisolvent procedure. The solution was spin-coated in two steps at 1500 rpm for 10 s followed by 6000 rpm for 30 s. Approximately ≈0.2- mL of chlorobenzene was dropped at 23rd second for about 3 s. Then the film was annealed at 100 °C for 1 h. The final film thickness is about 500 nm. The employment of a thin perovskite absorbing layer in a photodiode architecture allows both efficient charge collection and scalability onto ultrathin substrates. Different ETL and HTL were interfaced with the central perovskite layer in order to investigate their contribution to the principal detector performance parameters such as sensitivity, dark current, and limit of detection. The results from the devices are separated into two groups depending on the ETL, and the device structures are reported with the results. The first set of devices includes detectors employing solution processed PCBM as ETL, augmented with either bathocuproine (BCP) or TiO_x hole blocking buffer layer. In this configuration, the devices use Al as the top metal contact and UV curable epoxy in combination with polypropylene (PP) foil as an encapsulation layer. The other set of detectors uses PTCDI as ETL with Cr_2O_3 as buffer layer. In this configuration, Au top electrode was employed and was covered with ≈1 µm spin-coated polyurethane (PU) layer serving as a mechanical protection layer. As HTL the devices contained either PEDOT:PSS (formulation PH1000 Clevious) or solution processed NiO_x. In order to improve charge collection,

devices marked with LC (Large Contact) have 100 nm Au bottom contact extending over the entire detector active area.

PCBM based devices

PCBM is one of the standard ETL materials used in perovskite-based devices due to its simple low temperature solution processing. The large density of charge carrier traps at the perovskite surface has been identified as the major reason for the strong hysteresis effect, which can be passivated with the introduction of a fullerene-based material at the cathode interface. Shao et al. reported the use of PCBM to passivate the perovskite surface by reducing interface charge recombination, resulting in reduced hysteresis and overall improved device performance.[112] Here, PCBM-based X-ray photodiode architectures were characterized under X-rays, Figure 4.2a-c. From the J-V characteristics acquired in pristine conditions, a very low hysteresis effect is reported. The structure with the lowest hysteresis was the one employing TiO_x as buffer layer. However, is also the less stable structure under X-ray irradiation showing a pronounced change in the J-V after 360 mGy of accumulated dose. The low hysteresis directly translates to stable dark current confirmed by measuring the dynamic response of the detector Figure 4.2g-i at 0 V under irradiation at three different dose rates (318, 992, and 1885 $\mu Gy\ s^{-1}$), and over three ON/OFF beam cycles (10 s period 50% duty cycle). All PCBM-based detectors showed a fast and reproducible box-like response to X-rays, and a linear increase of the signal amplitude with increasing dose rate. The photocurrent density versus dose rate behaviour is reported for the three structures in Figure 4.2j-l. The detector performance as a function of the reverse bias was tested up to -1 V for the most stable devices and a low bias dependence of the photocurrent was observed. That suggests that the built-in electric field of the p-i-n diode structure is sufficient to collect all the charges generated by the absorption of the X-rays in the 500 nm thick perovskite layer. This allows the possibility of operating these detectors in passive mode (no external bias), a relevant feature for wearable flexible electronics.

Basiriccò et al. reported a one order of magnitude sensitivity change by applying -0.4 V to a n-i-p perovskite X-ray photodiode.[59] The bias effect could be ascribed to the 300 nm thick mesoporous TiO_x that could lead to the generation of charges outside the depletion region at 0 V. Further, we assessed the influence of ETL/electrode buffer interlayers on the overall performance of X-ray photodiodes by comparing the behaviour of PEDOT/Per/PCBM/BCP and PEDOT/Per/PCBM/TiO_x device architectures, Figure 4.2a and b. The buffer layer is used to decrease the electron injection barrier at the electrode interface. In this study, detectors containing thin TiO_x interlayer yield the highest X-ray induced photocurrent and highest sensitivity of 7.5 ± 0.3 μC Gy^{-1} cm^{-2} at 0 V within PCBM-based set of architectures. The higher performance of these devices can be associated with the TiO_x high electron affinity and lower conduction band (CB) level ($CB_{perovskite}$ = -4.2 eV, $CB_{TiOx} = -4.1$ eV, $LUMO_{BCP} = -3.5$ eV, where LUMO stands for Lowest Unoccupied Molecular Orbital). This lowers the charge transport resistance values and improves the electron extraction. Titanium oxide could also play a role in preventing perovskite ion diffusion through PCBM that can then react with the metal electrode, thus avoiding the formation of insulating layers at the PCBM/electrode interface.[113,114] Additionally, we observe lower dark current in PEDOT/Per/PCBM/TiO_x devices when compared to PEDOT/Per/PCBM/BCP, therefore presenting another advantage of using TiO_x as ETL/electrode buffer layer. The major contributing factors to photodiode dark current are reverse saturation current and current resulting from parallel shunt pathways.[115] Hailegnaw et al. showed that use of TiO_x considerably reduces the surface roughness and significantly improves PCBM surface coverage, thus increasing the parallel shunt resistance and contributing significantly to dark current reduction.[113] The low dark current combined with the high sensitivity allowed a low limit of detection of about 0.58 ± 0.05 μGy s^{-1} already at 0 V, well below the medical requirement (≈5 μGy s^{-1}).

This value is one of the lowest for perovskite thin-film detectors,[65,92,96] and it compares well with other thick perovskite X-ray detectors.[42,116]

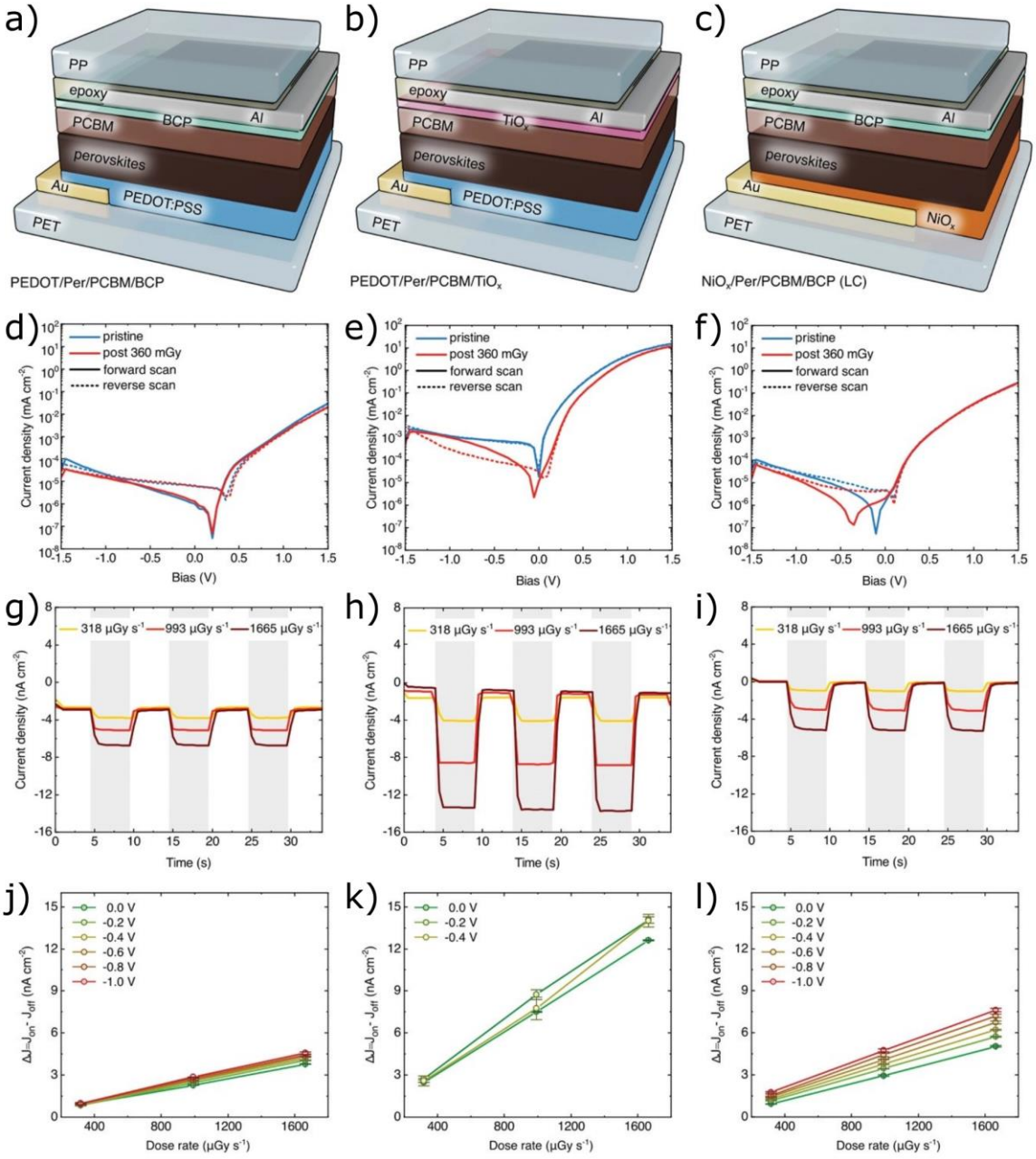

Figure 4.2: PCMB based device.[110] a), b) and c) PCBM based X-ray photodiode structures with the different layers differentiated by the colour. d), e) and f) J-V characteristics of the structures above acquired in pristine condition (in blue) and after 360 mGy X-ray exposure (in red). The continuous lines are the forward scan while the dotted lines the backward scan. g), h) and i) Dynamic response under 40 kVp X-ray at different dose rates. j) l) and l) Photocurrent density as a function of dose rate for the different bias tested.

To compare the influence of HTL, the performance of PEDOT/Per/PCBM/BCP and NiO_x/Per/PCBM/BCP (LC) detector architectures were compared. They have comparable sensitivities being 2.2 ± 0.1 μC Gy^{-1} cm^{-2} for PEDOT-based and 3.0 ± 0.2 for NiO_x/Per/PCBM/BCP (LC) detectors. But NiO_x based devices showed exceptionally low dark current with values as low as 30 pA cm^{-2}. This could be related to the high CB level of NiO_x (-1.8 eV) and thus excellent electron blocking properties of this HTL.

PTCDI

PTCDI (Pigment Red 179) is a small molecule organic semiconductor that belongs to perylene diimide derivative family. Commonly used for industrial-scale automotive and fiber coating, it is well known for its exceptional chemical, thermal, photo, and weather stability. In addition to the environmental durability of PTCDI, its low-lying HOMO level (-6.3 eV), high electron mobility (≈1–10 cm^2 V^{-1} s^{-1}), electron affinity, and lower rigidity when compared to inorganic materials like TiO_x, makes this material an excellent non-fullerene alternative ETL for flexible perovskites and organic solar cells.[117]

The PTCDI-based devices were fabricated with a thin 10 nm Cr_2O_3 interlayer between ETL and Au electrode, using PEDOT:PSS as HTL. The use of large metal bottom contact to improve charge extraction was tested, see Figure 4.3a, b. Metal oxide interfacial layers were reported to improve the performance of organic solar cells, due to its hole blocking capabilities (CB = 4.0 eV, E_g = 3.4 eV).[118] Moreover, it can effectively shield commonly used metal contacts from oxidizing reactions with halide species, making the devices more stable.[119] Compared to the PCBM-based detectors, PTCDI-based ones suffer from a strong hysteresis, even in pristine condition, visible in the J-V curves reported in Figure 4.3c, d. Like PCBM-based set, PTCDI-based detectors showed box-like highly reproducible X-ray response over three ON/OFF cycles with dose rates between 318 and 1665 μGy s^{-1}, Figure 4.3e, f.

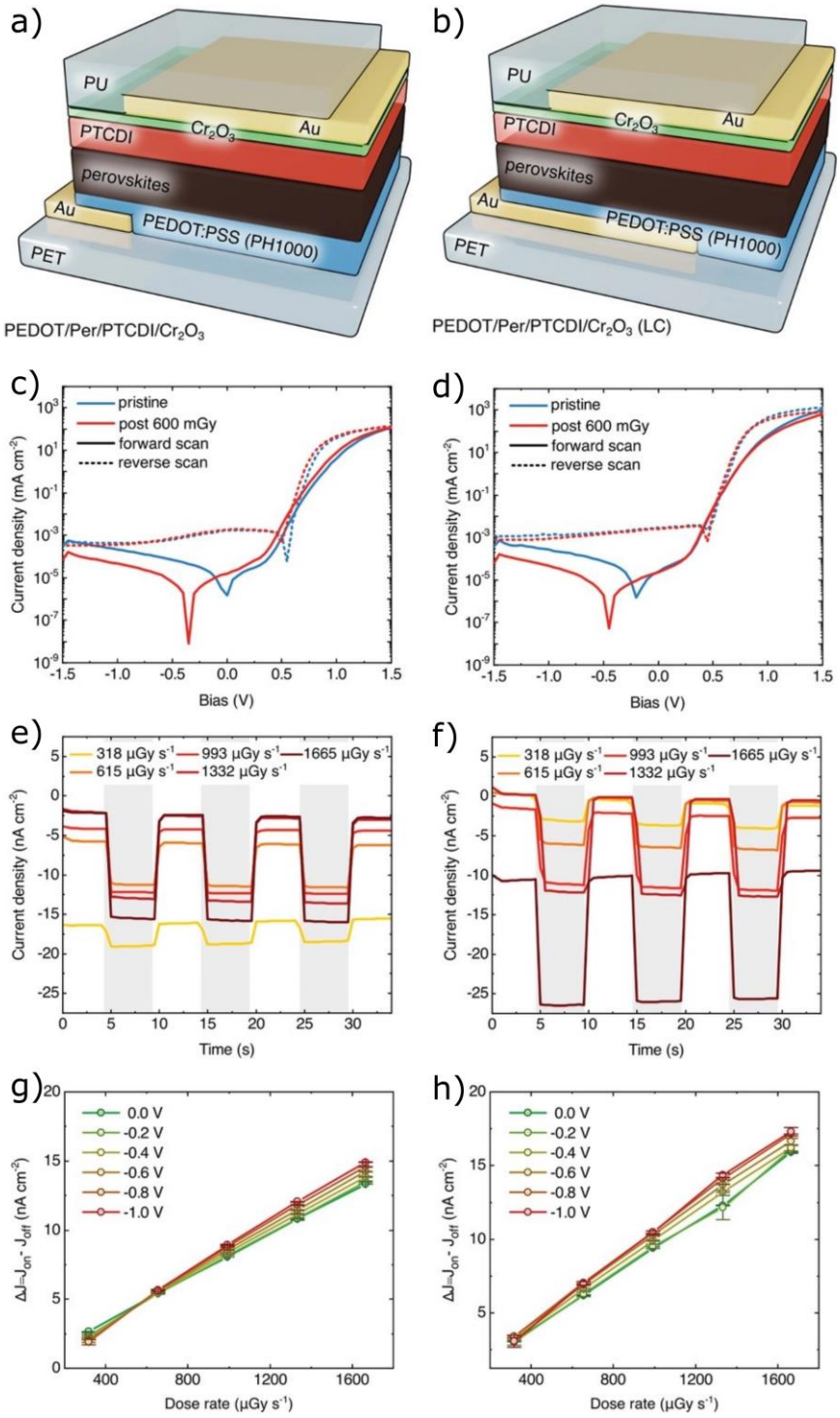

Figure 4.3: PTCDI based devices.[110] a) and b) PTCDI based X-ray photodiode structures with the different layers differentiated by the colour. The two structures differ from the dimensions of the bottom contact. c) and d) J-V characteristics of the structures above acquired in pristine condition (in blue) and after 600 mGy X-ray exposure (in red). The continuous lines are the forward scan while the dotted lines the backward scan. e) and f) Dynamic response under 40 kVp X-ray at different dose rates. g) and h) Photocurrent density as a function of dose rate for the different bias tested.

However, the current hysteresis present in J-V measurements translates into a shift in the dark current that can be observed during the dynamic response measurements. A linear increase of the photocurrent with the incident dose rate was observed with low bias dependence as in the PCBM case. The PEDOT/Per/PTCDI/Cr_2O_3 architecture results in devices with a top sensitivity of 7.9 ± 0.4 μC Gy^{-1} cm^{-2}, comparable to the best performing of the PCBM-based detectors employing TiO_x. The large Au bottom contacts in the PEDOT/Per/PTCDI/Cr_2O_3 (LC) architecture further increases charge collection efficiency, resulting in 9.3 ± 0.5 μC Gy^{-1} cm^{-2} sensitivity, the current record for thin-film (< 1 μm) perovskite X-ray detector operating in passive mode.[59] In Figure 4.4 is reported a summary of the performances of the architectures tested. All the devices were fabricated on ultra-thin PET foil placed on a PDMS covered glass used as a rigid substrate during fabrication and measurements. In the following graph, the code FS stands for free standing and refers to devices measured on a plastic frame and not on the glass support, as detailed in the section 4.1.2. The deposition of PU as mechanical protection layer was found to degrade the performances of PCBM-based detectors making impossible their use in the free-standing form. PTCDI tolerate the PU protection layer thus enabling the realization of free-standing ultraflexible detectors. Interestingly, a single structure outperforming all the others was not found.

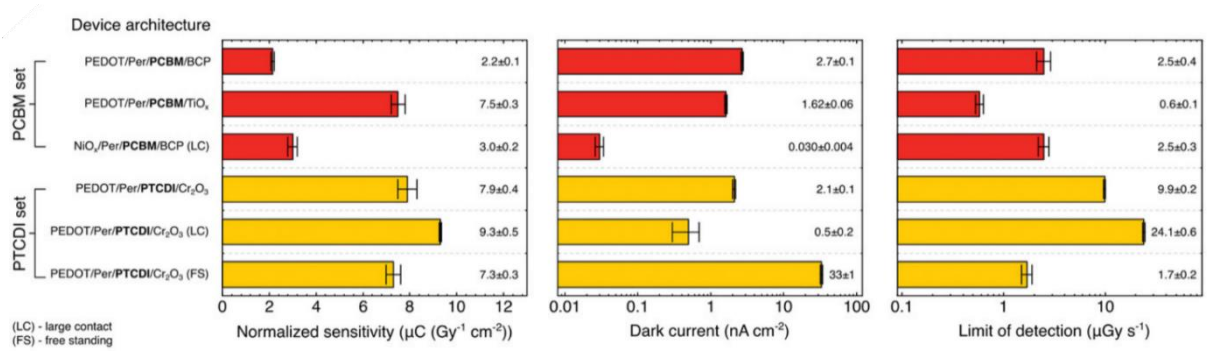

Figure 4.4: Architectures performance summary. Area sensitivity, dark current at 0 V and limit of detection of all the structures tested. In red the PCBM set and in yellow the PTCDI set.[110]

The highest sensitivity value was measured for PEDOT/Per/PTCDI/Cr_2O_3 (LC), while the NiO_x/Per/PCBM/BCP showed the lowest dark current. Finally, the best limit of detection was measured with the PEDOT/Per/PCBM/TiO_x. Depending on the specific application the proper architecture could be preferred. The free-standing PTCDI-based device showed a sensitivity compared to the glass counterpart, a LoD of 1.7 ± 0.2 μGy s^{-1} comparable to PCBM/BCP samples. The measured dark current was the highest among all the structures tested, probably because of a small degradation induced during the peal-off of the detector from the glass support.

4.1.2 Free-standing ultraflexible X-ray detector

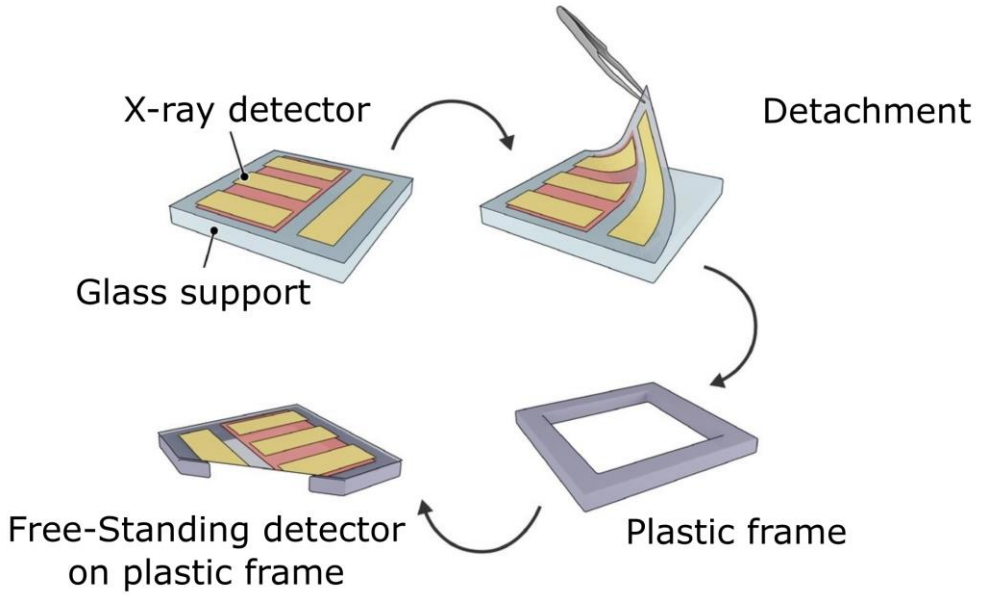

Figure 4.5: Free-standing detector. The X-ray photodiode on the glass support is carefully peeled off and placed on a plastic frame during the measurement.[110]

In this section, I report about the results obtained by free-standing (FS) ultraflexible perovskite X-ray detectors. The structure is the same as the PTCDI-based architecture in Figure 4.3a but the PET foil is carefully removed with tweezers from the PDMS

covered glass support and placed on a plastic frame as depicted in Figure 4.5. The PDMS layer ensure a good adhesion while allowing the detachment. By adjusting the PU layer thickness to 1 µm, the neutral mechanical plane calculated using the equation (4. 2) results at 1.8 µm from the bottom surface of the PET substrate, corresponding roughly to the center of the perovskite layer. As for the other devices, the X-ray response was tested under a 40 kVp beam obtaining a top sensitivity of 7.3 ± 0.3 µC Gy^{-1} cm^{-2} at 0 V, which is comparable to the value recorded for the same sample architecture on glass support, 7.9 ± 0.4 µC Gy^{-1} cm^{-2}. The exceptionally low limit of detection, down to 1.7 ± 0.2 µGy s^{-1}, makes this device appealing for medical applications where it could be placed directly on the patient's skin for dose monitoring. The comparison of dynamic response between the detector on rigid glass support and in free-standing form under X-ray irradiation is reported in Figure 4.6a Interestingly, the free-standing X-ray photodiode photocurrent amplitude does not degrade, but rather slightly increases. The enhanced photocurrent and slower time response to X-rays can be ascribed to the activation of a photoconductive gain process assisted by the defective states induced in the detector by the mechanical strain when the device is removed from the glass.

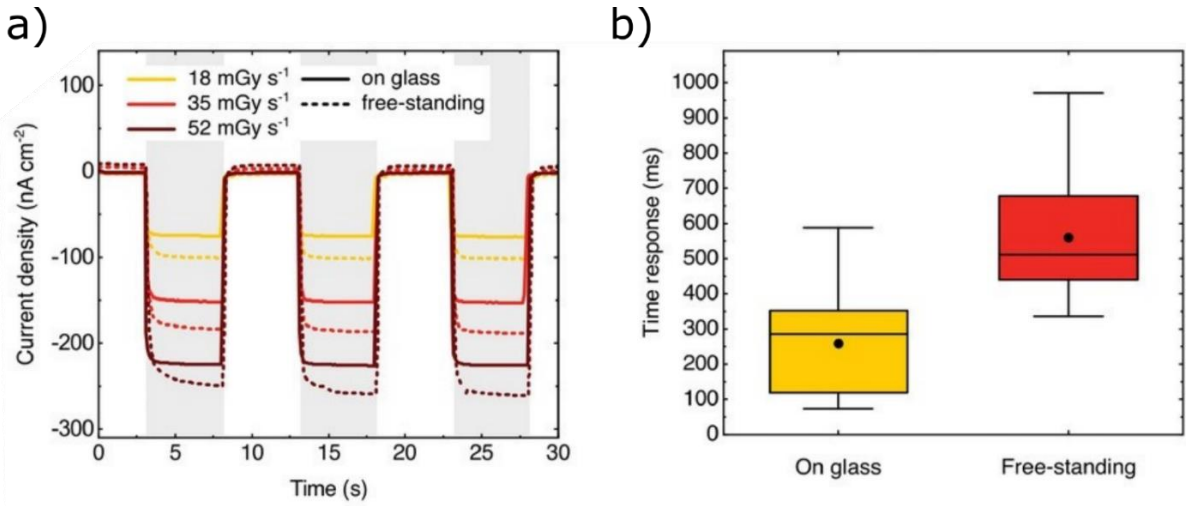

Figure 4.6: Dynamic and time response.[110] a) Comparison of the dynamic responses of a free-standing device and of a device on the glass support. b) Time repose comparison between free-standing and on glass devices.

The 1.4 µm thin and low absorbing PET substrates for ultraflexible perovskite X-ray detectors fabrication allows for the unique feature of isotropic operation, reported in Figure 4.7a, meaning that the response of the detector does not depends on the direction of the impinging radiation. In fact, due to similar X-rays attenuated fraction of PET and PU, equal to only about 0.01% difference at 15.2 keV, (i.e., the mean photon energy of the radiation emitted by the tube), the intensity of the X-rays impinging onto the device from the two sides is only slightly different. Thus, the free-standing ultrathin perovskite X-ray detectors show comparable photocurrent response to radiation impinging either on the front (PU layer side) or back (PET substrate side) of the device. The photocurrent increases linearly with the dose rate in both cases, as reported in Figure 4.7b, with slightly higher values for front side irradiation.

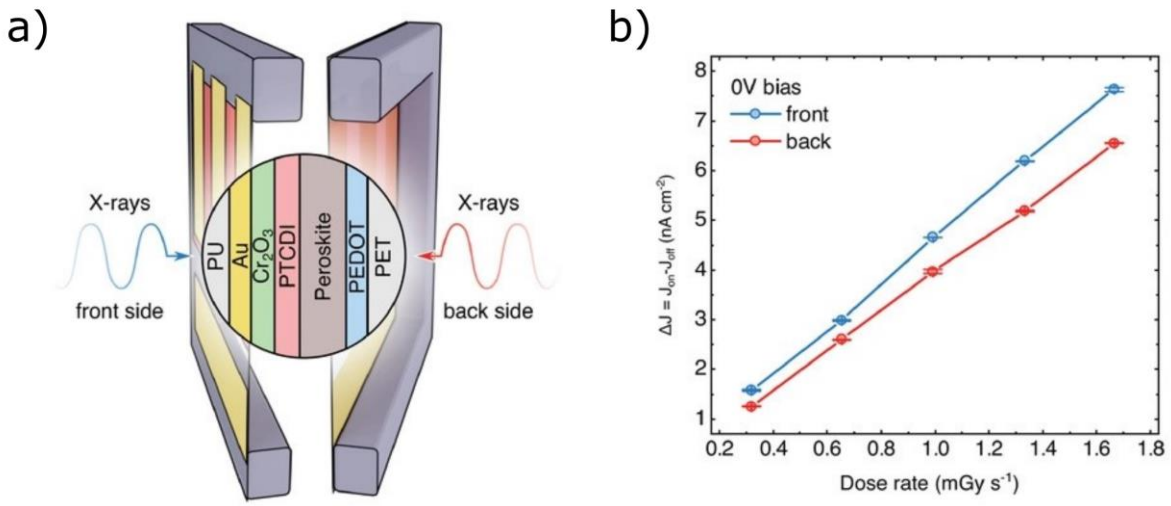

Figure 4.7: Isotropic operation.[110] a) The X-ray photodiode under the X-ray beam with two different orientations. In the front orientation the X-ray are coming from the PU side, while in the back configuration the X-ray photons are coming from the PET substrate.

Isotropic X-ray detectors could be interesting in applications where the direction of the incoming radiation is not known, thus allowing for reliable, real-time detection of ionizing radiation without the need to align or orient the device. This feature is quite unique among ionizing radiation detectors, indeed, silicon X-ray photodiodes have a

thickness > 200 µm and the charge is generated in the depletion region only if coming from one side of the detector.

4.1.3 A new concept: Rolled X-ray detector

I further pushed the ultraflexibility and isotropic response capabilities of these photodiodes by developing a rolled X-ray detector, scheme reported in Figure 4.8. To realize it I have designed ad made a rolling machine reported in section 3.1.7.

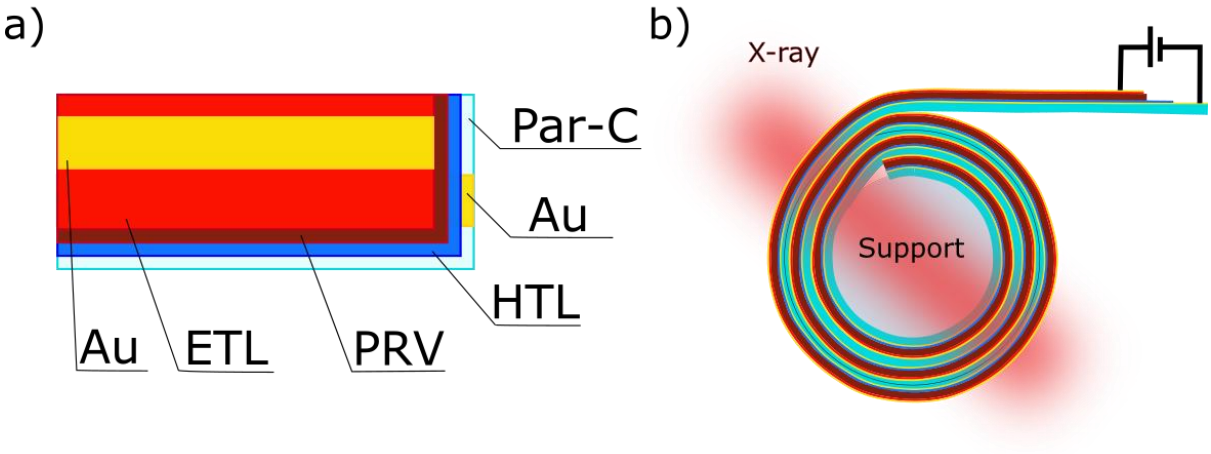

Figure 4.8: Rolled X-ray detector. a) Layered structure of the photodiode fabricated on 2 µm thick parylene C substrate. b) Cross-section the rolled detector.

The idea is to have a thin multilayer device over a smaller area, able to increase the absorption fraction and the sensitivity of the final dosimeter. The fabrication steps are similar to the ones described for the photodiodes reported above with the exception of the substrate. Here 2 µm thick parylene-C has been used simplifying the substrate preparation procedure and increasing the device yield. The parylene was deposited by CVD as described in section 3.1.4 on a silane treated glass to decrease the adhesion. The photodiode is then rolled around a straight and round shaped substrate, LP655 epoxy resin is used to encapsulate the rolled X-ray detectors. A picture of the final device with copper wires for measurements is reported in Figure 4.9a. The advantage

of the rolled photodiode is the increased absorption due to the overlay of the device during rolling while keeping the charge collection the same. In fact, X-rays cross several 500 nm thick perovskite layers, whose number depends on how many times the device is rolled around the substrate, but the distance the photo-charges generated inside the perovskite layer have to travel is always equal to the electrode distance in the flat configuration. For this experiment the active area was designed to be long and narrow with dimensions 14.70 x 0.81 mm^2. By rolling the device, the other effect is of area compression: once rolled, the pixel area decreases down to 0.91 mm^2. The diameter of the support used was 1.14 mm leading to 4-fold rolling. The J-V of the rolled device acquired before and after the X-ray measurement are reported in Figure 4.9b. The J-V shows a nice and flat dark current in pristine condition with very good rectification factor and low hysteresis. The good shape of the J-V curve indicates that the rolling procedure does not damage the perovskite layer or the device.

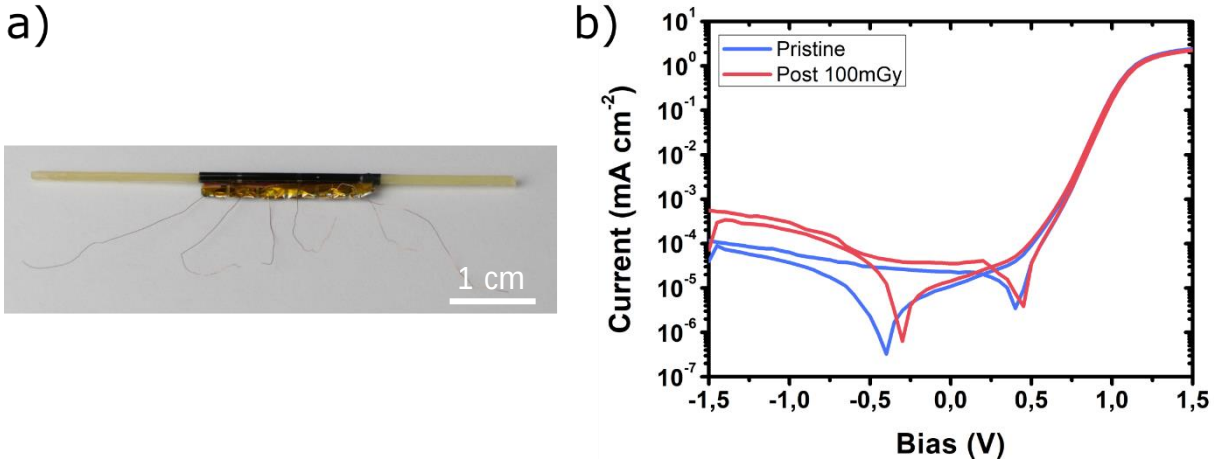

Figure 4.9: Rolled device . a) Picture of a rolled X-ray detector. b) J-V characteristic of a rolled device measured in pristine condition and after a total received dose of 100 mGy.

The device response to X-rays was tested under a modulated 40 kVp beam, the dynamic response in Figure 4.10a shows a box-like and reproducible response with 0 V bias. A linear behaviour of the photocurrent with the dose rate was found and from the slope a top sensitivity value of 26 ± 4 µC Gy-1 cm-2 was extracted. This value is more than

3 time the highest sensitivity value measured for PTCDI-based photodiode in the previous section.

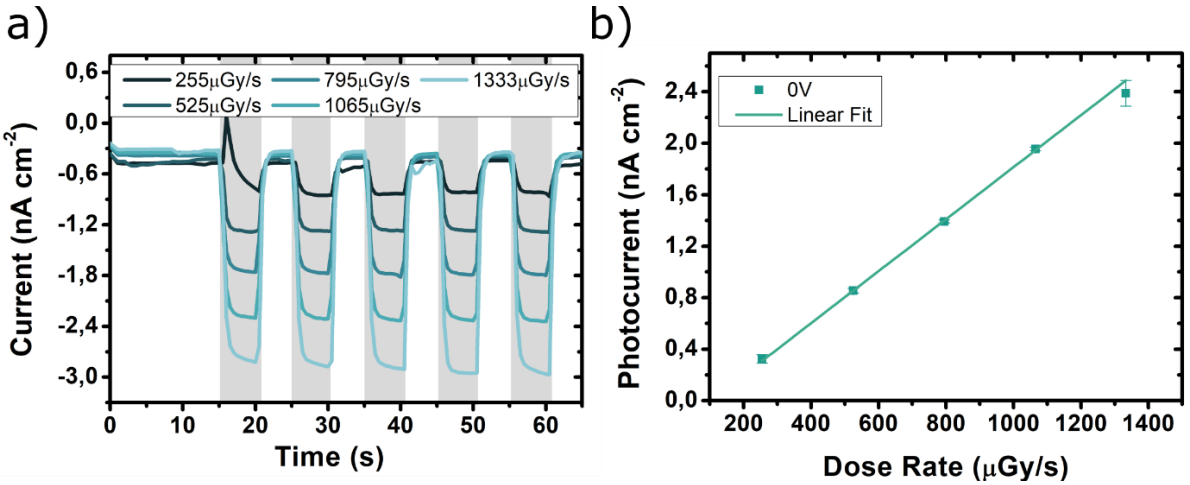

Figure 4.10: X-ray response of rolled photodiodes. a) Dynamic response of a rolled device with 0 V bias under 40 kVp X-ray beam at different dose rates with modulation period of 10 s and 50% duty cycle. b) Photocurrent as a function of the incident dose rates and linear fit for sensitivity extraction.

4.2 Role of PCBM in perovskite X-ray photoconductors

Photoconductors with $MAPbI_3$ (often called MAPI) nanocrystals as active layer have been proved to be very efficient light and ionizing radiation detectors.[93,120] Venugopalan et al. demonstrated the beneficial effect of PCBM addition over the printed MAPI layer increasing the performance of a visible detector. Ciavatti et al. used very similar device geometry with increased layer thickness (5 – 10 μm) demonstrating very high X-ray sensitivity in photoconductors containing PCBM. In this thesis, I tested similar

$MAPbI_3$ samples with or without PCBM under X-ray and studied the effect of the polymer at the perovskite interface.

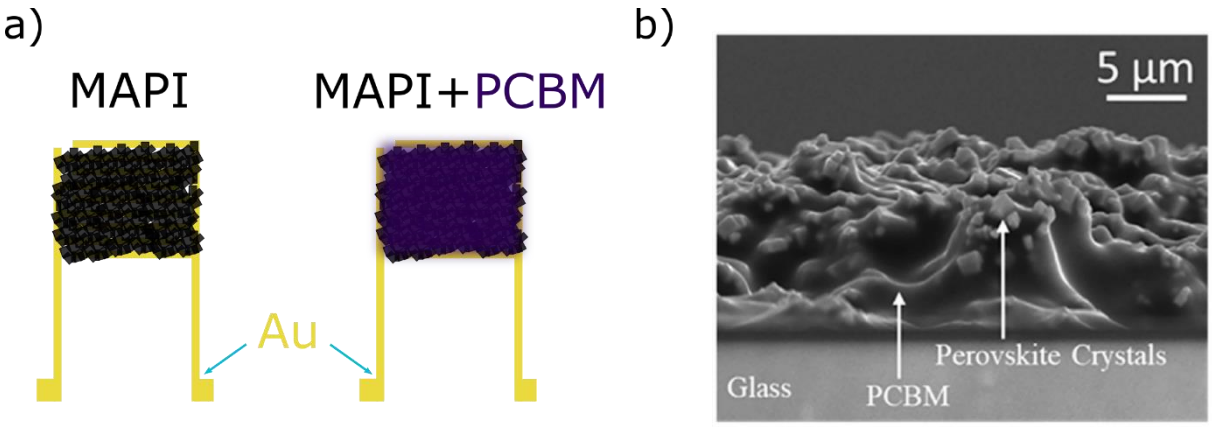

Figure 4.11: Sample structure. a) On the left, interdigitated Au metal contact with only MAPbI3 nanocrystals deposited on top and on the right the same device structure with the addition of PCBM on the perovskite layer. b) SEM image of the MAPI+PCBM sample showing the perovskite nanocrystals covered by PCBM.[120]

The samples were fabricated following the procedure reported in the literature.[120] The interdigitated electrodes were fabricated by using photolithography as described in section 3.1.5, followed by thermal evaporation of Cr (2 nm) and Au (30 nm). The perovskite ink was obtained using a cyclic approach. A commercial powder of PbI_2 is slowly added to a MAI solution in isopropanol (IPA) under stirring at 80 °C. After the addition, perovskite nanocrystals form and they are separated by sedimentation. Perovskite crystals are then washed with IPA. To restart the cycle water is added; the water molecules destroy the perovskite material by dissolving MA^+ and I^- ions in solution. What remains are thin sheets of poorly water-soluble PbI_2. The PbI_2 sheets can be used to restart the cycle adding them to MAI solution in IPA. The PbI_2 nanocrystals obtained are smaller in size than the precursor used at the beginning of the process. By using the smaller size precursors, the dimension of the $MAPbI_3$ can be reduced. The ink was then deposited by bar-coating in air. The deposition velocity was set to 30 mm s^{-1} with a bar of 10 µm in diameter. Multiple deposition steps are performed to reach the desired thickness, in this case ~ 5 µm. In the case of sample

with PCBM, the PCBM layer was deposited by drop-casting a solution in chlorobenzene (orthogonal solvent for perovskites) on top of the perovskite layer at 80 °C. The schemes of the two types of tested devices are reported in Figure 4.11a. In Figure 4.11b a SEM image of the device containing PCBM shows the organic semiconductor permeated through the perovskite layer.

The performances of the two configurations as X-ray detector are compared in Figure 4.12. Both showed fast and box-like response under 40 kVp X-ray beam and a bias dependence of the photocurrent signal. The sample containing PCBM presented higher photocurrent at all bias tested and a higher dark current at 2 V. The photocurrent has a linear behaviour with the increasing dose rate allowing the sensitivity extraction with a linear fit.

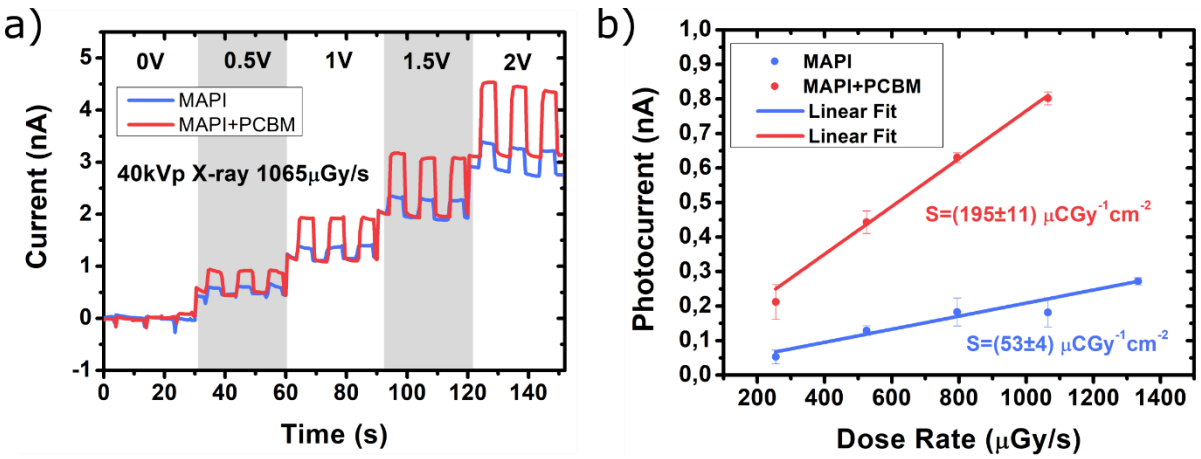

Figure 4.12: X-ray response. a) Comparison of dynamic response under 40 kVp X-ray beam modulated with 10 s period and 50% duty cycle. The applied bias was changed every three recorded photocurrent peaks. b) Extracted photocurrent at 1 V as a function of the dose rate for MAPI and MAPI+PCBM sample with the corresponding linear fit for the sensitivity estimation.

A sensitivity of 195 ± 11 μC Gy^{-1} cm^{-2} was extracted from the slope of the line for the MAPI+PCBM sample, almost 4 times the sensitivity of only MAPI photodetector. The experiment confirms the performance boost when PCBM is added to $MAPbI_3$ in photoconductor geometry.

4.2.1 X-ray nanoanalysis to study charge transport in perovskite X-ray detectors

To unravel the microscopic mechanism ruling the PCBM-enhanced performance, with particular attention to the role of PCBM at the perovskite grain interface, I performed simultaneous mapping of X-ray fluorescence (XRF) and X-ray Beam Induced Current (XBIC) signals on MAPI and MAPI+PCBM samples at the ID16B beamline of the European Synchrotron Radiation Facility. The experimental setup used is described in detail in section 3.3.1. Briefly, the storage ring provides the beamline with an intense 17.5 keV X-ray pink beam focused down to a spot diameter of 50 nm. The sample is mounted on a piezoelectric x-y stage allowing very precise movement. Two silicon drift detectors are positioned next to the sample to acquire the emitted fluorescence signal, a scheme of the setup is reported in Figure 4.13a.

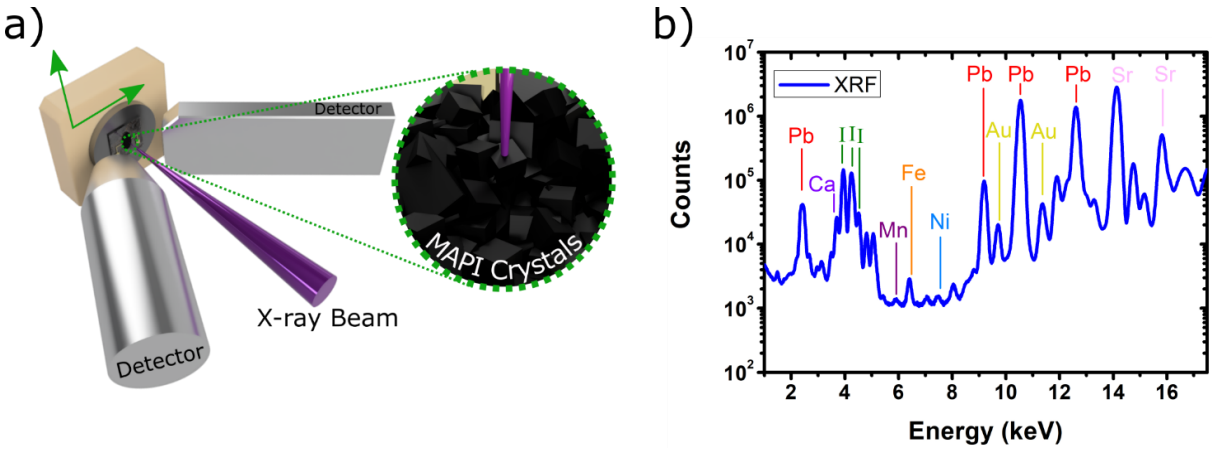

Figure 4.13: ID16B beamline setup. a) Scheme of the setup at the beamline. The sample is mounted on a piezoelectric stage allowing precise movement in the x-y plane. The X-ray beam is focus on a 50 nm diameter spot permit to probe the $MAPbI_3$ crystals. b) XRF fluorescence spectrum from the studied sample.

The nano-sized beam spot allowed to study the perovskite layer at the nanoscale with a probe much smaller than the average crystal size, thus clearly distinguishing the effect of grain boundaries. In Figure 4.13b is reported a typical X-ray fluorescence spectrum acquired from the tested samples. Using pyMCA software was possible to fit the XRF spectra and assign to the peaks the corresponding element. Combining the peak intensity with the elemental distribution maps reported in Figure 4.14 is possible to understand which element in the spectra is an impurity of the sample or it is present only in the substrate. The high energy beam used was able to excite the core electrons in the L shell of Pb and I present in the perovskite layer. Therefore, the Pb distribution defines the spatial region where there are perovskite grains. The Au fluorescence signal comes from the interdigitated metal contacts underneath the perovskite. The other elements found in the spectra are impurities in the perovskite layer or elements present in the glass substrates. In Figure 4.14b is reported the uniform distribution of Ca over the scanned area indicating its presence in both the glass and perovskite. Fe, Ni and Mn are impurities in the perovskite layer since their spatial distribution is similar to the Pb distribution in the same area, Figure 4.14a. The fluorescence map of Sr instead is the negative image of the Pb distribution, therefore suggesting its presence only in the glass substrate. The Strontium lines are located at higher energy in the spectra than the Pb ones, thus when emitted by the substrate they are absorbed by the perovskite. is clearly different as clear from the map in Figure 4.15e. The degradation can be ascribed to the heat and ionization induced by the strong X-ray absorption in the perovskite microcrystals.[43,121,122] By decreasing the accumulation time to 200 ms and the X-ray flux down to 8.4 x 10^{10} s^{-1}, the degradation is effectively contained. No degradation is observed after one scan and only a very slight modification of the Pb distribution is visible after 8 scans, see Figure 4.15b, d and f. All the data presented in the following were acquired under these last experimental conditions. To limit the degradation further, we did not scan the same region twice.

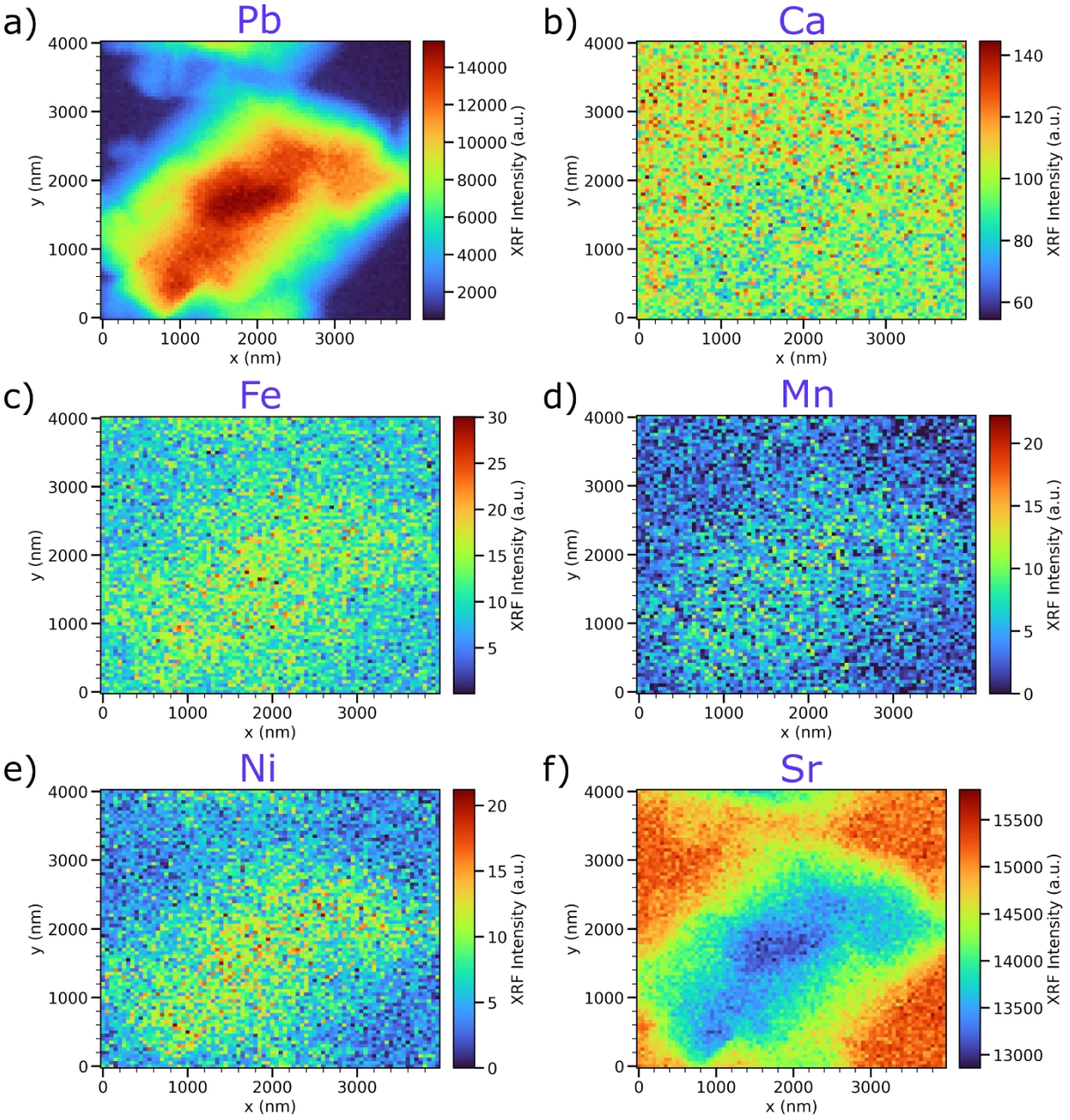

Figure 4.14: Impurities. a) XRF signal attributed to Pb where it is visible the perovskite grains. b) Uniform signal from Ca contained in both the substrate and the sample. c) Fe fluorescence signal present as impurity mainly in the perovskite. d) Very low signal from Mn contained in the perovskite. e) Ni impurities signal. f) Strong Sr signal with the opposite distribution of the Pb signal thus coming only form the glass substrate.

Perovskites are known to degrade under intense ionizing radiation like electrons and focused X-rays beams.[106] The stability of the devices under synchrotron beam was tested by acquiring 8 consecutive fluorescence maps of the same region without bias

applied. When acquiring the maps with 500 ms accumulation time and a flux equal to 10^{12} s^{-1}, a modification of the Pb distribution is already visible after one scan, Figure 4.15c. After 8 scans the shape of the grains

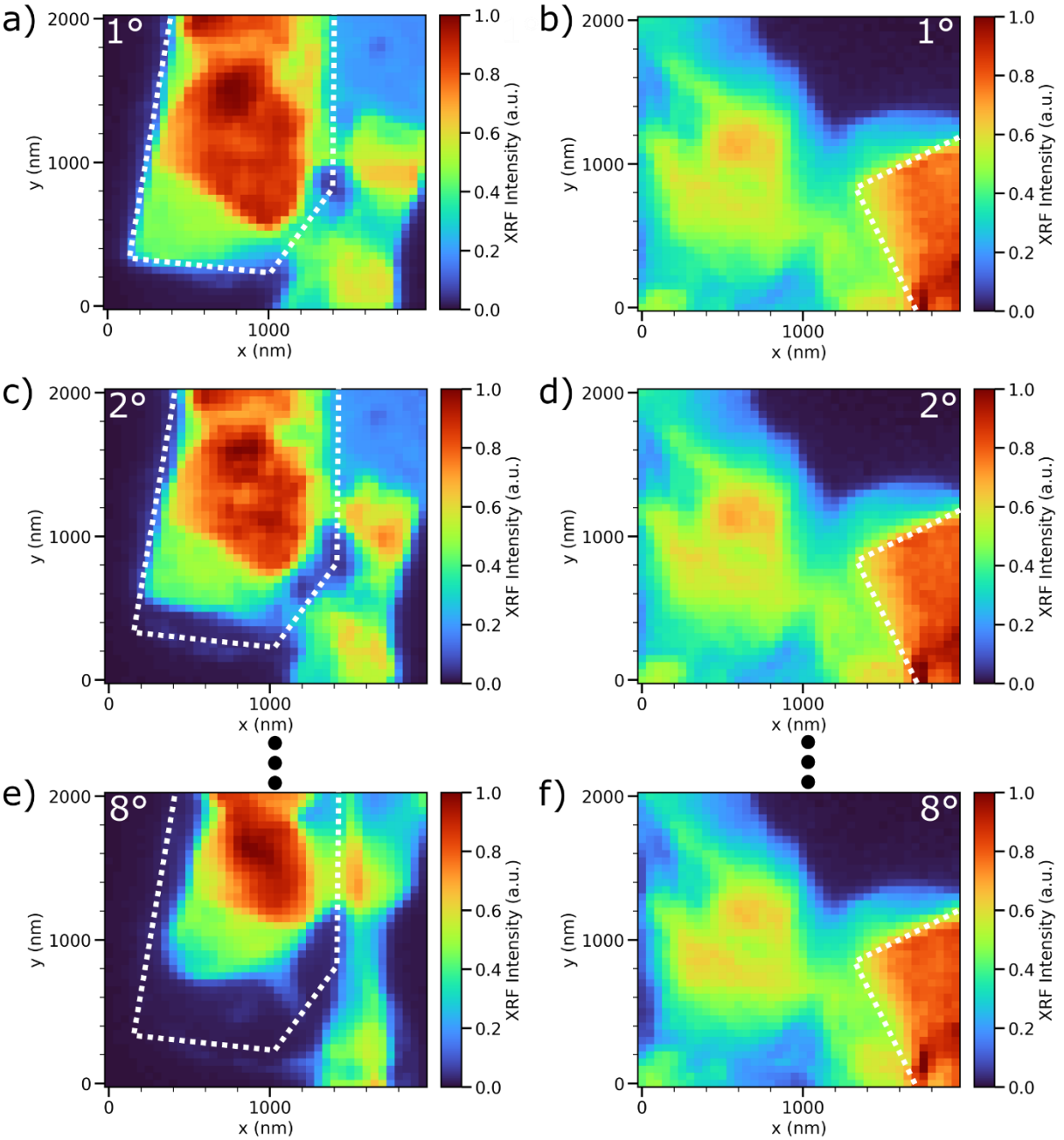

Figure 4.15: Perovskite degradation under intense X-ray beam. a), c) and e) From top to bottom, consecutive Pb fluorescence maps of the same region, acquired with 500 ms accumulation time and 10^{12} s^{-1} photon flux, showing a change already in the second scan. The with dashed line shows the initial perovskite grain dimensions. b), d) and f) Consecutive Pb fluorescence maps acquired with 200 ms accumulation time and a flux of 8.4 x 10^{10} s^{-1}. The reduced flux and accumulation time effectively reduce the material degradation.

The simultaneous acquisition of XRF and XBIC signals, described in section 3.3.1, at the nanoscale allows to correlate the elemental distribution and the morphology with the charge transport and collection properties. Figure 4.16a and b show the Pb distribution obtained by XRF analyses and the XBIC map for the same region for a MAPI sample.

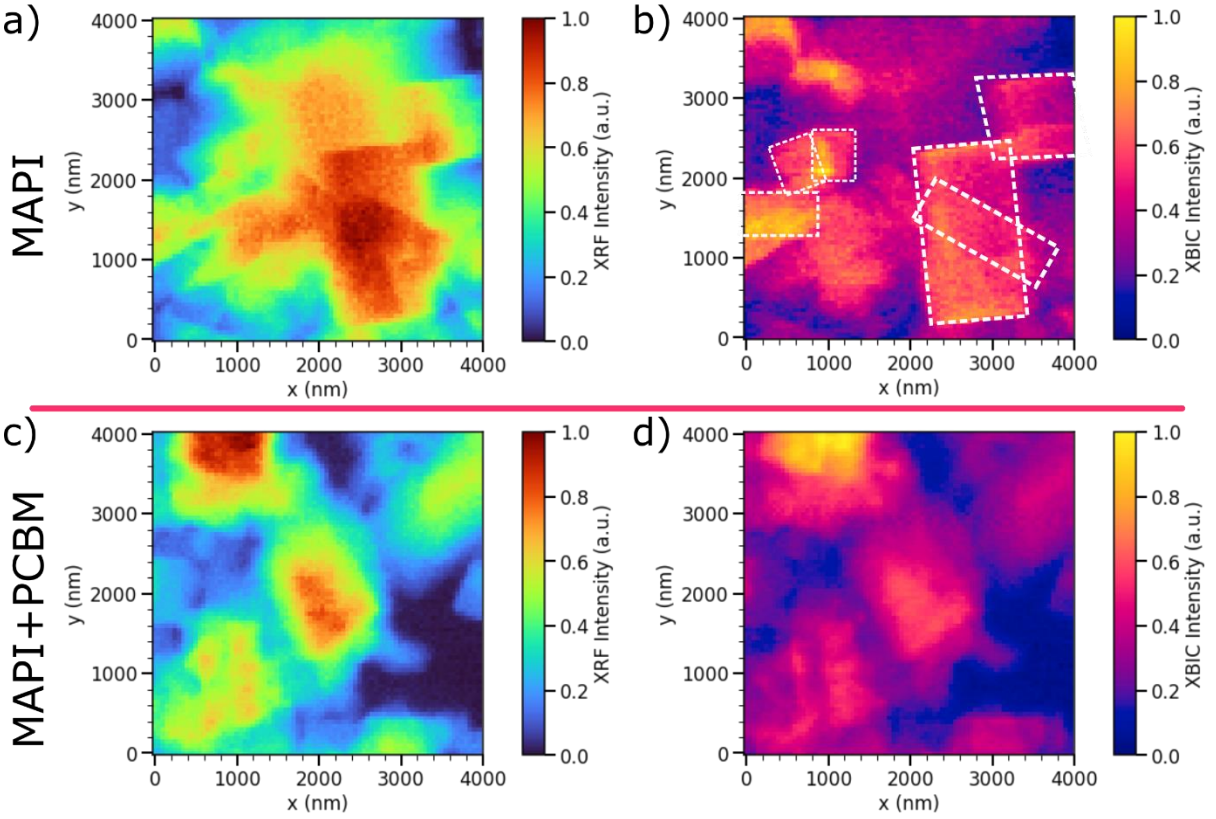

Figure 4.16: XRF and XBIC maps. a) 4 x 4 μm^2 Pb fluorescence map of a MAPI sample where the crystal grains are clearly distinguishable. b) XBIC signal coming from the same region as in (a), the perovskite grains are highlighted by white dashed lines. c), d) Pb XRF signal form a MAPI+PCBM sample and corresponding XBIC signal.

The perovskite grains are well distinguishable in the XRF map. The higher the XRF signal the higher is the perovskite layer thickness in that point. The thickness determines the charge generated inside the device, hence one should expect a direct correlation between the XRF intensity and the XBIC intensity. However, in the case for MAPI samples, the XBIC map (Figure 4.16b) shows a strong photocurrent signal at the grain boundaries and a low signal coming out from the center region of the

grains. The discrepancy between XRF and XBIC maps suggests a different charge collection mechanism at the grain boundaries. On the other hand, in MAPI+PCBM samples, the XBIC signal is clearly correlated to the XRF one and very uniform all over the single grains as in Figure 4.16d. This effect is more evident when overlapping the XRF and XBIC signals of the same region as described in the method section 3.3.1.

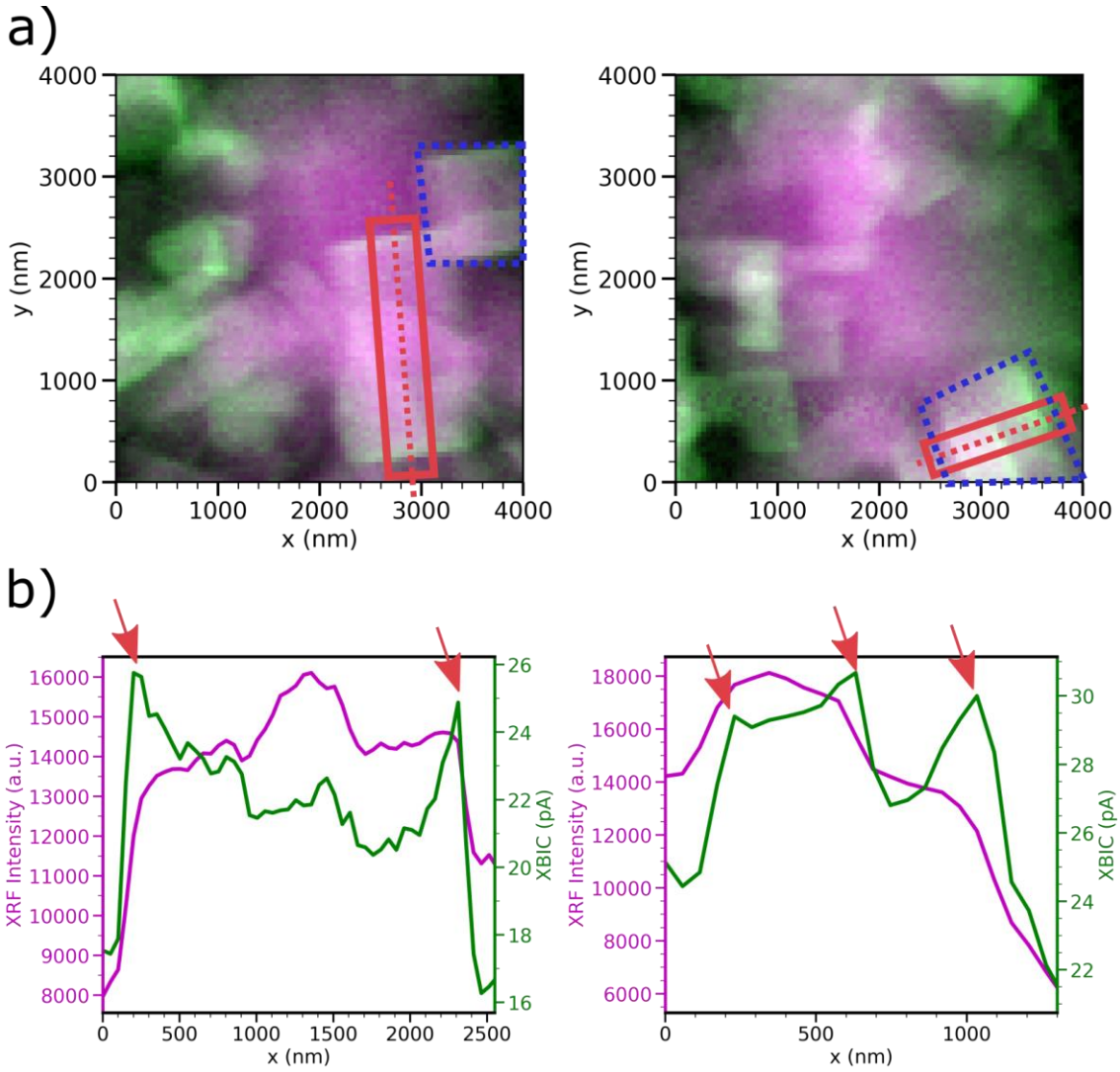

Figure 4.17: MAPI map profiling. a) XRF (purple) and XBIC (green) overlapped signals of two different MAPI sample regions. The dotted red line indicates the direction of the extracted line profile and the red rectangle represent the area over which the signal is averaged. In blue are highlighted two cubic perovskite grains where the edges clearly emerging from the images. b) XRF (purple) and XBIC (green) line profiles. The red arrows indicated the grain boundaries positions.

Overlayered images are reported for MAPI in Figure 4.17 and for MAPI+PCBM in Figure 4.18, respectively. The colour purple was assigned to the Pb XRF signal and green to the XBIC one. As a result, purple regions correspond to a dominant XRF signal, green regions to prevailing XBIC, and gray/white ones indicate where the two maps are correlated with the same signal intensity in the relative scale used. In MAPI regions, strong contrast between grain boundaries and the center of the grains is visible. In the center of the crystals, the colour purple is dominant while in the grain boundaries green prevails. Instead, the overlaid maps of MAPI+PCBM samples appear more uniform with low contrast at the grain boundaries. Figure 4.17a shows, in two different regions, two cubic crystal grains with the edge highlighted in green that gives a sort of 3-dimensional look at the crystals. Line profiles across entire grains from the overlaid maps of both MAPI and MAPI+PCBM were extracted and reported below the respective map in Figure 4.17b for MAPI samples and in Figure 4.18b for MAPI+PCBM samples. The line profile direction is represented by a red dotted line and a red rectangle indicates the area over which the signal is averaged. The line profile plots of MAPI samples further underline the difference between uncorrelated XRF and XBIC signals. The fluorescence profiles follow the nanocrystal morphology (i.e. central peak with smooth border at the edges); the current profiles, on the contrary, exhibit pronounced peaks at the border, corresponding to grain boundaries. In the middle graph of Figure 4.17b, three peaks appear in correspondence to the three edges of the cubic grain. In the MAPI+PCBM case as expected the line profiles are much more correlated with higher XRF and XBIC signal at the center of the grains and lower signal at the grain boundaries. For a quantitative comparison of the X-ray induced current, I calculated the induced photocurrent density values inside the perovskite grains in different regions of the two types of samples. The photocurrent density for each grain was calculated by integrating the XBIC values over the grain region

delimitated by the grain boundaries visible from the XRF spectrum. The current value is then normalized by the corresponding area.

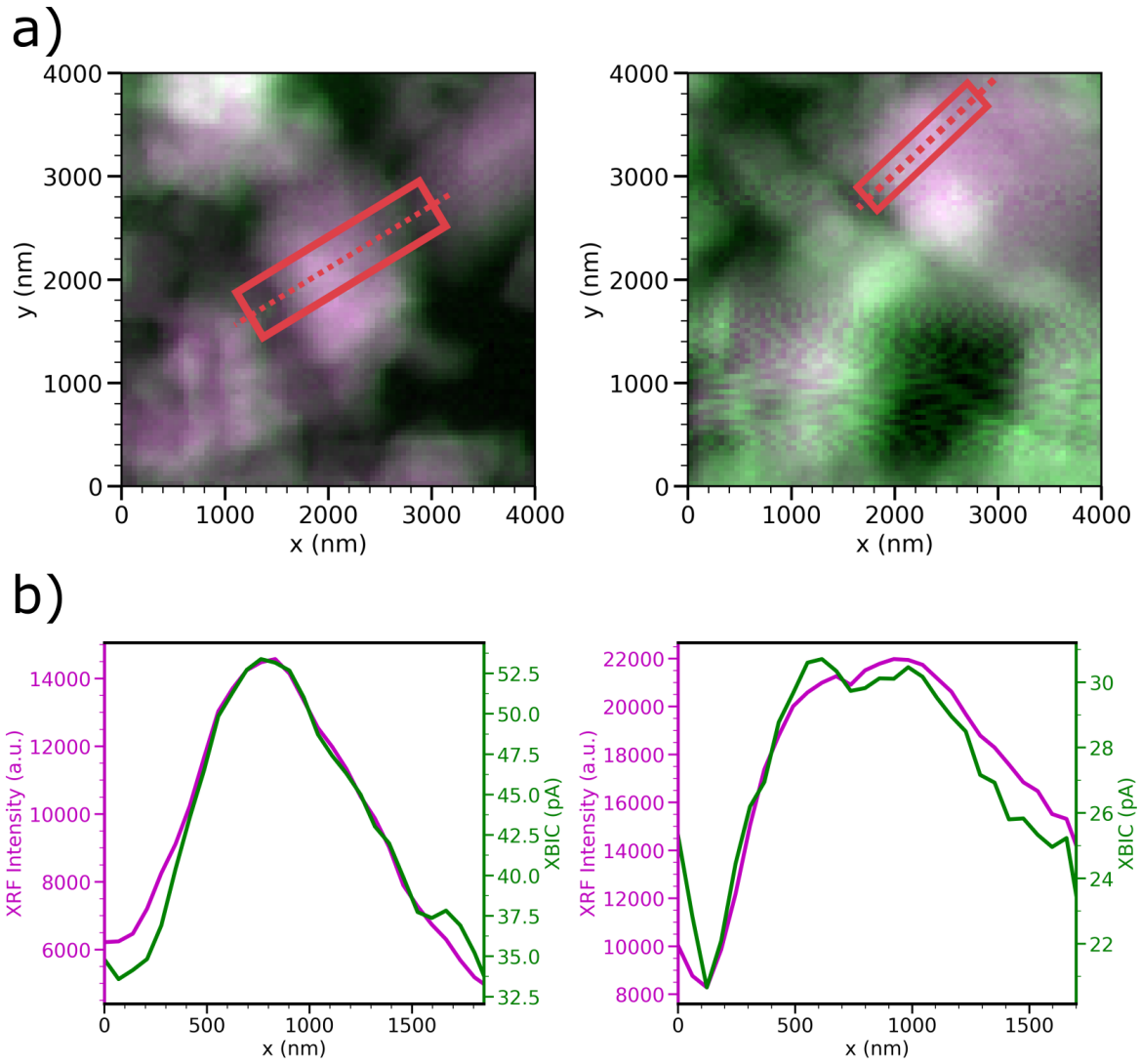

Figure 4.18: MAPI+PCBM map profiling. a) XRF (purple) and XBIC (green) overlapped signals of two different MAPI sample regions. The dotted red line indicates the direction of the extracted line profile and the red rectangle represent the area over which the signal is averaged. In blue are highlighted two cubic perovskite grains where the edges clearly emerging from the images. b) XRF (purple) and XBIC (green) line profiles. The red arrows indicated the grain boundaries positions.

The current density values were extracted from several perovskite grains and the results are reported in a box plot in Figure 4.19a. Despite the spikes at the grain boundaries of MAPI samples visible in the maps, the analysis confirms, as for the macroscopic

case, that the photocurrent density inside the grains of MAPI+PCBM samples is always higher than for MAPI. The average current density value for MAPI+PCBM samples is 15 ± 4 pA nm^{-2} almost twice the one of MAPI, equal to 8.1 ± 1.4 pA nm^{-2}. To give a quantitative estimation of the correlation between maps of different physical signals (i.e. XRF and XBIC) a correlation coefficient (Φ) was calculated by:

$$\Phi = 1 - \left(\frac{\sum_{i=0}^{N} |XRF_i - XBIC_i|}{N_{points}} \right)$$

Where XRF_i and $XBIC_i$ are the normalized fluorescence and current signals of the i^{th} point in the line profiles. The XRF and XBIC signals were normalized by mapping the acquired signals between 0 and 1. N is the total number of points in the profile. This coefficient is higher if the correlation between the line profile of the XBIC and XRF signals in the same perovskite grain is higher: its value is 1 for perfect overlapping and tends to 0 as the two signals diverge.

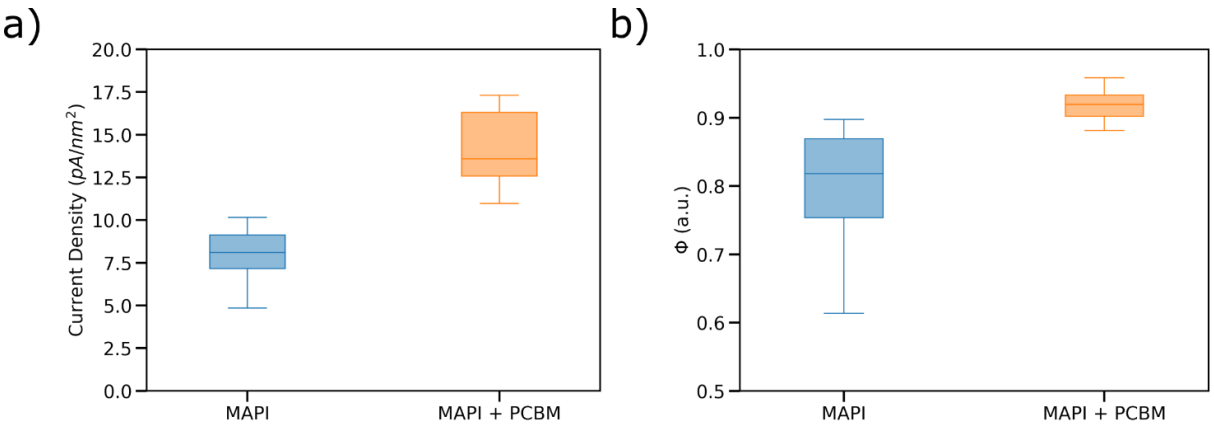

Figure 4.19: Statistical analysis. a) Current density for MAPI (blue) and MAPI+PCBM (orange) grains. b) Box plot of the correlation coefficient for MAPI (blue) and MAPI+PCBM (orange).

The correlation coefficients for the two cases are reported in Figure 4.19b. The correlation coefficient of MAPI+PCBM is equal to 0.92 ± 0.02 with small standard deviation. While the MAPI coefficient is 0.79 ± 0.09, with a larger deviation due to scattered values. The difference in the correlation coefficient and higher current density

prove that PCBM improves charge collection in perovskite films, allowing an efficient collection of charges from the entire volume of the active layer. The higher current and higher correlation, can be ascribed to an electron sink effect caused by PCBM. The high responsivity of MAPI perovskite nanocrystalline films photodetector has been ascribed to high photoconductive gain effect, above 200, for UV-VIS photons[120] and it has been suggested also for X-rays.[93] When the X-ray beam impinges on a region where there is a high trap concentration (typically grain boundaries) the generated charge carriers are trapped nearby the generation site before reaching the collection electrode. If the traps for minority (electrons in MAPI) carriers have a detrapping time that is higher than the time needed for the majority carriers to reach the electrode, majority carriers are injected from the electrode to maintain the charge balance, as visually illustrated in Figure 4.20a. That is the gain effect also present and well described for X-ray detector based on organic thin-film.[21,123] Therefore the XBIC is higher at the grain boundaries because when, during the scan, X-rays impinges on them a higher number of electrons are trapped with respect to the beam impinging on the grain center. A higher number of minority carrier trapped translates to higher gain, thus higher current. When PCBM is added on top of the perovskite it permeates through the film and passivates the carrier traps. Moreover, PCBM behaves as an electron acceptor creating a sink for electrons that are generated inside the perovskite and are transported towards the electrode through the PCBM layer, Figure 4.20b. Assuming the same X-ray absorption and e-h pairs generation rate in MAPI and MAPI+PCBM samples, the higher current in MAPI+PCBM films demonstrates a higher gain generated by the organic molecule. Differently on what happens in the MAPI samples, in MAPI+PCBM samples the gain is generated due to a difference in the transit time of electrons and holes to reach the electrodes. The PCBM layer is in contact with the electrodes thus generating an electric field in the organic layer. When the X-rays generates e-h pairs, electrons are transferred to the PCBM layer and transported

toward the electrodes. The electron mobility in PCBM is around 10^{-3} cm^2 V^{-1} s^{-1}.[124] Instead, the hole mobility in MAPI is as high as 100 cm^2, V^{-1} s^{-1}.[125] The high difference in mobility creates a charge unbalanced equilibrium since the holes reach the electrode much faster than the electros traveling through the PCBM. To keep the charge balance, more holes are injected in the perovskite layer increasing the current signal. Moreover, PCBM passivated traps at the interface and subtract electrons for possible recombination improving the overall performance. The more spatially uniform gain effect created by the sink effect of PCBM allows the fabrication of more sensitive X-ray detectors.

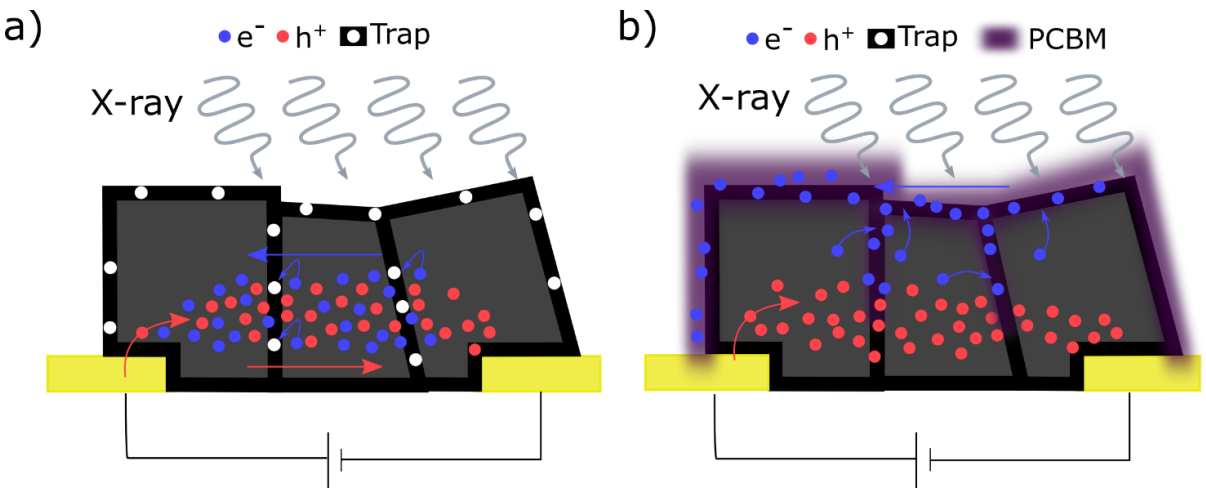

Figure 4.20: X-ray detection process. a) Sketch of the interpretation for charge collection in MAPI sample. The with circles represent the traps in the grain boundaries. Electrons get trapped and activate the gain effect injecting more holes in the device. b) In MAPI+PCBM samples the traps are passivated by the PCBM (purple) and the electrons are injected in the PCBM located around the grain boundaries. The difference in charge transport between the PCBM and perovskite layer generates an instantaneous unbalanced charge that generates a gain effect.

4.2.2 Au migration

In literature is known that the halide component of perovskites can migrate to the electrodes, driven by an electric field, and react causing device degradation.[126,127] As shown before, the presence of PCBM improves the performances of perovskite X-ray

photoconductors, but I also found it causes faster degradation of the Au interdigitated metal contacts underneath the perovskite layer. The Au fluorescence maps were measured in different regions for MAPI and MAPI+PCBM samples. 10 regions for both samples were selected and scanned to acquire the gold distribution in pristine condition, then the bias was switched on and the same areas were scanned twice. Consequently, the first regions scanned were the regions where the bias stress acted for a lower time. The last region instead is the one with the highest bias stress, i.e. the bias has been on for longer time. For MAPI samples with 1 V bias applied there is no sign of degradation even after 4 h and 25 min with identical Au distributions as visible in Figure 4.21. When the bias is increased to 4 V, the contact in the region scanned after 2 h and 27 min with the bias on shows a small change in the distribution at the contact edge, Figure 4.22d. After 3 h and 49 min the gold distribution looks pretty different than the pristine condition. The last region scanned for the second time after 5 h and 48 min with the bias at 4V applied shows a big change in the Au distribution. The small gold islands present in the pristine map agglomerate all in one wire-like gold mass. The MAPI+PCBM sample showed a gold migration only after 3 h and 40 min with 1 V bias stress. Form the Figure 4.23f is visible a migration of gold nanoparticles inside the channel covered by the perovskite with consequent destruction of the interdigitated finger. When a bias of 4 V is applied to a MAPI+PCBM sample the metal contacts degrade immediately with a completely different Au distribution after 2 h and 42 min, Figure 4.24f. Interestingly, in the MAPI case, the degradation of gold consists in an agglomeration of the Au particles in the finger of the interdigitated metal contact. While in the PCBM case, the Au particles migrate from the contact inside the channel covered by the perovskite and PCBM film.

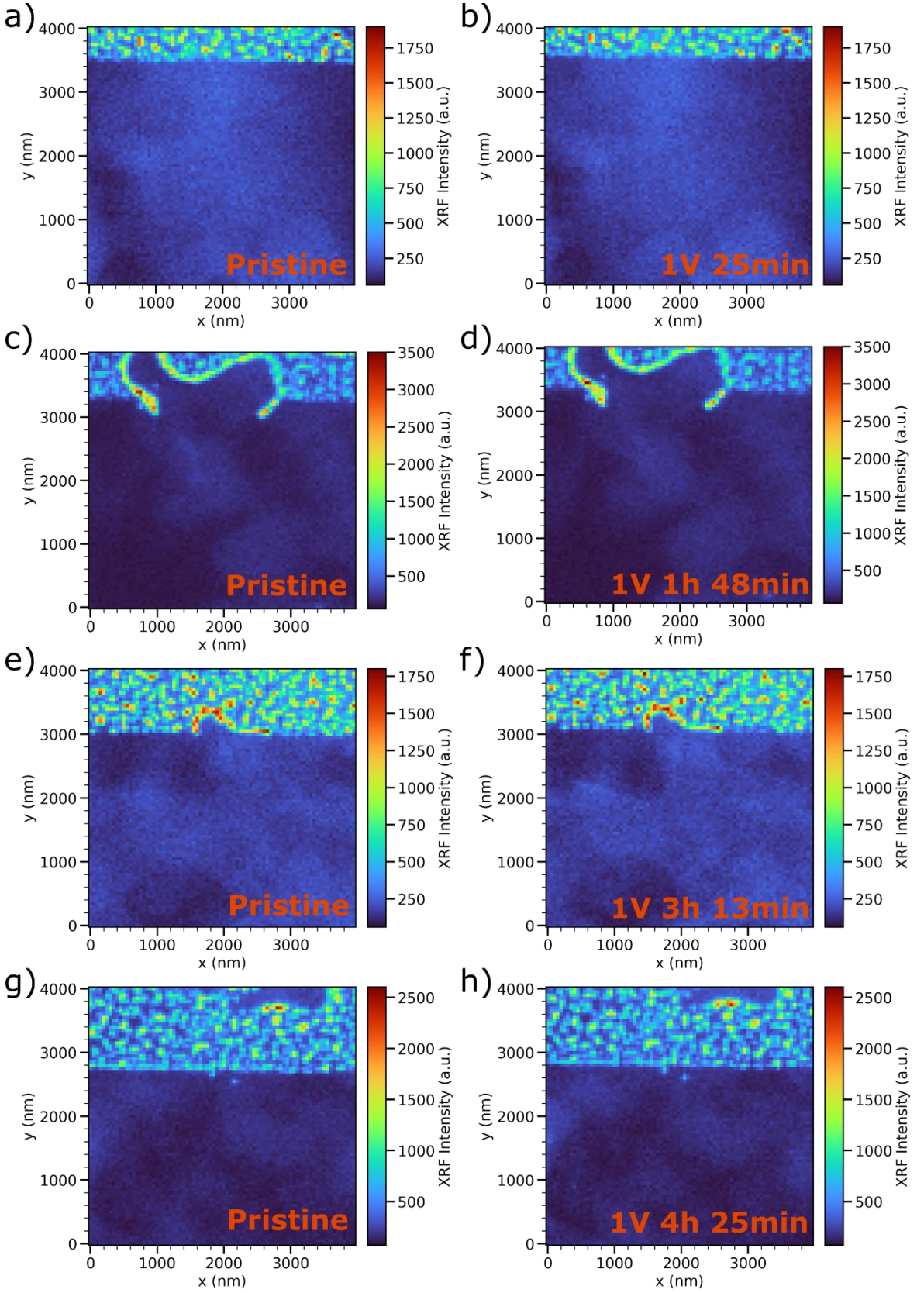

Figure 4.21: Au migration MAPI sample at 1V. a), c), e) and g) Au distribution in pristine condition. b), d), f) and h) Au distribution after 1 V bias stress.

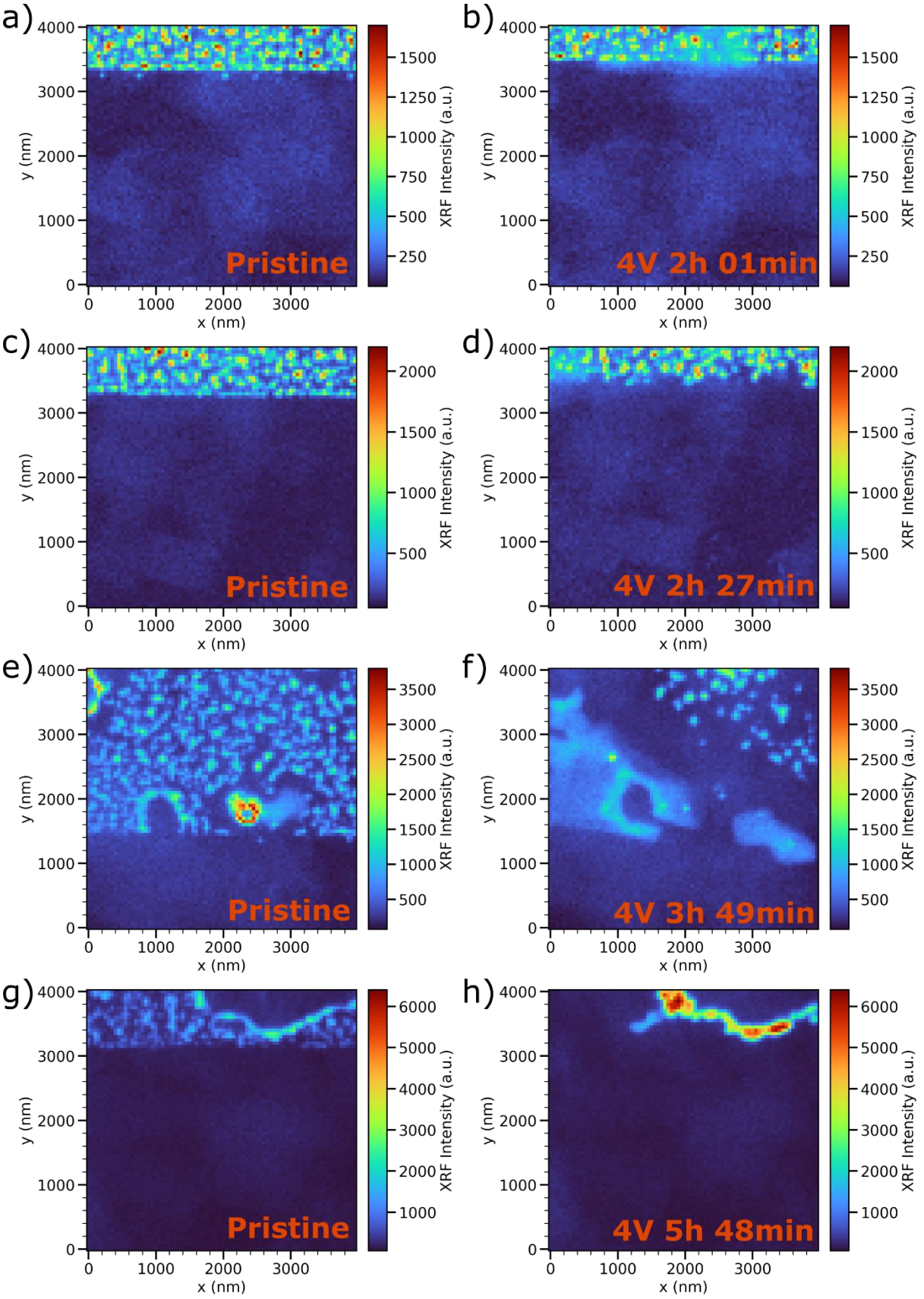

Figure 4.22: Au migration MAPI sample at 4V. a), c), e) and g) Au distribution in pristine condition. b), d), f) and h) Au distribution after 4 V bias stress.

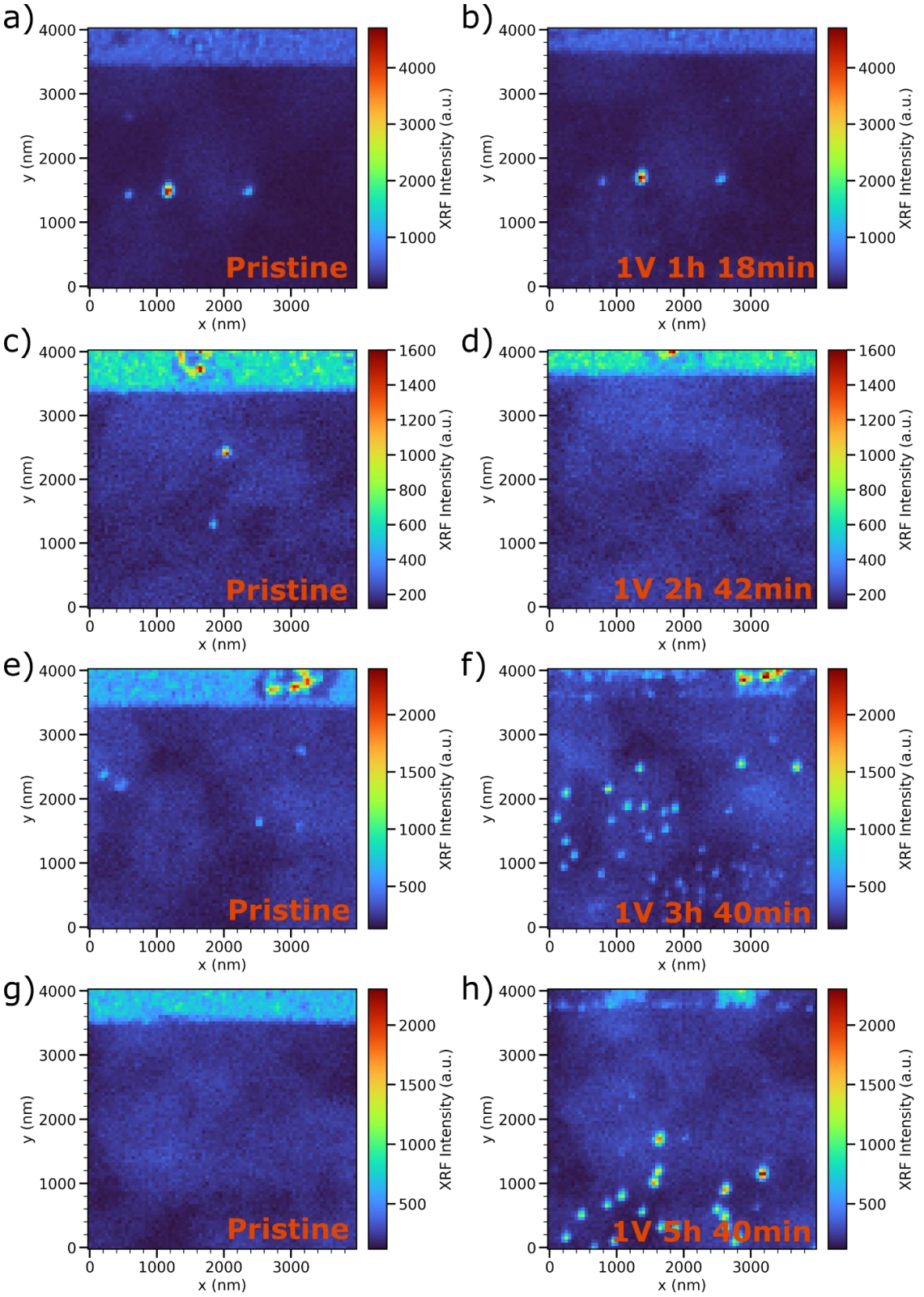

Figure 4.23: Au migration MAPI+PCBM sample at 1V. a), c), e) and g) Au distribution in pristine condition. b), d), f) and h) Au distribution after 1 V bias stress.

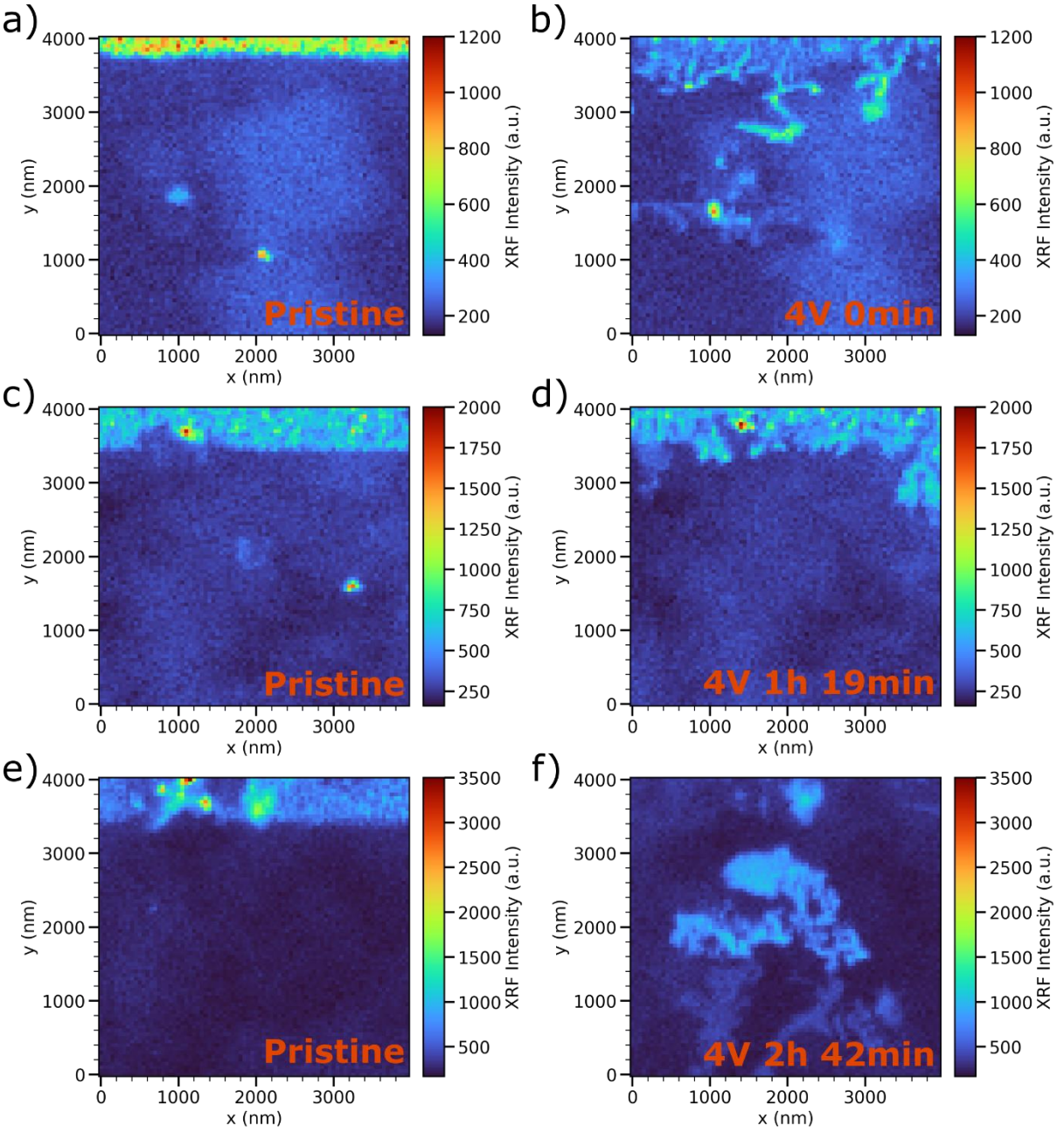

Figure 4.24: Au migration MAPI+PCBM sample at 4V. a), c) and e) Au distribution in pristine condition. b), d) and f) Au distribution after 4 V bias stress.

A large 10 x 10 μm^2 map of Au distribution in a MAPI+PCBM sample was acquired with 0.5 V bias applied. The image reported below in Figure 4.25 was captured with a raster scan starting from the bottom left corner. The large map took hours to complete and by the time the scan reached the edge of the first metal contact few hours were already passed. Under the constant bias stress, gold nanoparticles migrated from the top contact to the center of the channel leaving a corroded metal contact.

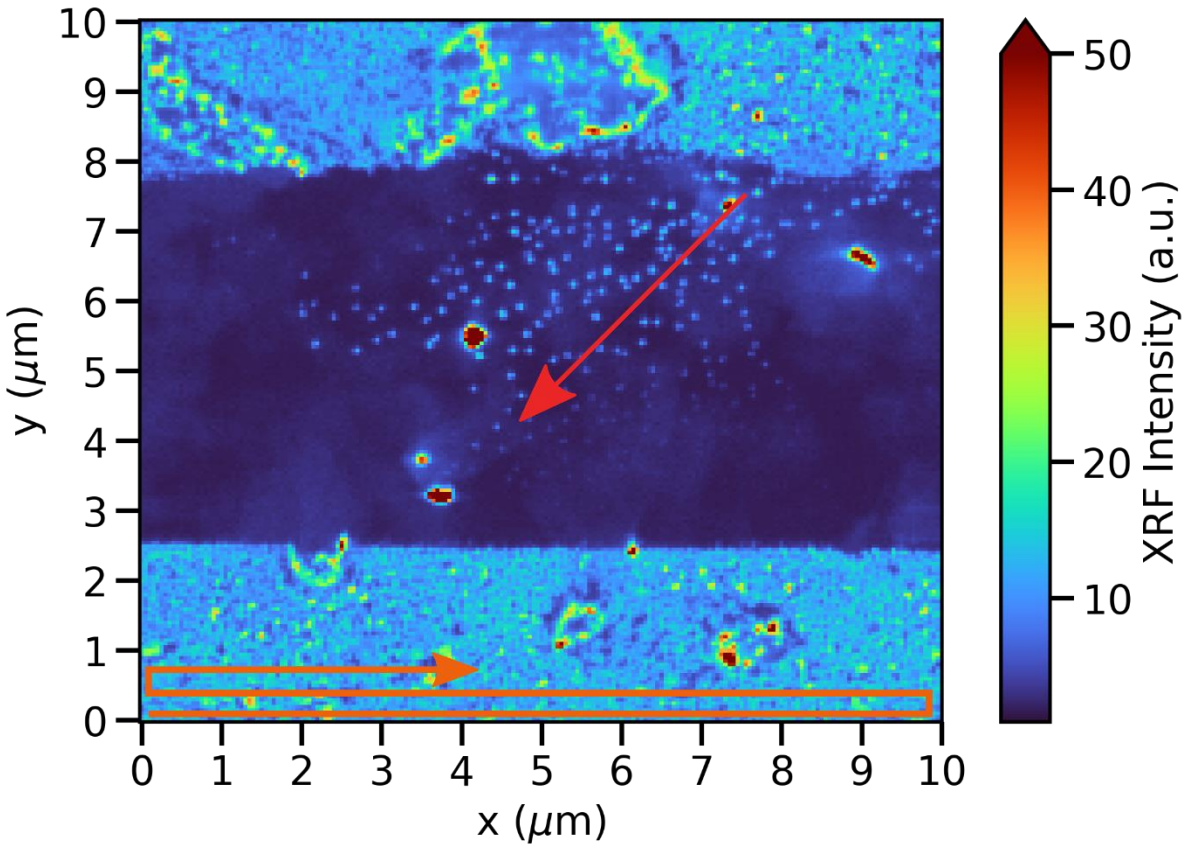

Figure 4.25: Gold migration. A 10 x 10 μm^2 map of Au distribution in a MAPI+PCBM sample where the entire 5 μm channel is visible. On the bottom the red arrow indicates the direction of the raster scan, on top the straight arrow indicates the possible gold migration direction.

5. 3D perovskite thin film for direct X-ray detection with improved stability

The high performance of 3D lead-halide perovskite comes with environmental instability, especially in the thin film case. The degradation mechanisms are detailed in section 2.5, a brief summary is reported in the following. Hybrid perovskites are sensible to H_2O and O_2 present in the atmosphere and the reactions with oxygen or catalysed by UV light lead to the formation of volatile organic species (such as methylamine) that can escape from the perovskite film bringing to the formation of PbI_2 in case of iodine based perovskites.[86,128] Since PbI_2 has a yellow colour, a clear sign of degradation is the change in colour from black/dark to yellow (and therefore the

absorption spectrum). Heat can also degrade perovskites producing volatile compounds.[129] Ion migration inside perovskites is another mechanism that can lead to device degradation.[130] However, medical devices require long shelf life, thus the resolution of the stability issue of 3D perovskite detectors is a strict requirement for the advancement of the field.[131] In fact, operational and environmental instabilities are limiting the commercialization of perovskite-based devices. While in the field of perovskite solar cells the monitoring of time stability is an established practice,[132] this is not the case for perovskite radiation detectors: among all the papers published in the last years on this topic, only few of them report about the device stability under operation[50,53,133–137]and even fewer about aging effects.[50,53,68,135,138-140] The few reports on aging measurements on 3D perovskite polycrystalline detectors deal with encapsulated detectors. Although encapsulation is a good contingency plan to limit device degradation, it is better to find a new structural solution to increase the intrinsic stability of perovskites.[141] The longest reported stability study on perovskite X-ray detectors is of Deumel et al. for encapsulated detectors that show a 20% decrease in sensitivity after 1.5 years after fabrication.[142] Another one shows the degradation of an aerosol-jet printed $MAPbI_3$ detector encapsulated in polydimethylsiloxane (PDMS) after 9 months stored in nitrogen atmosphere.[68] In the following, I report the results of different strategies to improve the thin-film device stability.

5.1 Perovskite thin-film with stable operation in air

The main strategies rely on changing the perovskite composition and the buffer layer, to obtain air stable devices. Here the perovskite used is a mixed cation mixed halide perovskite with the following formulation: $FA_{0.83}Cs_{0.17}Pb(I_{0.77}Br_{0.23})_3$. Compared to the previous reported 3D perovskite in the photodiode geometry the MA is removed.

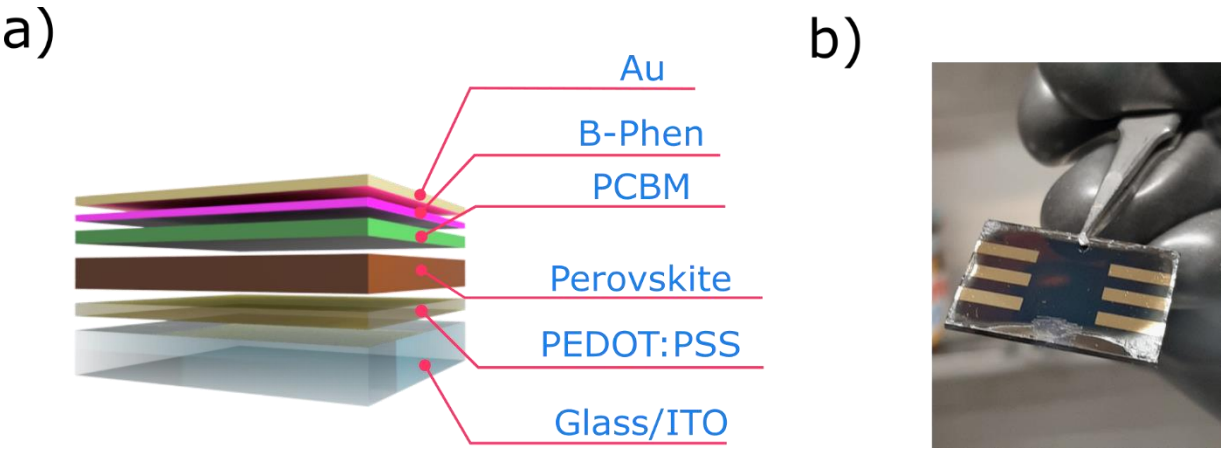

Figure 5.1: Device structure. a) Layered structure of the photodiode b) Picture of the final photodetector, the dark colour comes from the perovskite and the top metal contact in Au are visible.

The spin coated perovskite layer is in the middle of a p-i-n photodiode structure employing PCBM and PEDOT:PSS as ETL and HTL respectively. The structure and picture of a final device are reported in Figure 5.1a and b. This device configuration allows for stable operation in air as visible in Figure 5.2. The dynamic responses acquired under 40 kVp X-rays in ambient and nitrogen atmosphere are identical with box-like and repeatable response even when the device is exposed to air.

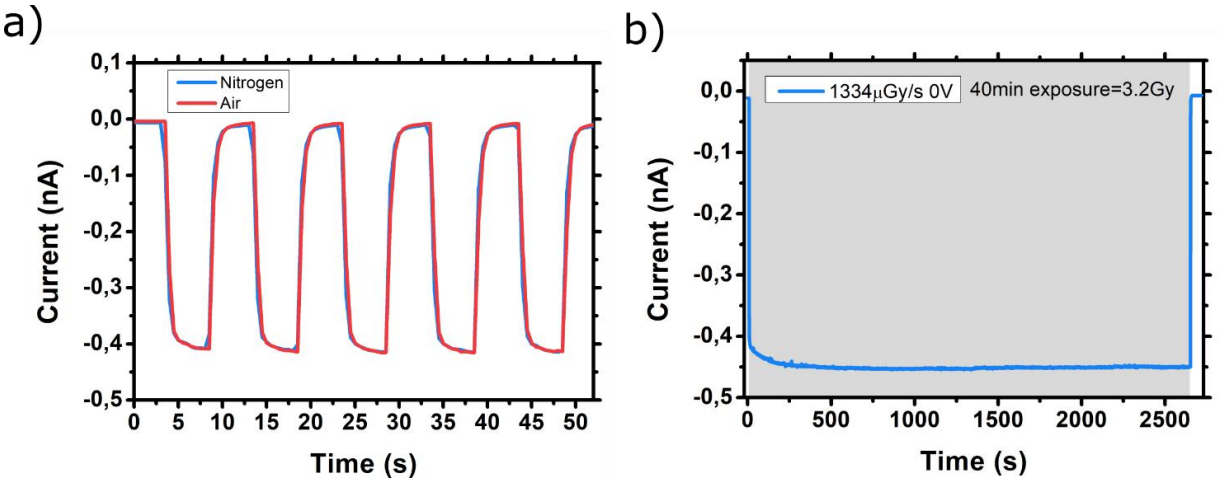

Figure 5.2: Operation in air. a) Comparison between dynamic curves acquired under 40 kVp X-rays in nitrogen and air atmosphere at dose rate 1334 uGy/s. Detector in passive mode (0 V bias). b) Continuous operation under irradiation for a total incident dose of 3.2 Gy.

The stability under continuous irradiation has been tested by irradiating the sample for 40 min at 1334 μGy s^{-1} X-rays for a total dose of 3.2 Gy. The test was performed in air and the response is flat and stable, apart for the initial part where few minutes are needed to reach a proper plateau. The IV characteristics and device sensitivities under X-rays were measured up to 54 days after fabrication storing the sample in ambient condition in dark. The IV plot (figure 4.3a) shows a current decrease of about one order of magnitude in forward regime, while no degradation is present in the reverse regime. The latter means that the dark current is stable over time, since the detectors typically operate at 0V or reverse bias. A very small increase in the hysteresis is present. The IVs acquired after 14 and 54 days are comparable. The sensitivity extracted by a linear fit of the X-ray induced current in function of the dose rate, showed a 25% decrease after 54 days of storage. The pristine sensitivity equal to 6.84 ± 0.05 μC Gy^{-1} cm^{-2} operating in passive mode (0 V) thanks to the photodiode architecture. After 54 days the sensitivity dropped down to 5.17 ± 0.06 μC Gy^{-1} cm^{-2} which still pretty high compared to values reported in literature.[59,110]

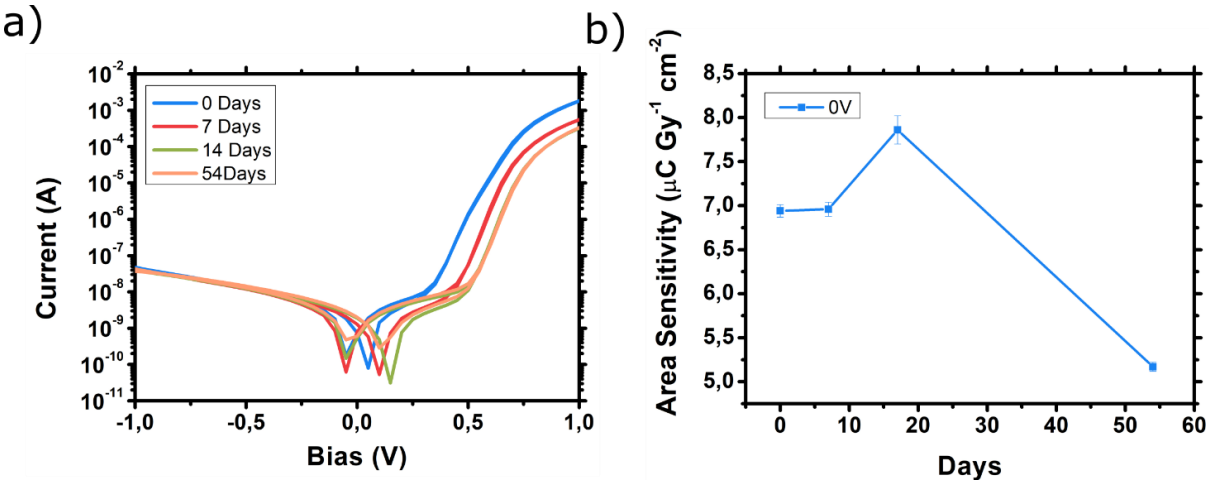

Figure 5.3: Aging. a) Dark I-V characteristic evolution in time from 0 (as-fabricated sample) to 54 days of storage in air. b) Monitoring of the sensitivity normalized by device area up to 54 days after fabrication.

5.2 Starch polymeric template for long term stability

A different strategy to improve the stability of perovskite thin film is the addition of starch as templating agent during the film deposition. Therefore, starch has been used as a polymeric template for the growth of perovskite polycrystalline film. The additive confers higher stability in ambient conditions, improved homogeneity of the film also at thicknesses above 1 μm, enhanced mechanical flexibility and robustness.[143,144] All the above characteristics are ideal requirements for portable and flexible X-ray devices.[143,144] I used methylammonium lead iodide (MAPbI3, called MAPI in the following) and mixed formamidinium-methylammonium lead iodide (FA0.6MA0.4PbI3, FAMA in the following) perovskite, combined with starch to form the ink to be deposited by spin-coating. The perovskite-starch mixtures identified as MAPI-xS and FAMA-xS respectively, where the x represent the concentration of starch expressed in wt% with

respect to the perovskite precursors following the same procedure reported by Giuri et al.[143] The perovskite precursor solutions were prepared starting from an equimolar stoichiometric ratio (1:1) of MA and PbI_2 in DMSO with a precursor concentration of 30 wt %. The solutions were stirred at 80 °C for 30 min. Starch was added to the solution in different percentage (i.e., 0, 10, 15, 20 wt %) then the solutions were stirred further at 80 °C for 5 h. The starch concentration modifies the viscosity of the starting solution to be deposited, thus it has a direct impact on the active layer thickness. A summary of all the active layers used and the respective thicknesses can be found in Table 1.

Perovskite-Starch composite	Perovskite formulation	Starch concentration (wt %)	Active layer Thickness (nm)	Rectification Factor (RR)
MAPI-10S	$MAPbI_3$	10	470	917
MAPI-15S	$MAPbI_3$	15	1050	235
MAPI-20S	$MAPbI_3$	20	1400	411
FAMA-10S	$FA_{0.6}MA_{0.4}PbI_3$	10	470	1145
FAMA-15S	$FA_{0.6}MA_{0.4}PbI_3$	15	1050	760
FAMA-20S	$FA_{0.6}MA_{0.4}PbI_3$	20	1400	127

Table 1: Perovskite-starch active layers. Different perovskite formulations, starch concentrations, the respective active layer thickness and rectifying factor calculated from the IVs.

The starch perovskite composite was employed as active layer of a p-i-n photodiode fabricated on patterned ITO covered glass substrate and with the structure reported in Figure 5.4a at NANOTECH-CNR laboratory in Lecce, Italy. A very good deposition is achieved by one step method without antisolvent by-spin-coating at 9000

rpm for 20 s on the HTL, followed by annealing at 100 °C for 30 min. A SEM picture of the MAPI-10S film is shown in Figure 5.4b. As ETL and HTL PCBM and the a layer of poly(N,N′-bis(4-butylphenyl)-N,N′-bis(phenyl)benzidine) (poly-TPD) were used. Poly-TPD is a p-type organic semiconductor with excellent energy alignment between the perovskite valence band minimum (-5.4 eV) and its lowest unoccupied molecular orbital (LUMO = -5.4 eV).[145] PolyTpD is used as an alternative to the PEDOT:PSS, which proven to accelerate the degradation of the perovskite layer due to its higher hydrophilicity and ionic mobility.[146] BCP was used as buffer layer to improve the ohmic contact with the top Au metal electrode. In this work, devices with three different active layer thicknesses were fabricated: the higher the starch concentration (more viscous solution), the thicker the perovskite layer is. The starch concentrations used (10, 15 and 20 wt %) resulted in 470, 1050 and 1400 nm thick active layers (Table 1).

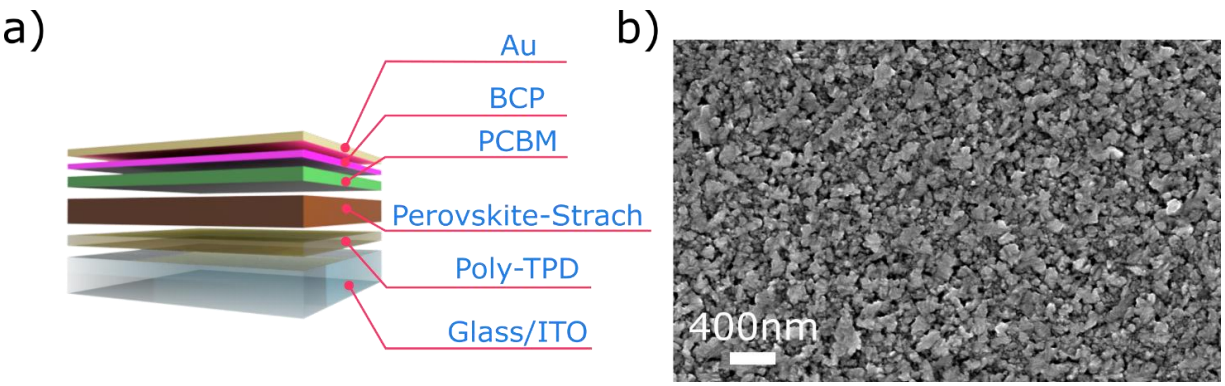

Figure 5.4: Perovskite-starch based devices. a) Photodiode architecture with the perovskite layer in the middle. b) SEM image of the perovskite-starch active layer.

The XRD pattern of the MAPI-10S composite, reported in Figure 5.5, shows the coexistence of the $MAPbI_3$ and starch phases. It presents the characteristic peaks of MAPI and a very broad background associated to the presence of the amorphous starch phase.

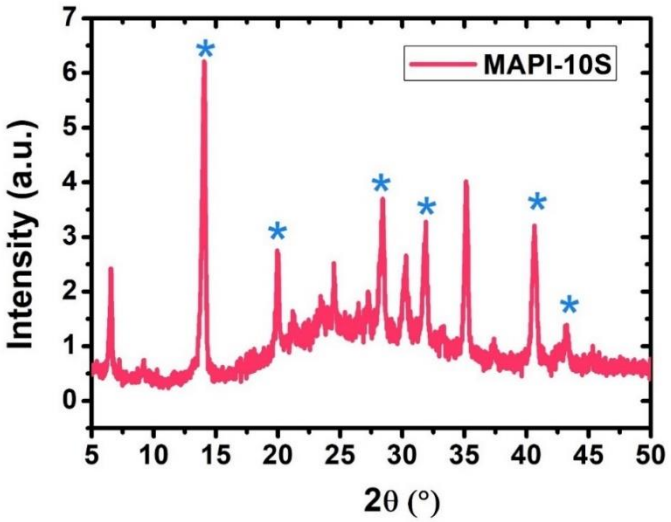

Figure 5.5: XRD. XRD spectrum of MAPI-10S spin-coated film. The peaks mark with the blue star are attributed to the $MAPbI_3$ tetragonal phase.

In the graph, peaks labelled with blue stars are attributed to the tetragonal MAPI perovskite phase, while the lower angle peaks at 2θ = 6.55°, 7.21° and 12.9° are attributed to an intermediate MAI-PbI_2-DMSO complex that remains in small amount after the deposition when the starch is present.[85] Starch is a polymeric carbohydrate consisting of numerous glucose units joined by glycosidic bonds. The glucose chain has exposed OH groups with which the organic part (MA of FA) interacts via hydrogen bonding at the grain boundaries as depicted in Figure 5.6. Therefore, starch increase the solution viscosity ensuring a good deposition and it could also passivate exposed MA or FA at the perovskite grain boundaries. The photodiodes were electrically characterized by measuring current-voltage scans (IV). The IVs measured for the two perovskites nanocomposite and three thicknesses are reported in Figure 5.7a and b. Higher starch concentrations lead to a decrease of the forward current in both MAPI and FAMA composites.

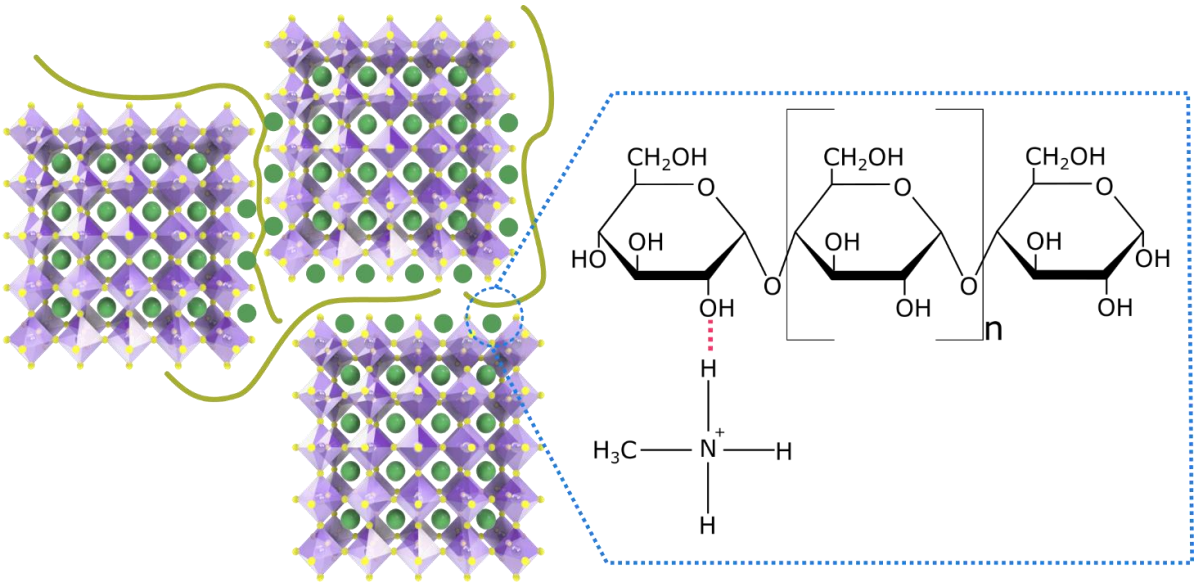

Figure 5.6: Starch-Perovskite. Starch molecules (green strings) interacting via hydrogen bonding with the perovskite at the grain boundaries (depicted as purple/green squared crystalline structure). In starch, repeating units of glucose are chemically bond together by glycosidic bonds forming a polymer chain. The exposed OH groups of glucose interact with the hydrogen in the organic component of perovskites.

In addition, FAMA-20S presents a reverse current 1 order of magnitude higher than FAMA-10S, while in the MAPI case the addition of starch does not strongly influence the reverse current. The rectification factor (RR), calculated as the ratio between the forward current at 1V and the reverse current at -1V (where $RR = |I_{fw}(+1V)/I_{rev}(-1V)|$), is reported in Table 1. For all the diode structures the rectification factor is at least above 10^2 (best $>10^3$ achieved by MAPI-10S) assessing the good photodiode fabrication quality. The presence of starch seems also to influence the hysteresis in the IV characteristics. The higher the starch concentration the higher is the bias distance between the current minima of the forwards and backwards scans. Interestingly, in MAPI-xS devices the backward scans minimum remains at the same bias whatever the starch concentration while the forward scan minimum goes to more negative biases. In FAMA-xS, instead, both minima are shifting to higher absolute bias values.

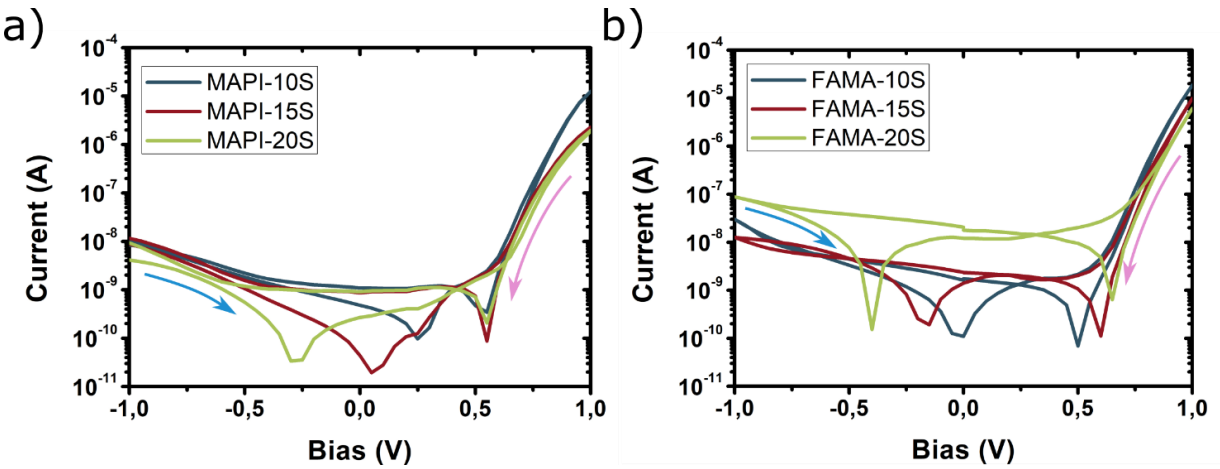

Figure 5.7: I-V Perovskite-starch. IV characteristics of MAPI (a) and FAMA (b) based photodiodes with different starch concentration. The blue arrows indicated the direction of the forward scan lines while the pink ones the backward scans.

Photocurrent spectra of MAPI-xS acquired under UV-Vis light show a different behaviour depending on the device thickness, see Figure 5.8. It is important to highlight that the samples have been illuminate through the transparent ITO bottom electrode. The photocurrent in MAPI-10S (470 nm) continues to increase after the band gap onset with the maximum value peaked at 2.91 eV. At higher layer thicknesses, the photocurrent progressively decreases instead. In MAPI-15S (1050 nm) the current generated inside the perovskite layer remain almost constant until a peak appears at 2.74 eV. After it, the photocurrent starts to decrease. In MAPI-20S (1400 nm) the photocurrent starts to decrease immediately after the band gap transition. Interestingly the peak "*B*" present in MAPI-10S is not aligned with the ones of MAPI-15S and MAPI-20S, which instead are aligned between the two layers ("*C*" peak). The measurement assessed the very good charge collection efficiency for 470 nm perovskite layer under UV-Vis light. The band gap value extracted by the Tauc plot resulted in 1.59 ± 0.02 eV for MAPI-10S, identical values were found for the other MAPI films. The shape of the photocurrent spectra can be explained by considering the absorption and charge collection processes under UV-Vis photons.

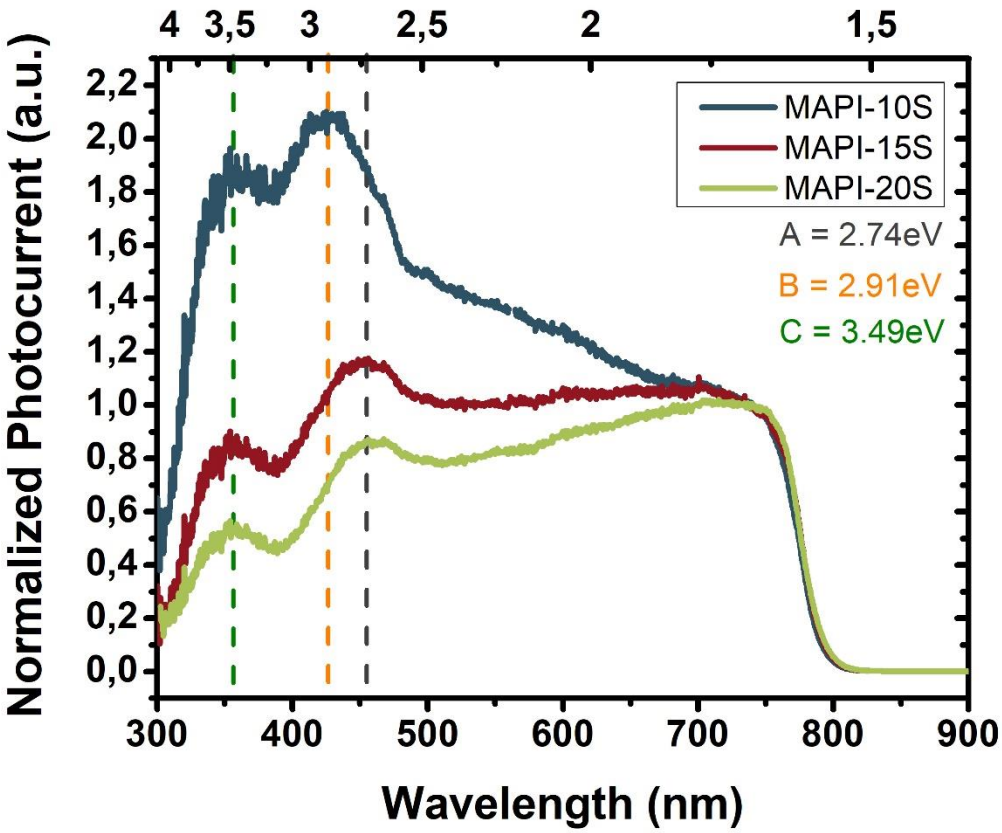

Figure 5.8: Photocurrent spectra MAPI-xS. UV-Vis photocurrent spectra of MAPI-xS composite at bias 0 V. The *A*, *B* and *C* indicates the positions of the above band gap peaks. Marker 1 and 3 are associated with peaks present in MAPI-15S and MAPI-20S, while marker 2 indicated the peak of MAPI-10S.

Depending on the incident wavelength, the photons are absorbed at different depth into the perovskite layer (10 – 100 nm). The absorption coefficient is higher at lower wavelength,[147] therefore when going toward the UV range the electron-hole pairs are generated close to the HTL interface as depicted in Figure 5.9a. The closer the pairs generation is to the HTL, the longer is the distance that the electrons have to travel to reach the opposite electrode, thus increasing the probability of electron trapping in the bulk of the film. When this concept is applied to layers with different thicknesses, it explains the different perovskite film behaviour of photocurrent spectra. In fact, at fixed incident wavelength, the electrons have to travel higher distance in thicker films.

Therefore, the charge collection efficiency drops at higher wavelength and a decrease in the current is visible in the spectra.

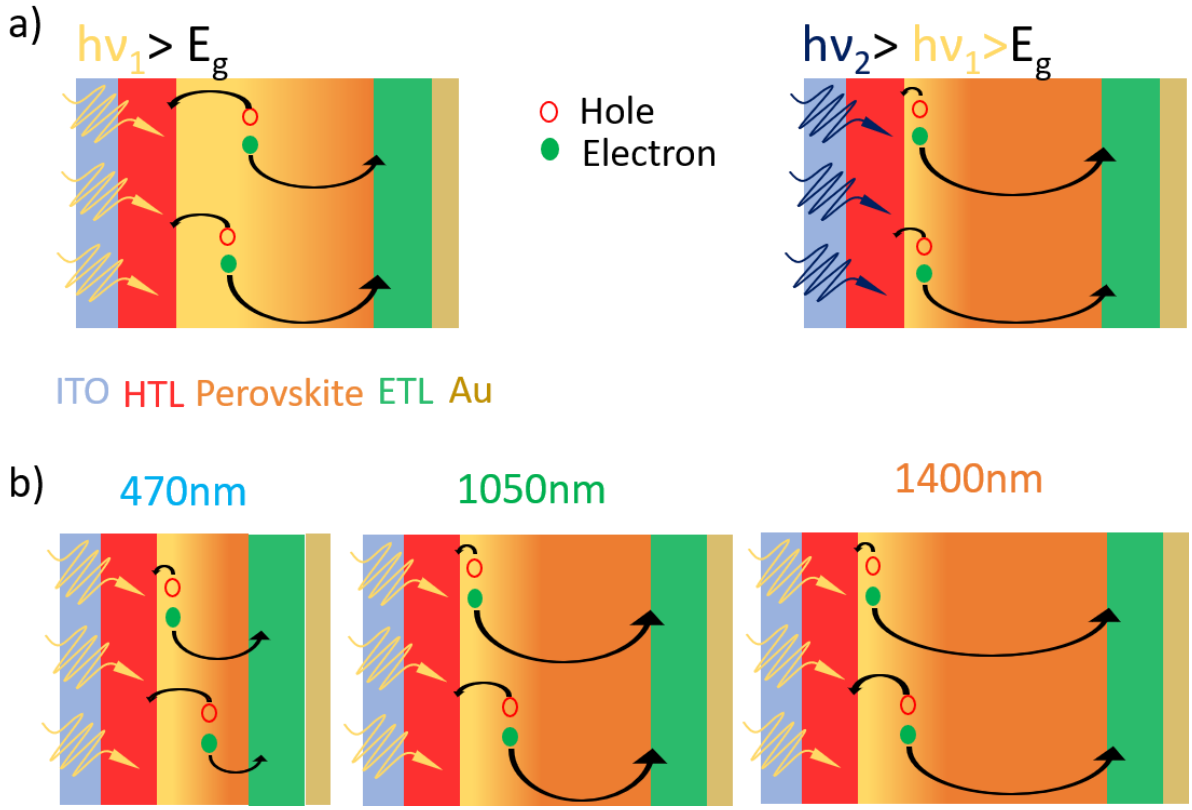

Figure 5.9: UV-Vis charge collection process. a) Scheme showing different penetration depth in the perovskite layer depending on the incident photon energy(wavelength). The generation of the electron-hole pair is closer to the HTL the higher is the incident photon energy. b) Effect of the layer thickness on the charge collection process. In thicker film, the charges have to travel higher distance to reach the electrode undergoing higher chance to be trapped.

5.2.1 Influence of perovskite thickness on X-ray photodiode performance

The X-ray detection performances of the starch perovskite-based p-i-n photodiodes were tested by measuring their current response under 40 kVp X-rays. The employed photodiode architecture worked in fully passive mode (bias = 0 V). As in the previous chapter the use of a multilayer structure gives rise to a heterojunction with a built-in

potential. When electron-hole pairs are generated inside the perovskite by the impinging X-ray photons, they are separated and driven towards the electrodes by the internal electric field with no need of external bias. The typical dynamic response of perovskite-starch films under different incident dose rates, ranging from 255 µGy s^{-1} to 1333 µGy s^{-1}, is shown in Figure 5.10a, for a 10 s modulation period of the X-ray beam with 50% duty cycle. At all starch concentration the devices showed fast, reproducible, and box-like response under radiation.

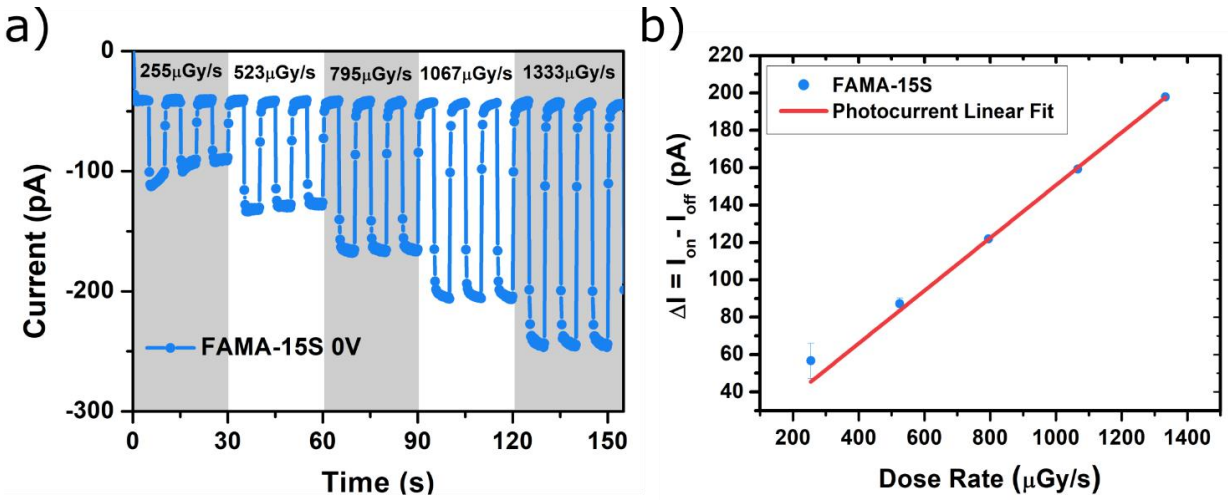

Figure 5.10: Perovskite-starch detectors X-ray response. a) Dynamic response of a FAMA-15S based X-ray photodiode with 0 V bias applied under increasing dose rate starting from 255 µGy s^{-1} up to 1333 µGy s^{-1}. b) Photocurrent as a function of incident dose rate for the same device in (a) with the linear fit for sensitivity extraction in red.

The linear response of the photocurrent as a function of the dose rate and the respective linear fit are reported as blue dots and a red line in Figure 5.10b. The angular coefficient of the linear fit of the photocurrent represents the sensitivity of the detector to the X-rays. In Figure 5.11 are reported the values of sensitivity divided per the detector area (4 mm^2) for the two different perovskite compositions and for all the thicknesses at 0V bias. FAMA based photodiodes present sensitivity values about 60% higher than their MAPI counterpart. Since the attenuated fraction of FAMA is comparable to the one of MAPI (~ 3% at 40 kVp X-rays), the higher sensitivity is due to a difference in charge collection efficiency. This agrees with previous literature

results that showed improved performances in mixed cations perovskites, both as radiation detectors,[50,59] and solar cells.[148–150] For both MAPI and FAMA the highest performance in terms of sensitivity was achieved with 15 wt % of starch, probably due to an optimum balance between thickness (about 1 μm) and mobility of charges through the film. Increasing the perovskite layer thickness increases the X-ray absorption and the number of charges generated in the film, but, at the same time, it also increases the distance that charges have to travel to be collected by the electrodes. The optimized balance between the two factors (absorption and charge collection efficiency) was obtained with a perovskite thickness of 1050 nm. The top sensitivity value (in passive mode) is 5.5 ± 0.2 μC Gy^{-1} s^{-1} for FAMA-15S and 3.64 ± 0.12 μC Gy^{-1} s^{-1} for MAPI-15S. These values are comparable to the other passive thin film perovskite X-ray detector presented in the previous chapter. The result seems in contrast with what reported for the same device under UV-Vis light, but under X-ray the charges are generated across the whole perovskite volume and not close to the HTL interface. The measured Limit of Detection (LoD) at 0V for MAPI-xS and FAMA-xS, for x equal to 10 and 20 wt % are shown in Figure 5.12a. The best LoD was found for MAPI-10S extracted from data acquired at lower dose rates (Figure 5.12b), I obtained 7.3 ± 0.4 μGy s^{-1}, a value comparable to the typical dose rates used in medical diagnostic applications and lower of some values reported in literature for thin film perovskites.[65,66] Noteworthy, the thinnest active layer in both MAPI and FAMA based devices exhibited the best LoD while the thickest layer exhibited a high LoD, the worst being the FAMA-20S.

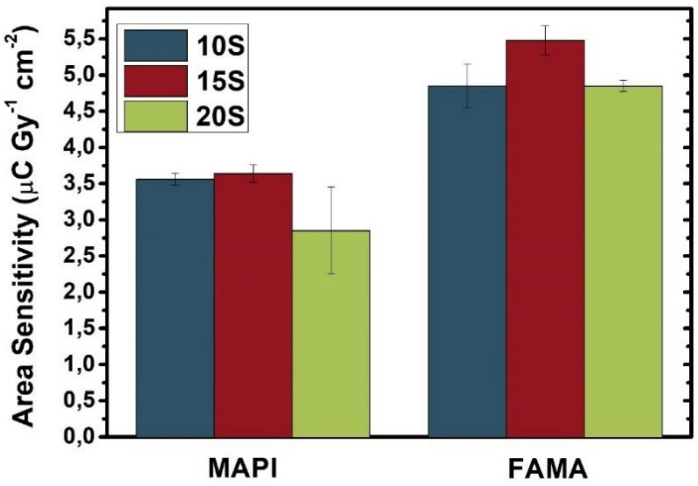

Figure 5.11: Perovskite-starch sensitivity. Sensitivity normalized by the device active area of 4 mm^2 for all the structure tested.

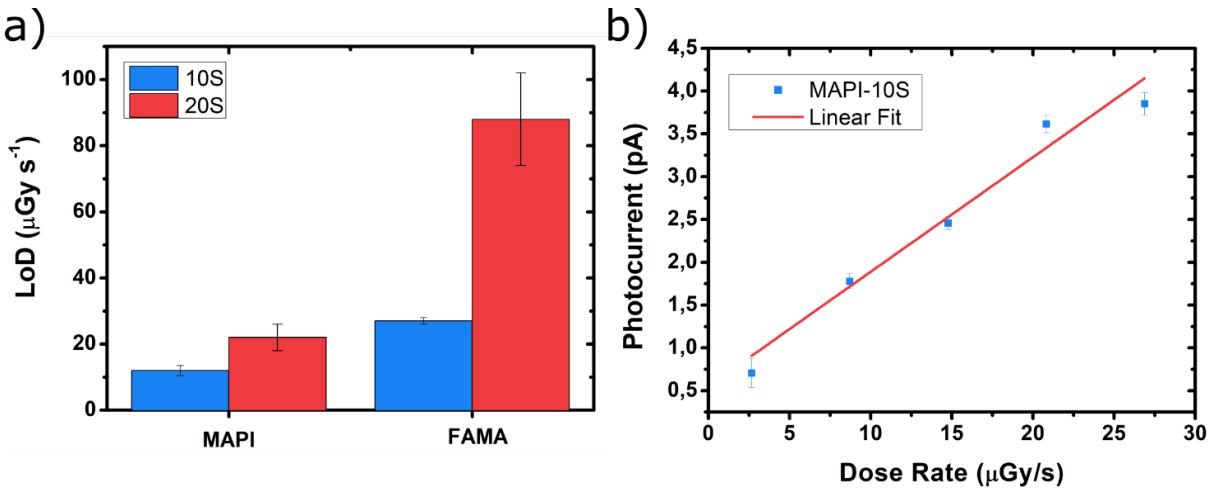

Figure 5.12. Perovskite-starch LoD. a) Limit of detection for the lowest and highest perovskite film thickness. b) Photocurrent at low incident dose rate and linear fit for the LoD estimation in a MAPI-10S sample.

Figure 5.13 reports the current voltage characteristic for a MAPI-10S device measured in the dark before and after exposure to a total 9.6 Gy incident dose of 40 kVp X-rays, a large dose, corresponding to thousands of X-ray images with standard medical diagnostic X-ray apparatuses. No sign of degradation is visible in the electrical characteristics, with almost identical reverse and forward current values. Therefore,

the high radiation tolerance of the detectors under study was assessed, another advantage of thin-film technology for ionizing radiation detection, especially when compared to other bulky perovskite detectors.[151]

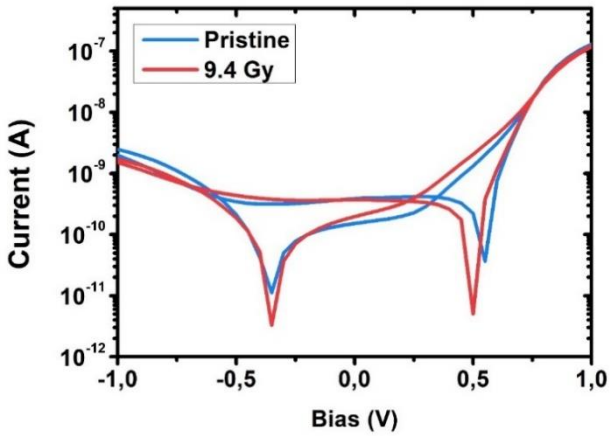

Figure 5.13: Radiation hardness. IV acquired from the same detector (MAPI-10S, 470 nm thick) before the X-ray measurement and after a total received dose of 9.4 Gy.

5.2.2 Bias effect on X-ray sensitivity

The charge collection efficiency of a photodiode can be improved by increasing the reverse bias applied increasing the electric field at the junction. Figure 5.14a and b report the normalized sensitivities as a function of the reverse bias for MAPI-xS and FAMA-xS. In the case of MAPI-10S and MAPI-15S detectors, the sensitivity does not scale with bias, likely because for these thicknesses the internal electric field is already strong enough to collect all the free charges created by the incoming radiation as for the devices reported in the previous chapter. In MAPI-20S detectors (1400 nm thick), the sensitivity increases with reverse bias up to -0.6 V. When the bias is increased further the performances decreased, due to an increase of the dark current and a reduction of the signal to noise ratio, Figure 5.14c. FAMA-10S (470 nm) present no noticeable effects with bias, while FAMA-15S (1050 nm film) based devices show a

slight sensitivity increase with reverse bias, reaching the highest value of 7.8±1.2 µC Gy^{-1} cm^{-2} at -1V. Similar to MAPI-20S, in FAMA-20S devices the effect of reverse bias is to decrease the performances. This observation could be due to the presence of high starch concentration in the precursor solution, possibly leading to the formation of phase segregation and localized higher conductive paths thus decreasing the shunt resistance for both MAPI-20S and FAMA-20S films.

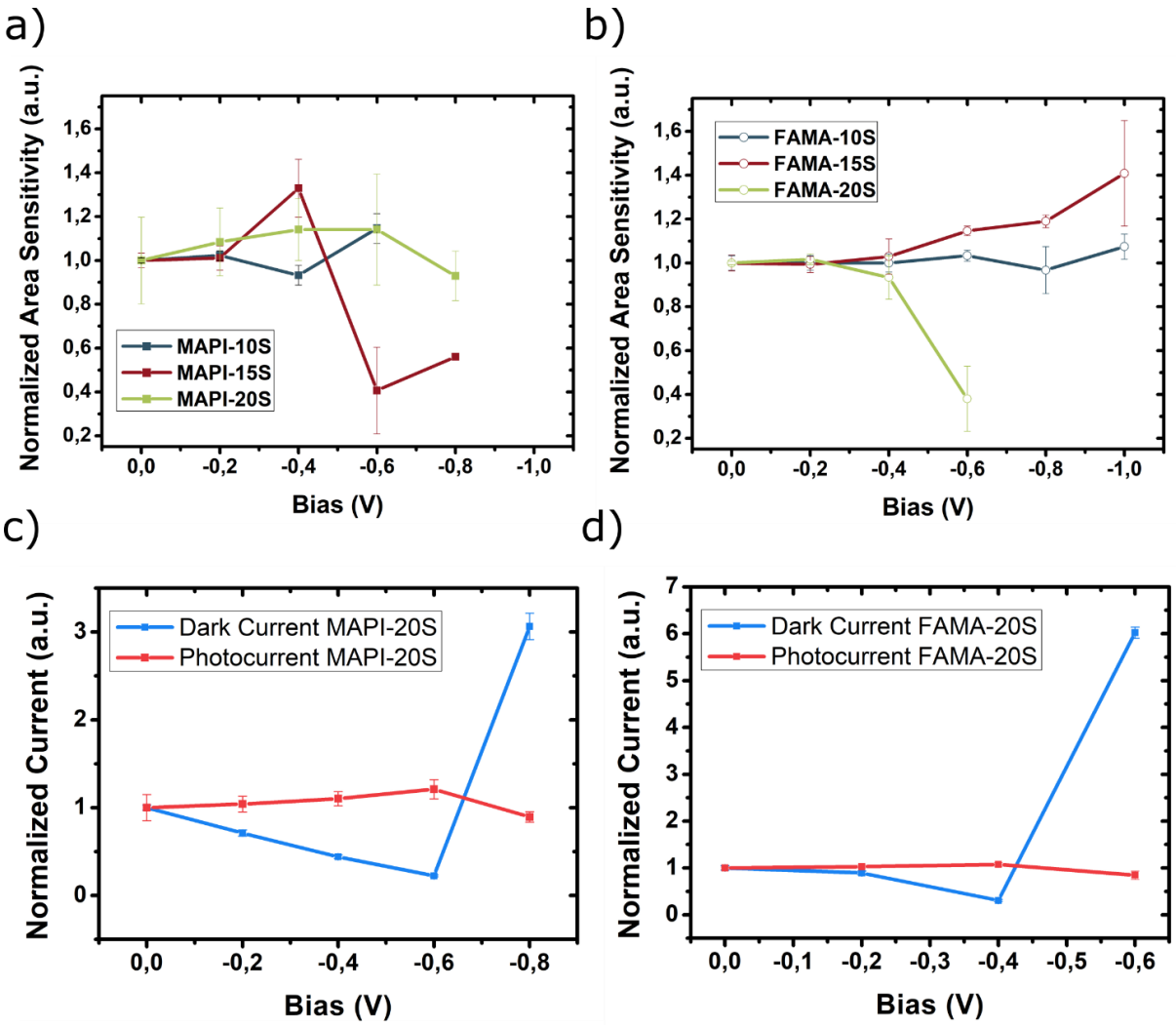

Figure 5.14: Bias effect. Sensitivity normalized by the active device area for MAPI-xS (a) and FAMA-xS (b). Photocurrent and dark current behaviour as a function of the reverse bias for MAPI-20S (c) and FAMA-20S (d).

As visible in Figure 5.14c and d, the small increase of X-ray photocurrent due to extra charges generated and collected inside the active layer results to be a minor effect

with respect to the steep rise of dark current above -0.6 V, thus leading to lower sensitivities. Ion migration is driven by the electric field present in the perovskite, thus bias related stability is a known issue in perovskite-based devices.[82] The ion migration could interfere with the dark current stability and increase its base line value. However dark current stability is crucial for high performance ionizing radiation detection. Therefore, the good charge collection efficiency in passive mode allows a stable operation reducing the bias stress on the photodiode. Indeed, if a bias is applied, even a small one, a drift in the dark current appears. In Figure 5.15 are reported for MAPI-10S the current response under repeated X-ray on/off cycles for more than 10 minutes with 10 s period and 50% duty cycle, in passive mode (Figure 5.15a) and with -0.5V of reverse bias (Figure 5.15b). The data acquired with the reverse bias applied show the presence of a strong drift in the dark current. Instead, when operating in passive mode, the detector shows a remarkably stable and repeatable response without any drift.

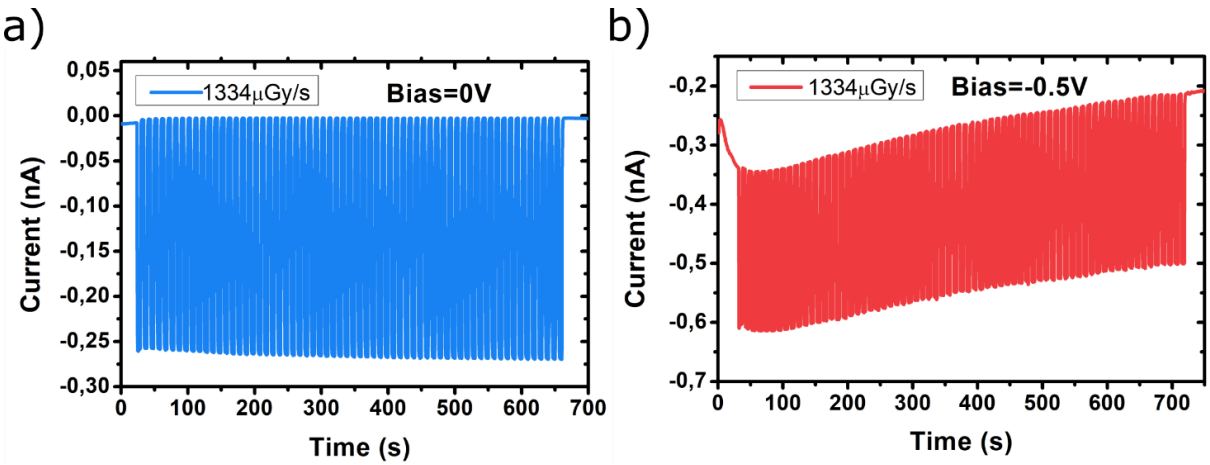

Figure 5.15: Bias stress. MAPI-10S bias stress evaluated by acquiring multiple X-ray photocurrent peaks with 0 V (a) and -0.5 V (b) bias applied.

5.2.3 Aging study

Due to the high surface to volume ratio, stability in air and aging effects are among the crucial aspects of thin-film perovskite devices. It has already been proved that the addition of starch strongly improves the stability in air of solar cells.[143] To assess aging effects and long term stability of perovskite X-ray photodiode, the samples were stored in ambient atmosphere and in dark. The dark condition was achieved by wrapping the samples boxes with aluminium foil. For the characterization, the photodiodes were exposed shortly to the room light and the measurement performed in air. The temperature and relative humidity variations in one year were monitored by placing a sensor near the samples storage and they are reported in Figure 5.16. The average temperature recorded form May 2019 to May 2020 was of 23.8°C and the average relative humidity was of 38.8%. However, the maximum temperature and humidity values at which the samples were expose after the fabrication were 33.8°C and 69.9% respectively. The samples were stored for 630 days and periodically measured.

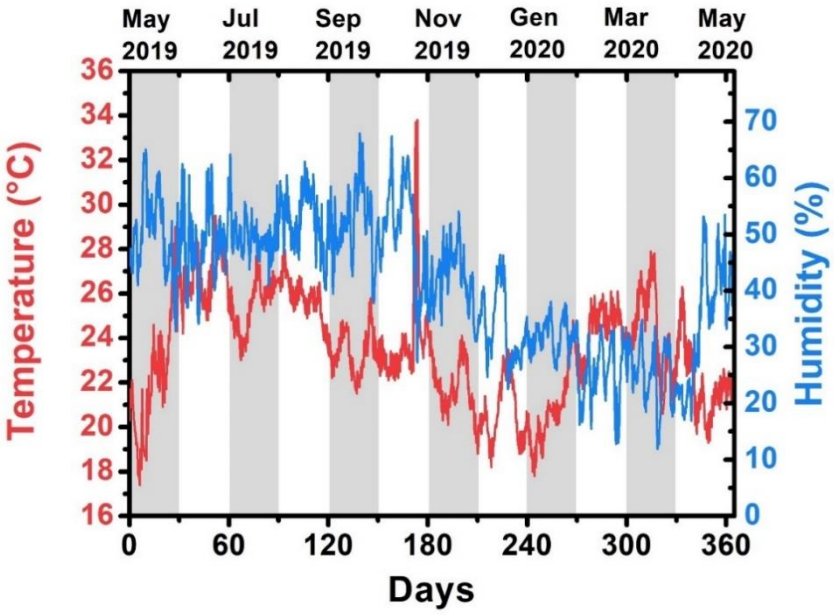

Figure 5.16: Temperature and relative humidity. Temperature and relative humidity recorded over one year (from May 2019 to May 2020) where the samples were stored.

It is well known that 3D iodine-based hybrid perovskite becomes yellow after exposure to air due to the formation of photo-inactive lead iodide PbI_2 which has a yellow colour.[128,152–154] All perovskite-starch films showed a dark colour with no visible sign yellow phase even after exposure to air for 630 days as testify by the optical pictures reported in Figure 5.17.

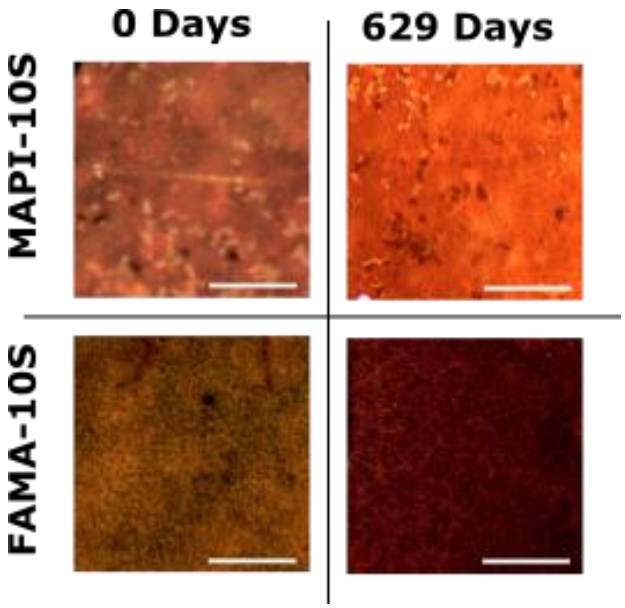

Figure 5.17: Film colour. Optical microscope images of perovskite-starch films after 630 days of storage in air still showing a dark/brownish colour. The scale bars are 500 µm.

I measured the sensitivity of the devices to 40 kVp X-rays for over one and a half years from the fabrication day, considered the day 0. Figure 5.18 shows the sensitivity variation for MAPI-xS and FAMA-xS devices. At day 0, FAMA based nanocomposites have higher sensitivities, as already described before, but they degrade faster than MAPI based ones. The fastest degradation is of FAMA-20S devices, where a drop of 72 % in performance occurs after 138 days. Instead, in MAPI based devices, the decrease in performance is only 23% after 138 days for MAPI-10S, while for MAPI-20S the point at 0 days and 138 days are comparable within the error bar. After 630 days of storage, between May 2019 and February 2021, FAMA-20S sensitivity decreases

down to 1.36 ± 0.02 µC Gy^{-1} s^{-1} (> 70% decrease), MAPI-10S show a 34% sensitivity decrease, while for MAPI-20S the percentage decrease is only 7%.

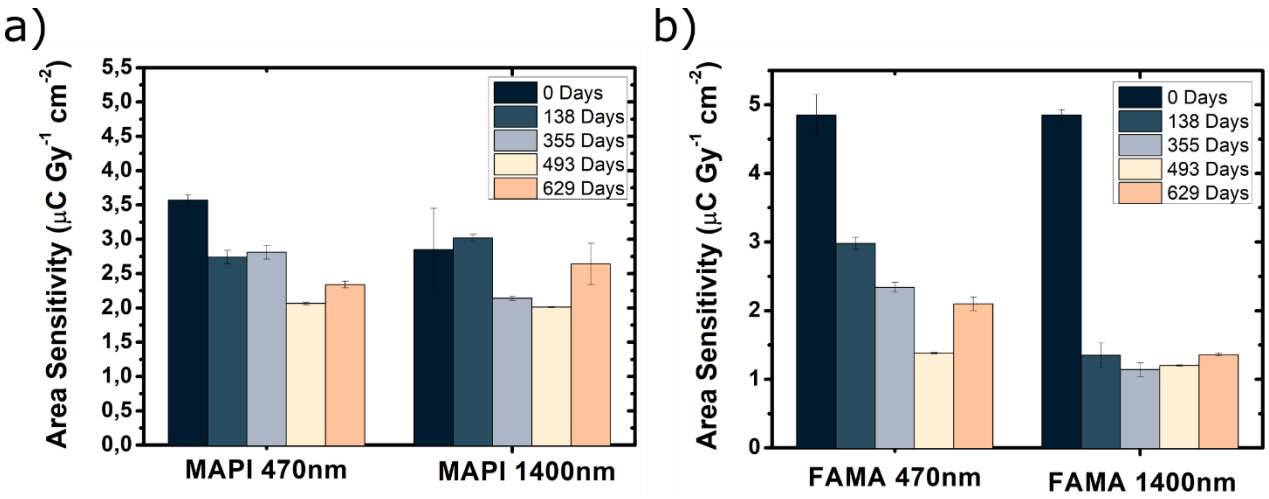

Figure 5.18: Sensitivity variation. Sensitivity normalized by the detector area as a function of time for MAPI-xS (a) and FAMA-xS (b) with x = 10, 20.

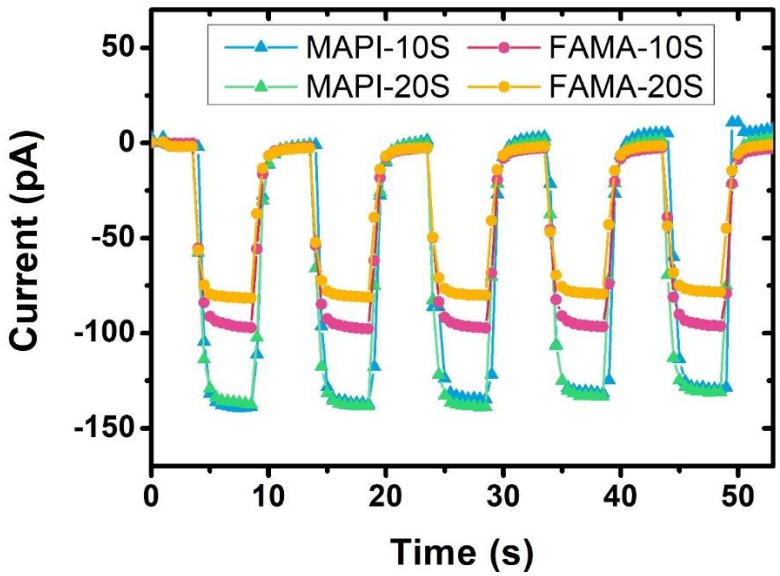

Figure 5.19: Dynamic response after aging. Current response under 40 kVp X-rays with modulating period of 10 s and 50% duty cycle acquired after 630 days of storage in air.

The better stability of MAPI nanocomposite compared to FAMA based ones is clearly visible from the histograms. After 630 days, MAPI-10S and MAPI-20S have

comparable normalized sensitivity values, while FAMA-10S has a higher response than FAMA-20S. Comparing the two composites, MAPI-xS have higher performances than FAMA-xS after the long storage period. In Figure 5.19 the dynamic response of perovskite-starch based photodetector under X-rays after the storage time are shown. After 630 days, both MAPI-xS and FAMA-xS showed box-like and reproducible response. In the graph is visible the higher photocurrent of MAPI based than the FAMA based ones after degradation. The MAPI-xS degradation behaviour is confirmed by the UV-Vis photocurrent spectra, at 0 V, acquired after 23 and 381 days of storage in air, see Figure 5.20a, b. In pristine MAPI-10S and after 23 days of storage, the photocurrent after the band gap onset increases as described previously. After 381 days, the charge collection performance of the film decreased showing a flat response after the band gap transition, and a variation in the band is visible. The extracted band gap values are reported in Table 2. While MAPI-20S shows a decreasing photocurrent even in pristine condition in accordance with the slightly lower sensitivity, see Figure 5.18a. But comparing the spectra acquired after storage the shape is comparable in accordance to the fact that MAPI-20s sensitivity degrade less.

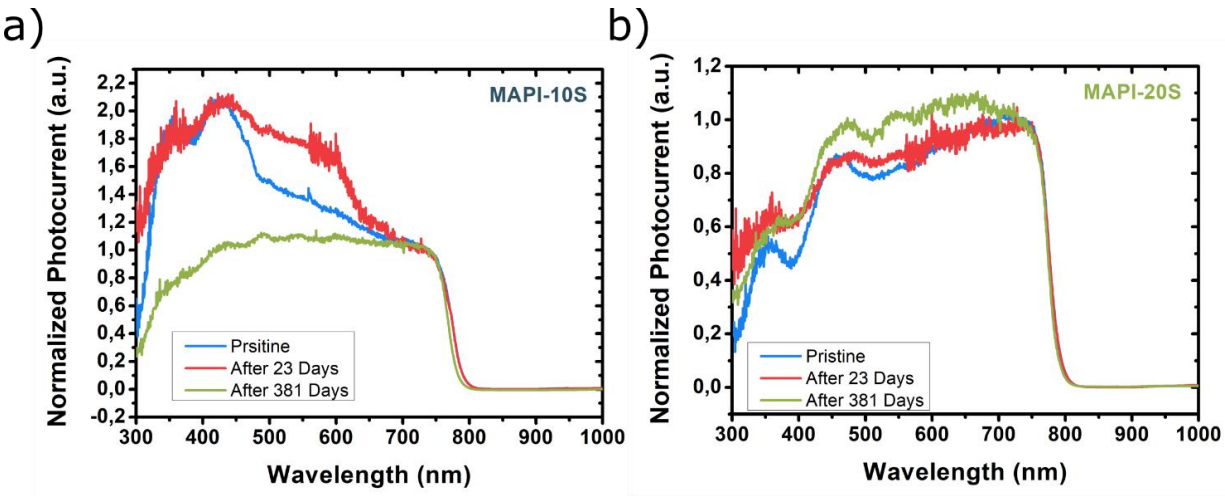

Figure 5.20: UV-Vis photocurrent spectra aging. Photocurrent spectra at 0 V bias of MAPI-10S (a) and MAPI-20S (b) acquired in pristine conditions and after 23 and 381 days of storage in air.

	Band gap (eV)	
Days	MAPI-10S	MAPI-20S
0	1.59 ± 0.02	1.59 ± 0.04
23	1.59 ± 0.06	1.59 ± 0.08
381	1.60 ± 0.06	1.59 ± 0.08

Table 2: Band gaps aging. Band gap variation for MAPI-10S and MAPI-20S

The present work reports, for the first time, a long-term monitoring of aging effects for not-encapsulated perovskite thin film radiation detectors. The effect of starch as an additive to increase the perovskite stability was assessed. The most stable devices (MAPI-20S) retain 97% of their sensitivity after 630 days of storage in air, a significantly longer period than any other report in the literature for unencapsulated devices and surpasses the longest aging test (630 days) for an unencapsulated device

6. Radiation detectors based on PEA_2PbBr_4 2D layered perovskite

Low dimensionality perovskites present some advantages as better environment stability, lower ion migration and higher resistance. These characteristics are very appealing for stable ionizing radiation detectors, thus, I studied 2D layered perovskite under X-ray (section 6.1) and gamma-ray (section 6.2) sources. In the third section (6.3), I described the fabrication and testing of a mixed perovskite as X-ray and proton detection. Indeed, by mixing the organic precursor of a 3D perovskite and the organic precursor of a 2D perovskite, mixed perovskite can be obtained with material properties between the 3D and 2D perovskite.

6.1 2D Perovskite for direct X-ray detectors

The object of the study of this section is a film of phenylethylammonium lead bromide (PEA_2PbBr_4) as active layer in a photoconductor geometry for direct X-ray detection.

6.1.1 PEA_2PbBr_4 thin film X-ray detector

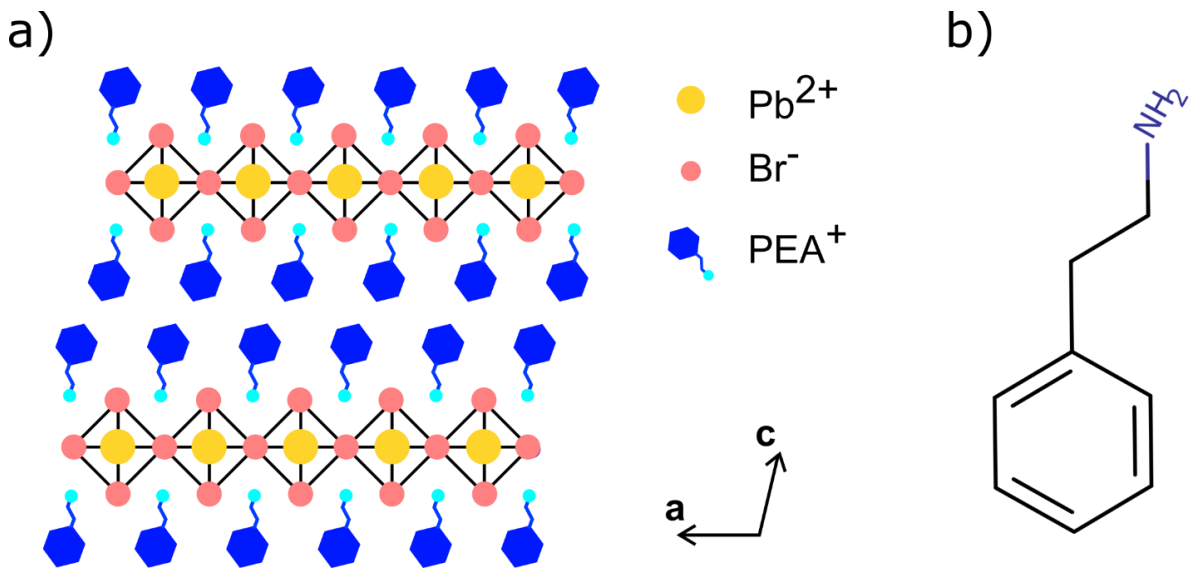

Figure 6.1: PEA_2PbBr_4. a) PEA_2PbBr_4 layered structure. b) Phenylethylamine molecule.

Recently, low dimensional perovskites have attracted interest in the fields of LEDs and UV–Vis photodetectors.[155,156] 2D perovskites are represented by the general chemical formula $(R\text{-}NH_3)_2A_{n-1}B_nX_{3n+1}$ with $n = 1,2,3\ldots$, where R is an alkyl or aryl group. 2D perovskites are characterized by a layered crystal structure in which BX_6 octahedra sheets (the inorganic part) are intercalated between bilayers of $R\text{-}NH_3^+$ organic spacers. The number n is equal to the number of inorganic octahedra sheets between the organic spacers. As already mentioned, their electronic structure is comparable to a multi-

quantum well where the inorganic layers constitute the wells and the organic spacers the barriers. For n = 1, the perovskite structure organizes in purely 2D planar monolayers, with only one octahedra sheet between the organic spacers. Due to the layered structure, the charge carriers are strongly confined in the inorganic layers and 2D perovskites present exciton binding energies (E_b) as high as 490 meV; a pretty high value if compared to $MAPbI_3$ with E_b ~ 15 meV. They also present highly anisotropic charge transport properties. Two dimensional lead-halide perovskite are characterized by weak interlayer bounds, granting remarkable mechanical flexibility even in the form of single crystals.[157] These properties can be exploited to fabricate flexible detectors. I used the 2D perovskite PEA_2PbBr_4 for the fabrication of ionizing radiation detectors with the photoconductor architecture.[158] In Figure 6.1a is reported a scheme of the layered structure. PEA stands for phenylethylamine, it is an organic molecule where the amino group is attached to a benzene ring through a two-carbon chain or ethyl group, see Figure 6.1b. As already anticipated, 2D perovskites possess several interesting properties as active layer in direct X-ray detection.

The interdigitated metal contacts were fabricated by means of photolithography as described in the method section 3.1.2. For this device, I used 125 µm thick PET as substrate and thermally evaporated Cr/Au contacts. Gold forms an ohmic contact with the 2D perovskite, moreover it offers high chemical stability. The interdigitated contacts used had 20 µm channel length and total channel width (W) of 7.56 mm. The perovskite solution was prepared by mixing PEABr and $PbBr_2$ in 2:1 molar ratio in DMF to obtain a 1M solution. The precursors and solvent were mixed overnight and filtered before use. The solution was then spin-coated at 2000 rpm for 60 s in ambient condition over the pre-patterned substrates. After the spin-coating an annealing was performed over the hotplate set to 70 °C. The device structure is represented in Figure 6.2. With planar electrode configuration, the conduction is almost in-plane parallel to the substrate surface. In 2D perovskite means that the conduction is mostly along the

octahedra sheets, the highest conduction direction. Using PET as substrate for the device fabrication, the final device detached from the glass support resulted flexible. The spin-coated PEA_2PbBr_4 films resulted in large crystal grains, with an average thickness of 1.9 ± 0.8 µm and an average size of 33.5 ± 8.3 µm. An optical picture of the film is reported in Figure 6.3a, where the big crystallites are visible. Most of the grains are big enough to bridge between the 20 µm channel. As a consequence, the conduction mainly occurs in single crystal-like domains.

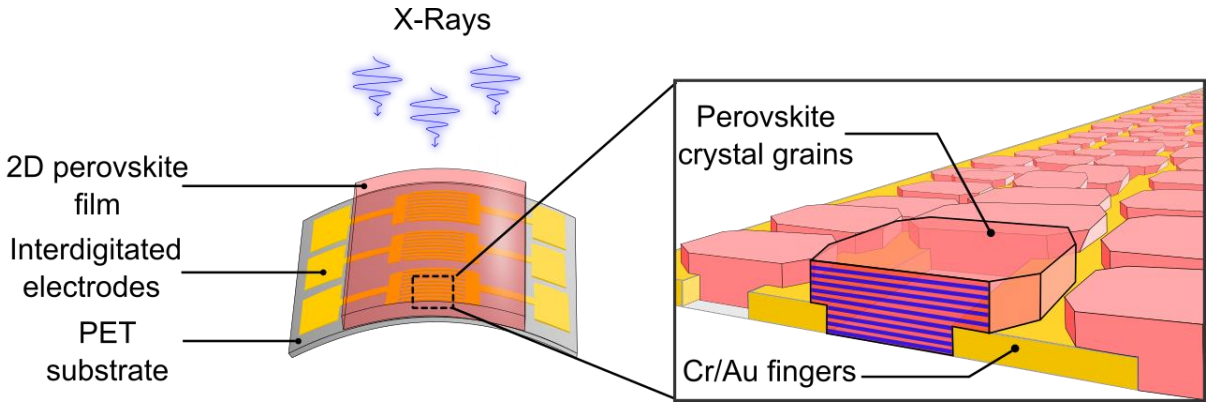

Figure 6.2: X-ray photodetector based on 2D perovskite. The device is fabricated on 125 µm PET substrate. The Cr/Au metal interdigitated contacts were obtained by means of photolithography and thermal evaporation. The 2D perovskite film was spin-coated on the substrate. In the channels the perovskite forms large grain with its layers parallel to the substrate surface.[158]

X-ray diffraction (XRD) analyses confirm the nature and crystallinity of the perovskite material. The thin-film XRD pattern of the device, shown in Figure 6.3b, presents a series of sharp and intense periodic peaks assigned to the $(0\ 0\ l)$ $(l = 1, 2, 3, \ldots)$ family of planes. The crystal structure is triclinic and belongs to the space group P-1.[159]

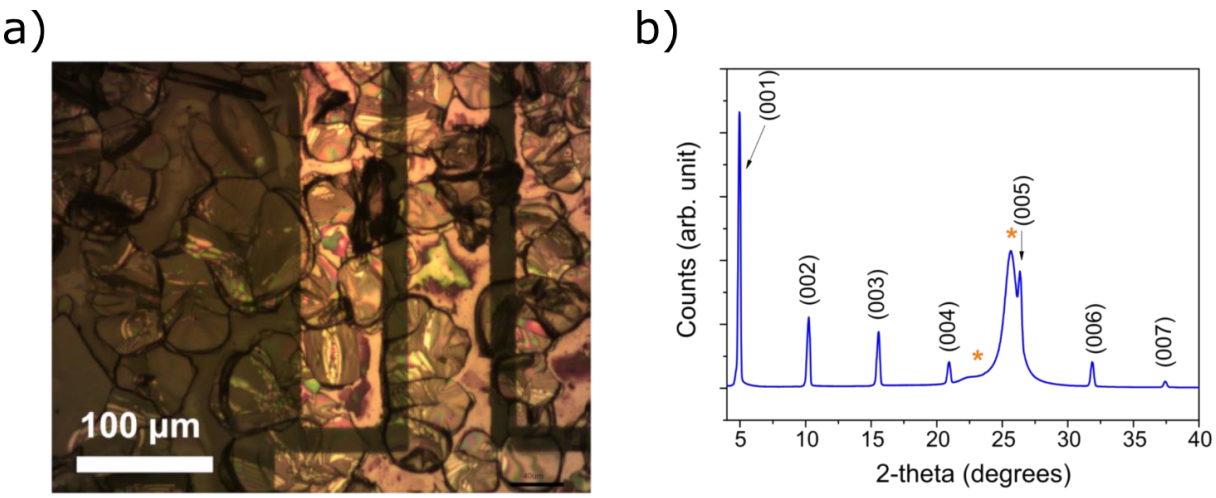

Figure 6.3: PEA_2PbBr_4 thin-film. a) Optical microscope image of the PEA_2PbBr_4 film deposited by spin-coating over a PET substrate with Au interdigitated metal contacts. b) XRD pattern of PEA_2PbBr_4 film. The orange asterisks mark the reflection from the PET substrate.[158]

The series of peaks indicates that PEA_2PbBr_4 thin-films grow preferentially with the in-plane direction parallel to the substrate, showing only the (0 0 l) planes corresponding to the different stacked layers. The broad peaks highlighted with an orange asterisk are attributed to the PET substrate underneath the perovskite layer. This configuration for a 2D perovskite is optimal, in fact, the high conductivity layers are aligned with the electric field generated by the electrodes. The photocurrent spectrum acquired between 325 and 500 nm using as radiation source a Xe arc lamp (150 W) is reported in Figure 6.4a. The Xe lamp was used because of the higher photon flux in the UV range than the QTH lamp. In the spectrum is visible the excitonic peak and the band onset. The narrow transition peaked at 410 nm is attributed to the 1s Rydberg series Wannier-Mott exciton transition.[160] The following Rydberg transitions are probably masked by the transitions between the continuous states. By applying the Tauc plot method described earlier (section 3.2.2) to the band-to-band transition a band gap value of 2.90 ± 0.04 eV is obtained.

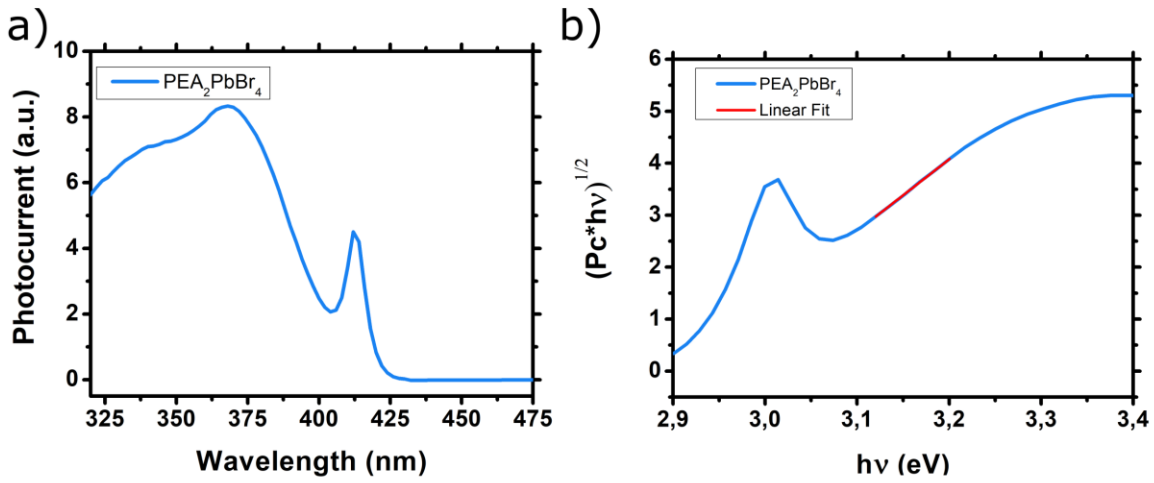

Figure 6.4: PEA_2PbBr_4 optoelectronic properties. a) Photocurrent spectra of a PEA_2PbBr_4 thin-film illuminated from the top. b) Tauc plot and linear fit used for the extraction of the band gap value.

As shown in Figure 6.4b, the fit was performed on the linear part of the band-to-band transition although the presence of the excitonic peak makes not easy to properly distinguish it. This value is very similar to the single crystal one reported in the literature,[156] compatible with the presence of big crystal grains. It is worth mentioning that in the UV range, 2D perovskites have a very high absorption coefficient (α_λ) in the range of 0.03 – 0.05 nm^{-1} at 300 - 400 nm wavelength.[161] According to the Lambert-Beer model the light intensity (I) through a medium follows the relation:

$$I = I_0 e^{-\alpha_\lambda d} \qquad (6.1)$$

Where I_0 is the impinging light intensity on the sample and d is the thickness. Therefore, in a few hundred of nanometres, the perovskites absorb almost all the incoming radiation. Remarkably, the obtained signal was good revealing the presence of charge collection in the out-of-plane direction since the electrodes are positioned at the bottom and the film thickness is around 2 µm. The transport properties were also evaluated by extracting the $\mu\tau$ product. A 380 nm LED was used to excite the sample inside the probe station and the photocurrent was measured as a function of the applied bias. The sample used for this experiment was a 2D perovskite film with lateral contacts

made of Ag creating a L = 1 mm channel. The photocurrent reported in semi-log scale is shown in Figure 6.5b where the red line represents the Hecht fit for the parameter extraction. The behaviour of the photocurrent can be modelled with the Hecht model:

$$I = \frac{I_{sat}\mu\tau V}{L^2}\left(1 - e^{-\frac{L^2}{\mu\tau V}}\right) \qquad (6.\ 2)$$

I this time is the electric current and I_{sat} is the current value in the saturation regime. V is the applied bias. A $\mu\tau$ value of (1.09 ± 0.07) × 10^{-5} cm^{-2} V^{-1} was obtained by the fit. This value is very close to the one reported by Zhang et al. for PEA_2PbBr_4 single crystal UV photodetector.[156] The high $\mu\tau$ could be ascribed once again to the large crystals bridging the metal contacts creating a single crystal-like behaviour. Although the nice result, it must be mentioned that the saturation regime is very hard to achieve, indicating that other methods to improve the $\mu\tau$ evaluation are needed. Here a bias up to 200 V was applied to the sample but a flat saturation was not reached. This creates a discrepancy in the model at low bias as visible in the plot.

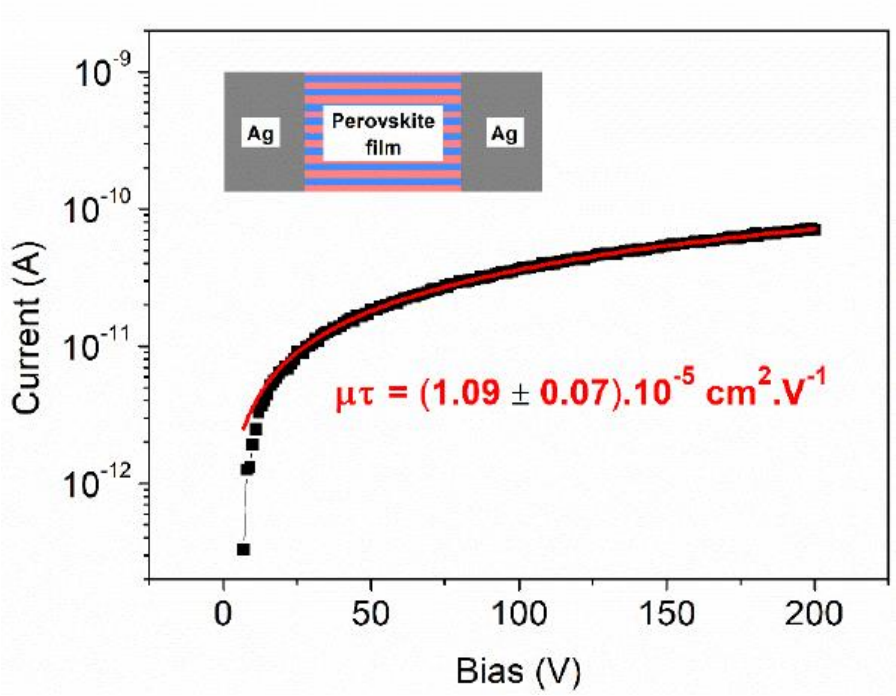

Figure 6.5: Hecht plot. Current under 380 nm LED as a function of bias up to 200 V. Inset shows the device structure used for the experiment, the charge is collected along the high conductivity planes.

6.1.2 UV Characterization

The response of the detector under UV light was evaluated using a LED and a picosencond LASER source. The I–V characteristics of PEA_2PbBr_4 films in dark conditions and under UV illumination using a 380 nm UV light LED are reported in Figure 6.6a. The dark current measured is extremely low down to 2×10^{-13} A at 10 V similar to single crystal values and one order of magnitude lower than high quality PEA_2PbI_4 (the iodine based perovskite counterpart) single crystals.[156,162] In samples with such high resistance the capacitive effect of the measurement setup (cables, connectors, holders) are important, introducing hysteresis and artifact effects in the I-Vs. As shown by Peng et al., the very low dark current in 2D perovskites originates from low intrinsic charge carrier densities due to low self-doping by intrinsic defects.[163] The light irradiance was increased in a range between 2×10^{-4} to 0.6 mW cm^{-2}, the photocurrent increases and shows an I_{on}/I_{dark} ratio as high as 10^4 at 0.6 mW cm^{-2}, indicating an efficient charge collection process.

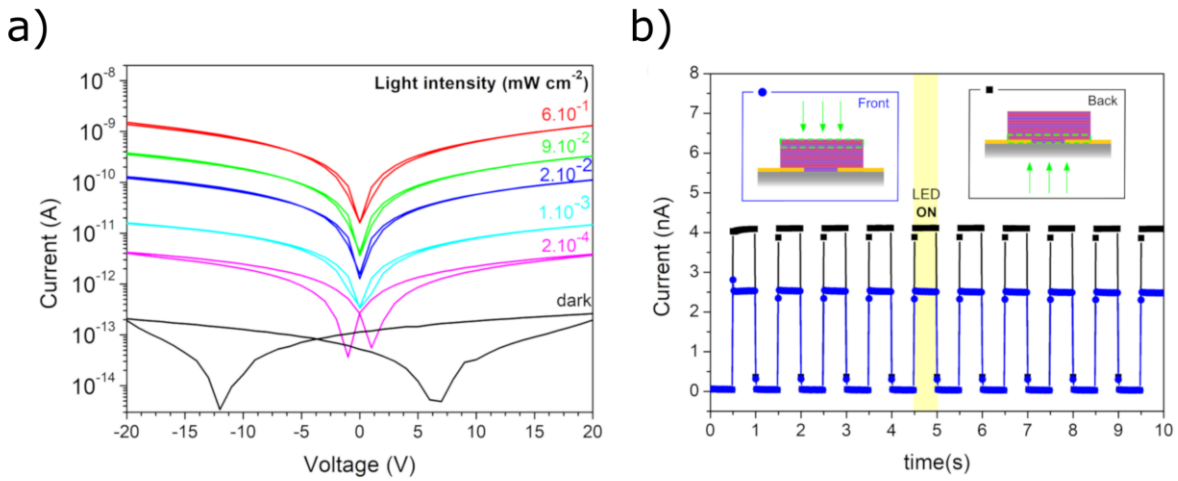

Figure 6.6: UV response. a) I-V characteristic under different light intensity generated by a 380 nm LED. b) Dynamic response under the same LED (380 nm, light intensity 6 x 10^{-1} mW cm^{-2}) in two different configurations shown in the insets. In the front configuration the light is coming from the perovskite side, while in the back configuration the light is coming from the PET side.[158]

To better understand the contribution of the out-of-plane charge collection, the samples were irradiated with the same LED source from the top (front configuration) and from the bottom (back configuration), see inset in Figure 6.6b. At 380 nm wavelength, the total absorption of UV light in PEA_2PbI_4 is expected to be accomplished before 500 nm distance deep inside the perovskite film. In the front configuration, the photons are absorbed close to the perovskite film top surface and the charges created have to travel out-of-planes across the 2D perovskite layers and reach the electrodes at the bottom. In the back configuration, instead, the electron-hole pairs are generated close to the electrodes the collection process should be more efficient as the charges travel mainly at in-plane direction and they have to cross fewer organic spacers. The photocurrent is higher in the back configuration but interestingly the photocurrent in the front configuration is only 37% lower. Even considering the absorption effect of the PET substrate, which at that wavelength is < 20%, the contribution of the out-off-plane direction is still pretty high. Though difficult to quantify with this measure, the transport and the collection processes in the out-of-plane direction can be mediated by *photon recycling*. Photon recycling is a charge carrier diffusion mechanism in which multiple emissions and absorption are involved. The external photon is absorbed in the perovskite layer creating an electron-hole pair. The recombination creates a photon that can travel in the material, and it can be absorbed generating a new electron-hole pair. The process can continue until the electron-hole pair is separated and collected by the electrodes. Photon recycling demands high absorption coefficient and refractive index, small Stokes shifts, and large internal photoluminescence quantum yield. Photon recycling was found recently to be efficient in the 2D layered perovskite BA_2PbI_4 (BA = $C_4H_9NH_3^+$).[164] The PEA_2PbBr_4 perovskite has all the prerequisites for photon recycling and it could explain also the good performances of stacked devices reported in the literature as the one presented in the first chapter.

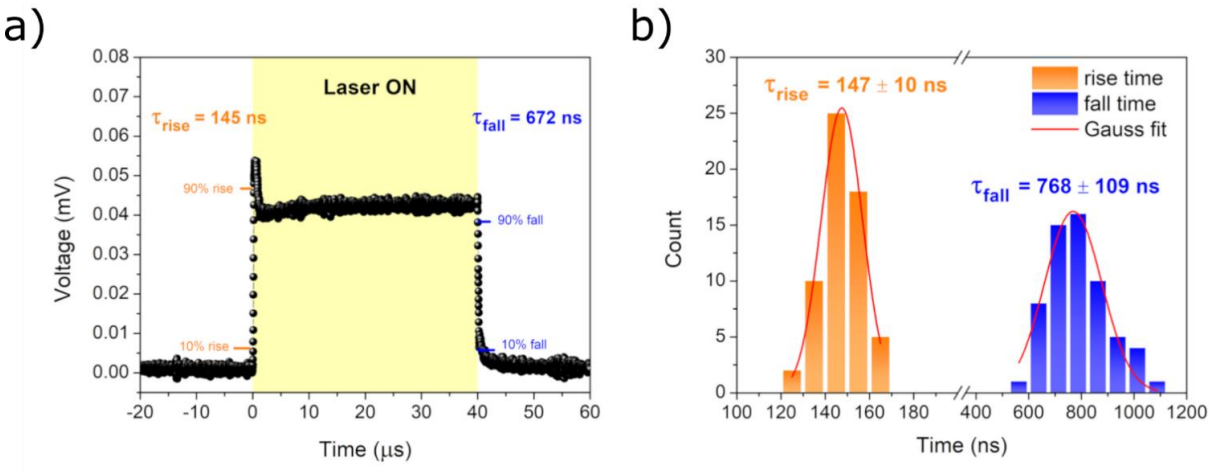

Figure 6.7: Time response. a) PEA_2PbBr_4 dynamic response under 375 nm light produced by a ps-LASER source used in bunch mode. The rise (τ_{rise}) and fall time (τ_{fall}) are calculated between the 10 % and 90 % of the rise or fall transient. b) Gaussian fit of the rise and fall times distributions.[158]

The time response of the device was evaluated by measuring the transient photocurrent under fast pulsed LASER. I used a 375 nm ps LASER working in bunch mode to excite the material. Figure 6.7a shows a photocurrent transient with rise time (τ_{rise}) of 145 ns and τ_{fall} = 672 ns. By acquiring multiple transients it was possible to make some statistics. In Figure 6.7b is reported the gaussian fit for the τ_{rise} and τ_{fall} distributions. The very fast rise time of 147 ± 10 ns is comparable to the state of the art photodetectors and it surpasses all the perovskite detectors reported in literature except for $MAPbI_3$/polymer heterojunctions.[165]

6.1.3 X-ray direct response

The 2D perovskite-based devices were tested under X-rays irradiation to evaluate their potentiality as direct ionizing radiation detectors. Compared to 3D perovskites, layered perovskites have slightly lower density due to the presence of larger organic spacers in the atomic structure.

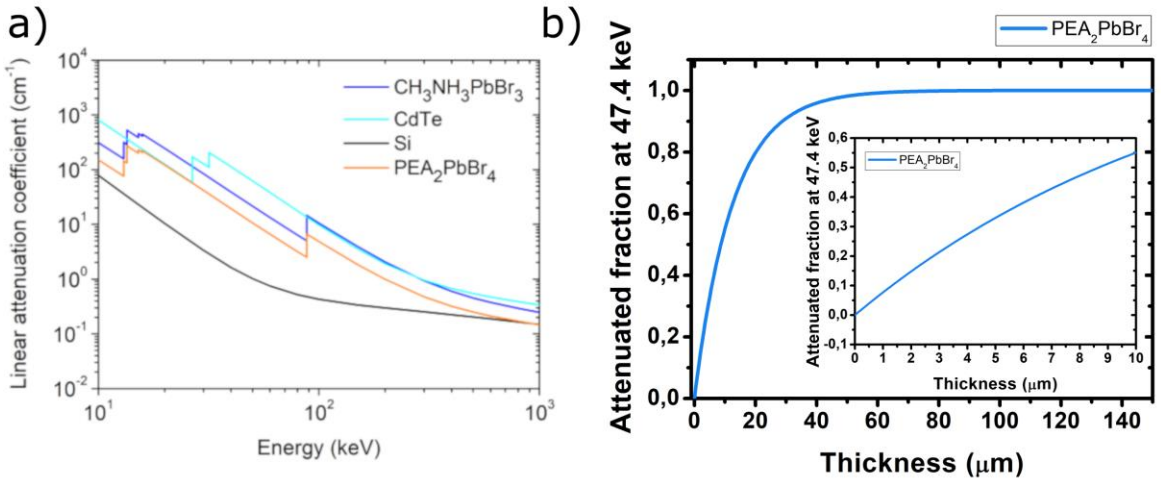

Figure 6.8: X-ray absorption. a) Linear attenuation coefficient as a function of the X-ray energy for different materials including PEA_2PbBr_4.[158] b) Attenuated fraction at 47.4 keV for PEA_2PbBr_4 film. IN the insect is reported a zoom of the low thickness region. At 2 µm the attenuated fraction results in 14%.

The PEA_2PbBr_4 density calculated from the unit cell parameter (triclinic, P-1; a = 11.6150 Å, b = 11.6275 Å, c = 17.5751 Å) results in 2.276 g cm^{-3}. Because of the smaller density, 2D perovskites have smaller X-ray attenuation coefficient as visible below in Figure 6.8a. However, PEA_2PbBr_4 has still much higher attenuation coefficient than silicon, and less than 1 order of magnitude lower than CdTe. In Figure 6.8b is reported the attenuated fraction as a function of the film thickness, at 2 µm the attenuated fraction is equal to 14% at 47.4 keV which is the average energy of the X-ray beam when the tungsten tube is used at 150 kVp.

Figure 6.9a shows the dynamic response of the PEA_2PbBr_4 photoconductor under 150 kVp X-ray beam with incident dose rates ranging from 8 to 66 µGy s^{-1} and 80 V applied bias. The sample was irradiated from the top, with a shutter period of 10 s and duty cycle of 50%, as illustrated in Figure 6.2. The detector exhibits a fast, stable and repeatable box-like response to X-rays proportional to the incident dose rate that was changed every three photocurrent peaks. The X-rays induced photocurrent scales with increasing the applied bias to the two-terminal device, while the dark current remains stable and low even at large applied bias (100 V) as visible in Figure 6.9b, where the

dose rate was kept constant and the bias was increased every three photocurrent peaks of 10V. The dark current is remarkably stable with minimal disturbances upon changing the bias. The Figure 6.9c shows the photocurrent extracted at 3 and 80 V. Increasing the bias applied the device performances significantly improve but it was possible also to work at low voltage, a prerequisite for wearable and battery-operated sensors. From the plot is also visible a non-linear behaviour of the photocurrent with the dose rate. In Figure 6.9d is reported the photocurrent, in orange, and the sensitivity normalized by the device area 0.63 mm^2, in black. For the photocurrent, a sub-linear behaviour was found with an exponent α = 0.65. At higher dose rates, the concentration of excitons in the material increases and the lower sensitivity observed could arise from exciton-exciton annihilation; that is an exciton non radiatively recombines in the course of colliding with another exciton transferring to it the energy reducing the available charges to be collected. This effect has been reported for iodine based 2D hybrid perovskite.[166] The sensitivity was calculated using the derivative of the photocurrent, finding values up to 806 ± 6 µC Gy^{-1} cm^{-2} under X-rays at 150 kVp, with an applied bias of 80 V and dose rates in the range 8 - 100 µGy s^{-1}. The extracted sensitivity is at least one order of magnitude higher than α-Se.

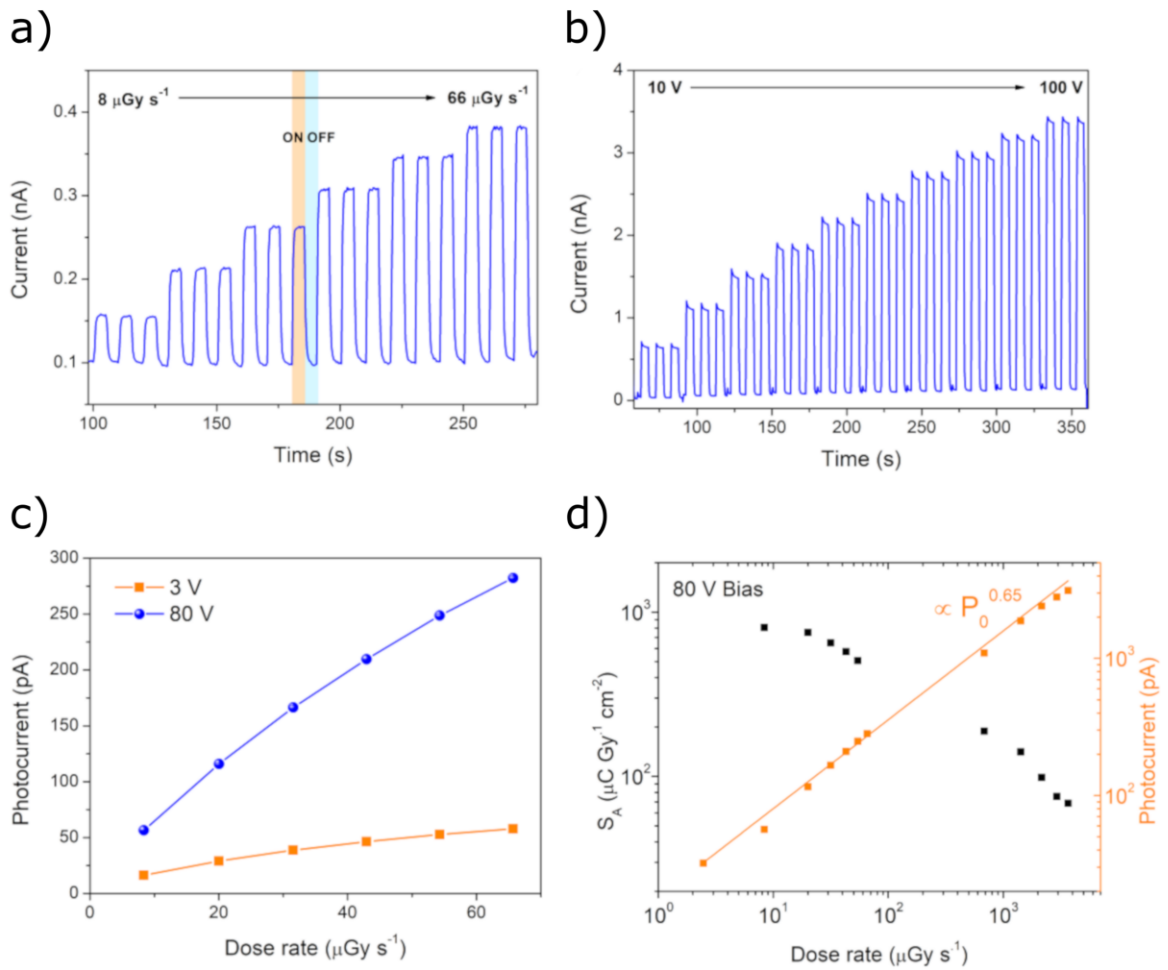

Figure 6.9: PEA_2PbBr_4 X-ray response. a) Dynamic response of PEA_2PbBr_4 thin-film under modulated 150 kVp X-ray beam. Every three peaks the incident dose rate in increased up to 66 μGy s^{-1}. b) Dynamic response under modulated 150 kVp X-ray beam as a function of the bias applied. Every three peaks the bias is increased of 10 V. c) Photocurrent versus incident dose rate with 3 and 80 V applied to the sample. d) Area Sensitivity in black and photocurrent in orange as a function of the dose rate for a large dose rate range.[158]

In Figure 6.10 is reported the acquired transient at the lowest detectable dose rate 57 nGy s^{-1}. This value is the lowest reported for thin-film perovskite detectors,[92,96,110,167] and it is comparable or even lower than some single crystal detectors.[49,52] From the graph is possible to see the extremely low dark current. Although an initial drift, it stabilizes just above 80 fA. This measurement was performed by positioning the sample as far as possible from the X-ray tube, using Al filters and by measuring the current with the electrometer.

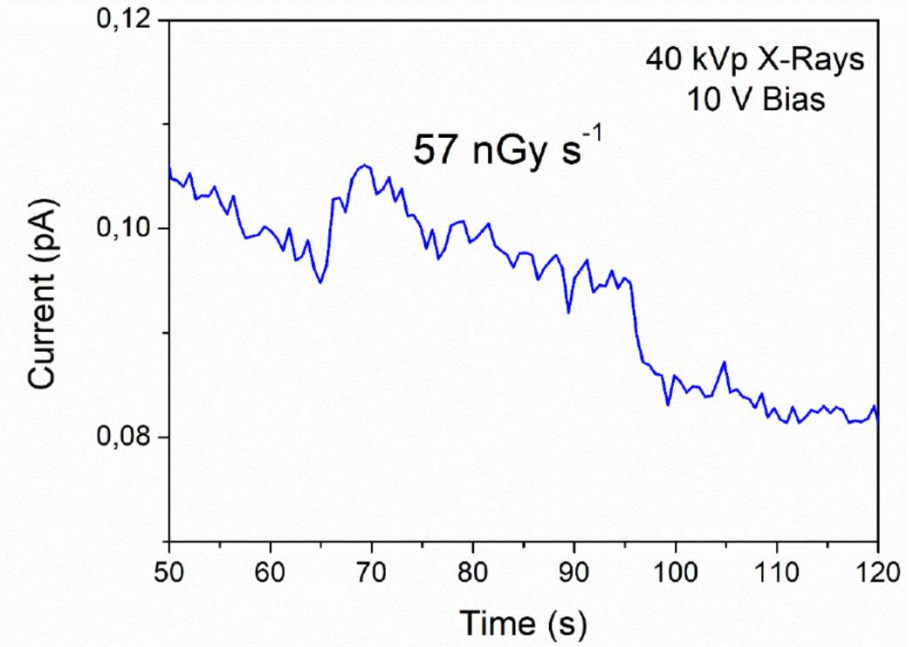

Figure 6.10: LoD. Current signal acquired under extremely low dose rate at 10V bias.[158]

The PEA_2PbBr_4 devices are exceptionally stable under long-term operation and exhibit no signs of drifting or bias stress under increasing bias, as shown in Figure 6.11.

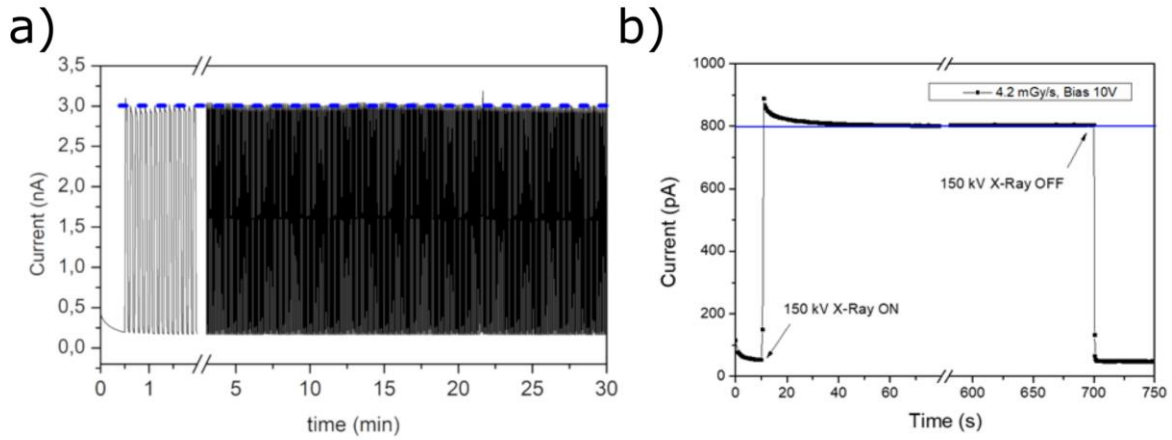

Figure 6.11: Operational stability.[158] a) Stability of the dynamic response to X-rays at a constant 80 V applied bias. The dose rate impinging on the sample was 4.2 mGy s^{-1} and the total dose resulted equal to 3.8 Gy over 300 pulses. The test was performed after 80 days of storage in ambient conditions b) Operational stability under constant illumination with 150 kVp X-ray beam and a dose rate of 4.2 mGy s^{-1} for a total dose of 2.9 Gy.

The photocurrent and dark current remain perfectly stable even after 30 min of continuously pulsed exposure to X-rays at 150 kVp, with high dose rate of 4.2 mGy s^{-1} and a high applied bias of 80 V for a total received dose of about 3.8 Gy. The measurement shown in Figure 6.11a was performed 80 days after the fabrication of the device, which was stored at room temperature and with ≈ 20% relative humidity, proving the high environmental stability of the material. The operation stability was also tested under continuous 150 kVp X-ray exposure, see Figure 6.11b. Initially, a decrease of the photocurrent is observed until the current stabilize and remains constant for more than 10 min, for a total dose of 2.9 Gy.

To assess the feasibility of a flexible device, we monitor the dark current and the photocurrent under bending conditions gradually decreasing substrate curvature radii thus increasing the strain in the perovskite layer.

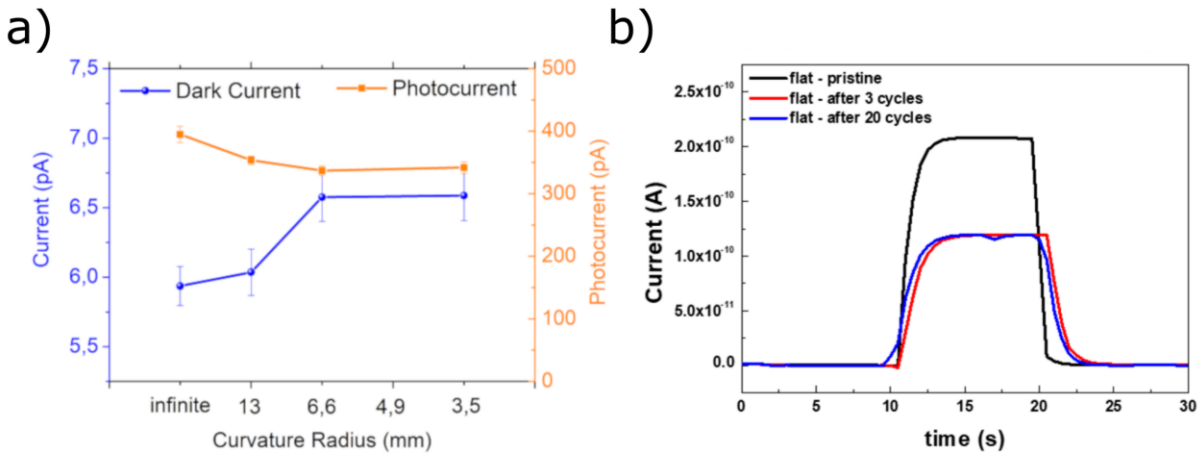

Figure 6.12: Flexibility.[158] a) Dark current (in blue) and photocurrent (orange) as a function of the bending radius under 40 kVp X-ray beam with a dose rate of 3.6 mGy s^{-1}. b) Dynamic response under 380 nm wavelength LED measured in the flat position after multiple bending cycles.

Figure 6.12a shows the device behaviour from infinite bending radius (flat) to 3.5 mm. For radii smaller than 6.6 mm the dark current increases and the photocurrent slightly decrease, with small variations of about 10%. At smaller radii, they are stable down to of 3.5 mm. The photocurrent acquired under UV light in the flat position after

multiple bending cycles shows permanent damage after a few bending cycles, but interestingly the damage does not increase after 30 bending cycles.

6.2 Gamma ray detector based on 2D perovskite

The 2D perovskite photoconductor detectors described in the previous section showed extremely low limit of detection and considerable response at 150keV of X-ray. The detectors have been optimized (i.e. channel length and active area) to work at low bias for the detection of gamma ray emitted by radiotracers at the IRCCS of Reggio Emilia, with the aim to develop a wearable dosimeter to monitor the intravenous injection of radiopharmaceutical drugs.

6.2.1 Detecting 511 keV gamma ray from ^{18}F

^{18}F is a positron emitter with a half-life of 109.7 min and it is used as radiotracer in PET imaging systems. The emitted positron annihilates with a nearby electron emitting two 511 keV photons in opposite directions. I tested the 2D perovskite detector with the apparatus described in section 3.2.4 of the experimental chapter. Three different radiotracer solutions with different activity were prepared and measured with a calibrated commercial detector. The shutter was set with a period of 20 s with duty cycle of 50%. Every three peaks the source was changed while the shutter was in the off state. I tested two devices with the same channel length (10 µm)

but different active area. The dynamic response is reported in Figure 6.13a; the signal is reported as current density for a better comparison.

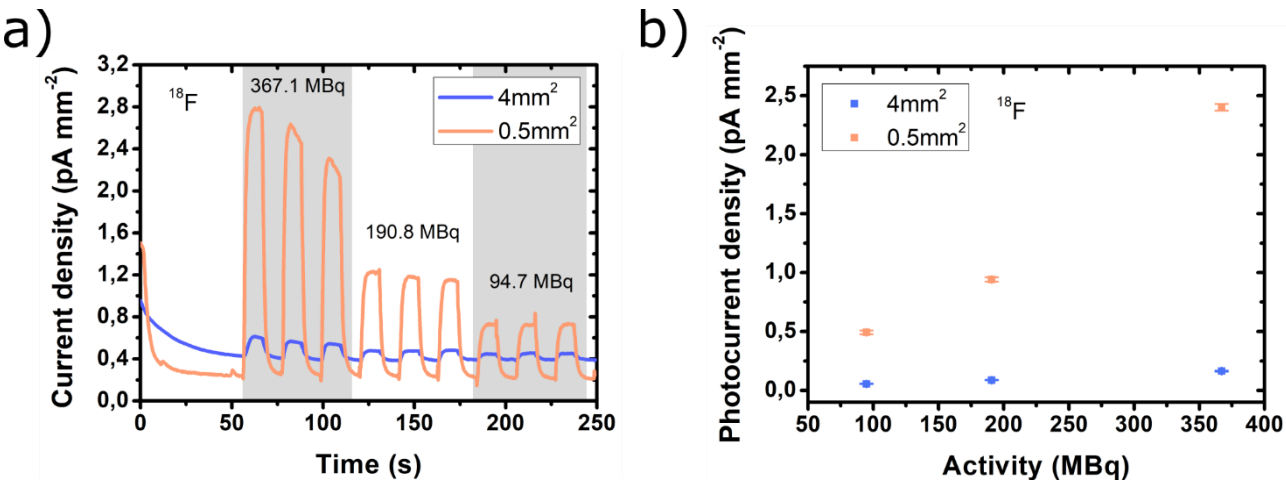

Figure 6.13: PEA_2PbBr_4 response to ^{18}F. a) Dynamic response at 2 V of two detectors with different active areas. The data were collected using three ^{18}F with decreasing activity with a source to sample distance of 8 mm. b) Photocurrent density as a function of the source activity.

The device with 4 mm^2 active area showed a longer relaxation time and higher dark current. The longer relaxation time can be understood by considering capacitive effects, the larger the area larger the capacitance of the system. When a bias is applied the time for the system to reach equilibrium will be higher if the capacitance is higher. Interestingly, the device with 0.5 mm^2 area showed a nice response with one order of magnitude higher photocurrent with the 367.1 MBq source. Although the first three peaks are not properly stable, the remaining peaks even at low activity are repeatable. In Figure 6.13b, the photocurrent as a function of the source activity is reported. The smaller area detector performed better than the 4 mm^2 one. The reason is probably a not sufficient homogeneity in the perovskite film leading a non-scalable response with the device area.

A device with a matrix of 4 identical pixels was used to measure the decay of ^{18}F. The device was positioned underneath the radiotracer vial and kept there for more than 4 hours; the result is reported in the figure below (Figure 5.13). To acquire the signal a

portable, battery powered electronic board with Bluetooth was used. With this configuration, the source and the sample were kept in a closed room and the measurement was controlled safely. The 4 pixels have very similar response, with an exponential decay following the natural radioactive decay of fluorine.

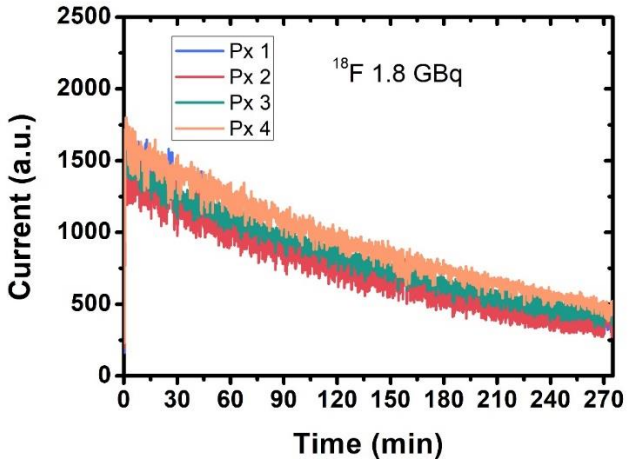

Figure 6.14: ^{18}F decay. Current signal from 4 different detector pixels positioned underneath a ^{18}F source for more than 4 hours.

6.2.2 Detecting ^{99}Tc gamma ray

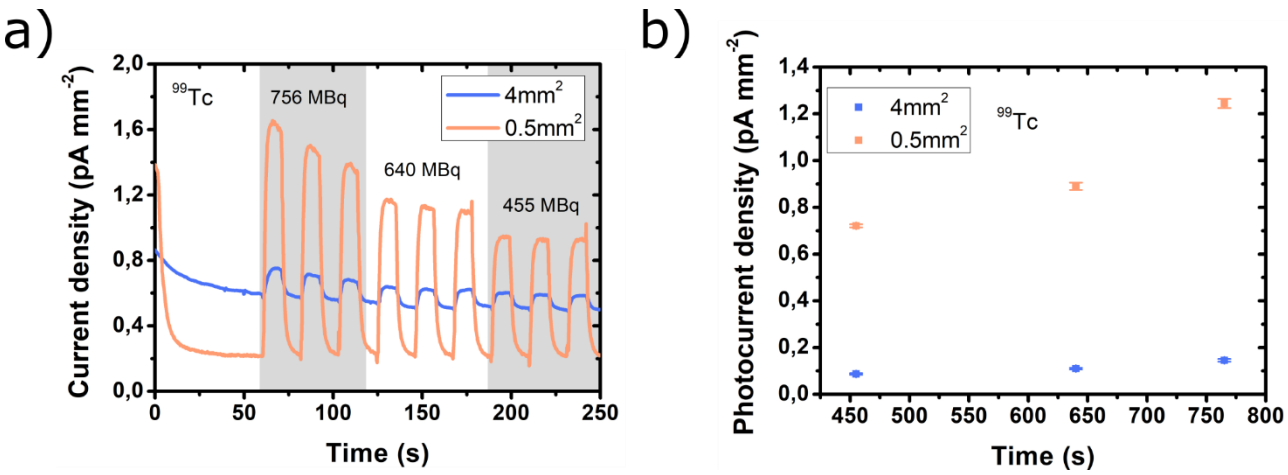

Figure 6.15: PEA_2PbBr_4 response to ^{99}Tc. a) Dynamic response at 2 V of two detectors with different active areas. The data were collected using three ^{99}Tc with decreasing activity located at 8 mm from the sample. b) Photocurrent density as a function of the source activity.

The detector response under the 140 keV photons emitted by ^{99}Tc, the radiotracer used in SPECT analysis. As for fluorine, different activities were tested in decreasing order. The findings concerning the area effect are the same as for fluorine.

6.2.3 Monitoring the injection of radioactive drugs

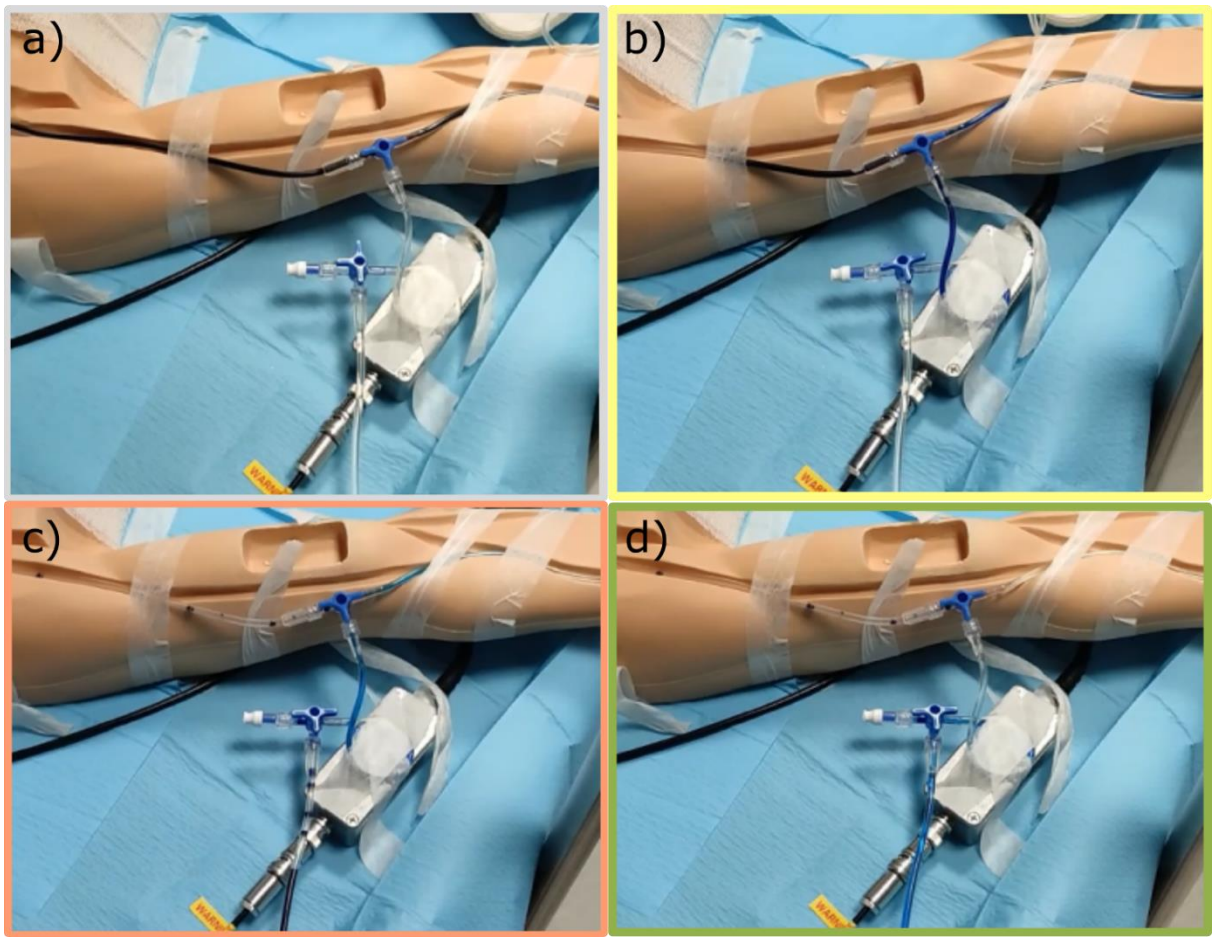

Figure 6.16: Injection sequence. a) The blue coloured radiotracer solution is injected in the plastic main tube simulating the vein. b) The valve controlling the extravasation is opened and the radiotracer starts to flow in the secondary line rolled up and placed over the sample box simulating the accumulation of radiotracer in an unwanted region of the body. c) After a while the extravasation line is opened and the radiotracer starts to flow away from the detector, to note that the colour now is less intense. d) A physiological solution is injected in the system flushing away the remaining radiotracer.

In medical treatment or diagnostic, the radiotracer needs to be injected in the patient's body. Sometimes, after the injection, an extravasation can occur. The radiotracer leaks out from the vein and accumulates in unwanted regions of the body. The accumulation causes severe injury in the patient. The detector was used to monitor the flow of the ^{18}F radiotracer in a simulated injection procedure. A phantom with plastic tubing was used to simulate the blood vessels. A lead shielded syringe was used to inject the radioactive solution with a blue dye in the system. The detector was placed inside a faraday cage an electrically connected to the electrometer for current measurement. The main vain was simulated by an almost straight plastic tube, while the extravasation region, close to the detector, was simulated by a plastic tube rolled up. The experimental sequence is reported in Figure 6.16. Here is listed the sequence used to simulate the extravasation:

A. *Injection (grey).* The radiotracer is injected in the main vein and It flows to the opposite direction of the injection point (towards the heart, in the real case). In the picture, an intense blue colour is visible.
B. *Extravasation (yellow).* A valve is opened causing a partial flow of radiotracer in the secondary tube accumulating above the detector.
C. *Release of the accumulated radiotracer (orange).* A valve at the end of the system is opened causing the radiotracer accumulated over the detector to flow away.
D. *Flushing (green).* At the end, physiological solution is released inside the tube cleaning all the system from the radioactive drug.

In Figure 6.17 is reported the recorded signal, the coloured regions correspond to the different steps in the injection procedure. The activity used for the experiment is comparable to the one used during clinical procedures and the detector was able to monitor the whole processes. A small increase in the current was measured soon after the injection of the radiotracer in the main vein (grey). When the valve was opened

leading the extravasation, a higher increase in the sensor current was observed. The current started to decrease immediately when the accumulated radiotracer was released from the extravasation region. A low current signal remained until the physiological solution reached the extravasation region and cleaned the tube from the ^{18}F atoms. After few seconds the signal returned to the base line level. The amplitude of the signal involved are very small but tanks to the unique dark current stability of 2D perovskite it was possible to measure the signal emitted by a radiotracer.

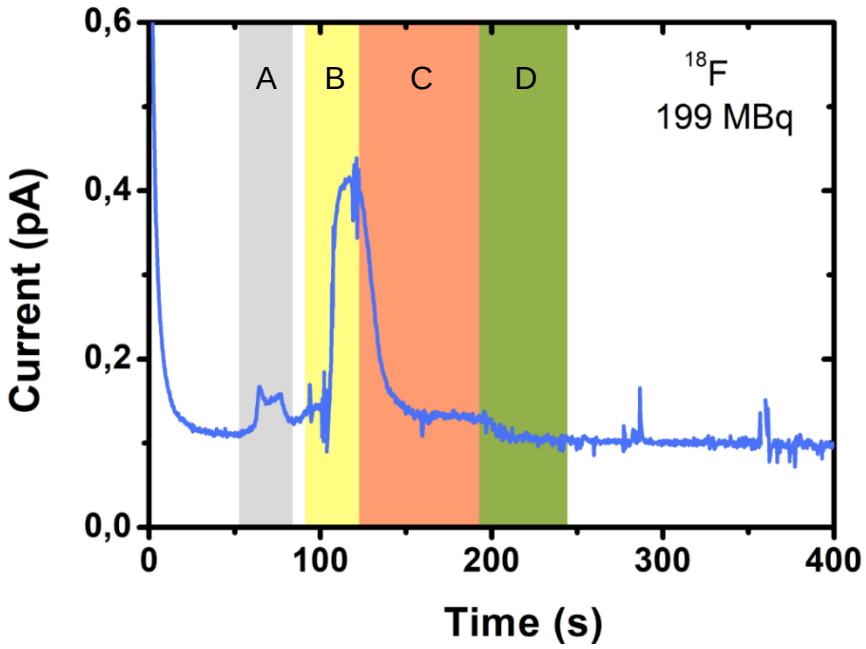

Figure 6.17: Monitoring the injection. Detector current signal, acquired at 2 V, during the whole injection procedure described above. The coloured region refers to different regime in according to the Figure 6.16.

6.2.4 FORTRSS Demo

My research on gamma detectors was founded by the flexible large-area patches for real-time detection of ionizing radiation (FORTRESS) project. In the framework of the project I developed a 8 pixels sensor based on PEA_2PbBr_4 thin-film. INFN-TTLab

developed the readout electronics able to provide bias and measure the current of 8 pixels simultaneously with pA precision. In Figure 6.18a is reported a picture of the readout electronics, closed in the plastic box with the project logo, connected via a commercial flat-cable and a ziff connector to the sensor.

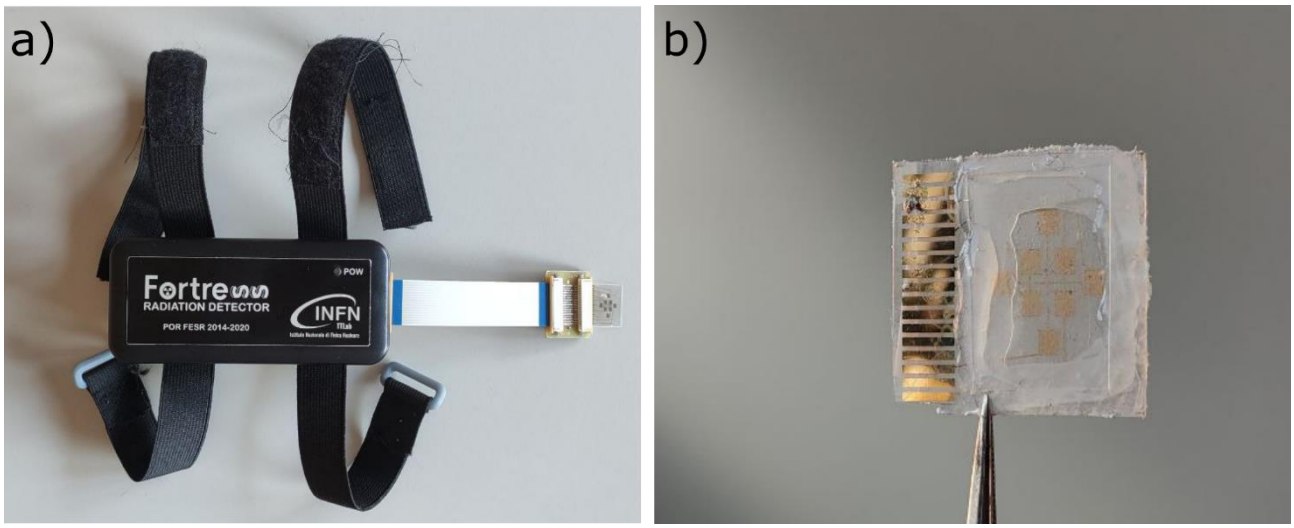

Figure 6.18: Demo FORTRESS. a) Picture of the demo developed in the FORTRESS project. The sensor is connected via a ziff connector to the readout electronics that can read 8 channels simultaneously. The measured signal is sent via Wi-Fi to a computer for the data visualization. b) Picture of the sensor patch with 8 pixels. The metal contacts were design to fit a commercial ziff connector and it was encapsulated with 125 µm PEN.

In Figure 6.18b a detail of the patch developed with 8 pixels and gold traces fabricated with photolithography to match the commercial ziff. The demo was developed to monitor a radiotracer injection, so the straps were added to wear the electronic and sensor on the patient's harm and the detector can be placed in contact to the skin near the injection point. The measured signals are transmitted via Wi-Fi connection to a computer for data visualization and recording.

6.3 Mixed 2D-3D perovskite for proton beam monitoring

Hadrontherapy treatments are the cutting-edge medical tool for fighting cancer[168]. During the treatment, the real-time monitoring of proton beam's flux, energy and position is of extreme importance for successful therapies. 2D hybrid lead-halide perovskites have low, stable dark current and high environmental stability. On the other hand, 3D perovskite offers high charge transport performance. The combination of 3D and 2D perovskite has been used in the literature for the fabrication of solar cell and LEDs with quasi-2D perovskite as an absorbing layer with increased stability.[169,170] Quasi-2D perovskite are layered perovskite with chemical formula $(A)_2(A')_{n-1}Pb_nX_{3n+1}$ with n > 1. They possess the same layered structure of pure 2D perovskite with n=1, but they have n octahedra sheets between the organic spacer A. Here, I combined $MAPbBr_3$ with PEA_2PbBr_4 to obtain a perovskite with n = 6. Interestingly, the obtained perovskite layer is a combination of $MAPbBr_3$ and PEA_2PbBr_4 rather than a new quasi-2D perovskite phase. The perovskite deposited on interdigitated metal contacts has been used for direct real-time proton beam monitoring.[171]

The 1M 3D perovskite ($MAPbBr_3$) was obtained from $PbBr_2$ and MABr mixed overnight in DMF with 1:1 molar ratio. The 2D perovskite solution was obtained by mixing PEABr and $PbBr_2$ in 1:2 molar ratio in DMF to obtain a 1M solution. The mixed perovskite solution was prepared by adding a defined volume of 1M PEA_2PbBr_4 solution to the 1M $MAPbBr_3$ solution. Different 2D perovskite concentrations were mixed and the resulting solutions were deposited by spin-coating at 2000 rpm for 30 s

on 125 µm thick PET substrates with pre-patterned interdigitated gold electrodes. The metal electrodes were fabricated on plastic substrates with the same lithographic technique described in the experimental section 3.1.2. The resulting interdigitated electrodes have 30 µm channel length, 9.6 mm channel width and 1 mm^2 total area.

6.3.1 Improving film coverage by adding 2D perovskite PEA_2PbBr_4 in the 3D $MAPbBr_3$

For the realization of the 3D/2D mixed perovskite films we used a solution composed of the two precursor solutions mixed together.

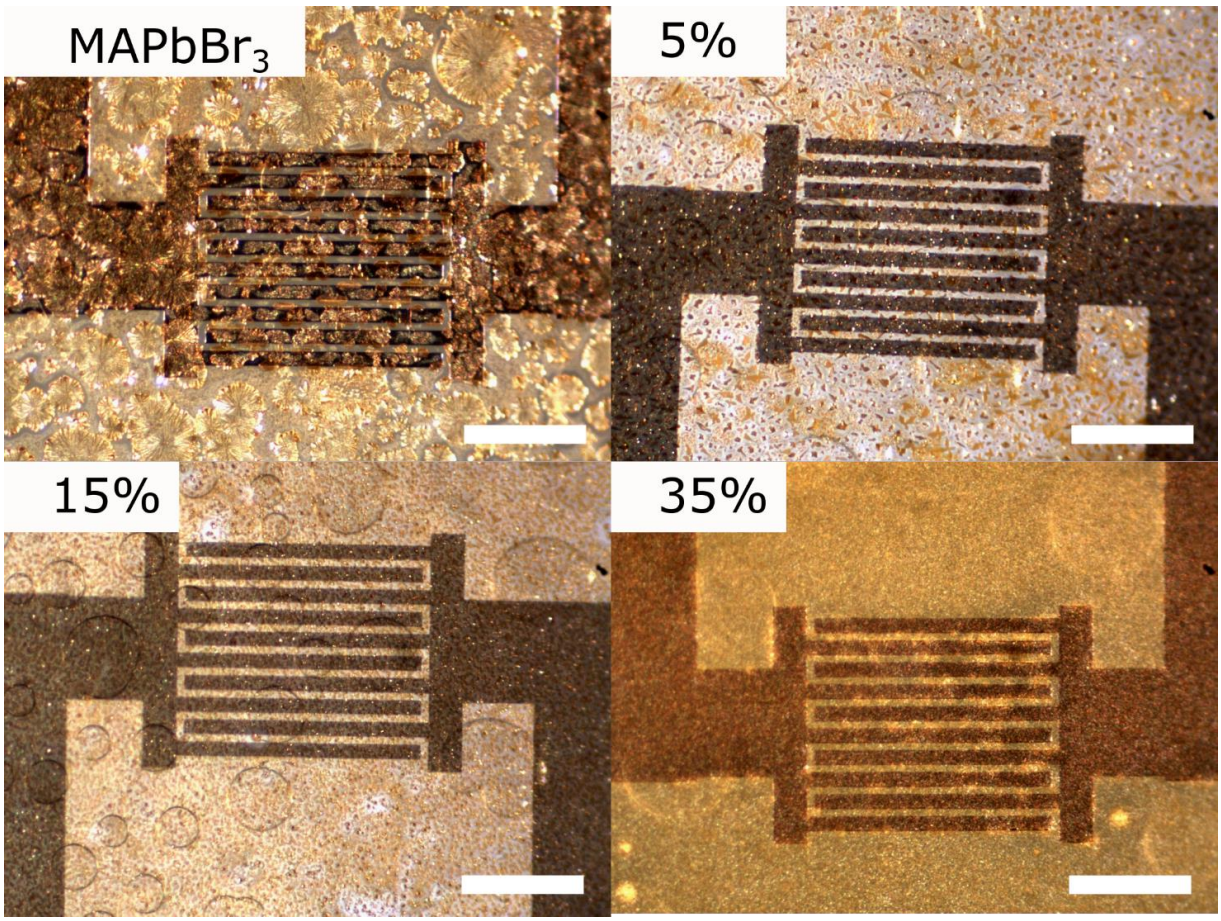

Figure 6.19: Material coverage. Optical microscope images of pure $MAPbBr_3$ and $MAPbBr_3$ mixed with X% mol/mol of PEA_2PbBr_4 films deposited by spin-coating on a PET substrate with interdigitated Au metal contacts. The scale bar in all the pictures is 500 µm.

In Figure 6.19 are reported the optical microscope picture of films with different 2D perovskite concentrations On PET pure $MAPbBr_3$ formed flower-like crystals with poor surface coverage, from the picture are visible the empty channels of the interdigitated metal contact. With 5 % mol/mol, corresponding to 5 %v/v since the solution are 1M, the perovskite crystallized preferentially in needle-like crystals with better surface coverage. Increasing the 2D perovskite concentration to 15 %, the needles disappear and the surface coverage and uniformity improve even more. I tested concentrations up to 35 % of PEA_2PbBr_4, which resulted in the best mixture concerning surface coverage with no pin-holes or gap in the channels. The film was characterized by means of grazing incidence X-ray diffraction (GIXRD) and atomic force microscopy (AFM) for the morphology. The AFM maps acquired showed small cubic crystallites with 2.5 µm side on the surface of the deposited films, see Figure 6.20a. By scratching the sample and measuring the AFM profile a thickness of 4 µm was measured. The GIXRD pattern in Figure 6.20b was acquired at the XRD1 beamline at the Electra synchrotron facility. The software GIDVis allowed to represent the diffracted intensity in the real space on the detector as a function of reciprocal lattice vectors components q_{xy} and q_z and to project on the image the predicted positions for the different phases present in the samples.[172]

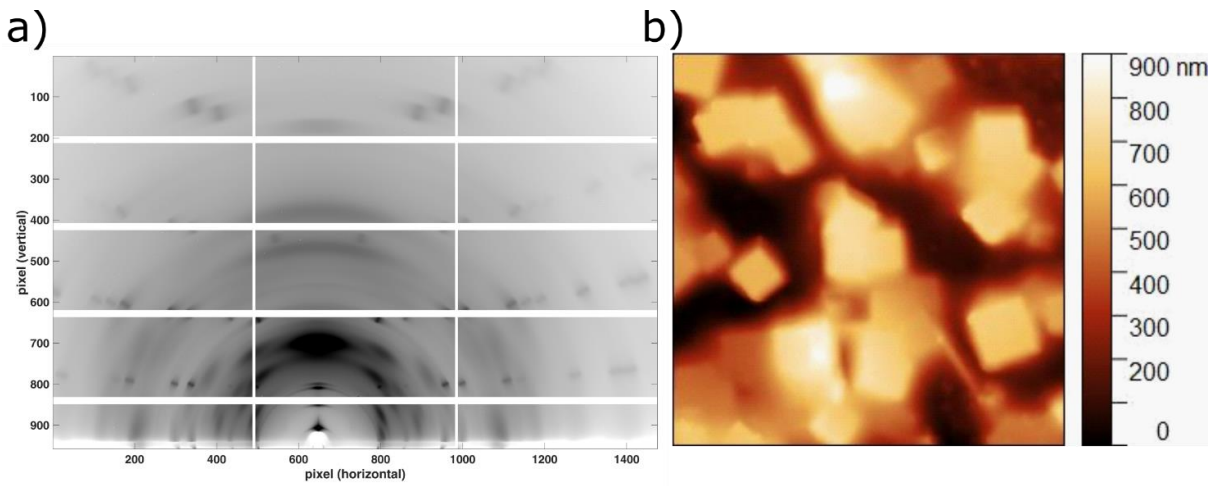

Figure 6.20: Film crystallinity and morphology.[171] a) GIXRD pattern of the mixed perovskite film with 35 % of 2D perovskite. b) AFM image of the mixed perovskite film showing cubic crystallites on the surface. Scale bar 5 µm

The predicted positions of the peaks were drawn using the following cell informations :

- $MAPbBr_3$ perovskite phase, (COD: 1545320): Space group Pm-3m (221) – cubic

  a = 5.9195 Å; b = 5.9195 Å; c = 5.9195 Å

  α = 90°; β = 90°; γ = 90°

  Orientation (0 0 1)

- $(PEA)_2PbBr_4$ phase (COD: 2224096): Space-group P-1 (2) - triclinic

a=11.6150 Å; b=11.6275 Å; c=17.5751 Å

α = 99.5472°; β = 105.7245°; γ = 89.9770°

Orientation (0 0 1)

- PET phase33: Space-group P-1 (2) triclinic

a = 4.56Å; b = 5.94 Å; c = 10.75 Å

α = 98.5°; β = 118°; γ = 112°

Orientation (1 0 0)

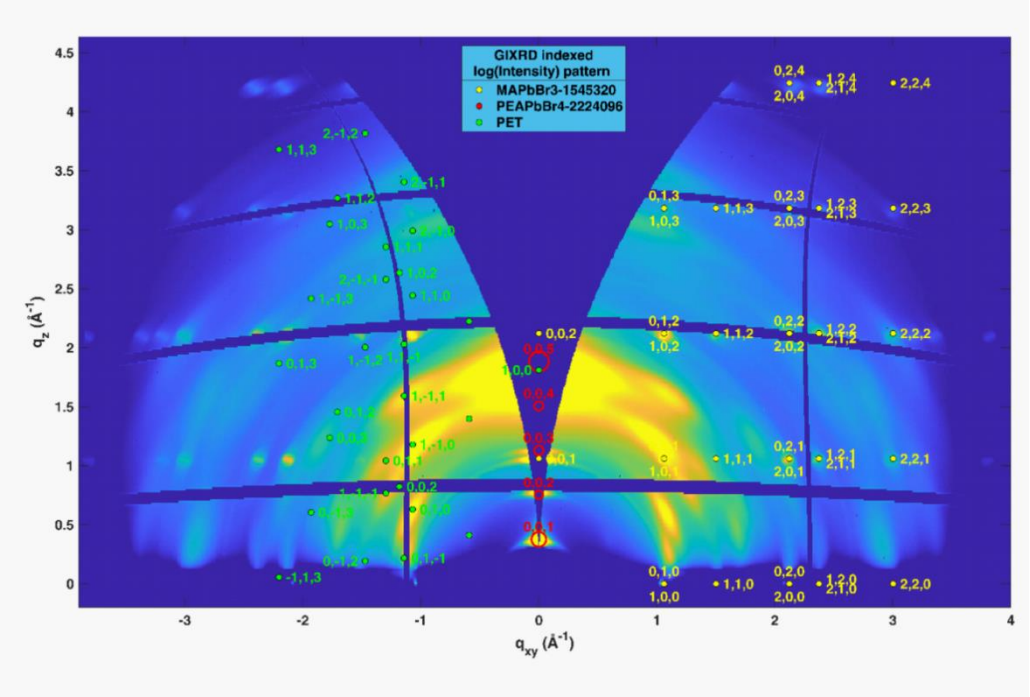

Figure 6.21: Mixed perovskite film GIXRD. The square root of diffracted intensity as a function of reciprocal lattice vector components q_{xy} and q_z. On the image are reported expected diffraction spots positions and indexes from the three components of the sample, namely 3D phase $MAPbBr_3$ (yellow) 2D phase $(PEA)_2PbBr_4$ (red), both oriented with c axis perpendicular to the sample surface, and PET from the sample substrate, with a axis out of sample surface.

The pattern shows the characteristic peaks of $MAPbBr_3$ and $(PEA)_2PbBr_4$ as well as those of the PET substrate. It appears that the $MAPbBr_3$ perovskite phase is well-oriented both in the substrate plane and perpendicularly to it, while (PEA)2PbBr4 shows clear spots only in the out of plane direction, denoting a multi-layered organization with repetition parameter c, showing poor long-range order in the substrate plane. In accordance to what is visible from the AFM image, the two perovskites formed two different phases as also confirmed by the optoelectronic characterizations shown in Figure 6.22. The optoelectronic properties of the mixed perovskite film were investigated to evaluate its suitability for the fabrication of ionizing radiation detectors. The photocurrent spectrum shows a clear onset at 550 nm, from the Tauch plot a band gap of 2.29 ± 0.08 eV was extracted. The obtained value

is comparable to the single crystal band gap reported in literature and identical to the band gap of $MAPbBr_3$ single crystal fabricated in our lab with the same precursors.[151,173,174] The photoluminescence (PL) spectrum of perovskite films is shown in Figure 6.22b exhibits the characteristic peak of $MAPbBr_3$ microcrystals at 521 nm and that of $(PEA)_2PbBr_4$ at 400 nm,[175,176] confirming the co-existence of the two phases in the compound. The $(PEA)_2PbBr_4$ photoluminescence peak is cut by the optical filter used to avoid the signal coming from the 375 nm LASER used as the excitation source.

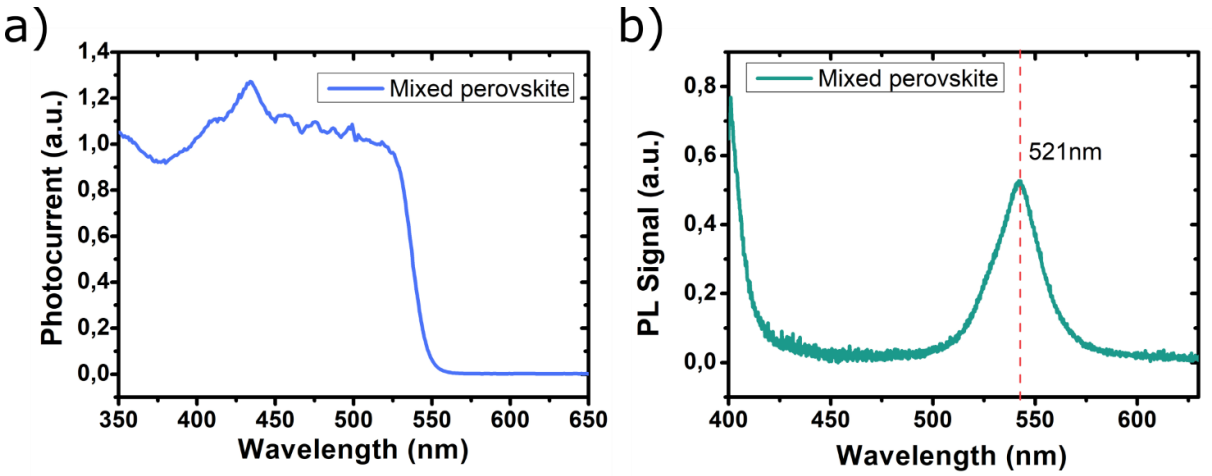

Figure 6.22: Optoelectronic characterization of mixed perovskite films.[171] a) Photocurrent spectrum of a mixed perovskite film. b) PL spectrum of the same film showing a peak at 521 nm and one at 400 nm cut by an optical filter.

Although both phases seem to be optically active, form the photocurrent spectra it seems that the main material contributing to the collection of photogenerated charges is the 3D perovskite phase. The time response of the mixed material was evaluated using the pulsed laser source with 50 ms burst duration at 5.3 mW. The photocurrent transients are reported in Figure 6.23. The rise and fall time, equivalent to the time interval needed to increase the photocurrent from 10% to 90% of its maximum value or decrease from 90% to 10%, resulted in 32 ± 1 µs and 275 ± 12 µs respectively.

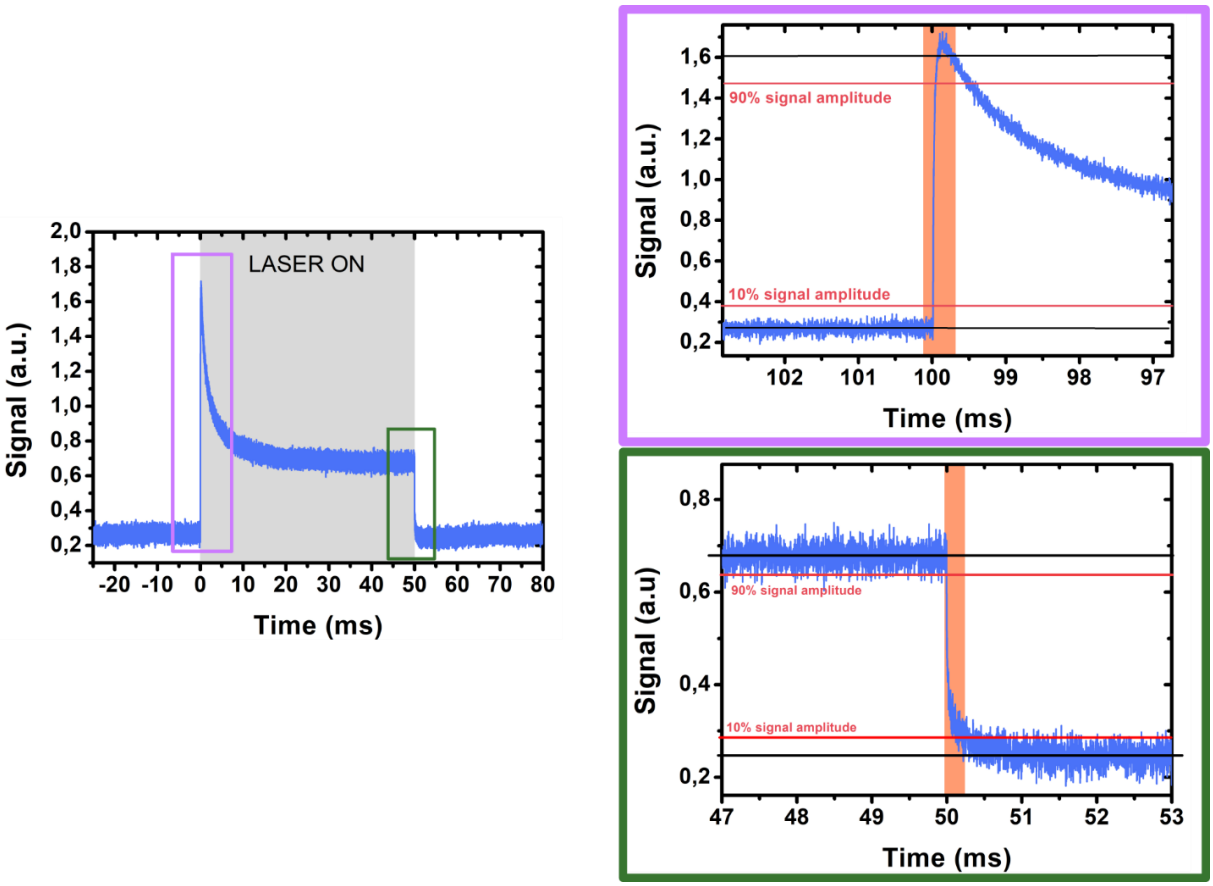

Figure 6.23: Time response of mixed perovskite films. Rise and fall time extracted by the rise and fall transient of a 50 ms long 375 nm LASER pulse.

For medical applications, the possibility to have a flexible and conformable ionizing radiation detector is desirable, especially in beam monitoring where a wearable device can be positioned on the patient for a dose delivered measurement as precise as possible. The flexibility tests of the fabricated devices are shown in Figure 6.24. Under increasing bending radii the I-V characteristics of the mixed perovskite film exhibited excellent stability down to a bending radius of 4.7 mm, comparable to the dimension of a human finger. Increasing the bending radius to 3.1 mm the current starts to decrease. However, the detector completely recovers its original current value once brought back in flat condition. The device also demonstrates high stability to the mechanical stress provided by multiple bending cycles, with unvaried I-V curves after up to 50 bending cycles at 4.7 mm radius, as shown in Figure 6.24d.

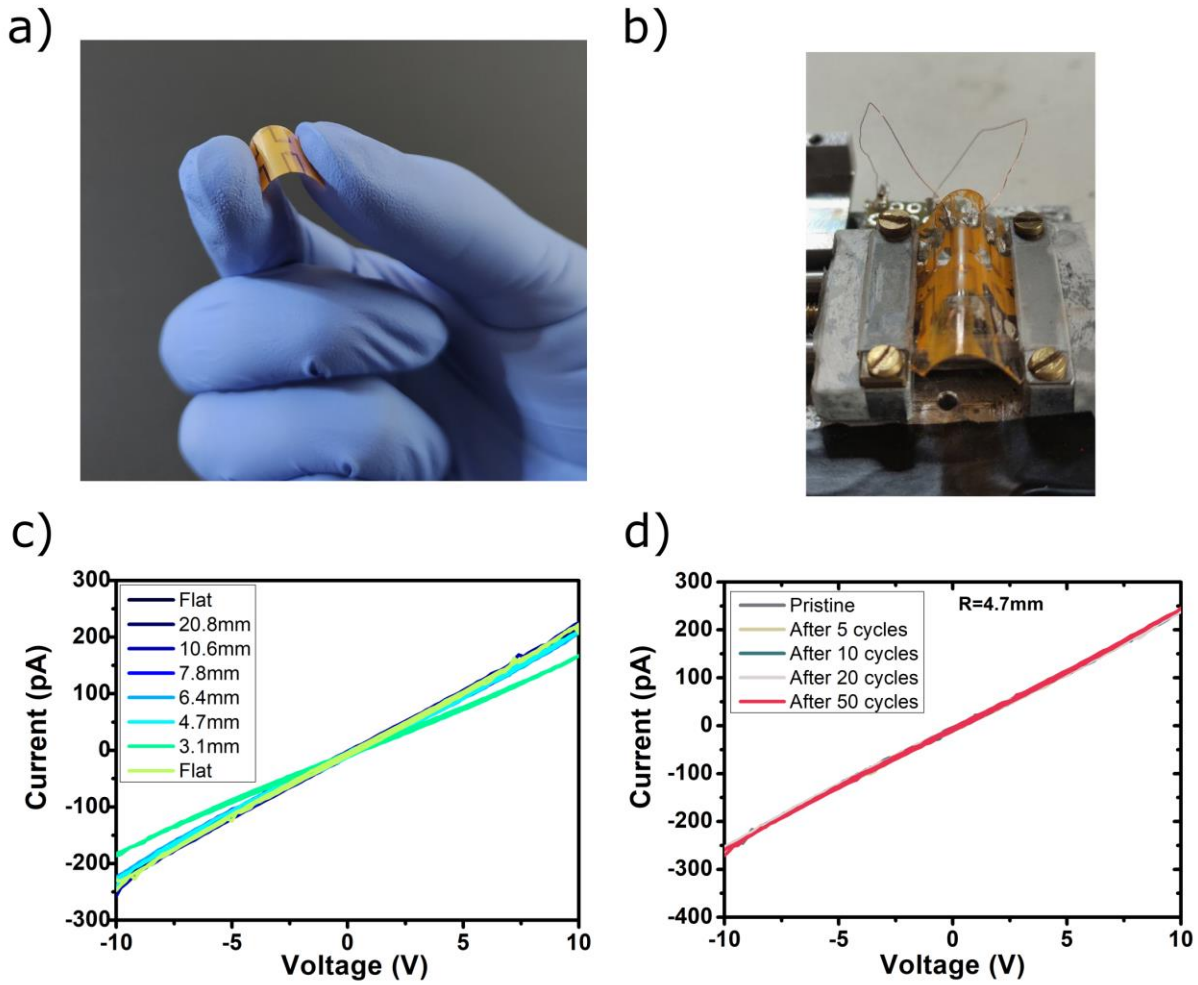

Figure 6.24: Flexibility test.[171] a) Picture of a bent device. b) Stretcher mechanism used to bend the sample during the measurements. c) I-V characteristics measured at various banding radii showing a slight degradation at 3.1 mm. At the end of the series, the sample was remeasured in the flat position. d) I-V curves measured in the flat position after multiple banding cycles.

6.3.2 Proton detection by mixed 2D-3D perovskite

The measurements under proton beams of the mixed perovskite detectors were performed at the LABEC ion beam center (Laboratory of Nuclear Techniques for the Environment and Cultural Heritage, INFN Firenze, Italy),[177] employing a 5 MeV proton beam extracted into the atmosphere, provided by the 3 MV Tandetron

accelerator as described in the experimental section 3.2.5. To understand the energy released by the protons inside the perovskite layer a stopping and range of ions in matter (SRIM) simulation has been performed.[178] The linear energy transfer (LET) as a function of the penetration depth is reported in Figure 6.25. The proton beam loses 390 keV in the air between the extraction point and the sample. The energy released by each proton inside the 4 µm thick mixed perovskite layer and inside the 125 µm PET substrate resulted about 59 keV and 1550 keV respectively.

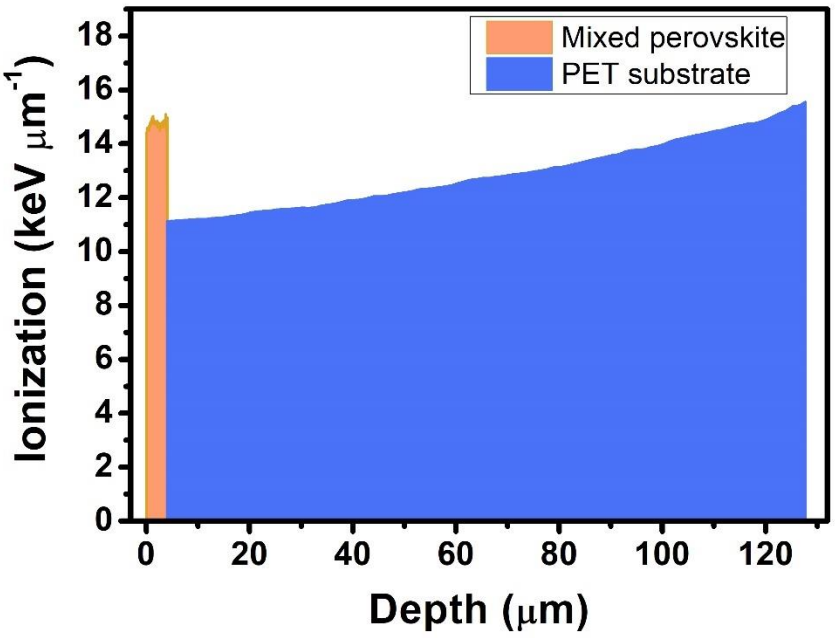

Figure 6.25: Proton interaction. Energy released in the sample and in the substrate by a single 5 MeV proton, calculated by SRIM Monte-Carlo simulation.[171]

The response under the proton beam was characterized by measuring the current flowing in the detector upon 10 s irradiation cycles at different bias voltages, i.e. 10 V, 5 V, 1 V. The low bias tested are compatible with a wearable device. Figure 6.26a reports the current flowing in the detector upon 10 s irradiation shots of increasing fluxes between 4.5×10^5 H^+ cm^{-2} s^{-1} and 1.4×10^9 H^+ cm^{-2} s^{-1} with 1 V of bias applied. Even at low bias, the response to protons is fast, box-like and proportional to the incident flux within the wide range (almost 4 order of magnitude) of fluxes employed.

While for organic semiconductors under the same proton beam an integration effect was observed,[179] here the signal returned to the base line value as soon as the beam turns off. The proton induced current as a function of the proton flux is shown in Figure 6.26b. For all the bias tested, the detector showed a non-linear behaviour with the flux, the plot is reported in logarithmic scale for better data readability. Thus, the sensitivity was extracted by calculating the derivative of the proton induced current over the proton flux. The top value sensitivity normalized by the area resulted to be equal to 116 ± 16 nC Gy^{-1} cm^{-2}.

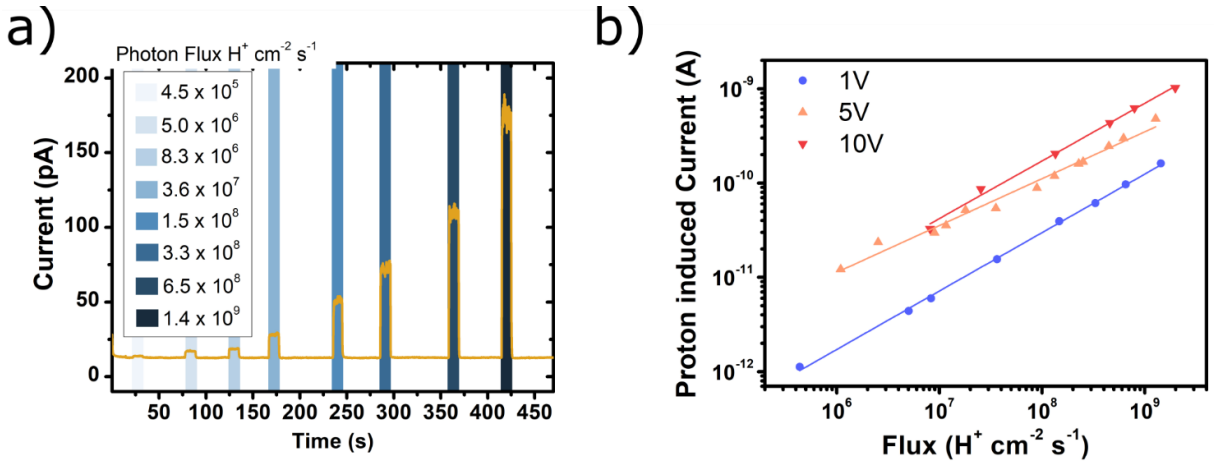

Figure 6.26: Response under 5 MeV proton beam.[171] a) Dynamic response as a function of time for the detector biased at 1 V and irradiated with 10 s proton beam shots. The coloured boxes indicate the increasing proton flux, in the range 4.5 × 10^5 - 1.4 × 10^9 H^+ cm^{-2} s^{-1}. b) Photocurrent as a function of the proton flux for different applied bias.

For the conversion between proton flux and dose the following relation was employed:

$$Dr = \frac{E_{abs} N_p}{\rho_{mixed} V} \qquad (5.3)$$

Where E_{abs} is the energy absorbed by the active layer calculated with SRIM simulations (59 keV); N_p is the proton flux; ρ_{mixed} is the density of the mixed perovskite (3.43 g cm^{-3}), calculated as the weighted average between the 3D and the 2D perovskite composing the mixture, and V is the volume of the active layer, considered as the

product of the perovskite layer thickness (4 µm) and the whole area of the detector (1 mm^2)

To evaluate the LoD, the signal to noise ratio (SNR) was plotted as a function of proton flux in Figure 6.27 and the LoD value was then linearly extrapolated from the plot for a SNR =3. For 1V bias the LoD resulted as low as 1.06 ± 0.03 × 10^5 $H^+s^{-1}cm^{-2}$ corresponding to 729.2 ± 0.2 µGy s^{-1}.

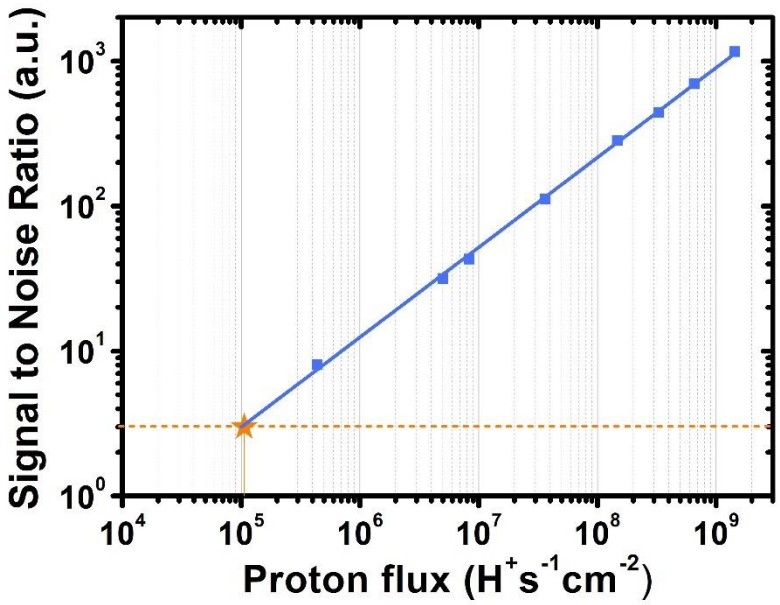

Figure 6.27: LoD.[171] Signal to noise ratio versus proton flux for 1 V bias, the blue squares represent the experimental data, the orange star represent the estimated LoD with a signal to noise ratio of 3.

To assess the stability under operation of the detector, 10 repeated irradiation cycles were performed. The signal variation resulted within 12% with respect to the mean value over 10 repetitions, as reported in Figure 6.28a. Due to the intrinsic fluctuations of the proton flux over different irradiation cycles the data points have been normalized by the relative impinging flux to be compared, and then by the mean value. The radiation hardness of the detector was evaluated by measuring its response in pristine condition and after 40 min irradiation tests, corresponding to a total of 1.7 × 10^{12}

protons impinging on the beam spot area. Figure 6.28b reports the relative variation of induced proton current before and after the prolonged exposure showing no degradation and confirming the reliability of the detector for proton beam monitoring.

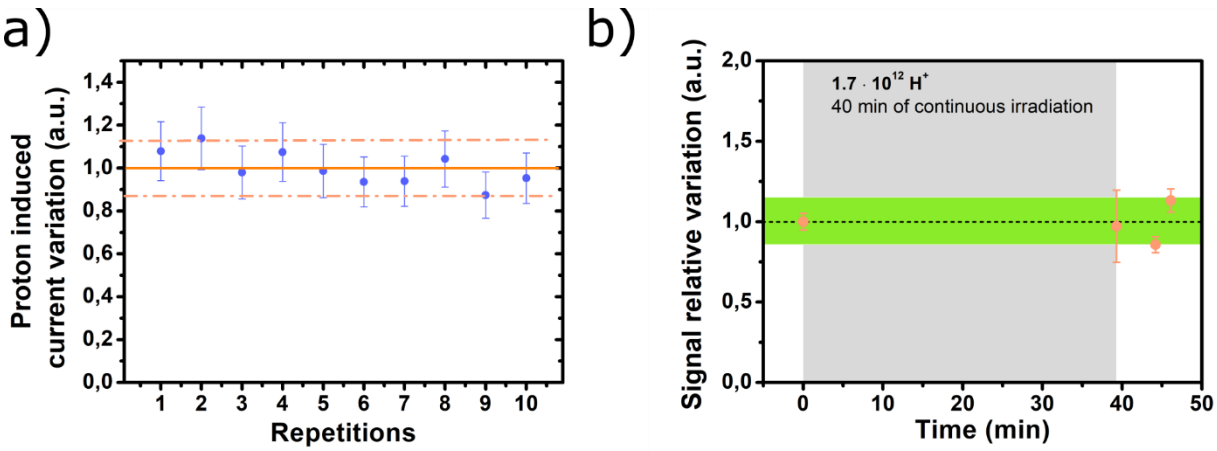

Figure 6.28: Stability under operation.[171] a) Stability of the proton induced photocurrent over 10 repetitions of 10 s irradiation shots, with 5 V bias applied. The dashed orange lines identify the semi-dispersion around the mean value (continuous line). Each data point has been normalized for the impinging proton flux and for the mean value. b) Radiation hardness test. The response of the detector biased at 5 V was measured in pristine condition (first point) and after 40 min of irradiation (second point), for a total of 1.7 × 10^{12} protons impinging on the beam spot area. The measurement was repeated after a few minutes other two times (last two points). The green area indicates the semi-dispersion around the pristine value.

Conclusions

In this thesis, I describe the research activity I have carried out over three years in studying and demonstrating the feasibility of thin-film perovskite based flexible ionizing radiation detectors. In collaboration with different research groups, I successfully fabricated and tested, under different radiation sources, perovskite detectors based on two architectures: photoconductors and photodiodes.

The perovskite active layer has been interfaced with different organic and inorganic materials and the role of interfaces on the X-ray detection was studied. In the p-i-n photodiode architecture different electron and hole transport layer were studied without finding a winning structure outperforming the others. In fact the lowest limit of detection was obtained by using PEDOT:PSS as hole transport layer and PCBM/TiO_x as electron transport and buffer layer respectively, reaching 0.58 ± 0.05 µGy s^{-1}. The X-ray sensitivity under 40 kVp was maximized by employing PTCDI and Cr_2O_3 as electron transport and buffer layer. The top sensitivity recorded was 9.3 ± 0.5 µC Gy^{-1} cm^{-2} at 0 V bias, constituting the current record for hybrid perovskite thin-film X-ray detector operating in passive mode. By fabricating those photodiodes on ultra-thin plastic foil substrates, the first ultraflexible X-ray detector was build, able to be conformed over surfaces with small curvature radius. Thanks to the low substrate X-ray absorption, the device showed an isotropic response to X-ray. Taking advantage of the isotropic response and the ultraflexibility, I design and developed a novel detector concept: the rolled X-ray detector. Rolling the device around a cylindrical support the active volume is compressed in a small area increasing the fraction of absorbed X-ray and the sensitivity up to 26 ± 4 µC Gy^{-1} cm^{-2}.

In photoconductors, the role of PCBM in boosting the detection performance of thin films of PCBM+$MAPbI_3$ blends was studied at the nanoscale combining X-ray fluorescence (XRF) and X-ray Beam Induced Current (XBIC) maps. The experiment conducted at the ID16B beamline at ESRF showed a direct proof of the passivation effect of PCBM at the perovskite grain boundaries. Moreover, the PCBM act as an electron sink creating unbalance charges in the device that activate a gain mechanism improving the response under X-rays. With X-ray fluorescence maps, I captured the degradation of the gold metal electrodes studying its diffusion at different external bias. I compared samples containing PCBM+$MAPbI_3$ with samples featuring only $MAPbI_3$ as active layer finding a faster contact degradation for samples containing PCBM.

Despite the good performance obtained with 3D perovskite-based devices, their instability limits their practical use. Here I studied different perovskite formulations, structures and additives to increase the stability of perovskite thin-films. Stable operation in air was achieved by tuning the perovskite formulation, while long term stability was demonstrated for perovskite-starch composites. The addition of starch as an additive in the precursors' solution allows to control the film thickness obtaining good films with thickness up to 1.4 μm. Three different starch concentrations, corresponding to different film thicknesses, were studied in a photodiode architecture under X-rays. The optimal balance between charge generation and collection was found to be 1050 nm with a top sensitivity of 5.5 ± 0.2 μC Gy^{-1} s^{-1} at 0 V bias. The passive mode operation allowed by the p-i-n architecture increases the device stability decreasing the bias stress on the material. An aging study on perovskite-starch films was performed between May 2019 and February 2021 demonstrating for $MAPbI_3$ with the addition of 20% of starch only a 7% decrease in sensitivity after 630 days of storage in dark in ambient conditions. This is the longest aging study reported so far in literature for perovskite X-ray detectors.

2D perovskites have recently emerged as alternatives to 3D perovskite for ionizing radiation detection thanks to their high environmental stability. In this thesis, I fabricated PEA_2PbBr_4 thin-film detectors by spin-coating directly on interdigitated metal contacts. The devices showed a sensitivity of 806 ± 6 µC Gy^{-1} cm^{-2} under X-rays at 150 kVp. The extremely low and stable dark current permitted the measurement of outstanding 57 nGy s^{-1} as lowest detectable dose rate. The time response of the material was tested under ps-pulsed UV LASER demonstrating an ultrafast rise time of 147 ± 10 ns. The 2D perovskite-based detector was used to measure the gamma-ray radiation emitted by ^{18}F and ^{99}Tc, radio tracers used in medical diagnostics. I proved the possibility to use the detector for monitoring a radiotracer injection in the human body. This technology could be used to predict in real-time wether an injection is succesful or an extravasation occurred that can cause serious problem in the patient. I developed a mixture of the 3D $MAPbBr_3$ and the 2D PEA_2PbBr_4 perovskites featuring a low dark current and good charge transport given by the 3D part of the mixture. The material developed was used as absorbing layer for the first perovskite-based proton detector ever reported. The measurement performed at LABEC under 5 MeV proton beam demonstrated a sensitivity of 116 ± 16 nC Gy^{-1} cm^{-2}. The detectors were fabricated on flexible plastic substrates envisioning future patch on the patient's skin to monitor the delivered dose during hadrontherapy treatments.

Bibliography

1. Hessenbruch, A. A brief history of x-rays. *Endeavour* 26, 137–141 (2002).

2. Knoll, G. F. *Radiation detection and measurement*. (John Wiley, 2010).

3. Lusic, H. & Grinstaff, M. W. X-ray-Computed Tomography Contrast Agents. *Chem. Rev.* 113, 1641–1666 (2013).

4. Fendler, W. P., Rahbar, K., Herrmann, K., Kratochwil, C. & Eiber, M. ^{177}Lu-PSMA Radioligand Therapy for Prostate Cancer. *J Nucl Med* 58, 1196–1200 (2017).

5. Schötzig, U., Schrader, H., Schönfeld, E., Günther, E. & Klein, R. Standardisation and decay data of 177Lu and 188Re. *Applied Radiation and Isotopes* 55, 89–96 (2001).

6. Schardt, D. Hadrontherapy. in *Basic Concepts in Nuclear Physics: Theory, Experiments and Applications* (eds. García-Ramos, J.-E., Alonso, C. E., Andrés, M. V. & Pérez-Bernal, F.) vol. 182 55–86 (Springer International Publishing, 2016).

7. Klassen, N. V., van der Zwan, L. & Cygler, J. GafChromic MD-55: Investigated as a precision dosimeter. *Med. Phys.* 24, 1924–1934 (1997).

8. Chand, S., Mehra, R. & Chopra, V. Recent developments in phosphate materials for their thermoluminescence dosimeter (TLD) applications. *Luminescence* 36, 1808–1817 (2021).

9. Kabir, M. Z. & Kasap, S. Photoconductors for X-Ray Image Detectors. in *Springer Handbook of Electronic and Photonic Materials* (eds. Kasap, S. & Capper, P.) 1–1 (Springer International Publishing, 2017). doi:10.1007/978-3-319-48933-9_45.

10. Fang, J. *et al.* Understanding the Average Electron–Hole Pair-Creation Energy in Silicon and Germanium Based on Full-Band Monte Carlo Simulations. *IEEE Trans. Nucl. Sci.* 66, 444–451 (2019).

11. Basiricò, L., Ciavatti, A. & Fraboni, B. Solution-Grown Organic and Perovskite X-Ray Detectors: A New Paradigm for the Direct Detection of Ionizing Radiation. *Adv. Mater. Technol.* 6, 2000475 (2021).

12. Wang, Y. *et al.* Gleaming Uranium: An Emerging Emitter for Building X-ray Scintillators. *Chem. Eur. J.* 26, 1900–1905 (2020).

13. Wei, H. & Huang, J. Halide lead perovskites for ionizing radiation detection. *Nat Commun* 10, 1066 (2019).

14. Cowen, A. R., Kengyelics, S. M. & Davies, A. G. Solid-state, flat-panel, digital radiography detectors and their physical imaging characteristics. *Clinical Radiology* 63, 487–498 (2008).

15. *X-ray flat panel detectors market size, share and industry analysis by product type*. 160 (2018).

16. Chotas, H. G., Dobbins, J. T. & Ravin, C. E. Principles of Digital Radiography with Large-Area, Electronically Readable Detectors: A Review of the Basics. *Radiology* 210, 595–599 (1999).

17. Hajdok, G., Battista, J. J. & Cunningham, I. A. Fundamental x-ray interaction limits in diagnostic imaging detectors: Spatial resolution: Fundamental resolution limits in diagnostic imaging detectors. *Med. Phys.* 35, 3180–3193 (2008).

18. Huang, H. & Abbaszadeh, S. Recent Developments of Amorphous Selenium-Based X-Ray Detectors: A Review. *IEEE Sensors J.* 20, 1694–1704 (2020).

19. Kasap, S. *et al.* Amorphous selenium and its alloys from early xeroradiography to high resolution X-ray image detectors and ultrasensitive imaging tubes: Amorphous Se from early xeroradiography to high resolution X-ray image detectors. *phys. stat. sol. (b)* 246, 1794–1805 (2009).

20. Gao, X. *et al.* Large-area CdZnTe thick film based array X-ray detector. *Vacuum* 183, 109855 (2021).

21. Temiño, I. *et al.* Morphology and mobility as tools to control and unprecedentedly enhance X-ray sensitivity in organic thin-films. *Nat Commun* 11, 2136 (2020).

22. Tamayo, A. *et al.* X-ray Detectors With Ultrahigh Sensitivity Employing High Performance Transistors Based on a Fully Organic Small Molecule Semiconductor/Polymer Blend Active Layer. *Adv Elect Materials* 2200293 (2022) doi:10.1002/aelm.202200293.

23. Goldschmidt, V. M. Die Gesetze der Krystallochemie. *Naturwissenschaften* 14, 477–485 (1926).

24. Forrester, W. F. & Hinde, R. M. Crystal Structure of Barium Titanate. *Nature* 156, 177–177 (1945).

25. Kagan, C. R., Mitzi, D. B. & Dimitrakopoulos, C. D. Organic-Inorganic Hybrid Materials as Semiconducting Channels in Thin-Film Field-Effect Transistors. *Science* 286, 945–947 (1999).

26. Kojima, A., Teshima, K., Shirai, Y. & Miyasaka, T. Organometal Halide Perovskites as Visible-Light Sensitizers for Photovoltaic Cells. *J. Am. Chem. Soc.* 131, 6050–6051 (2009).

27. Jeong, J. *et al.* Pseudo-halide anion engineering for α-FAPbI3 perovskite solar cells. *Nature* 592, 381–385 (2021).

28. Stoumpos, C. C. *et al.* Crystal Growth of the Perovskite Semiconductor CsPbBr$_3$: A New Material for High-Energy Radiation Detection. *Crystal Growth & Design* 13, 2722–2727 (2013).

29. Kakavelakis, G. *et al.* Metal Halide Perovskites for High-Energy Radiation Detection. *Adv. Sci.* 7, 2002098 (2020).

30. Krishnamoorthy, T. *et al.* Lead-free germanium iodide perovskite materials for photovoltaic applications. *J. Mater. Chem. A* 3, 23829–23832 (2015).

31. Stoumpos, C. C., Malliakas, C. D. & Kanatzidis, M. G. Semiconducting Tin and Lead Iodide Perovskites with Organic Cations: Phase Transitions, High Mobilities, and Near-Infrared Photoluminescent Properties. *Inorg. Chem.* 52, 9019–9038 (2013).

32. Tai, Q., Cao, J., Wang, T. & Yan, F. Recent advances toward efficient and stable tin-based perovskite solar cells. *EcoMat* 1, (2019).

33. Yu, H. *et al.* The Role of Chlorine in the Formation Process of "$CH_3NH_3PbI_{3-x}Cl_x$" Perovskite. *Adv. Funct. Mater.* n/a-n/a (2014) doi:10.1002/adfm.201401872.

34. Eperon, G. E. *et al.* Formamidinium lead trihalide: a broadly tunable perovskite for efficient planar heterojunction solar cells. *Energy Environ. Sci.* 7, 982 (2014).

35. Mao, L., Stoumpos, C. C. & Kanatzidis, M. G. Two-Dimensional Hybrid Halide Perovskites: Principles and Promises. *J. Am. Chem. Soc.* 141, 1171–1190 (2019).

36. Sestu, N. *et al.* Absorption F-Sum Rule for the Exciton Binding Energy in Methylammonium Lead Halide Perovskites. *J. Phys. Chem. Lett.* 6, 4566–4572 (2015).

37. Lan, C., Zhou, Z., Wei, R. & Ho, J. C. Two-dimensional perovskite materials: From synthesis to energy-related applications. *Materials Today Energy* 11, 61–82 (2019).

38. Depuydt, B., Theuwis, A. & Romandic, I. Germanium: From the first application of Czochralski crystal growth to large diameter dislocation-free wafers. *Materials Science in Semiconductor Processing* 9, 437–443 (2006).

39. He, Y. *et al.* High spectral resolution of gamma-rays at room temperature by perovskite CsPbBr3 single crystals. *Nat Commun* 9, 1609 (2018).

40. He, Y. *et al.* Perovskite CsPbBr3 single crystal detector for alpha-particle spectroscopy. *Nuclear Instruments and Methods in Physics Research Section A: Accelerators, Spectrometers, Detectors and Associated Equipment* 922, 217–221 (2019).

41. Matt, G. J. *et al.* Sensitive Direct Converting X-Ray Detectors Utilizing Crystalline $CsPbBr_3$ Perovskite Films Fabricated via Scalable Melt Processing. *Adv. Mater. Interfaces* 7, 1901575 (2020).

42. Pan, W. *et al.* Hot-Pressed $CsPbBr_3$ Quasi-Monocrystalline Film for Sensitive Direct X-ray Detection. *Adv. Mater.* 31, 1904405 (2019).

43. Dualeh, A., Gao, P., Seok, S. I., Nazeeruddin, M. K. & Grätzel, M. Thermal Behavior of Methylammonium Lead-Trihalide Perovskite Photovoltaic Light Harvesters. *Chem. Mater.* 26, 6160–6164 (2014).

44. Saidaminov, M. I. *et al.* High-quality bulk hybrid perovskite single crystals within minutes by inverse temperature crystallization. *Nat Commun* 6, 7586 (2015).

45. Yakunin, S. *et al.* Detection of gamma photons using solution-grown single crystals of hybrid lead halide perovskites. *Nature Photon* 10, 585–589 (2016).

46. Huang, Y. *et al.* A-site Cation Engineering for Highly Efficient $MAPbI_3$ Single-Crystal X-ray Detector. *Angew. Chem. Int. Ed.* 58, 17834–17842 (2019).

47. Wei, W. *et al.* Monolithic integration of hybrid perovskite single crystals with heterogenous substrate for highly sensitive X-ray imaging. *Nature Photon* 11, 315–321 (2017).

48. Zhang, H. *et al.* High-sensitivity X-ray detectors based on solution-grown caesium lead bromide single crystals. *J. Mater. Chem. C* 10.1039.C9TC05490A (2020) doi:10.1039/C9TC05490A.

49. Wei, H. *et al.* Dopant compensation in alloyed CH3NH3PbBr3−xClx perovskite single crystals for gamma-ray spectroscopy. *Nature Mater* 16, 826–833 (2017).

50. Liu, Y. *et al.* Triple-Cation and Mixed-Halide Perovskite Single Crystal for High-Performance X-ray Imaging. *Adv. Mater.* 33, 2006010 (2021).

51. Andričević, P. *et al.* Kilogram-Scale Crystallogenesis of Halide Perovskites for Gamma-Rays Dose Rate Measurements. *Adv. Sci.* 8, 2001882 (2021).

52. Wei, H. *et al.* Sensitive X-ray detectors made of methylammonium lead tribromide perovskite single crystals. *Nature Photon* 10, 333–339 (2016).

53. Li, H. *et al.* Sensitive and Stable 2D Perovskite Single-Crystal X-ray Detectors Enabled by a Supramolecular Anchor. *Adv. Mater.* 32, 2003790 (2020).

54. Ji, C. *et al.* 2D Hybrid Perovskite Ferroelectric Enables Highly Sensitive X-Ray Detection with Low Driving Voltage. *Adv. Funct. Mater.* 1905529 (2019) doi:10.1002/adfm.201905529.

55. Shrestha, S. *et al.* High-performance direct conversion X-ray detectors based on sintered hybrid lead triiodide perovskite wafers. *Nature Photon* 11, 436–440 (2017).

56. Daum, M. *et al.* Self-Healing $Cs_3Bi_2Br_3I_6$ Perovskite Wafers for X-Ray Detection. *Adv Funct Materials* 31, 2102713 (2021).

57. Hu, M. *et al.* Large and Dense Organic–Inorganic Hybrid Perovskite $CH_3NH_3PbI_3$ Wafer Fabricated by One-Step Reactive Direct Wafer Production with High X-ray Sensitivity. *ACS Appl. Mater. Interfaces* 12, 16592–16600 (2020).

58. Yakunin, S. *et al.* Detection of X-ray photons by solution-processed lead halide perovskites. *Nature Photon* 9, 444–449 (2015).

59. Basiricò, L. *et al.* Detection of X-Rays by Solution-Processed Cesium-Containing Mixed Triple Cation Perovskite Thin Films. *Adv. Funct. Mater.* 29, 1902346 (2019).

60. Tsai, H. *et al.* A sensitive and robust thin-film x-ray detector using 2D layered perovskite diodes. *Sci. Adv.* 6, eaay0815 (2020).

61. Kim, Y. C. *et al.* Printable organometallic perovskite enables large-area, low-dose X-ray imaging. *Nature* 550, 87–91 (2017).

62. Jia, Z. *et al.* Spray-coating of AgI incorporated metal halide perovskites for high-performance X-ray detection. *Chemical Engineering Journal* 450, 138229 (2022).

63. Gou, Z. *et al.* Self-Powered X-Ray Detector Based on All-Inorganic Perovskite Thick Film with High Sensitivity Under Low Dose Rate. *Phys. Status Solidi RRL* 13, 1900094 (2019).

64. Peng, X. *et al.* Perovskite and Organic Solar Cells Fabricated by Inkjet Printing: Progress and Prospects. *Adv. Funct. Mater.* 27, 1703704 (2017).

65. Liu, J. *et al.* Perovskite X-Ray Detectors: Flexible, Printable Soft-X-Ray Detectors Based on All-Inorganic Perovskite Quantum Dots (Adv. Mater. 30/2019). *Adv. Mater.* 31, 1970214 (2019).

66. Mescher, H. *et al.* Flexible Inkjet-Printed Triple Cation Perovskite X-ray Detectors. *ACS Appl. Mater. Interfaces* 12, 15774–15784 (2020).

67. Kumar, S. *Additive Manufacturing Processes*. (Springer International Publishing, 2020). doi:10.1007/978-3-030-45089-2.

68. Glushkova, A. *et al.* Ultrasensitive 3D Aerosol-Jet-Printed Perovskite X-ray Photodetector. *ACS Nano* 15, 4077–4084 (2021).

69. He, Y., Hadar, I. & Kanatzidis, M. G. Detecting ionizing radiation using halide perovskite semiconductors processed through solution and alternative methods. *Nat. Photon.* 16, 14–26 (2022).

70. Murty, R. C. Effective Atomic Numbers of Heterogeneous Materials. *Nature* 207, 398–399 (1965).

71. Owens, A. & Peacock, A. Compound semiconductor radiation detectors. *Nuclear Instruments and Methods in Physics Research Section A: Accelerators, Spectrometers, Detectors and Associated Equipment* 531, 18–37 (2004).

72. Ke, W., Stoumpos, C. C. & Kanatzidis, M. G. "Unleaded" Perovskites: Status Quo and Future Prospects of Tin-Based Perovskite Solar Cells. *Adv. Mater.* 31, 1803230 (2019).

73. Schileo, G. & Grancini, G. Lead or no lead? Availability, toxicity, sustainability and environmental impact of lead-free perovskite solar cells. *J. Mater. Chem. C* 9, 67–76 (2021).

74. Yaffe, O. *et al.* Local Polar Fluctuations in Lead Halide Perovskite Crystals. *Phys. Rev. Lett.* 118, 136001 (2017).

75. Miyata, K. & Zhu, X.-Y. Ferroelectric large polarons. *Nature Materials* 17, 379–381 (2018).

76. Srimath Kandada, A. R. & Silva, C. Exciton Polarons in Two-Dimensional Hybrid Metal-Halide Perovskites. *J. Phys. Chem. Lett.* 11, 3173–3184 (2020).

77. Brenner, T. M., Egger, D. A., Kronik, L., Hodes, G. & Cahen, D. Hybrid organic—inorganic perovskites: low-cost semiconductors with intriguing charge-transport properties. *Nature Reviews Materials* 1, 15007 (2016).

78. Shi, D. *et al.* Low trap-state density and long carrier diffusion in organolead trihalide perovskite single crystals. *Science* 347, 519–522 (2015).

79. Yin, W.-J., Shi, T. & Yan, Y. Unusual defect physics in CH3NH3PbI3 perovskite solar cell absorber. *Appl. Phys. Lett.* 104, 063903 (2014).

80. Schilcher, M. J. *et al.* The Significance of Polarons and Dynamic Disorder in Halide Perovskites. *ACS Energy Lett.* 6, 2162–2173 (2021).

81. Haughn, C. R. *et al.* Quantification of trap state densities in GaAs heterostructures grown at varying rates using intensity-dependent time resolved photoluminescence. *Appl. Phys. Lett.* 102, 182108 (2013).

82. Yuan, Y. & Huang, J. Ion Migration in Organometal Trihalide Perovskite and Its Impact on Photovoltaic Efficiency and Stability. *Acc. Chem. Res.* 49, 286–293 (2016).

83. Luo, Y. *et al.* Direct Observation of Halide Migration and its Effect on the Photoluminescence of Methylammonium Lead Bromide Perovskite Single Crystals. *Adv. Mater.* 29, 1703451 (2017).

84. Yuan, Y. *et al.* Photovoltaic Switching Mechanism in Lateral Structure Hybrid Perovskite Solar Cells. *Advanced Energy Materials* 5, 1500615 (2015).

85. Jeon, N. J. *et al.* Solvent engineering for high-performance inorganic–organic hybrid perovskite solar cells. *Nature Mater* 13, 897–903 (2014).

86. Niu, G., Guo, X. & Wang, L. Review of recent progress in chemical stability of perovskite solar cells. *J. Mater. Chem. A* 3, 8970–8980 (2015).

87. Wang, R. *et al.* A Review of Perovskites Solar Cell Stability. *Adv. Funct. Mater.* 29, 1808843 (2019).

88. He, Y. *et al.* CsPbBr3 perovskite detectors with 1.4% energy resolution for high-energy γ-rays. *Nat. Photonics* 15, 36–42 (2021).

89. Xu, Q. *et al.* Detection of charged particles with a methylammonium lead tribromide perovskite single crystal. *Nuclear Instruments and Methods in Physics Research Section A: Accelerators, Spectrometers, Detectors and Associated Equipment* 848, 106–108 (2017).

90. El Bouanani, L. *et al.* Solid-State Neutron Detection Based on Methylammonium Lead Bromide Perovskite Single Crystals. *ACS Appl. Mater. Interfaces* 13, 28049–28056 (2021).

91. Deumel, S. *et al.* High-sensitivity high-resolution X-ray imaging with soft-sintered metal halide perovskites. *Nat Electron* 4, 681–688 (2021).

92. Mescher, H. *et al.* Flexible Inkjet-Printed Triple Cation Perovskite X-ray Detectors. *ACS Appl. Mater. Interfaces* 12, 15774–15784 (2020).

93. Ciavatti, A. *et al.* High-Sensitivity Flexible X-Ray Detectors based on Printed Perovskite Inks. *Adv. Funct. Mater.* 31, 2009072 (2021).

94. Zhao, J. *et al.* Perovskite-filled membranes for flexible and large-area direct-conversion X-ray detector arrays. *Nat. Photonics* 14, 612–617 (2020).

95. Gao, Y. *et al.* Ultrathin and Ultrasensitive Direct X-ray Detector Based on Heterojunction Phototransistors. *Adv. Mater.* 33, 2101717 (2021).

96. Tsai, H. *et al.* A sensitive and robust thin-film x-ray detector using 2D layered perovskite diodes. *Sci. Adv.* 6, eaay0815 (2020).

97. Emslie, A. G., Bonner, F. T. & Peck, L. G. Flow of a Viscous Liquid on a Rotating Disk. *Journal of Applied Physics* 29, 858–862 (1958).

98. Yin, X. *et al.* Highly Efficient Flexible Perovskite Solar Cells Using Solution-Derived NiO_x Hole Contacts. *ACS Nano* 10, 3630–3636 (2016).

99. Reverchon, J.-L., Huet, F., Poisson, M.-A. & Duboz, J.-Y. Photoconductance measurements on thin InGaN layers. *Journal of Applied Physics* 88, 5138–5141 (2000).

100. Poludniowski, G., Landry, G., DeBlois, F., Evans, P. M. & Verhaegen, F. *SpekCalc* : a program to calculate photon spectra from tungsten anode x-ray tubes. *Phys. Med. Biol.* 54, N433–N438 (2009).

101. Poludniowski, G. G. & Evans, P. M. Calculation of x-ray spectra emerging from an x-ray tube. Part I. Electron penetration characteristics in x-ray targets: Calculation of x-ray spectra. Part I. *Med. Phys.* 34, 2164–2174 (2007).

102. Poludniowski, G. G. Calculation of x-ray spectra emerging from an x-ray tube. Part II. X-ray production and filtration in x-ray targets: Calculation of x-ray spectra. Part II. *Med. Phys.* 34, 2175–2186 (2007).

103. Ziegler, J. F., Ziegler, M. D. & Biersack, J. P. SRIM – The stopping and range of ions in matter (2010). *Nuclear Instruments and Methods in Physics Research Section B: Beam Interactions with Materials and Atoms* 268, 1818–1823 (2010).

104. Raimondi, P. ESRF-EBS: The Extremely Brilliant Source Project. *Synchrotron Radiation News* 29, 8–15 (2016).

105. Martínez-Criado, G. *et al.* ID16B: a hard X-ray nanoprobe beamline at the ESRF for nano-analysis. *J Synchrotron Rad* 23, 344–352 (2016).

106. Kodur, M. *et al.* X-Ray Microscopy of Halide Perovskites: Techniques, Applications, and Prospects. *Adv. Energy Mater.* 10, 1903170 (2020).

107. Solé, V. A., Papillon, E., Cotte, M., Walter, Ph. & Susini, J. A multiplatform code for the analysis of energy-dispersive X-ray fluorescence spectra. *Spectrochimica Acta Part B: Atomic Spectroscopy* 62, 63–68 (2007).

108. Ferrari, L. M., Keller, K., Burtscher, B. & Greco, F. Temporary tattoo as unconventional substrate for conformable and transferable electronics on skin and beyond. *Multifunct. Mater.* 3, 032003 (2020).

109. Kaltenbrunner, M. *et al.* An ultra-lightweight design for imperceptible plastic electronics. *Nature* 499, 458–463 (2013).

110. Demchyshyn, S. *et al.* Designing Ultraflexible Perovskite X-Ray Detectors through Interface Engineering. *Adv. Sci.* 2002586 (2020) doi:10.1002/advs.202002586.

111. Rathore, S., Han, G., Kumar, A., Leong, W. L. & Singh, A. Elastic modulus tailoring in CH3NH3PbI3 perovskite system by the introduction of two dimensionality using (5-AVA)2PbI4. *Solar Energy* 224, 27–34 (2021).

112. Shao, Y., Xiao, Z., Bi, C., Yuan, Y. & Huang, J. Origin and elimination of photocurrent hysteresis by fullerene passivation in CH3NH3PbI3 planar heterojunction solar cells. *Nat Commun* 5, 5784 (2014).

113. Hailegnaw, B. *et al.* Inverted (p–i–n) perovskite solar cells using a low temperature processed TiO_x interlayer. *RSC Adv.* 8, 24836–24846 (2018).

114. Back, H. *et al.* Achieving long-term stable perovskite solar cells via ion neutralization. *Energy Environ. Sci.* 9, 1258–1263 (2016).

115. Sutherland, B. R. *et al.* Sensitive, Fast, and Stable Perovskite Photodetectors Exploiting Interface Engineering. *ACS Photonics* 2, 1117–1123 (2015).

116. Matt, G. J. *et al.* Sensitive Direct Converting X-Ray Detectors Utilizing Crystalline $CsPbBr_3$ Perovskite Films Fabricated via Scalable Melt Processing. *Adv. Mater. Interfaces* 7, 1901575 (2020).

117. Huang, C., Barlow, S. & Marder, S. R. Perylene-3,4,9,10-tetracarboxylic Acid Diimides: Synthesis, Physical Properties, and Use in Organic Electronics. *J. Org. Chem.* 76, 2386–2407 (2011).

118. Lou, Y.-H., Wang, Z.-K., Yuan, D.-X., Okada, H. & Liao, L.-S. Interfacial degradation effects of aqueous solution-processed molybdenum trioxides on the stability of organic solar cells evaluated by a differential method. *Appl. Phys. Lett.* 105, 113301 (2014).

119. Kaltenbrunner, M. *et al.* Flexible high power-per-weight perovskite solar cells with chromium oxide–metal contacts for improved stability in air. *Nature Mater* 14, 1032–1039 (2015).

120. Venugopalan, V. *et al.* High-Detectivity Perovskite Light Detectors Printed in Air from Benign Solvents. *Chem* 5, 868–880 (2019).

121. Lawrence Bright, E., Giacobbe, C. & Wright, J. P. Beam heating from a fourth-generation synchrotron source. *J Synchrotron Rad* 28, 1377–1385 (2021).

122. Rosenthal, M. *et al.* High-resolution thermal imaging with a combination of nano-focus X-ray diffraction and ultra-fast chip calorimetry. *J Synchrotron Rad* 21, 223–228 (2014).

123. Basirico, L. *et al.* Direct X-ray photoconversion in flexible organic thin film devices operated below 1 V. *NATURE COMMUNICATIONS* 9.

124. Armin, A., Shoaee, S., Lin, Q., Burn, P. L. & Meredith, P. On the unipolarity of charge transport in methanofullerene diodes. *npj Flex Electron* 1, 13 (2017).

125. Herz, L. M. Charge-Carrier Mobilities in Metal Halide Perovskites: Fundamental Mechanisms and Limits. *ACS Energy Lett.* 2, 1539–1548 (2017).

126. Domanski, K. *et al.* Not All That Glitters Is Gold: Metal-Migration-Induced Degradation in Perovskite Solar Cells. *ACS Nano* 10, 6306–6314 (2016).

127. Pospisil, J. *et al.* Reversible Formation of Gold Halides in Single-Crystal Hybrid-Perovskite/Au Interface upon Biasing and Effect on Electronic Carrier Injection. *Adv. Funct. Mater.* 29, 1900881 (2019).

128. Boyd, C. C., Cheacharoen, R., Leijtens, T. & McGehee, M. D. Understanding Degradation Mechanisms and Improving Stability of Perovskite Photovoltaics. *Chem. Rev.* 119, 3418–3451 (2019).

129. Shi, L. *et al.* Gas chromatography–mass spectrometry analyses of encapsulated stable perovskite solar cells. *Science* 368, eaba2412 (2020).

130. Zhang, T., Hu, C. & Yang, S. Ion Migration: A "Double-Edged Sword" for Halide-Perovskite-Based Electronic Devices. *Small Methods* 4, 1900552 (2020).

131. Chandrashekar, N., Gautam, S. M., Srinivas, K. S. & Vijayananda, J. Challenges in Requirements Engineering for a Platform group: Case Study with a Medical Imaging Platform. in *Fourth International Conference on Software Engineering Research, Management and Applications (SERA'06)* 5–12 (IEEE, 2006). doi:10.1109/SERA.2006.21.

132. Saliba, M. Perovskite solar cells must come of age. *Science* 359, 388–389 (2018).

133. Pan, W. *et al.* Cs2AgBiBr6 single-crystal X-ray detectors with a low detection limit. *Nature Photon* 11, 726–732 (2017).

134. Zhuang, R. *et al.* Highly sensitive X-ray detector made of layered perovskite-like (NH4)3Bi2I9 single crystal with anisotropic response. *Nat. Photonics* 13, 602–608 (2019).

135. Liu, Y. *et al.* Large Lead-Free Perovskite Single Crystal for High-Performance Coplanar X-Ray Imaging Applications. *Adv. Optical Mater.* 8, 2000814 (2020).

136. Wu, J. *et al.* Self-Powered $FA_{0.55}MA_{0.45}PbI_3$ Single-Crystal Perovskite X-Ray Detectors with High Sensitivity. *Adv Funct Materials* 32, 2109149 (2022).

137. Zhou, Y. *et al.* Heterojunction structures for reduced noise in large-area and sensitive perovskite x-ray detectors. *Sci. Adv.* 7, eabg6716 (2021).

138. Zhao, J. *et al.* Perovskite-filled membranes for flexible and large-area direct-conversion X-ray detector arrays. *Nat. Photonics* 14, 612–617 (2020).

139. Zhang, H. *et al.* Encapsulated X-Ray Detector Enabled by All-Inorganic Lead-Free Perovskite Film With High Sensitivity and Low Detection Limit. *IEEE Trans. Electron Devices* 67, 3191–3198 (2020).

140. Song, Y. *et al.* Elimination of Interfacial-Electrochemical-Reaction-Induced Polarization in Perovskite Single Crystals for Ultrasensitive and Stable X-Ray Detector Arrays. *Advanced Materials* 33, 2103078 (2021).

141. Fu, Q. *et al.* Recent Progress on the Long-Term Stability of Perovskite Solar Cells. *Adv. Sci.* 5, 1700387 (2018).

142. Deumel, S. *et al.* Organometal halide perovskite imager: a comparison 1.5 years after fabrication. in *Medical Imaging 2022: Physics of Medical Imaging* (eds. Zhao, W. & Yu, L.) 8 (SPIE, 2022). doi:10.1117/12.2610586.

143. Giuri, A. *et al.* Polymeric rheology modifier allows single-step coating of perovskite ink for highly efficient and stable solar cells. *Nano Energy* 54, 400–408 (2018).

144. Giuri, A. *et al.* Robust, High-Performing Maize–Perovskite-Based Solar Cells with Improved Stability. *ACS Appl. Energy Mater.* 4, 11194–11203 (2021).

145. Malinkiewicz, O. *et al.* Perovskite solar cells employing organic charge-transport layers. *Nature Photon* 8, 128–132 (2014).

146. Chen, H. *et al.* Extending the environmental lifetime of unpackaged perovskite solar cells through interfacial design. *J. Mater. Chem. A* 4, 11604–11610 (2016).

147. Patel, J. B. *et al.* Photocurrent Spectroscopy of Perovskite Solar Cells Over a Wide Temperature Range from 15 to 350 K. *J. Phys. Chem. Lett.* 9, 263–268 (2018).

148. Jeon, N. J. *et al.* Compositional engineering of perovskite materials for high-performance solar cells. *Nature* 517, 476–480 (2015).

149. Lyu, M. & Park, N.-G. Effect of Additives AX (A = FA, MA, Cs, Rb, NH_4, X = Cl, Br, I) in $FAPbI_3$ on Photovoltaic Parameters of Perovskite Solar Cells. *Sol. RRL* 4, 2000331 (2020).

150. Pellet, N. *et al.* Mixed-Organic-Cation Perovskite Photovoltaics for Enhanced Solar-Light Harvesting. *Angew. Chem. Int. Ed.* 53, 3151–3157 (2014).

151. Armaroli, G. *et al.* X-Ray-Induced Modification of the Photophysical Properties of $MAPbBr_3$ Single Crystals. *ACS Appl. Mater. Interfaces* 13, 58301–58308 (2021).

152. Frost, J. M. *et al.* Atomistic Origins of High-Performance in Hybrid Halide Perovskite Solar Cells. *Nano Lett.* 14, 2584–2590 (2014).

153. Berhe, T. A. *et al.* Organometal halide perovskite solar cells: degradation and stability. *Energy Environ. Sci.* 9, 323–356 (2016).

154. Mamun, A. A., Mohammed, Y., Ava, T. T., Namkoong, G. & Elmustafa, A. A. Influence of air degradation on morphology, crystal size and mechanical hardness of perovskite film. *Materials Letters* 229, 167–170 (2018).

155. Quan, L. N. *et al.* Tailoring the Energy Landscape in Quasi-2D Halide Perovskites Enables Efficient Green-Light Emission. *Nano Lett.* 17, 3701–3709 (2017).

156. Zhang, Y. *et al.* Two-dimensional (PEA)2PbBr4 perovskite single crystals for a high performance UV-detector. *J. Mater. Chem. C* 7, 1584–1591 (2019).

157. Liu, Y. *et al.* Multi-inch single-crystalline perovskite membrane for high-detectivity flexible photosensors. *Nat Commun* 9, 5302 (2018).

158. Lédée, F., Ciavatti, A., Verdi, M., Basiricò, L. & Fraboni, B. Ultra-Stable and Robust Response to X-Rays in 2D Layered Perovskite Micro-Crystalline Films Directly Deposited on Flexible Substrate. *Advanced Optical Materials* 10, 2101145 (2022).

159. Shibuya, K., Koshimizu, M., Nishikido, F., Saito, H. & Kishimoto, S. Poly[bis(phenethylammonium) [dibromidoplumbate(II)]-di-μ-bromido]]. *Acta Crystallogr E Struct Rep Online* 65, m1323–m1324 (2009).

160. Blancon, J.-C. *et al.* Scaling law for excitons in 2D perovskite quantum wells. *Nat Commun* 9, 2254 (2018).

161. Zhou, W. *et al.* Electronic and optical absorption properties of organic–inorganic perovskites as influenced by different long-chain diamine molecules: first-principles calculations. *RSC Adv.* 9, 14718–14726 (2019).

162. Liu, Y. *et al.* Surface-Tension-Controlled Crystallization for High-Quality 2D Perovskite Single Crystals for Ultrahigh Photodetection. *Matter* 1, 465–480 (2019).

163. Peng, W. *et al.* Ultralow Self-Doping in Two-dimensional Hybrid Perovskite Single Crystals. *Nano Lett.* 17, 4759–4767 (2017).

164. Gan, Z. *et al.* The Dominant Energy Transport Pathway in Halide Perovskites: Photon Recycling or Carrier Diffusion? *Adv. Energy Mater.* 9, 1900185 (2019).

165. Shen, L. *et al.* Integration of perovskite and polymer photoactive layers to produce ultrafast response, ultraviolet-to-near-infrared, sensitive photodetectors. *Mater. Horiz.* 4, 242–248 (2017).

166. Delport, G. *et al.* Exciton–Exciton Annihilation in Two-Dimensional Halide Perovskites at Room Temperature. *J. Phys. Chem. Lett.* 10, 5153–5159 (2019).

167. Gou, Z. *et al.* Self-Powered X-Ray Detector Based on All-Inorganic Perovskite Thick Film with High Sensitivity Under Low Dose Rate. *Phys. Status Solidi RRL* 13, 1900094 (2019).

168. Grau, C., Durante, M., Georg, D., Langendijk, J. A. & Weber, D. C. Particle therapy in Europe. *Mol Oncol* 14, 1492–1499 (2020).

169. Zhang, Y. & Park, N.-G. Quasi-Two-Dimensional Perovskite Solar Cells with Efficiency Exceeding 22%. *ACS Energy Lett.* 7, 757–765 (2022).

170. Zhang, L. *et al.* High-performance quasi-2D perovskite light-emitting diodes: from materials to devices. *Light Sci Appl* 10, 61 (2021).

171. Basiricò, L. *et al.* Mixed 3D–2D Perovskite Flexible Films for the Direct Detection of 5 MeV Protons. *Advanced Science* 10, 2204815 (2023).

172. Schrode, B. *et al. GIDVis*: a comprehensive software tool for geometry-independent grazing-incidence X-ray diffraction data analysis and pole-figure calculations. *J Appl Crystallogr* 52, 683–689 (2019).

173. Droseros, N., Tsokkou, D. & Banerji, N. Photophysics of Methylammonium Lead Tribromide Perovskite: Free Carriers, Excitons, and Sub-Bandgap States. *Adv. Energy Mater.* 10, 1903258 (2020).

174. Mannino, G. *et al.* Temperature-Dependent Optical Band Gap in $CsPbBr_3$, $MAPbBr_3$, and $FAPbBr_3$ Single Crystals. *J. Phys. Chem. Lett.* 11, 2490–2496 (2020).

175. Kahmann, S. *et al.* Photophysics of Two-Dimensional Perovskites—Learning from Metal Halide Substitution. *Adv Funct Materials* 31, 2103778 (2021).

176. Droseros, N. *et al.* Origin of the Enhanced Photoluminescence Quantum Yield in $MAPbBr_3$ Perovskite with Reduced Crystal Size. *ACS Energy Lett.* 3, 1458–1466 (2018).

177. Chiari, M. *et al.* LABEC, the INFN ion beam laboratory of nuclear techniques for environment and cultural heritage. *Eur. Phys. J. Plus* 136, 472 (2021).

178. Ziegler, J. F., Ziegler, M. D. & Biersack, J. P. SRIM – The stopping and range of ions in matter (2010). *Nuclear Instruments and Methods in Physics Research Section B: Beam Interactions with Materials and Atoms* 268, 1818–1823 (2010).

179. Fratelli, I. *et al.* Direct detection of 5-MeV protons by flexible organic thin-film devices. *Sci. Adv.* 7, eabf4462 (2021).

Acknowledgement

There are many people to thank behind this work, I will probably not be able to properly thank them in these few lines. Thank you to everyone who supported me during my Ph.D.

I would like to thank my supervisor Prof. Beatrice Fraboni for giving me the possibility to start the Ph.D. and continuing the work started together during my master's. Thank you for all the support, teachings, and advices you offered me in the last years despite the pandemic. Your advices were precious and lead to this final work.

An enormous thanks to Laura Basiricò and Andrea Ciavatti. I couldn't desire better guides for my academic journey. Thank you for your patience, and for making those years amazing with yours always present advices and personal support.

A special thanks to Prof. Martin Kaltenbrunner who offered me the possibility to spend a period at the JKU university in Linz. Thank you for your support. I would also like to specially thank all the SoMaP team members who worked with me: Stepan, Beki, Lukas and Christoph. Thank you for all the teachings about perovskite and device fabrication.

Thanks to Silvia Colella, Aurora Rizzo and Antonella Giuri for the fruitful collaboration on perovskite-starch composites.

I would like to acknowledge Margerita Bolognasi, Marco Natali and Margherita Taddei for our collaboration during the FORTRESS project.

Thanks to Federica Fioroni, Elisa, Lorenzo Piergallini and Muaro Iori for hosting me in the laboratories of the IRCCS of Reggio Emilia and for the support during the gamma measurements.

A special thank goes to Valentina Cicero, Nicolò Tosi and Alessandro Montanari for the development of the readout electronics that lead to the creation of a working detector demo.

A huge thanks to Ferdinand Lédée for everything, we spent a lot of time together in the lab. I had a lot of fun with you.

Thanks to all the guys of the Ph.D. room and not, DIFA is not DIFA without you. These years would not be the same without you. You made every single day special. I will miss every one of you in my new adventure. Giovanni, you supported me for 7 years in my Bologna adventure. We did everything together at UNIBO and it was amazing, hopefully our road will meet again somewhere because I do not know if I can work without you... Never tried...

I want to thank my friends from Serramazzoni that magical land where my hart will always belong, you were there always. Thank you.

Thank you Costanzolina to be at my side supporting end encouraging me. Despite your attempts to make me sound ridiculous with your cute nicknames in front of my colleagues, I am here at the end of this journey using your nickname in my thesis.

Thanks to my family for the support, none of this would have been possible at the start without you. No matter how far I will go you will always be my starting point.